

COMPUTATIONAL INTELLIGENCE IN PERSONALIZED MEDICINE

EDITED BY: Khin Wee Lai, Khairunnisa Hasikin, Yuanpeng Zhang and
Yan Chai Hum

PUBLISHED IN: Frontiers in Pharmacology





frontiers

Frontiers eBook Copyright Statement

The copyright in the text of individual articles in this eBook is the property of their respective authors or their respective institutions or funders. The copyright in graphics and images within each article may be subject to copyright of other parties. In both cases this is subject to a license granted to Frontiers.

The compilation of articles constituting this eBook is the property of Frontiers.

Each article within this eBook, and the eBook itself, are published under the most recent version of the Creative Commons CC-BY licence.

The version current at the date of publication of this eBook is CC-BY 4.0. If the CC-BY licence is updated, the licence granted by Frontiers is automatically updated to the new version.

When exercising any right under the CC-BY licence, Frontiers must be attributed as the original publisher of the article or eBook, as applicable.

Authors have the responsibility of ensuring that any graphics or other materials which are the property of others may be included in the CC-BY licence, but this should be checked before relying on the CC-BY licence to reproduce those materials. Any copyright notices relating to those materials must be complied with.

Copyright and source acknowledgement notices may not be removed and must be displayed in any copy, derivative work or partial copy which includes the elements in question.

All copyright, and all rights therein, are protected by national and international copyright laws. The above represents a summary only. For further information please read Frontiers' Conditions for Website Use and Copyright Statement, and the applicable CC-BY licence.

ISSN 1664-8714

ISBN 978-2-83250-592-2

DOI 10.3389/978-2-83250-592-2

About Frontiers

Frontiers is more than just an open-access publisher of scholarly articles: it is a pioneering approach to the world of academia, radically improving the way scholarly research is managed. The grand vision of Frontiers is a world where all people have an equal opportunity to seek, share and generate knowledge. Frontiers provides immediate and permanent online open access to all its publications, but this alone is not enough to realize our grand goals.

Frontiers Journal Series

The Frontiers Journal Series is a multi-tier and interdisciplinary set of open-access, online journals, promising a paradigm shift from the current review, selection and dissemination processes in academic publishing. All Frontiers journals are driven by researchers for researchers; therefore, they constitute a service to the scholarly community. At the same time, the Frontiers Journal Series operates on a revolutionary invention, the tiered publishing system, initially addressing specific communities of scholars, and gradually climbing up to broader public understanding, thus serving the interests of the lay society, too.

Dedication to Quality

Each Frontiers article is a landmark of the highest quality, thanks to genuinely collaborative interactions between authors and review editors, who include some of the world's best academicians. Research must be certified by peers before entering a stream of knowledge that may eventually reach the public - and shape society; therefore, Frontiers only applies the most rigorous and unbiased reviews.

Frontiers revolutionizes research publishing by freely delivering the most outstanding research, evaluated with no bias from both the academic and social point of view. By applying the most advanced information technologies, Frontiers is catapulting scholarly publishing into a new generation.

What are Frontiers Research Topics?

Frontiers Research Topics are very popular trademarks of the Frontiers Journals Series: they are collections of at least ten articles, all centered on a particular subject. With their unique mix of varied contributions from Original Research to Review Articles, Frontiers Research Topics unify the most influential researchers, the latest key findings and historical advances in a hot research area! Find out more on how to host your own Frontiers Research Topic or contribute to one as an author by contacting the Frontiers Editorial Office: frontiersin.org/about/contact

COMPUTATIONAL INTELLIGENCE IN PERSONALIZED MEDICINE

Topic Editors:

Khin Wee Lai, University of Malaya, Malaysia

Khairunnisa Hasikin, University of Malaya, Malaysia

Yuanpeng Zhang, Nantong University, China

Yan Chai Hum, Universiti Tunku Abdul Rahman, Malaysia

Citation: Lai, K. W., Hasikin, K., Zhang, Y., Hum, Y. C., eds. (2022).
Computational Intelligence in Personalized Medicine.

Lausanne: Frontiers Media SA. doi: 10.3389/978-2-83250-592-2

Table of Contents

- 04 Editorial: Computational Intelligence in Personalized Medicine**
Yuanpeng Zhang, Khairunnisa Hasikin, Samiappan Dhanalakshmi,
Yan Chai Hum and Khin Wee Lai
- 06 Association of Gut Microbiota and Biochemical Features in a Chinese Population With Renal Uric Acid Stone**
Cheng Cao, Bo Fan, Jin Zhu, Na Zhu, Jing-Yuan Cao and Dong-Rong Yang
- 18 Systematic Bibliometric and Visualized Analysis of Research Hotspots and Trends on the Application of Artificial Intelligence in Ophthalmic Disease Diagnosis**
Junqiang Zhao, Yi Lu, Shaojun Zhu, Keran Li, Qin Jiang and Weihua Yang
- 30 Network-Based Pharmacological Study on the Mechanism of Guishao-Liujun Decoction in the Treatment of Gastric Cancer**
Xiaoqing Qian, Lingle Zhang, Feng Xie, Yingsheng Cheng and Daxiang Cui
- 38 Semi-supervised Vision Transformer With Adaptive Token Sampling for Breast Cancer Classification**
Wei Wang, Ran Jiang, Ning Cui, Qian Li, Feng Yuan and Zhifeng Xiao
- 51 Vicious LQT Induced by a Combination of Factors Different From hERG Inhibition**
Xinping Xu, Yue Yin, Dayan Li, Binwei Yao, Li Zhao, Haoyu Wang, Hui Wang,
Ji Dong, Jing Zhang and Ruiyun Peng
- 60 Medical Image Registration Utilizing Tissue P Systems**
Saleem Sanatan Kujur and Sudip Kumar Sahana
- 77 TVGG Dental Implant Identification System**
Jianbin Guo, Pei-Wei Tsai, Xingsi Xue, Dong Wu, Qui Tran Van,
Chanaka Nimantha Kaluarachchi, Hong Thi Dang and Nikhitha Chintha
- 85 Transjugular Intrahepatic Portosystemic Shunt for the Prevention of Rebleeding in Patients With Cirrhosis and Portal Vein Thrombosis: Systematic Review and Meta-analysis**
Ding-Fan Guo, Lin-Wei Fan, Qi Le and Cai-Bin Huang
- 99 Multimodal Neuroimage Data Fusion Based on Multikernel Learning in Personalized Medicine**
Xue Ran, Junyi Shi, Yalan Chen and Kui Jiang
- 110 Function-Wise Dual-Omics Analysis for Radiation Pneumonitis Prediction in Lung Cancer Patients**
Bing Li, Ge Ren, Wei Guo, Jiang Zhang, Sai-Kit Lam, Xiaoli Zheng,
Xinzhi Teng, Yunhan Wang, Yang Yang, Qinfu Dan, Lingguang Meng,
Zongrui Ma, Chen Cheng, Hongyan Tao, Hongchang Lei, Jing Cai and
Hong Ge



OPEN ACCESS

EDITED AND REVIEWED BY
Heike Wulff,
University of California, Davis,
United States

*CORRESPONDENCE
Khin Wee Lai,
lai.khinwee@um.edu.my

SPECIALTY SECTION
This article was submitted to
Experimental Pharmacology
and Drug Discovery,
a section of the journal
Frontiers in Pharmacology

RECEIVED 16 September 2022
ACCEPTED 26 September 2022
PUBLISHED 12 October 2022

CITATION
Zhang Y, Hasikin K, Dhanalakshmi S,
Hum YC and Lai KW (2022), Editorial:
Computational intelligence in
personalized medicine.
Front. Pharmacol. 13:1046271.
doi: 10.3389/fphar.2022.1046271

COPYRIGHT
© 2022 Zhang, Hasikin, Dhanalakshmi,
Hum and Lai. This is an open-access
article distributed under the terms of the
[Creative Commons Attribution License](#)
(CC BY). The use, distribution or
reproduction in other forums is
permitted, provided the original
author(s) and the copyright owner(s) are
credited and that the original
publication in this journal is cited, in
accordance with accepted academic
practice. No use, distribution or
reproduction is permitted which does
not comply with these terms.

Editorial: Computational intelligence in personalized medicine

Yuanpeng Zhang¹, Khairunnisa Hasikin²,
Samiappan Dhanalakshmi³, Yan Chai Hum⁴ and Khin Wee Lai^{5*}

¹Department of Medical Informatics, Nantong University, Nantong, China, ²Department of Biomedical Engineering, Faculty of Engineering, Universiti Malaya, Kuala Lumpur, Malaysia, ³Department of Electronics and Communication Engineering, Faculty of Engineering and Technology, SRM Institute of Science and Technology, Kattankulathur, India, ⁴Department of Mechatronics and Biomedical Engineering, Lee Kong Chian Faculty of Engineering and Science, Universiti Tunku Abdul Rahman, Kajang, Malaysia, ⁵Department of Biomedical Engineering, Faculty of Engineering, Universiti Malaya, Kuala Lumpur, Malaysia

KEYWORDS

computational intelligence, personalized medicine, machine learning, deep learning, clinical decision support

Editorial on the Research Topic

Computational intelligence in personalized medicine

Emerging developments and innovations in digital healthcare technologies, also known as digital transformation, may drastically enhance current healthcare operations. Among advanced technologies, artificial intelligence, particularly computational intelligence, has proven successful as a technology trend contributing to the digital transformation of the healthcare and medical industries. For example, Zhang et al. proposed a multimodal neuroimaging embedding feature selection and fusion method for the multiclass diagnosis of Alzheimer's disease (Zhang et al., 2021). Zhang et al. also proposed an imbalance classification framework and a high-generalizable classifier for distant metastases prediction of advanced nasopharyngeal carcinoma (Zhang et al., 2022). In this research topic, the publications have been rigorously peer-reviewed by external reviewers with strong backgrounds in computational intelligence research. These high-quality publications provide efficient and precise intelligent algorithms for the field of personalized medicine.

Among these publications, two research groups focused on personalized medicine in cancer, and each has described a very good computational intelligent algorithm. Wang et al. (Xu et al.) proposed a semi-supervised learning framework based on Vision Transformer (ViT) for the diagnosis of breast cancer, which unifies both supervised and consistency training to enhance the robustness of the model. The authors validated the proposed model on both ultrasound and histopathology images. The experimental results demonstrated its promising performance. The other group focused on the prediction of radiation pneumonitis in patients with lung cancer based on lung perfusion functional images (Li et al.). The study first divided the whole lung volume into function-wise lung regions. Next, the authors extracted radiomics and dose features

from function-wise and full lung regions, respectively. Finally, the authors proposed a multi-feature fusion model to fuse radiomics features, dose features, and combined dual-omics features. The experimental results demonstrated the promise of the function-wise dual-omics analysis method to improve the prediction of radiation pneumonitis in patients with lung cancer.

Additionally, three research groups designed a multimodal fusion algorithm, a registration system, and an identification system for personalized medicine in the field of brain diseases, and dental implants. Neuroimaging has been widely used as a precision diagnostic technique for brain diseases. [Ran et al.](#) collected 103 subjects with magnetic resonance imaging (MRI) and positron emission tomography (PET) data from the Alzheimer's Disease Neuroimaging Initiative, and then proposed a multi-kernel model to fuse MRI and CT modalities for the diagnosis of Alzheimer's disease. In the multi-kernel model, unlike the modality-consistent regularization used in previous studies, the authors designed a novel "all-single" fusion strategy that considers every single feature and the possible combinations, which allowed full exploration of the complementary information. Moreover, [Ran et al.](#) extended the compactness graph mechanism from the linear space to the multi-kernel space to reduce the overfitting problems in multi-kernel space. Image registration plays a significant role in the computational intelligence-assisted diagnosis of brain diseases. [Kujur et al.](#) proposed a general registration framework using the tissue P system for image registration. The innovation is that the proposed registration framework optimizes upon the mutual information similarity metric to identify a global solution. [Kujur et al.](#) evaluated the registration framework on single- and multi-modality brain image data collected from the Montreal Neurological Institute. The experimental results indicated that among all the state-of-the-art models, the proposed registration framework provided better mutual information values with minimum deviation in a range of experiment setups conducted iteratively. In the field of dental implants, identifying the appropriate accessories for installing a dental implant is a vital factor that impacts dental prosthesis sustainability and reliability. X-ray images are usually used to assist dentists in identifying the implant manufacturer to determine further treatment procedures. [Guo et al.](#) developed a dental implant identification system based on a novel thinner VGG (Visual Geometry Group) model with an on-demand client-server structure. The experimental results demonstrated the advantages of the proposed systems compared to state-of-the-art systems.

Another takeaway from this topic are two review manuscripts. [Zhao et al.](#) performed a systematic review on the application of computational intelligence in the diagnosis of ophthalmic disease.

Specifically, the authors collected citation data from the Web of Science Core Collection database to evaluate the extent of the application of computational intelligence in the diagnosis of ophthalmic disease in publications between 1 January 2012 and 31 December 2021. They found that the hotspots of computational intelligence research on this topic have transitioned from the development of computational intelligence algorithms and the analysis of abnormal eye physiological structures to the investigation of more mature systems for ophthalmic disease diagnosis. The meta-analysis by [Guo et al.](#) analyzed the use of the transjugular intrahepatic portosystemic shunt (TIPS) for the prevention of rebleeding in patients with cirrhosis and portal vein thrombosis. The authors reported that TIPS is feasible and effectively prevents rebleeding in these patients, regardless of cavernous transformation of the portal vein.

In conclusion, this Research Topic mainly focused on computational intelligence in personalized medicine. Some representative works made use of classic computational intelligence technologies directly, while other representative works were based on newly proposed computational intelligence algorithms. In general, these works are excellent and open a new window for the development of computational intelligent algorithms in personalized medicine. Finally, we sincerely thank all the authors who contributed their work and provided articles, allowing us to coordinate and edit this outstanding collection.

Author contributions

All authors listed have made a substantial, direct, and intellectual contribution to the work and approved it for publication.

Conflict of interest

The authors declare that the research was conducted in the absence of any commercial or financial relationships that could be construed as a potential conflict of interest.

Publisher's note

All claims expressed in this article are solely those of the authors and do not necessarily represent those of their affiliated organizations, or those of the publisher, the editors, and the reviewers. Any product that may be evaluated in this article, or claim that may be made by its manufacturer, is not guaranteed or endorsed by the publisher.

References

Zhang, Y., Lam, S., Yu, T., Teng, X., Zhang, J., Lee, F. K. H., et al. (2022). Integration of an imbalance framework with novel high-generalizable classifiers for radiomics-based distant metastases prediction of advanced nasopharyngeal carcinoma. *Knowledge-Based Syst.* 235, 107649. doi:10.1016/j.knsys.2021.107649

Zhang, Y., Wang, S., Xia, K., Jiang, Y., and Qian, P., Alzheimer's Disease Neuroimaging Initiative. (2021). Orosomucoid-like protein 3, rhinovirus and asthma. *World J. Crit. Care Med.* 66, 170–182. doi:10.5492/wjccm.v10.i5.170



Association of Gut Microbiota and Biochemical Features in a Chinese Population With Renal Uric Acid Stone

Cheng Cao^{1,2}, Bo Fan², Jin Zhu^{1*}, Na Zhu³, Jing-Yuan Cao⁴ and Dong-Rong Yang^{1*}

¹Department of Urology, The Second Affiliated Hospital of Soochow University, Suzhou, China, ²Department of Urology, Changshu Hospital Affiliated to Soochow University, Changshu, China, ³Department of Rheumatology, Changshu Hospital Affiliated to Soochow University, Changshu, China, ⁴Department of Nephrology, Taizhou People's Hospital, Taizhou, China

OPEN ACCESS

Edited by:

Khin Wee Lai,
University of Malaya, Malaysia

Reviewed by:

Saneera Hemantha Kulathilake,
Rajarata University of Sri Lanka, Sri Lanka

Jing Xue,
Wuxi People's Hospital Affiliated to
Nanjing Medical University, China

*Correspondence:

Dong-Rong Yang
ydrsuda@163.com
Jin Zhu
oceanzhu79@qq.com

Specialty section:

This article was submitted to
Experimental Pharmacology and Drug
Discovery,
a section of the journal
Frontiers in Pharmacology

Received: 03 March 2022

Accepted: 01 April 2022

Published: 19 May 2022

Citation:

Cao C, Fan B, Zhu J, Zhu N, Cao J-Y
and Yang D-R (2022) Association of
Gut Microbiota and Biochemical
Features in a Chinese Population With
Renal Uric Acid Stone.
Front. Pharmacol. 13:888883.
doi: 10.3389/fphar.2022.888883

Previous studies suggest that patients with nephrolithiasis exhibit dysbiosis in their gut microbiota, but those studies were conducted in calcium oxalate stone patients. We aimed to explore the association of gut microbiota and biochemical features of renal uric acid stone (UAS) patients in a Chinese population and identify the related bacteria that may affect the pathopoiesis of UAS. A case-control study of 117 patients with UAS, 123 patients with gout, and 135 healthy controls were included from January 2014 to October 2020. For each subject, data on demographics, biochemical parameters of blood and urine were analyzed. Fifteen patients with gout, 16 patients with UAS, 17 UAS patients with gout, and 17 healthy subjects were enrolled and provided fecal samples. The characteristics of gut microbiota were explored by using 16S ribosomal RNA (rRNA) gene sequencing and analyzed by using a combination of software mother and R. Hyperuricemia was the main risk factor for the development of gout and UAS. Obesity, dyslipidemia, and aciduria were unique risk factors for UAS patients. The richness, diversity, and relative abundance of dominant bacteria at the phylum and genus levels of gut microbiota in UAS patients were significantly distinct from other subjects. Abundance of *Bacteroides* and *Fusobacterium* was significantly positively correlated with the serum uric acid (UA) level of UAS patients. *Fusobacteria* was involved in the metabolism and degradation of certain short-chain fatty acids, amino acids, and sugars in pathopoiesis of UAS, and inhibited their synthesis pathways. *Fusobacteria* may be related to the pathogenesis of UAS, and this finding contributes to the personalized treatment of UAS from the perspective of maintaining micro-ecological equilibrium in gut.

Keywords: gut microbiota, uric acid stone, nephrolithiasis, 16srRNA, biomarker, computational intelligence

INTRODUCTION

Nephrolithiasis is a global disease across regions and ethnicities, which is considered an important public health problem. It has a severe impact on human health and causes a huge social and economic burden (Sakhaee, 2008). To make matters worse, the recurrence rate of nephrolithiasis remains high, with a recurrence rate of 50% within 10 years. Renal uric acid stone (UAS) is indicated in the presence of a radiolucent stone (Ganesan et al., 2018), accounting for 10–15% of all urinary calculi, and its prevalence rate varies globally (Abou-Elela, 2017; Trinchieri and Montanari, 2017). The recurrence rate of patients with UAS is close to 100% (Wang et al., 2017). Although no large-scale epidemiological studies have been conducted, the prevalence of UAS in China has increased

significantly in the past 30 years. In the economically developed areas of southern China, the prevalence of UAS is as high as 12–18% (Ma et al., 2018).

The microbiota of the human intestinal tract is a complex community composed of more than 100 trillion microbial cells, including more than 1,000 different kinds of species (De Sordi et al., 2017). High-throughput sequencing has facilitated great advances in our understanding of gut microbiome. Gut microbiota is increasingly linked to the development of various metabolic diseases such as obesity, diabetes, dyslipidemia, kidney disease, and nephrolithiasis (Langille et al., 2013; Stern et al., 2016; Stanford et al., 2020). The discovery of *Oxalobacter formigenes*, which is a kind of oxalate degrading bacteria, makes it possible that the gut microbiota affects absorption and secretion of solutes relevant to kidney stone formation (Siva et al., 2009). To date, more studies on the relationship between gut microbiota and nephrolithiasis are reported (Tang et al., 2018). They found that the cause of calcium oxalate stone was related to a group of bacteria involved in oxalate degradation and transportation, rather than a single kind of bacteria (Lee and Stern, 2019). The relationship of gut microbiota and calcium oxalate stone has been investigated in a limited amount (Stern et al., 2016; Lee and Stern, 2019), especially with no study of gut microbiota and UAS, to the best of our knowledge.

Although hyperuricemia is the common physiological and pathological bases of UAS and gout, only part of the population will develop UAS or gout, and the mechanism is still being studied. Patients with a history of gout have greater risk of forming UAS, and patients with obesity, diabetes, dyslipidemia, or other metabolic syndrome (Joosten et al., 2020). However, many patients with UAS are not accompanied by gout. The loss of bicarbonate leads to the formation of acidic urine, which is the most direct risk factor for UAS. Gastrointestinal diseases such as inflammatory bowel disease have been shown to cause bicarbonate

loss clearly, and we have the reason to believe that gut microbiota and its metabolites regulate urine pH. We attempted to explore the differences in biochemical and gut microbiota features between UAS and gout patients, and find out bacteria genera, which involved in the pathogenesis of UAS. Through the analysis and detection of target bacteria by computational intelligence, it facilitates a new thinking for the personalized diagnosis and treatment of UAS patients.

MATERIALS AND METHODS

Human Study Designs, Subjects, and Sampling

This study was approved by the Ethics Review Committee of Changshu Hospital affiliated to Soochow University. All the participants were local residents of unrelated southern Han Chinese. A case-control study of 123 gout patients (Gout group), 87 UAS patients without gout (UAS group), 30 UAS patients complicated with gout (Gout + UAS group), and 135 stone-free healthy people (Control Group) who received physical examination in Changshu Hospital affiliated to Soochow University from January 2014 to October 2020 were conducted. All the stone patients were diagnosed by ultrasound of the urinary system or abdominal-computed tomography, and received ureteroscopy or percutaneous nephrolithotomy. The stones obtained after operation were identified as pure or mixed uric acid calculus (uric acid content is greater than 50%) by Fourier-transformed infrared spectrophotometry LIIR-20 (Lanmode scientific instrument Co., Ltd., Tianjin, China). Patients who had a history of statins, chronic liver insufficiency, malignant tumors, and thyroid or parathyroid diseases were excluded from the study. Controls with a history or any evidence of nephrolithiasis, self-reported history of dyslipidemia or use of statins were excluded from the study.

TABLE 1 | Comparison of general characteristics between each group.

Variables	Gout	UAS	Gout + UAS	Control	p value
Age, years	61.46 ± 15.58	60.32 ± 14.74	57.77 ± 14.39	59.25 ± 16.56	0.571 [#]
Gender (%)					0.310 [*]
Male	105 (85.37)	67 (77.01)	26 (86.67)	106 (78.52)	
Female	18 (14.63)	20 (22.99)	4 (13.33)	29 (21.48)	
BMI	23.88 ± 2.46 ^b	24.92 ± 3.53 ^{a,c}	26.80 ± 2.19 ^d	23.75 ± 1.51	<0.001 [#]
Hypertension (%)					<0.001 [*]
Yes	54 (43.90) ^d	36 (41.38) ^c	17 (56.67) ^c	31 (22.96)	
No	69 (56.10) ^d	51 (58.62) ^c	13 (43.33) ^c	104 (77.04)	
Diabetes (%)					0.413 [*]
Yes	7 (5.69)	6 (6.90)	4 (13.33)	7 (5.19)	
No	116 (94.31)	81 (93.10)	26 (86.67)	128 (94.81)	

[#]Analysis of variance (ANOVA)

^{*}2-sided Chi-square test.

^ap < 0.05 (compared with the Gout + UAS, group).

^bp < 0.001 (compared with the Gout + UAS, group).

^cp < 0.05 (compared with the control group).

^dp < 0.001 (compared with the control group).

UAS, uric acid stone; BMI, body mass index.

Bold values indicate significant difference.

TABLE 2 | Biochemical parameters in different groups studied.

Variables	Gout	UAS	Gout + UAS	Control
Lipid levels, mmol/L				
TG	1.74 ± 1.08 ^{a,c}	1.81 ± 0.98 ^{a,d}	2.66 ± 1.97 ^c	1.37 ± 0.61
TC	4.66 ± 0.98	4.83 ± 0.87	4.77 ± 1.23	4.83 ± 0.98
HDL-C	1.18 ± 0.30 ^c	1.23 ± 0.35 ^a	1.06 ± 0.25 ^d	1.31 ± 0.34
LDL-C	2.60 ± 0.69	2.77 ± 0.63	2.72 ± 0.81	2.77 ± 0.71
Electrolyte levels, mmol/L				
K	4.04 ± 0.37 ^{a,c}	4.08 ± 0.41 ^a	4.33 ± 0.62	4.15 ± 0.42
Na	140.31 ± 3.37	140.95 ± 2.54	140.94 ± 2.74	140.79 ± 2.18
Cl	103.95 ± 3.39	104.54 ± 3.23	105.31 ± 3.46	104.24 ± 2.98
Ca	2.29 ± 0.15 ^{a,c}	2.34 ± 0.16	2.38 ± 0.16	2.35 ± 0.13
P	1.07 ± 0.24	1.05 ± 0.22	1.12 ± 0.36	1.03 ± 0.18
Mg	0.86 ± 0.10	0.87 ± 0.10	0.89 ± 0.20	0.88 ± 0.08
UA (μmol/L)	465.54 ± 126.22 ^{b,d}	392.71 ± 93.12 ^{b,d}	559.13 ± 76.57 ^d	336.09 ± 76.75
Urinary pH	5.72 ± 0.55 ^d	5.64 ± 0.55 ^d	5.57 ± 0.63 ^c	5.99 ± 0.67

^a*p* < 0.05 (compared with the Gout + UAS, group).^b*p* < 0.001 (compared with the Gout + UAS, group).^c*p* < 0.05 (compared with the control group).^d*p* < 0.001 (compared with the control group).

UAS, uric acid stone; TG, triglycerides; TC, total cholesterol; HDL-C, high-density lipoprotein cholesterol; LDL-C, low-density lipoprotein cholesterol; and UA, serum uric acid.

Comparisons made using Student's *t* test.

General body measurements (height, weight, and blood pressure), past medical history, and test of blood and urine were carried out in all subjects. About 5 ml fasting venous blood sample and mid-stream urine of the first urine in the morning were drawn from each subject. Under the matching of age, sex, and BMI, 15 patients in the Gout group, 16 patients in the UAS group, 17 patients in the Gout + UAS group, and 17 patients in the controls were selected (**Supplementary Table S1**). All subjects were long-term residents with similar dietary habits, and underwent food frequency questionnaire before enrollment. After 3 days of eating uniform diet provided by the hospital (**Supplementary Table S2**), fresh fecal samples from the aforementioned people were collected, froze immediately, and stored under −80°C until analysis. Subjects who support fecal samples were excluded if they used antibiotics within 3 months, had a history of chronic diarrhea or constipation, chronic enteritis, irritable bowel syndrome, gastrointestinal tumor, or intestinal surgery.

16s DNA Extraction, PCR Amplification, and Target Gene Sequencing

The DNA was extracted from 200 mg samples using the QIAamp DNA fecal mini kit (QIAGEN, Hilden, Germany) following the manufacturer's instructions. DNA was checked by running the samples on 1.2% agarose gels.

The V3–V4 hyper-variable regions of the bacteria 16SrRNA gene were amplified with primers 357F (5'-ACTCCTACGGRAGGCAGCAG-3') and 806R (5'-GGACTACHVGGGTWTCTAAT-3') by the polymerase chain reaction (PCR) system. Prior to library pooling, the barcoded PCR products were purified using a DNA gel extraction kit (Axygen, United States) and quantified using the FTC-3000 TM real-time PCR (Funglynn Shanghai). The PCR products from different samples were indexed and mixed at equal ratios

for sequencing on the illumina platform at TinyGen Bio-Tech (Shanghai) Co., Ltd.

Statistical and Bioinformatics Analysis

The general characteristics and biochemical parameters of the subjects were analyzed by SPSS22.0 and 2-sided *p* < 0.05 was defined as statistically significant. Continuous variables were summarized with mean and standard deviation if they satisfied the homogeneity of normality and variance. Otherwise, they were reported with median and inter quartile range (IQR). The quantitative variables were tested by the analysis of variance (ANOVA), Kruskal–Wallis test, and Mann–Whitney test. The chi-square test was used for categorical variables. Multiple logistic regression analysis was used to analyze the risk factors of disease in each group, and OR values were adjusted according to age and sex.

16S sequences were analyzed using a combination of software mother and R. The demultiplexed reads were clustered at 97% sequence identity into operational taxonomic units (OTUs) and the singleton OTUs were deleted using the UPARSE pipeline. OTU taxonomies were determined based on the NCBI. Based on taxonomic information, the community structure was statistically analyzed from the classification level of phylum, class, order, family, genus, and species. For the alpha-diversity analysis, Shannon, Simpson, Chao, ACE index, and rarefaction curves were calculated using mothur and plotted by R. The Kruskal–Wallis test was used to detect the significant changes of Shannon, Simpson, Chao, and ACE index between each group. For the beta-diversity metrics, the weighted UniFrac distance matrix were calculated using mothur and visualized with principal coordinate analysis (PCoA) by ape package in R. Linear discriminant analysis effect size (LEfSe) analysis was performed. Linear discriminant analysis was performed on samples with different grouping conditions according to the taxonomic composition. LDA was used to screen the

TABLE 3 | Multivariate logistic analysis of risk factors in each group studied.

Variables	Gout		UAS		Gout + UAS	
	<i>p</i> value ^a	Adjusted OR (95% CI)	<i>p</i> value ^a	Adjusted OR (95% CI)	<i>p</i> value ^a	Adjusted OR (95% CI)
BMI	0.612 ^b	1.03 (0.91–1.17)	0.019	1.16(1.03–1.32)	0.015	12.57(1.62–97.47)
Hypertension	0.088	1.75 (0.92–3.34)	0.066	1.93 (0.96–3.87)	0.415	0.12 (0.01–19.00)
Hypertriglyceridemia	0.154 ^b	1.76 (0.81–3.82)	0.002	4.19(1.67–10.40)	0.208	13.90 (0.23–839.09)
Low HDL-cholesterolemia	0.080	1.96 (0.92–4.17)	0.213	1.70 (0.74–3.93)	0.051	89.59 (0.98–8.19e-3)
Hyperuricemia	<0.001	10.08(5.27–19.27)	<0.001	4.81(2.30–10.07)	0.021	2.87e-6(9.74–8.46e-11)
Urinary pH	0.122	0.68 (0.42–1.11)	0.027	0.55(0.32–0.93)	0.662	0.60 (0.06–6.09)

^aAdjusted for age and sex in the multivariate logistic regression model.

^bResults of univariate logistic regression analysis.

UAS, uric acid stone and BMI, body mass index.

Bold values indicate significant difference.

communities or species which had significant influence on the differences in sample division with a cutoff of 2.0. The Spearman correlation analysis was used to evaluate association of dominant bacteria genera and biochemical parameters. The metabolic pathways of Kyoto Encyclopedia of Genes and Genomes (KEGG) were predicted by PICRUST software package.

RESULTS

General Characteristics of the Study Population

The proportion of hypertensive patients and body mass index (BMI) in observation groups were significantly higher than the controls. Age ($p = 0.571$), gender ($p = 0.310$), and prevalence of diabetes mellitus ($p = 0.413$) were not significantly different among each group. However, BMI of the two stone groups, especially the Gout + UAS group was significantly higher than the other groups ($p < 0.001$). More hypertension individuals were found among the three observation groups and the Gout + UAS group is still with the highest prevalence rate ($p < 0.001$) (Table 1).

Biochemical Features and Risk Factors Analysis Among the Groups

Hyperuricemia was the main risk factor for the development of gout as well as UAS. Obesity, hypertriglyceridemia, and aciduria were unique risk factors for UAS patients. Main biochemical features are summarized in Table 2 or Supplementary Figure S1. Compared to the controls, the triglycerides (TG) level in the three observation groups was significantly higher, and the level of TG in the Gout + UAS group was the highest ($p < 0.05$). The level of high-density lipoprotein cholesterol (HDL-C) in Gout as well as Gout + UAS group was significantly lower than that in the control group. The concentration of potassium in the Gout and UAS groups was significantly lower than that in the Gout + UAS group ($p < 0.05$), and the serum calcium concentration in the Gout group was also significantly lower than the Gout + UAS group and the controls ($p < 0.05$). All the three observation groups have significantly higher serum uric acid (UA) value than the controls

($p < 0.001$), and among them the Gout + UAS group's UA value was the highest ($p < 0.001$). All the patients in three observation groups demonstrated obvious aciduria, especially in the Gout + UAS group (Table 2, Supplementary Figure S1).

Univariate logistic analysis suggested that hypertension, low HDL-cholesterolemia, hyperuricemia, and aciduria were independent risk factors for gout. Obesity, hypertension, hypertriglyceridemia, low HDL-cholesterolemia, hyperuricemia, and aciduria were common independent risk factors for all UAS groups (Supplementary Table S3). Adjusted for age and sex, multivariate logistic analysis indicated that only hyperuricemia was the common risk factor for the development of gout as well as UAS. For patients with UAS alone, obesity, hypertriglyceridemia, and aciduria were the other three risk factors. While obesity was another risk factor for patients with UAS complicated with gout besides hyperuricemia (Table 3).

16S Sequencing Depth and Analysis of the Sample Size

The study was carried out with reasonable sample collection and high species rich, and the amount of data was reasonable and could reflect the majority of gut microbiota information objectively among groups. After eliminating the sequences of repetitive and fuzzy bases that affect the quality of analysis, a total of 2,329,290 high-quality sequences with an average length of 459 were received. The number of total OTUs in this study was 700, including one kingdom, 12 phylum, 21 class, 29 order, 46 family, 132 genus, and 181 species. The Venn diagram shows the common and unique OUTs among each group. Among the 648 known OUTs, the number of OUTs in the Gout + UAS group was lower than other groups (Figure 1A). With the curve reached the saturation plateau, more data contribute little to the discovery of new OUTs (Figure 1B), which means the depth of sequencing was reasonable. ANOSIM analysis calculated the relationship ranking among samples through variables, and performed the substitution test to determine whether the difference between groups was significantly different from the difference within groups. The results showed that the difference of the gut microbiota structure among the four groups was statistically significant ($R = 0.155$, $p = 0.001$) (Figure 1C).

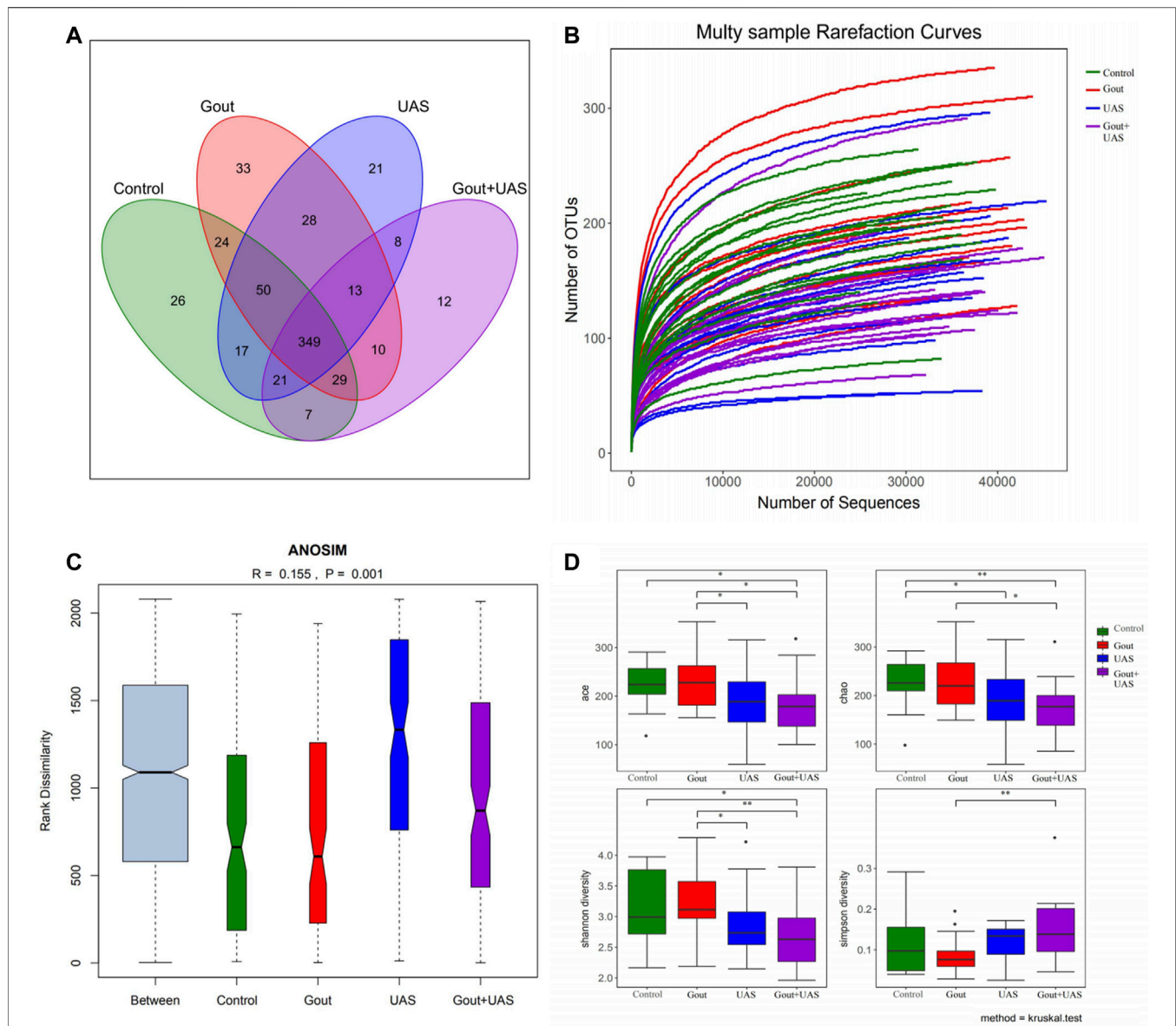


FIGURE 1 | Analysis of gut microbiota among each group by using 16s rRNA. **(A)** Venn diagram for indicating the common and unique OTUs among four groups. **(B)** Multi-sample rarefaction curves for comparing the abundance of diverse species in each sample. **(C)** ANOSIM analysis for identifying the existence of differences between each group. **(D)** Comparison of alpha diversity of gut microbiota between each group. The ACE, Chao, Shannon, and Simpson indices at the operational taxonomic units (OTUs) level were compared between each group by Kruskal–Wallis test ($*p < 0.05$ $**p < 0.01$).

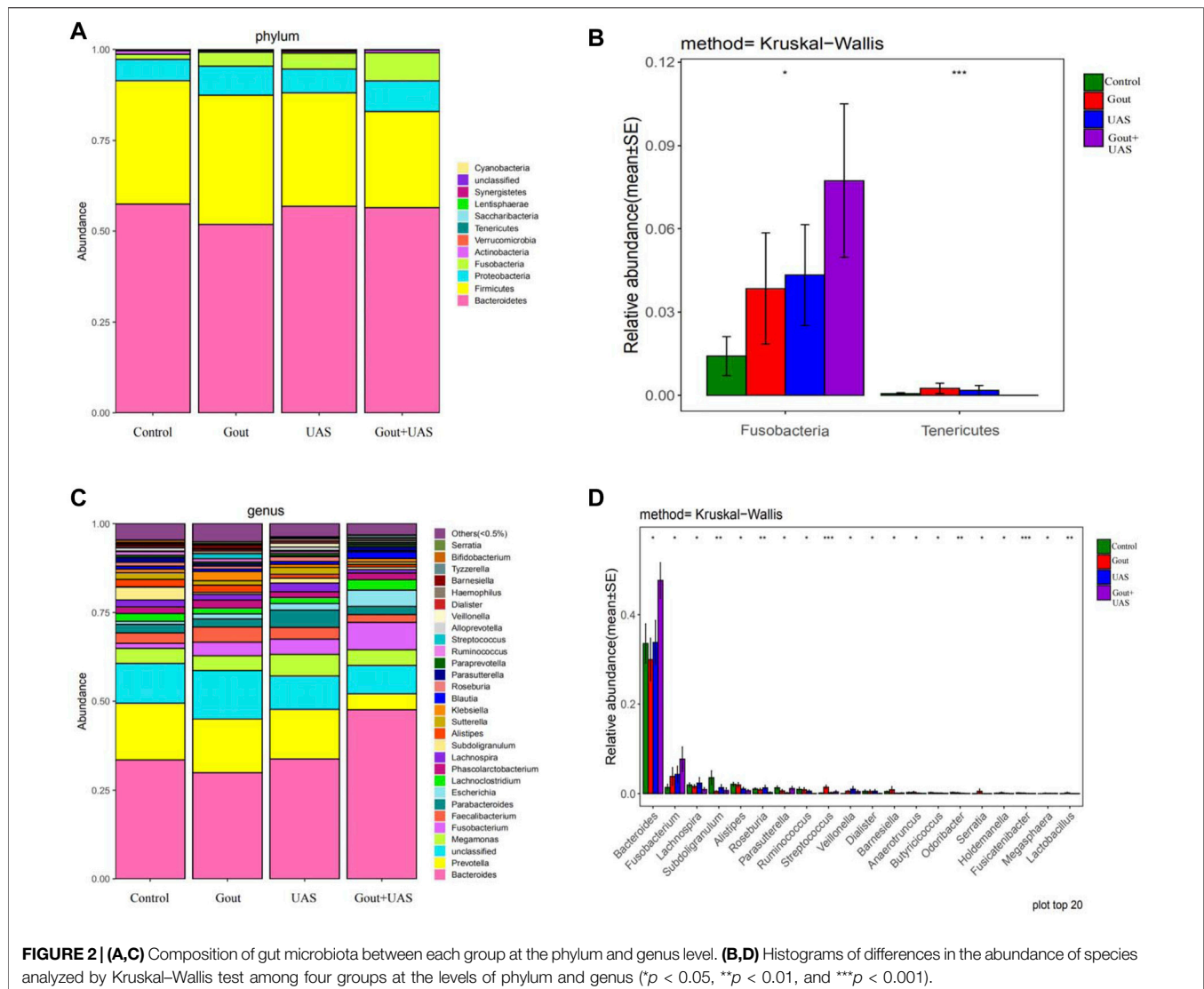
Richness and Diversity of Gut Microbiota Among Each Group

The richness and diversity of gut microbiota in UAS patients, especially in stone patients complicated with gout, were significantly lower than gout patients and controls. The richness and bacterial diversity of gut microbiota in the Gout + UAS group were significantly lower than that in the Gout and Control groups (**Figure 1D**) from the ACE, Chao, Shannon, and Simpson indices by the Kruskal–Wallis test. PCoA analysis indicated that there are significant differences in microbiota

communities in specific evolutionary lineages among the four groups. (**Supplementary Figure S2**).

Analysis Based on Species Information of Microbiota Between Each Group

The species diversity and relative abundance of dominant bacteria at the phylum and genus levels among the four groups were different, and certain bacteria were dominant in UAS patients. At the level of phylum, Bacteroidetes, Firmicutes,



Proteobacteria, Fusobacteria, Actinobacteria were the most five abundant bacterial in each group. In the Gout + UAS group, the relative abundance of Fusobacteria was significantly higher than other groups ($p = 0.02$), while Tenericutes was significantly lower than other groups ($p < 0.001$) (Figures 2A,B). At the level of genus, the most five abundant bacterial were Bacteroides, Prevotella, Megamonas, Fusobacterium, and Faecalibacterium. The relative abundance of *Bacteroides* and *Fusobacterium* in the Gout + UAS group was significantly higher than other groups (Figures 2C,D). The linear discriminant analysis effect size diagram indicated that there were the following specific genera in each group on the phylum and genus levels Fusobacteria in the Gout + UAS group on the phylum level, Tenericutes in the Gout Group on the phylum level, *Bacteroides* and *Fusobacterium* in the Gout + UAS group on the genus level, *Streptococcus*, *Lactobacillus*, *Weissella*, *Gemella*, and *Campylobacter* in the Gout group on the genus level, *Dialister* in the UAS group on

the genus level, *Subdoligranulum* in controls on the genus level (Figure 3).

Association of Dominant Bacteria Genera and Biochemical Parameters

Bacteroides and *Fusobacterium* were significantly positively correlated with the serum UA level of patients with UAS. We looked for the dominant species whose LDA value was more than two and the relative abundance was in the top 20 in each group at the genus level, and screened out the following six species: *Bacteroides*, *Fusobacterium*, *Subdoligranulum*, *Streptococcus*, *Dialister*, and *Lactobacillus*. The correlation of the aforementioned genera abundance and the significant different biochemical parameters were analyzed. *Bacteroides* was positively correlated with the UA level in the Gout + UAS group ($r = 0.520$, $p = 0.033$), and positively correlated with the serum potassium

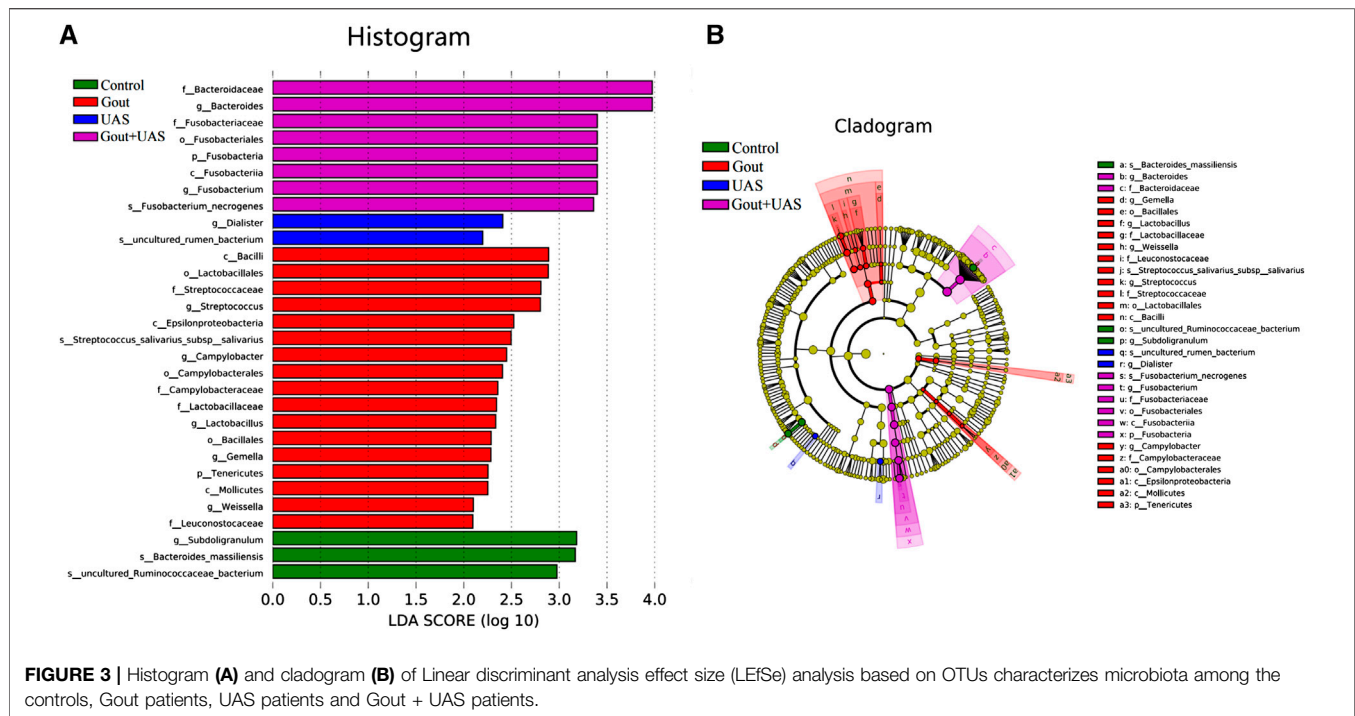


FIGURE 3 | Histogram (A) and cladogram (B) of Linear discriminant analysis effect size (LEfSe) analysis based on OTUs characterizes microbiota among the controls, Gout patients, UAS patients and Gout + UAS patients.

level in the controls ($r = 0.829$, $p < 0.001$). *Fusobacterium* was positively correlated with the UA level in the UAS group ($r = 0.560$, $p = 0.024$). *Subdoligranulum* was positively correlated with the HDL-C level in the controls ($r = 0.493$, $p = 0.044$). *Streptococcus* was positively correlated with urinary pH in the Gout group ($r = 0.536$, $p = 0.039$), and inversely correlated with the TG level in the Gout + UAS group ($r = -0.517$, $p = 0.034$). *Dialister* was positively correlated with the HDL-C level ($r = 0.726$, $p = 0.001$), but was inversely correlated with the UA level in the UAS group ($r = -0.629$, $p = 0.009$) (Table 4, Supplementary Figure S3).

Prediction of Metabolic Function of Gut Microbiota

Fusobacteria was involved in the metabolism and degradation of certain short-chain fatty acids, amino acids, and sugars in pathogenesis of UAS, and inhibited their synthesis pathways. The PICRUSt tool was used to predict the differences in metabolic pathways between all the stone patients (Group S) and the controls (Group N) (Figure 4). *Fusobacteria* played a dominant role in microbiota metabolism in UAS patients and had a significant positive correlation in propanoate and butanoate metabolism, beta-alanine and tryptophan metabolism, amino sugar and nucleotide sugar metabolism, fructose and mannose metabolism, lysine, valine, leucine and isoleucine degradation and other metabolism or degradation pathway. The biosynthesis of short-chain fatty acids, the biosynthesis of phenylalanine, tyrosine, tryptophan and arginine, the biosynthesis of peptidoglycan and glucosinolate, the metabolism of cysteine, methionine, histidine, alanine,

aspartate, and glutamate were inversely correlated with *Fusobacteria* while they were positively correlated with probiotic bacteria genera in controls.

DISCUSSION

In the present study, there were significant differences in biochemical features between UAS formers and gout patients. Whether for gout or UAS patients, hyperuricemia was always a risk factor. Obesity, hypertriglyceridemia, and aciduria were the risk factors of UAS, while obesity and hyperuricemia were more associated with UAS complicated with gout. The richness and diversity of gut microbiota in UAS patients were significantly lower than those in controls. *Bacteroides* and *Fusobacterium* were the dominant species that distinguish the intestinal flora of UAS patients from normal population, and they had a significant positive correlation with the level of serum UA. *Fusobacteria* was mainly involved in the metabolism and degradation of certain short-chain fatty acids, amino acids, and sugars in patients with UAS, and played an important role in inhibiting their synthesis pathways.

It is well known that uric acid is a weak organic acid with an ionization constant (PKA) of 5.5, the solubility of uric acid crystals decreases sharply in acidic urine with pH less than 5.5 (Tran and Maalouf, 2020). The disturbance of Na^+/H^+ exchange and decrease of ammonia secretion in renal proximal tubule will reduce the urinal pH value, promoting the formation of UAS and depositing of monosodium urate monohydrate, as known as the gout crystals (Friedlander et al., 2014; Rajkumar and Pluznick, 2018).

TABLE 4 | Spearman correlation coefficient of significant different biochemical parameters and major bacterial genera in each group.

Variables	Bacteroides		Fusobacterium		Subdoligranulum		Streptococcus		Dialister		Lactobacillus	
	R	P	R	P	R	P	R	P	R	P	R	P
Gout												
TG (mmol/L)	−0.354	0.196	0.139	0.621	0.079	0.781	−0.096	0.732	0.057	0.839	0.171	0.542
HDL-C (mmol/L)	0.374	0.170	0.295	0.286	−0.401	0.138	0.297	0.282	−0.219	0.433	−0.050	0.861
K (mmol/L)	−0.414	0.125	−0.257	0.355	0.234	0.401	−0.361	0.187	−0.241	0.374	−0.339	0.217
Ca (mmol/L)	−0.442	0.099	−0.292	0.292	0.477	0.072	−0.034	0.904	0.359	0.189	0.069	0.806
UA (μmol/L)	−0.401	0.132	−0.129	0.648	0.379	0.164	−0.329	0.232	0.007	0.980	0.070	0.803
Urinary pH	0.489	0.064	−0.075	0.790	−0.235	0.399	0.536	0.039	−0.075	0.789	0.194	0.487
UAS												
TG (mmol/L)	−0.036	0.895	0.184	0.495	0.016	0.952	0.137	0.613	−0.310	0.243	0.053	0.846
HDL-C (mmol/L)	−0.301	0.257	−0.137	0.614	−0.048	0.859	−0.218	0.417	0.726	0.001	0.021	0.937
K (mmol/L)	−0.467	0.068	−0.070	0.797	0.228	0.395	0.491	0.053	−0.179	0.507	0.084	0.757
Ca (mmol/L)	−0.493	0.052	0.146	0.589	0.332	0.208	0.207	0.442	0.090	0.740	−0.092	0.735
UA (μmol/L)	0.231	0.390	0.560	0.024	−0.022	0.937	0.026	0.924	−0.629	0.009	−0.358	0.173
Urinary pH	−0.057	0.835	−0.212	0.430	0.240	0.371	−0.172	0.525	0.352	0.181	0.249	0.352
Gout + UAS												
TG (mmol/L)	0.373	0.141	−0.103	0.694	0.201	0.438	−0.517	0.034	0.040	0.880	−0.446	0.073
HDL-C (mmol/L)	−0.248	0.338	0.293	0.254	−0.098	0.707	0.080	0.761	−0.033	0.899	0.083	0.752
K (mmol/L)	−0.012	0.963	−0.292	0.256	−0.135	0.605	−0.064	0.808	−0.217	0.402	−0.442	0.076
Ca (mmol/L)	−0.306	0.233	0.043	0.869	0.137	0.599	0.021	0.936	0.355	0.162	−0.039	0.882
UA (μmol/L)	0.520	0.033	−0.091	0.729	−0.479	0.052	−0.059	0.823	−0.122	0.642	−0.112	0.668
Urinary pH	0.160	0.539	−0.357	0.159	0.376	0.136	0.043	0.869	0.190	0.466	0.106	0.687
Control												
TG (mmol/L)	0.020	0.940	0.444	0.074	0.007	0.978	0.303	0.237	0.048	0.856	0.056	0.831
HDL-C (mmol/L)	−0.085	0.747	−0.342	0.179	0.493	0.044	−0.036	0.892	−0.096	0.715	0.255	0.323
K (mmol/L)	0.829	<0.001	0.273	0.289	0.001	0.996	0.101	0.700	−0.086	0.743	0.074	0.777
Ca (mmol/L)	0.249	0.334	−0.063	0.811	0.090	0.732	−0.376	0.137	−0.372	0.141	0.048	0.855
UA (μmol/L)	0.140	0.593	0.351	0.168	−0.234	0.366	−0.037	0.889	−0.088	0.738	−0.214	0.409
Urinary pH	−0.037	0.889	−0.213	0.412	0.033	0.900	−0.363	0.152	0.412	0.101	0.094	0.721

TG, triglycerides; HDL-C, high-density lipoprotein cholesterol; UA, serum uric acid; and UAS, uric acid stone.

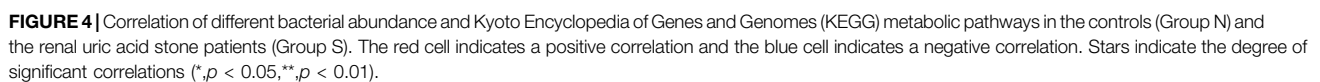
Spearman correlation coefficient values were further adjusted for age and sex.

Bold values indicate significant difference.

Our study indicated that the urine pH of UAS patients, especially stone formers with gout, was significantly lower than other subjects. The diseases that cause acidic urine included obesity, cardiovascular disease, insulin resistance, and chronic diarrhea (Bobulescu et al., 2019). The baseline characteristics of UAS patients in our study were partly consistent with the aforementioned clinic features. Epidemiological investigation has demonstrated that increased metabolic syndrome related factors significantly promoted the risk of UAS (Boyd et al., 2018). Several researchers have reported and confirmed that there was an inverse correlation between BMI and urine pH (Nakajima et al., 2016). Multivariate analysis was carried out in 459 24-h urine samples of 183 adult patients with nephrolithiasis and found that hyperglycemia was associated with lower pH and higher urinary saturation with respect to uric acid, suggesting that glycemic control may be considered a target for the treatment of UAS (Maciolek et al., 2018). In addition, a cross-sectional study analyzed 24-h urine parameters and abdominal CT scan results of 98 patients with nephrolithiasis and reported that the greater abdominal visceral fat content was associated with lower urinary pH and higher risk of UAS (Patel et al., 2017). Our results suggested that the incidence of diabetes in UAS patients with gout was higher than that in other groups, but there was no statistical significance, possibly due to an insufficient sample size.

Our study revealed significant differences in the levels of TG and HDL-C between the Gout + UAS group and the other three groups, which indicated a positive correlation between the severity of dyslipidemia and the risk of metabolic disorders in patients with UAS. This conclusion was roughly similar to our previous study's results (Ding et al., 2019).

Nephrolithiasis is a known risk factor for chronic kidney disease (CKD), while UAS formation is associated with greater CKD risk compared with other stone types. Studies of patients with nephrolithiasis in Taiwan and Saudi Arabia found that the glomerular filtration rate (GFR) in UAS patients were significantly lower than those with other types of stones (Li et al., 2018; Nassir et al., 2018). While the serum potassium concentration of the Gout + UAS group was higher than other groups, suggesting decreased GFR and impaired renal tubule potassium excretion. On the flip side, the serum calcium concentration of the gout patients was the lowest, which was related to the calcium and phosphorus metabolism disorder caused by gouty nephropathy. Interestingly, there was no significant difference in the serum potassium level between gout patients and the controls. Glucocorticoid, as one of the treatment drugs for acute gout, can promote the sodium retention and potassium excretion of distal convoluted tubules and collecting tubules.



Under normal circumstances, the gut microbiota and host remains in a dynamic balance, which participates in various physiological processes of host nutrition absorption and metabolism. The gut microbiota can also affect the urine composition of the host, so the destruction of gut microbiota may lead to the occurrence of nephrolithiasis. Ticinesi et al. studied 52 patients with calcium oxalate nephrolithiasis and 48 healthy subjects, and found that the fecal microbial diversity in the stone group was significantly lower than that of the controls (Ticinesi et al., 2018). Stern et al. collected feces and urine samples of stone and non-stone patients, concluded that *Bacteroides* genus was the most abundant in stone formers and *Prevotella* genus was the most abundant in the control group. They also indicated that the composition of 24-h urine seemed to be related to the abundance of gut microbiota (Stern et al., 2016). A larger sample size and open-source project on the relationship between *Oxalobacter formigenes* and nephrolithiasis is being carried out in the United States (Liu et al., 2017).

Different from previous studies, we focused on the characteristics of gut microbiota in UAS patients for the first time. The healthy people rely on rich micro-ecosystem so as to maintain the necessary nutrition and metabolism, but with the aggravation of metabolic disorder, the intestinal microecology is destroyed. *Bacteroides* and Firmicutes accounted for more than 85% in the total amount of gut microbiota in our subjects, consistent with other experimental results at home and abroad (Ruan et al., 2020). However, there was a significant difference in the specific gravity of *Fusobacteria* at the phylum level. The relative abundance of *Fusobacteria* increased with the aggravation of metabolic disorders, and the specific gravity in Gout + UAS patients was the highest. At the genus level, *Fusobacterium* and *Bacteroides* were the dominant bacteria in patients with UAS, especially in the Gout + UAS group. Furthermore, Spearman correlation analysis results indicated that the abundance of *Bacteroides* and *Fusobacterium* was positively correlated with the serum UA level in UAS patients.

The involvement of the gut microbiota in multiple metabolic pathways in the host is widely recognized. Shotgun metagenomics sequencing technology is of course the most powerful approach to identify specific bacteria involved in metabolic pathways and identify gene function using the KEGG database. Liu et al. found a highly expressed bacterial gene in patients with recurrent calcium oxalate nephrolithiasis, which was involved in oxalate degradation and oxalate synthesis, and was related to high levels of urinary oxalate and acetic acid excretion (Liu et al., 2020). In this study, our PICRUSt analysis showed that *Fusobacteria* altered the microbial community functions, especially participated in the metabolism and degradation of certain short-chain fatty acids, amino acids, and sugars in UAS patients, but significantly inhibited their synthetic pathway. Future work including shotgun metagenomics analysis would help to confirm the specific gene functions.

Fusobacteria is a kind of anaerobic Gram-negative bacteria, which is widely colonized in human intestinal and oral mucosa and is related to the invasion of tumor cells (Kelly et al., 2018; Wang et al., 2020). There was a strong correlation between the abundance of *Fusobacteria* and the expression of pro-

inflammatory markers such as COX-2, suggesting that *Fusobacteria* could create a pro-inflammatory micro-environment conducive to colorectal cancer by recruiting tumor-infiltrating immune cells (Kostic et al., 2013; Sears, 2018; King et al., 2020). *Fusobacteria* might potentially enhance the invasiveness of cancer cells when it existed in the micro-environment of oral tumor (Harrandah et al., 2020). In addition, studies have shown that the enrichment of *Fusobacteria* is related to acute appendicitis in children (Zhong et al., 2014; Rogers et al., 2016).

Our study indicated that the enrichment of *Fusobacteria* in the intestinal tract of UAS formers was higher than that of normal population for the first time. On one hand, hyperuricemia can improve the excretion level of uric acid in urine; on the other hand, it can cause dysfunction of the function of renal tubules to secrete acid and then form stones. The unique risk factors for UAS include persistent acidic urine and hyperuricuria, which can also be verified in biochemical parameters (Table 2) and multivariate logistic analysis (Table 3) in this study. *Fusobacterium* may be involved in the degradation and metabolism of certain short-chain fatty acids (Figure 4), and these metabolic pathways are related to the acid-secreting function of renal tubules. The specific expression of *Fusobacterium* may induce a pro-inflammatory micro-environment that gout patients do not have.

Whether *Fusobacteria* promotes the expression of inflammatory factors in renal tubular epithelial cells, whether these inflammatory factors promote the formation of stones caused by urine acidification, and whether the metabolic pathway involved in *Fusobacteria* can be targeted for pharmacological intervention? With the rapid development of computational intelligence, the application scenarios of artificial intelligence (AI) are becoming richer and richer. In the future, computational intelligence can be applied to pharmacological intervention of gut microbiota to treat metabolic diseases such as UAS. The computer obtained the basic data group of gut microbiota of target patients through meta-analysis of a large number of literatures. Through algorithm improvement, a suitable retrieval model was established to complete the application research of the AI-based gut microbiota intervention model for UAS. The computer intelligently learned the basic data processing in data mining, data processing, data cleaning and so on. Through the analysis, it can be concluded whether pharmacological intervention for gut microbiota of UAS is feasible based on data mining, so that computational intelligence can learn more pharmacological intervention plans on the basis of disease association rules. Research and development of drugs through AI can greatly shorten the time of drug development, improve the efficiency of research, control the cost of research, and improve the efficiency of doctors' personalized treatment.

Until now, the number of subjects included in this study was not large enough, and the results need to be further verified by expanding the sample size. Second, there was no 24-h urine composition analysis for stone formers in this study. The last but not least, due to financial constraints, collected fecal samples were

not tested for short-chain fatty acids and lacked metabonomic analysis.

CONCLUSION

Renal uric acid stone formers, especially complicated with gout, often have various types of dyslipidemia, persistent hyperuricemia, and aciduria. The richness and diversity of their gut microbiota were different from the gout patients as well as normal population. *Bacteroides* and *Fusobacterium* were positively correlated with the serum UA level of patients with UAS. The pro-inflammatory bacteria, *Fusobacteria*, may be related to the pathogenesis of UAS and has the potential to become the biomarker. These findings may provide a novel and non-invasive target for the prevention and treatment of UAS, which requires further large-scale investigation.

DATA AVAILABILITY STATEMENT

The datasets presented in this study can be found in online repositories. The names of the repository/repositories and accession number(s) can be found below: <https://www.ncbi.nlm.nih.gov/Traces/study/SRP332626>.

REFERENCES

- Abou-Elela, A. (2017). Epidemiology, Pathophysiology, and Management of Uric Acid Urolithiasis: A Narrative Review. *J. Adv. Res.* 8 (5), 513–527. doi:10.1016/j.jare.2017.04.005
- Bobulescu, I. A., Park, S. K., Xu, L. H. R., Blanco, F., Poindexter, J., Adams-Huet, B., et al. (2019). Net Acid Excretion and Urinary Organic Anions in Idiopathic Uric Acid Nephrolithiasis. *Clin. J. Am. Soc. Nephrol.* 14 (3), 411–420. doi:10.2215/cjn.10420818
- Boyd, C., Wood, K., Whitaker, D., and Assimios, D. G. (2018). The Influence of Metabolic Syndrome and its Components on the Development of Nephrolithiasis. *Asian J. Urol.* 5 (4), 215–222. doi:10.1016/j.ajur.2018.06.002
- De Sordi, L., Khanna, V., and Debarbieux, L. (2017). The Gut Microbiota Facilitates Drifts in the Genetic Diversity and Infectivity of Bacterial Viruses. *Cell Host Microbe* 22 (6), 801–e3. doi:10.1016/j.chom.2017.10.010
- Ding, Q., Ouyang, J., Fan, B., Cao, C., Fan, Z., Ding, L., et al. (2019). Association between Dyslipidemia and Nephrolithiasis Risk in a Chinese Population. *Urol. Int.* 103 (2), 156–165. doi:10.1159/000496208
- Friedlander, J. I., Moreira, D. M., Hartman, C., Elsamra, S. E., Smith, A. D., and Okeke, Z. (2014). Comparison of the Metabolic Profile of Mixed Calcium Oxalate/uric Acid Stone Formers to that of Pure Calcium Oxalate and Pure Uric Acid Stone Formers. *Urology* 84 (2), 289–294. doi:10.1016/j.urology.2014.04.019
- Ganesan, V., De, S., Shkumat, N., Marchini, G., and Monga, M. (2018). Accurately Diagnosing Uric Acid Stones from Conventional Computerized Tomography Imaging: Development and Preliminary Assessment of a Pixel Mapping Software. *J. Urol.* 199 (2), 487–494. doi:10.1016/j.juro.2017.09.069
- Harrandah, A. M., Chukkappalli, S. S., Bhattacharyya, I., Progulske-Fox, A., and Chan, E. K. L. (2020). *Fusobacteria* Modulate Oral Carcinogenesis and Promote Cancer Progression. *J. Oral Microbiol.* 13 (1), 1849493. doi:10.1080/20002297.2020.1849493
- Joosten, L. A. B., Crişan, T. O., Bjornstad, P., and Johnson, R. J. (2020). Asymptomatic Hyperuricaemia: a Silent Activator of the Innate Immune System. *Nat. Rev. Rheumatol.* 16 (2), 75–86. doi:10.1038/s41584-019-0334-3
- Kelly, D., Yang, L., and Pei, Z. (2018). Gut Microbiota, *Fusobacteria*, and Colorectal Cancer. *Diseases* 6 (4). doi:10.3390/diseases6040109

AUTHOR CONTRIBUTIONS

CC, JZ, and D-RY contributed to conception and design of the study. CC analyzed the data and wrote the manuscript. Data collection was performed by BF, J-YC, and ZN. D-RY and JZ revised the manuscript. All authors read and approved the final manuscript.

FUNDING

This study was funded by the Suzhou Youth Science and Technology Project (KJXW2019060), the Changshu Medical Science and Technology Program (cswsq202002), the Suzhou Science and Technology Project (SKJY2021008) and the Suzhou Medical Research Key Talents Program (GSWS2021016).

SUPPLEMENTARY MATERIAL

The Supplementary Material for this article can be found online at: <https://www.frontiersin.org/articles/10.3389/fphar.2022.888883/full#supplementary-material>

- King, M., Hurley, H., Davidson, K. R., Dempsey, E. C., Barron, M. A., Chan, E. D., et al. (2020). The Link between *Fusobacteria* and Colon Cancer: a Fulminant Example and Review of the Evidence. *Immune Netw.* 20 (4), e30. doi:10.4110/in.2020.20.e30
- Kostic, A. D., Chun, E., Robertson, L., Glickman, J. N., Gallini, C. A., Michaud, M., et al. (2013). *Fusobacterium Nucleatum* Potentiates Intestinal Tumorigenesis and Modulates the Tumor-Immune Microenvironment. *Cell Host Microbe* 14 (2), 207–215. doi:10.1016/j.chom.2013.07.007
- Langille, M. G., Zaneveld, J., Caporaso, J. G., McDonald, D., Knights, D., Reyes, J. A., et al. (2013). Predictive Functional Profiling of Microbial Communities Using 16S rRNA Marker Gene Sequences. *Nat. Biotechnol.* 31 (9), 814–821. doi:10.1038/nbt.2676
- Lee, J. A., and Stern, J. M. (2019). Understanding the Link between Gut Microbiome and Urinary Stone Disease. *Curr. Urol. Rep.* 20 (5), 19. doi:10.1007/s11934-019-0882-8
- Li, C. C., Chien, T. M., Wu, W. J., Huang, C. N., and Chou, Y. H. (2018). Uric Acid Stones Increase the Risk of Chronic Kidney Disease. *Urolithiasis* 46 (6), 543–547. doi:10.1007/s00240-018-1050-1
- Liu, M., Koh, H., Kurtz, Z. D., Battaglia, T., PeBenito, A., Li, H., et al. (2017). *Oxalobacter Formigenes*-Associated Host Features and Microbial Community Structures Examined Using the American Gut Project. *Microbiome* 5 (1), 108. doi:10.1186/s40168-017-0316-0
- Liu, Y., Jin, X., Hong, H. G., Xiang, L., Jiang, Q., Ma, Y., et al. (2020). The Relationship between Gut Microbiota and Short Chain Fatty Acids in the Renal Calcium Oxalate Stones Disease. *FASEB J.* 34 (8), 11200–11214. doi:10.1096/fj.202000786R
- Ma, Q., Fang, L., Su, R., Ma, L., Xie, G., and Cheng, Y. (2018). Uric Acid Stones, Clinical Manifestations and Therapeutic Considerations. *Postgrad. Med. J.* 94 (1114), 458–462. doi:10.1136/postgradmedj-2017-135332
- Macielek, K. A., Penniston, K. L., Jhagroo, R. A., and Best, S. L. (2018). Successful Diabetic Control as Measured by Hemoglobin A1c Is Associated with Lower Urine Risk Factors for Uric Acid Calculi. *J. Endourol.* 32 (8), 771–776. doi:10.1089/end.2018.0376
- Nakajima, K., Oda, E., and Kanda, E. (2016). Latent Association between Low Urine pH and Low Body Weight in an Apparently Healthy Population. *Scand. J. Clin. Lab. Invest.* 76 (1), 58–63. doi:10.3109/00365513.2015.1092049

- Nassir, A., Saada, H., Alnajjar, T., Nasser, J., Jameel, W., Elmorsy, S., et al. (2018). The Impact of Stone Composition on Renal Function. *Urol. Ann.* 10 (2), 215–218. doi:10.4103/ua.Ua_85_17
- Patel, N. D., Ward, R. D., Calle, J., Remer, E. M., and Monga, M. (2017). Computerized Tomography Based Diagnosis of Visceral Obesity and Hepatic Steatosis Is Associated with Low Urine pH. *J. Urol.* 198 (5), 1085–1090. doi:10.1016/j.juro.2017.05.079
- Rajkumar, P., and Pluznick, J. L. (2018). Acid-base Regulation in the Renal Proximal Tubules: Using Novel pH Sensors to Maintain Homeostasis. *Am. J. Physiol. Ren. Physiol.* 315 (5), F1187–F1190. doi:10.1152/ajprenal.00185.2018
- Rogers, M. B., Brower-Sinning, R., Firek, B., Zhong, D., and Morowitz, M. J. (2016). Acute Appendicitis in Children Is Associated with a Local Expansion of Fusobacteria. *Clin. Infect. Dis.* 63 (1), 71–78. doi:10.1093/cid/ciw208
- Ruan, W., Engevik, M. A., Spinler, J. K., and Versalovic, J. (2020). Healthy Human Gastrointestinal Microbiome: Composition and Function after a Decade of Exploration. *Dig. Dis. Sci.* 65 (3), 695–705. doi:10.1007/s10620-020-06118-4
- Sakhaee, K. (2008). Nephrolithiasis as a Systemic Disorder. *Curr. Opin. Nephrol. Hypertens.* 17 (3), 304–309. doi:10.1097/MNH.0b013e3282f8b34d
- Sears, C. L. (2018). The Who, where and How of Fusobacteria and colon Cancer. *eLife* 7. doi:10.7554/eLife.28434
- Siva, S., Barrack, E. R., Reddy, G. P., Thamilselvan, V., Thamilselvan, S., Menon, M., et al. (2009). A Critical Analysis of the Role of Gut Oxalobacter Formigenes in Oxalate Stone Disease. *BJU Int.* 103 (1), 18–21. doi:10.1111/j.1464-410X.2008.08122.x
- Stanford, J., Charlton, K., Stefoska-Needham, A., Ibrahim, R., and Lambert, K. (2020). The Gut Microbiota Profile of Adults with Kidney Disease and Kidney Stones: a Systematic Review of the Literature. *BMC Nephrol.* 21 (1), 215. doi:10.1186/s12882-020-01805-w
- Stern, J. M., Moazami, S., Qiu, Y., Kurland, I., Chen, Z., Agalliu, I., et al. (2016). Evidence for a Distinct Gut Microbiome in Kidney Stone Formers Compared to Non-stone Formers. *Urolithiasis* 44 (5), 399–407. doi:10.1007/s00240-016-0882-9
- Tang, R., Jiang, Y., Tan, A., Ye, J., Xian, X., Xie, Y., et al. (2018). 16S rRNA Gene Sequencing Reveals Altered Composition of Gut Microbiota in Individuals with Kidney Stones. *Urolithiasis* 46 (6), 503–514. doi:10.1007/s00240-018-1037-y
- Ticinesi, A., Milani, C., Guerra, A., Allegri, F., Lauretani, F., Nouvenne, A., et al. (2018). Understanding the Gut-Kidney axis in Nephrolithiasis: an Analysis of the Gut Microbiota Composition and Functionality of Stone Formers. *Gut* 67 (12), 2097–2106. doi:10.1136/gutjnl-2017-315734
- Tran, T. V. M., and Maalouf, N. M. (2020). Uric Acid Stone Disease: Lessons from Recent Human Physiologic Studies. *Curr. Opin. Nephrol. Hypertens.* 29 (4), 407–413. doi:10.1097/mnh.0000000000000610
- Trinchieri, A., and Montanari, E. (2017). Prevalence of Renal Uric Acid Stones in the Adult. *Urolithiasis* 45 (6), 553–562. doi:10.1007/s00240-017-0962-5
- Wang, P., Ding, S., Sun, L., Feng, Y., Guo, K., Zhu, Y., et al. (2020). Characteristics and Differences of Gut Microbiota in Patients with Different Traditional Chinese Medicine Syndromes of Colorectal Cancer and normal Population. *J. Cancer* 11 (24), 7357–7367. doi:10.7150/jca.50318
- Wang, W., Fan, J., Huang, G., Li, J., Zhu, X., Tian, Y., et al. (2017). Prevalence of Kidney Stones in mainland China: A Systematic Review. *Sci. Rep.* 7, 41630. doi:10.1038/srep41630
- Zhong, D., Brower-Sinning, R., Firek, B., and Morowitz, M. J. (2014). Acute Appendicitis in Children Is Associated with an Abundance of Bacteria from the Phylum Fusobacteria. *J. Pediatr. Surg.* 49 (3), 441–446. doi:10.1016/j.jpedsurg.2013.06.026

Conflict of Interest: The authors declare that the research was conducted in the absence of any commercial or financial relationships that could be construed as a potential conflict of interest.

Publisher's Note: All claims expressed in this article are solely those of the authors and do not necessarily represent those of their affiliated organizations, or those of the publisher, the editors, and the reviewers. Any product that may be evaluated in this article, or claim that may be made by its manufacturer, is not guaranteed or endorsed by the publisher.

Copyright © 2022 Cao, Fan, Zhu, Zhu, Cao and Yang. This is an open-access article distributed under the terms of the Creative Commons Attribution License (CC BY). The use, distribution or reproduction in other forums is permitted, provided the original author(s) and the copyright owner(s) are credited and that the original publication in this journal is cited, in accordance with accepted academic practice. No use, distribution or reproduction is permitted which does not comply with these terms.



Systematic Bibliometric and Visualized Analysis of Research Hotspots and Trends on the Application of Artificial Intelligence in Ophthalmic Disease Diagnosis

OPEN ACCESS

Edited by:

Yuanpeng Zhang,
Nantong University, China

Reviewed by:

Huiying Liu,
Institute for Infocomm Research
(A*STAR), Singapore
Yiqi Chen,
Zhejiang Provincial People's Hospital,
China

Yalin Zheng,
University of Liverpool,
United Kingdom

*Correspondence:

Weihua Yang
benben0606@139.com
Qin Jiang
jqin710@vip.sina.com
Keran Li
kathykeran860327@126.com

[†]These authors have contributed
equally to this work

Specialty section:

This article was submitted to
Experimental Pharmacology and Drug
Discovery,
a section of the journal
Frontiers in Pharmacology

Received: 28 April 2022

Accepted: 23 May 2022

Published: 08 June 2022

Citation:

Zhao J, Lu Y, Zhu S, Li K, Jiang Q and
Yang W (2022) Systematic Bibliometric
and Visualized Analysis of Research
Hotspots and Trends on the
Application of Artificial Intelligence in
Ophthalmic Disease Diagnosis.
Front. Pharmacol. 13:930520.
doi: 10.3389/fphar.2022.930520

Junqiang Zhao^{1†}, Yi Lu^{1†}, Shaojun Zhu², Keran Li^{3*}, Qin Jiang^{3*} and Weihua Yang^{3*}

¹Department of Nursing, Xinxiang Medical University, Xinxiang, China, ²School of Information Engineering, Huzhou University, Huzhou, China, ³The Laboratory of Artificial Intelligence and Bigdata in Ophthalmology, Affiliated Eye Hospital of Nanjing Medical University, Nanjing, China

Background: Artificial intelligence (AI) has been used in the research of ophthalmic disease diagnosis, and it may have an impact on medical and ophthalmic practice in the future. This study explores the general application and research frontier of artificial intelligence in ophthalmic disease detection.

Methods: Citation data were downloaded from the Web of Science Core Collection database to evaluate the extent of the application of Artificial intelligence in ophthalmic disease diagnosis in publications from 1 January 2012, to 31 December 2021. This information was analyzed using CiteSpace.5.8. R3 and Vosviewer.

Results: A total of 1,498 publications from 95 areas were examined, of which the United States was determined to be the most influential country in this research field. The largest cluster labeled “Brownian motion” was used prior to the application of AI for ophthalmic diagnosis from 2007 to 2017, and was an active topic during this period. The burst keywords in the period from 2020 to 2021 were system, disease, and model.

Conclusion: The focus of artificial intelligence research in ophthalmic disease diagnosis has transitioned from the development of AI algorithms and the analysis of abnormal eye physiological structure to the investigation of more mature ophthalmic disease diagnosis systems. However, there is a need for further studies in ophthalmology and computer engineering.

Keywords: ophthalmic disease, artificial intelligence, diagnosis, bibliometric, CiteSpace

INTRODUCTION

Artificial intelligence (AI) is a broad term that refers to the use of computers to simulate intelligent behavior with little or no human intervention (Hamet and Tremblay, 2017). It is a multifaceted technology that includes complex algorithms, machine learning, and deep learning, transfer learning, among other components (Balyen and Peto, 2019; Kora et al., 2022). Medicine has long been identified as one of the most promising fields for the application of AI. Many clinical decision support systems have been proposed and developed by researchers since the mid-twentieth century

(Miller, 1994). AI has been used in ophthalmology to diagnose diseases in conjunction with imaging technologies such as optical coherence tomography, and fundus fluorescein angiography (Ruiz Hidalgo et al., 2017; Hemalakshmi et al., 2020; Wan et al., 2021c; Ran et al., 2021). In addition, several simple and low-cost diagnostic system models have been under development (Bourouis et al., 2014; Metha et al., 2021). As a possible solution for the screening of major ophthalmic diseases and telemedicine, AI has been applied to the study of ophthalmic disease diagnosis. For example, diabetic retinopathy, glaucoma, hypertensive retinopathy, high myopia, age-related macular degeneration, familial amyloidosis, cataract, and other related conditions have been investigated using this technology (Fang et al., 2017; Asaoka et al., 2019; Araujo et al., 2020; Juneja et al., 2020; Kessel et al., 2020; Zhou et al., 2020; Wan et al., 2021a; Grzybowski and Brona, 2021; Szeskin et al., 2021; Xu et al., 2022). AI may have an impact on medical and ophthalmic practice in the coming decades, based on the results of several published reports (Ting et al., 2019; Dai et al., 2021).

Previous studies have used bibliometric methods to study the application of artificial intelligence in ophthalmic diseases in China (Dong et al., 2021; Koh et al., 2021; Saeed et al., 2021; Boudry et al., 2022). However, there is no bibliometric research on the application of artificial intelligence in ophthalmic disease diagnosis. This study aimed to gain a comprehensive understanding of the general use and research frontier of artificial intelligence in ocular illness detection by examining multiple aspects. For example, Scientific Citation Index (SCI) papers on the application of artificial intelligence to ocular illness diagnosis were analyzed using bibliometric approaches. The analysis emphasized data related to countries, regions, institutions, journals, research categories, keywords, and references. A critical aspect of our study was the development of a repeatable and unbiased strategy for exploring the active knowledge frontier in the research field. In particular, we examined the active areas of applied artificial intelligence, future development areas, and potential hurdles, relative to ocular disease diagnostics. This report is intended to serve as a resource for artificial intelligence professionals, ophthalmologists, diagnosticians, and medical imaging researchers.

MATERIALS AND METHODS

On 1 April 2022, citation data published between 1 January 2012, to 31 December 2021, were retrieved from the Web of Science Core Collection (WoSCC). These data were independently verified by two authors (Weihua Yang and Yi Lu). The search formula was TS= (retinal or ophthalmology or eye or ophthalmic or corneal or eyelid or orbital or uveal or scleral) AND (AI or "Artificial Intelligence" or "neural network" or "transfer learning" or "Machine Learning" or "Deep Learning") AND (diagnos* or grad* or classification). The search selected English literature and articles and excluded early access, proceedings papers, book chapters, data papers, and retracted publications. To obtain the most accurate analysis results, we manually deleted data after reading the title and abstract of each literature. The criteria for manual exclusion are as follows: 1) the

research discipline does not include medicine; 2) The study organ is an organ other than the eye; 3) The research method does not use artificial intelligence method; 4) The study disease is not an eye disease. All the data we included in the analysis were the research of artificial intelligence in the diagnosis of ophthalmic diseases. For each publication, we extracted the title, publication year, country or region, institution, journal, references, and keywords. The detailed search and analysis processes are depicted in **Figure 1**.

Collaborative networks of countries, institutions, journals, keywords, references, and research categories were analyzed using CiteSpace5.8. R3 and Vosviewer. The article describes all citation features.

RESULTS

Distribution of Articles by Publication Year

This study analyzed 1,498 papers that were published between 2012 and 2021 that focused on the use of AI in the diagnosis of ophthalmic diseases. Using the Web of Science (WoS) citation analyzer to count the annual number of citations retrieved and using the duplicate removal function of CiteSpace software to verify the data of the number of citations. The number of annually published reports for this period is shown in **Figure 2**. Since 2018, the annual number of articles on the application of AI in the diagnosis of ophthalmic diseases has exceeded 100 and has increased rapidly in subsequent years.

Countries or Regions

The citation analyzer of WoS database is used to count the number of documents sent by countries or regions, and the default setting of CiteSpace software analyzes the cooperative relationship between countries and regions. These citations involve a total of 95 countries or regions. The size of each label and green node area in **Figure 3** represents the number of documents sent. Countries with large green node areas include the people's Republic of China (415 articles), the United States (365 articles) and India (263 articles). The connection between nodes represents the cooperative relationship between regions. Countries with more connecting lines have regions with strong influence, The area of purple circle indicates the influence of national documents, which is expressed by the centrality in **Table 1**. The purple circle in the United States has the largest area (0.25), indicating that the articles published in the United States in the field of ophthalmic diagnosis have the greatest overall influence. The data in **Table 1** objectively substantiate these conclusions. The H index can accurately reflect academic achievement (Hirsch, 2005). The higher the centrality and H index, the greater the influence of a paper. In general, China had the largest number of articles and the United States had the greatest influence.

Institutions

Table 2 lists the top 10 institutions for published articles that were analysed. The displayed data is outcome from the default settings of CiteSpace software and vosviewer software. These

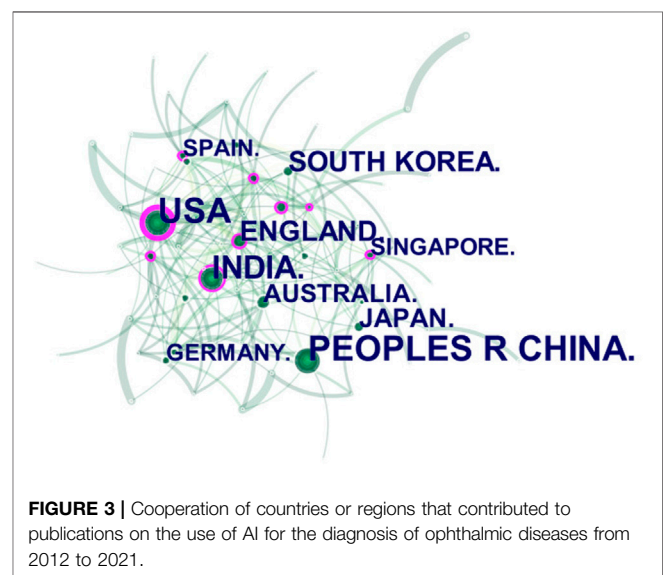
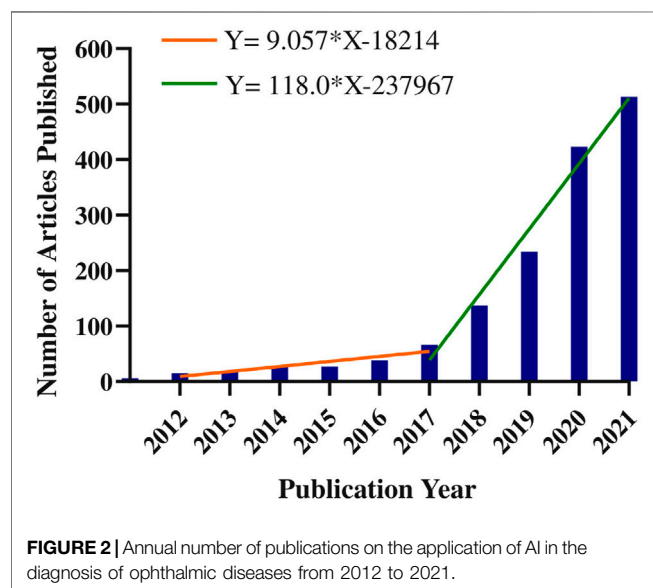
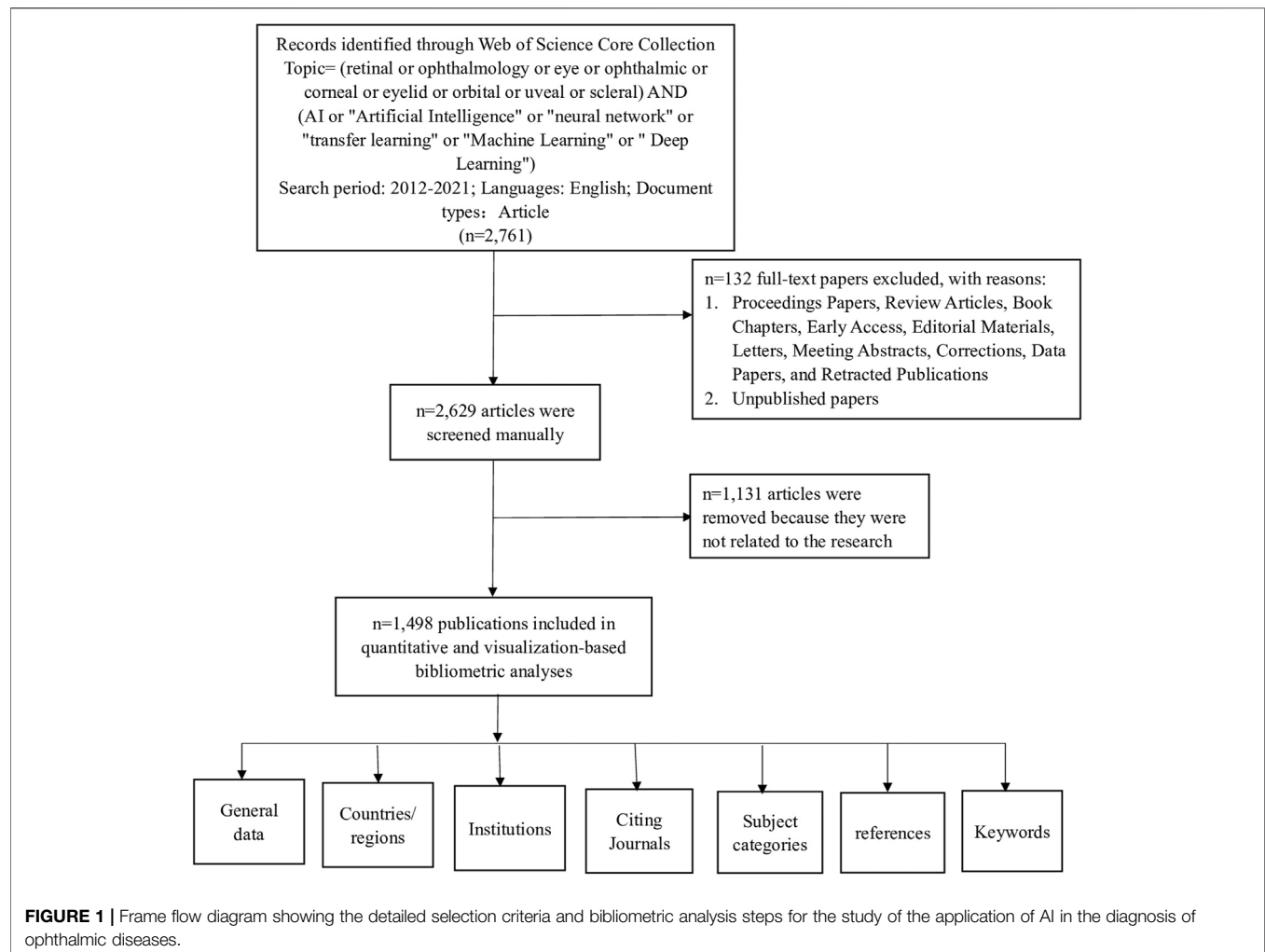
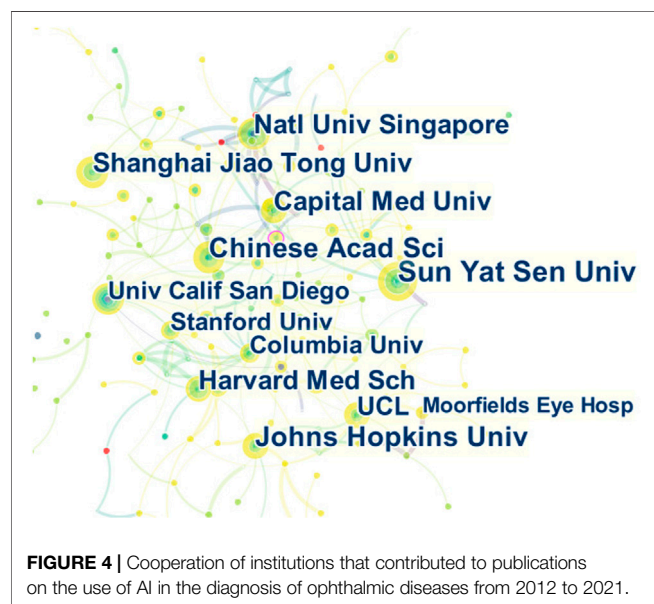


TABLE 1 | Top 10 countries or regions with publications on the application of the use of AI in the diagnosis of ophthalmic diseases from 2012 to 2021.

Rank	Countries or regions	Counts	Centrality	H-index
1	China	415	0.07	38
2	United States	365	0.25	48
3	India	263	0.12	31
4	England	119	0.18	24
5	South Korea	109	0.04	21
6	Japan	76	0.03	19
7	Australia	73	0.08	19
8	Singapore	53	0.14	20
9	Germany	48	0.04	15
10	Spain	48	0.17	13

TABLE 2 | Top 10 Institutions with publications on the application or the use of AI in the diagnosis of ophthalmic diseases from 2012 to 2021.

Rank	Institution	Count	H-index	Countries or regions
1	University of California System	49	17	United States
2	Harvard University	47	15	United States
3	University of London	46	13	England
4	University College London	44	13	England
5	Moorfields Eye Hospital NHS foundation Trust	40	12	England
6	Chinese Academy of Sciences	38	10	Chinese
7	Sun Yat Sen University	38	10	Chinese
8	National University of Singapore	35	17	Singapore
9	Johns Hopkins University	33	12	US
10	Shanghai Jiao Tong University	31	8	Chinese



included three American institutions, three England institutions, three Chinese institutions, and one Singapore institution. Two of the top five institutions with the highest h-index were from the United States and England. The connection between the tags in **Figure 4** shows the inter-agency cooperation. The node size indicates the number of documents sent.

Journals and Research Category

The documents in the cited journals constitute the knowledge base of the referenced articles. The research fields in highly cited journals constitute an active area of interest or hotspot. We use CiteSpace to draw the citation relationship in the field of journal research. The paths of the two colors shown in **Figure 5** represent the citation relationship of highly active research fields. Among them, the red path represents the classification of the journals with the most papers. The research field of the citing journals is represented on the left, and the research field of the cited journals is shown on the right. The knowledge-based research fields of AI application in ophthalmic disease diagnosis in the recent

10 years include systems/computing/computer/molecular/biology/genetics/health/nursing/medicine/ophthalmology, which constitute the hotspot subjects involved in the research frontier such as mathematics/systems/mathematical/neurology/sports/ophthalmology. **Tables 3, 4** list the discipline categories of the citing journals and cited journals/proceedings that rank among the top ten in terms of citations. The most common research field of the citing journals includes engineering technology/computers. The discipline that was most involved in the extracted version was classified as medicine/ophthalmology.

Keywords

To better understand the adoption of AI in the field of ophthalmic disease diagnosis in the recent 10 years based on an analysis diagram of keyword co-occurrence cooperation network, the emerging keywords that progressed over time were analyzed. This represented the migration of research hotspots. The default setting of CiteSpace is changed to the following mode: “Year Per Slice” = 2, “Top N%” = 30.0%, and “Minimum Duration” = 1. We get the result of **Figure 6**. The red square in **Figure 6** represents emerging keywords for the investigated timeline. The bursts keywords from 2012 to 2021 included machine learning classifier (2012–2015), artificial neural network (2012–2015), nerve fiber layer (2012–2015), retinal layer (2018–2019), head (2018–2019), macular degeneration (2018–2019), cup (2018–2019), system (2020–2021), disease (2020–2021), and model (2020–2021).

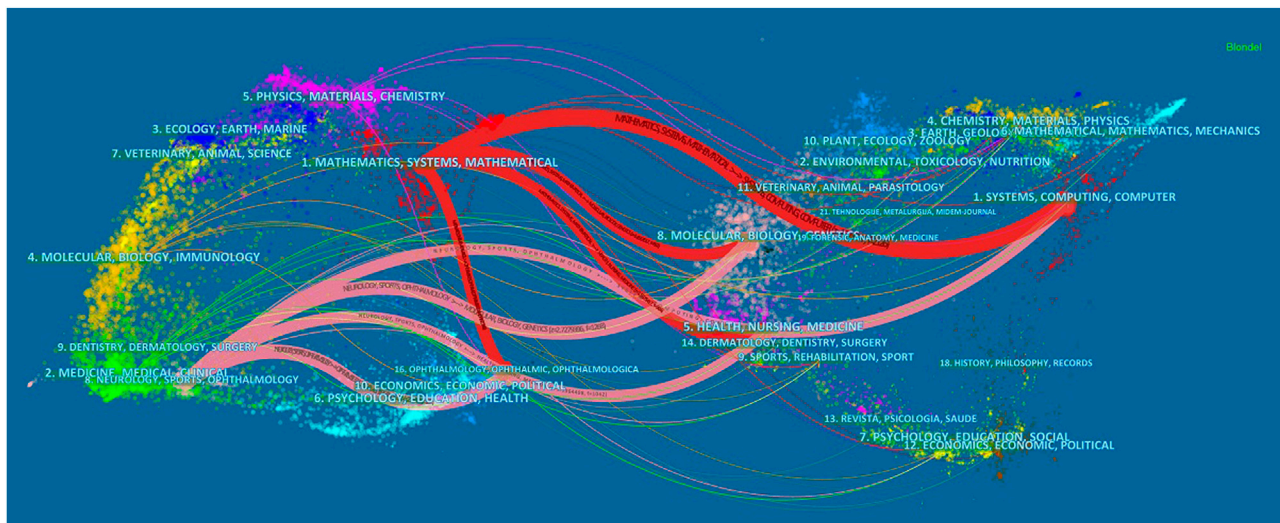


FIGURE 5 | Dual map overlay of journals that contributed to publications on the use of AI in the diagnosis of ophthalmic diseases from 2012 to 2021.

TABLE 3 | Top 10 citing journals of publications on the use of AI in the diagnosis of ophthalmic diseases from 2012 to 2021.

Rank	Citing journals	Research fields	Counts	Journal impact factor 2020
1	IEEE Access	Engineering Technology/Computer: Information System	73	3.367
2	Translational Vision Science & Technology	Medicine Ophthalmology	68	3.283
3	Scientific Reports	Comprehensive journal	59	4.38
4	Biomedical Signal Processing and Control	Engineering Technology/Engineering: Biomedicine	37	3.88
5	Computer Methods and Programs in Biomedicine	Engineering Technology/Computer: Interdisciplinary Applications	33	5.428
6	Multimedia Tools and Applications	Engineering Technology/Computer: Information System	32	2.757
7	American Journal of Ophthalmology	Medicine/Ophthalmology	30	5.258
8	PLOS ONE	Comprehensive journal	30	3.24
9	IEEE Transactions on Medical Imaging	Medicine/Computer: Interdisciplinary Applications	27	10.048
10	Neurocomputing	Engineering Technology/Computer: Artificial Intelligence	24	5.719

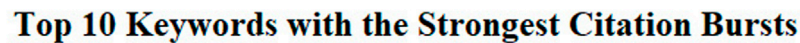
TABLE 4 | Top 10 cited journals of publications on the use of AI in the diagnosis of ophthalmic diseases from 2012 to 2021.

Rank	Citing journals	Research fields	Counts	Journal impact factor 2020
1	Ophthalmology	Medicine/Ophthalmology	702	12.079
2	Investigative Ophthalmology & Visual Science	Medicine/Ophthalmology	660	4.799
3	IEEE Transactions on Medical Imaging	Medicine/Computer: Interdisciplinary Applications	579	10.048
4	British Journal of Ophthalmology	Medicine/Ophthalmology	527	4.638
5	American Journal of Ophthalmology	Medicine/Ophthalmology	437	5.258
6	PLOS ONE	Comprehensive journal	430	3.24
7	Journal of Perianesthesia Nursing	Engineering Technology/Computer: Artificial Intelligence	396	1.084
8	JAMA-Journal of the American Medical Association	Medicine/Internal Medicine	384	56.274
9	Computers in Biology and Medicine	Engineering Technology/Biology	342	4.5892
10	IEEE Transactions on Pattern Analysis and Machine Intelligence	Engineering Technology/Computer: Artificial Intelligence	338	16.389

Citing Articles and References

The cited documents were highly related to the research topics. Using the default setting of CiteSpace to cluster the co cited documents and choose label clusters with indexing terms. The cluster labels that represented the research frontiers of the co-

cited documents were obtained from these documents. The cited literature constituted the knowledge base of the research, and the size of the clusters obtained from the literature are listed in order from top to bottom on the right side of **Figure 7**. The largest cluster label #0 "Brownian motion" was obtained during













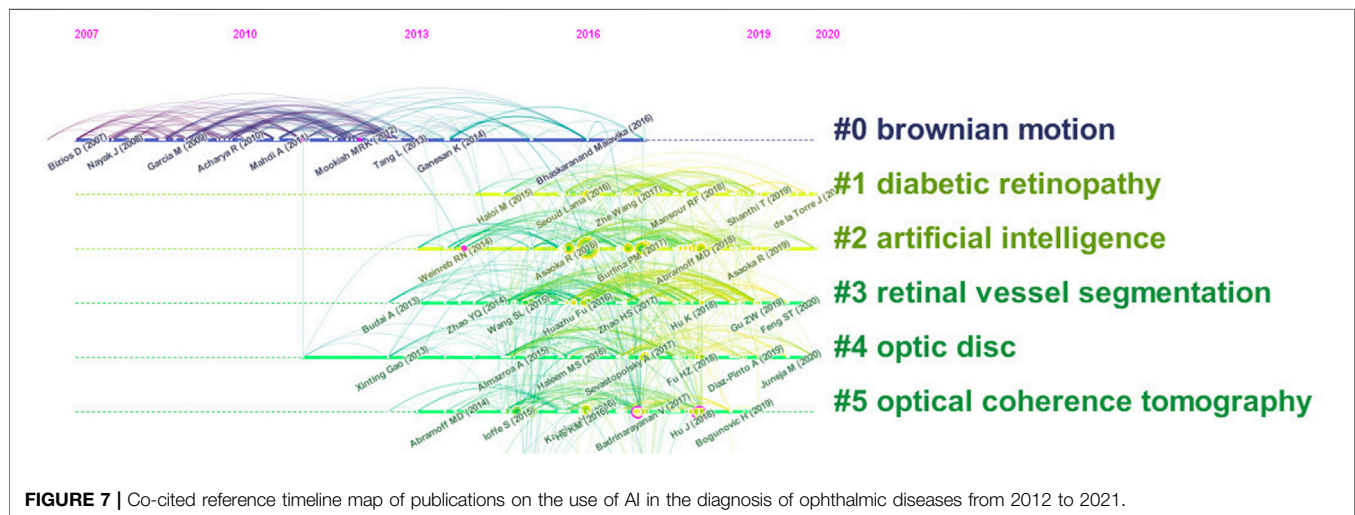
Keywords	Year	Strength	Begin	End	2012 - 2021
machine learning classifier	2012	3.79	2012	2015	
artificial neural network	2012	3.2	2012	2015	
nerve fiber layer	2012	2.61	2012	2015	
retinal layer	2012	3.41	2018	2019	
head	2012	3.21	2018	2019	
maculardegeneration	2012	2.75	2018	2019	
cup	2012	2.74	2018	2019	
system	2012	4.89	2020	2021	
disease	2012	3.46	2020	2021	
model	2012	2.86	2020	2021	

FIGURE 6 | Keywords with the strongest citation bursts for publications on the use of AI in the diagnosis of ophthalmic diseases from 2012 to 2021.



the pre-period of the application of AI for ophthalmic diagnosis, which was 2007–2017, and was a research hotspot. **Table 5** lists the top ten citing literature from “times cited in all databases” among the relevant literature based on the application of AI for ophthalmic diagnosis. It was determined that AI techniques are promising for use in the diagnosis of ophthalmic diseases although there are some limitations associated with their use.

DISCUSSION

Principal Results

Based on the preceding results, it is apparent that the published literature on the application of AI in the diagnosis of ophthalmic diseases has increased sharply in the past 5 years. This indicates that this research field has gradually attracted significant interest in recent years. The World

Economic 2016 Forum identified the open artificial intelligence ecosystem as one of the ten most important emerging technologies (President et al., 2016). Gulshan, V et al. established that deep learning algorithms had high sensitivity and specificity for detecting diabetic retinopathy and macular edema (Gulshan et al., 2016). Although it is impossible to predict the number of literature on AI for ophthalmic disease diagnosis that will be published in the future, it is still a promising research field and the efficacy of the application of AI has been confirmed by many studies (Giardini and Livingstone, 2020).

In terms of the number of national documents, the United States has the highest centrality and h-index. This indicates that this country has a leading position in this research field. In addition, developed countries such as Britain, Spain, and Singapore exhibited strong centrality and influence. Although China published a large number of papers, it lacked

TABLE 5 | Top 10 citing articles on the application of the use of AI in the diagnosis of ophthalmic diseases from 2012 to 2021.

Rank	Title of citing documents	DOI	Times cited	Interpretation of the findings	Research limitations
1	Development and Validation of a Deep Learning Algorithm for Detection of Diabetic Retinopathy in Retinal Fundus Photographs (Gulshan et al., 2016)	10.1001/jama.2016.17216	2,591	Deep machine learning-based algorithms have high sensitivity and specificity for detecting actionable diabetic retinopathy.	<p>1. Image subtly was difficult for ophthalmologists to interpret.</p> <p>2. The algorithm only displayed the lesion grade and did not count the actual diabetic retinopathy lesions.</p> <p>3. Ophthalmic examination image data sets were limited in number.</p> <p>4. The algorithm identified only diabetic retinopathy and diabetic macular edema.</p> <p>5. The clinical utility of user interface settings is unknown.</p>
2	Development and Validation of a Deep Learning System for Diabetic Retinopathy and Related Eye Diseases Using Retinal Images From Multiethnic Populations With Diabetes (Ting et al., 2017)	10.1001/jama.2017.18152	769	Deep learning systems for the evaluation of retinal images in multiethnic diabetic patients are highly sensitive and specific for identifying diabetic retinopathy and associated eye diseases.	<p>1. Inconsistencies in diagnostic criteria among ophthalmologists.</p> <p>2. The algorithm only displayed the lesion grade and did not count the actual diabetic retinopathy lesions.</p> <p>3. Diagnosis of all diabetic macular edema still requires the use of optical coherence tomography</p>
3	Segmenting Retinal Blood Vessels with Deep Neural Networks (Liskowski and Krawiec, 2016)	10.1109/TMI.2016.2546227	481	Deep neural networks are a viable methodology for medical imaging.	Only a limited set of image data including drive database, start database, and chase database, were used. These data sets contained limited examination populations.
4	Automated Identification of Diabetic Retinopathy using Deep Learning (Gargeya and Leng, 2017)	10.1016/j.ophtha.2017.02.008	478	This study presented a novel deep learning-based automatic feature learning method for Diabetic Retinopathy detection that offered an efficient, low-cost, and objective diagnostic method, which has high efficiency without relying on clinicians to manually review and grade images.	<p>1. It was difficult for the algorithm to automatically distinguish between partial and early-stage cases of diabetic retinopathy.</p> <p>2. Limitations in the number of image datasets analyzed.</p>
5	Improved Automated Detection of Diabetic Retinopathy on a Publicly Available Dataset Through Integration of Deep Learning (Abramoff et al., 2016)	10.1167/iov.16-19964	403	Deep learning enhanced algorithms have the potential to improve the efficiency of diabetic retinopathy screening	<p>1. The ophthalmic disease examination images in the disclosed data set represented only part of the clinical examination images.</p> <p>2. Different reference standards may cause differences in the performance of device measurement algorithms.</p> <p>3. The approach lacked the same flexibility as an actual clinical diagnosis.</p>
6	Pivotal Trial of an Autonomous AI-Based Diagnostic System for Detection of Diabetic Retinopathy in Primary Care Offices (Abramoff et al., 2018)	10.1038/s41746-018-0040-6	355	The algorithm developed in this study is the first autonomous artificial intelligence diagnosis system for the detection of diabetic retinopathy in any medical field authorized by the United States Food and Drug Administration.	<p>1. Limitations of the spectrum of disease tested in the system.</p> <p>2. The sensitivity of the AI system was lower than that of a similar AI system that was tested using a laboratory dataset.</p>

(Continued on following page)

TABLE 5 | (Continued) Top 10 citing articles on the application of the use of AI in the diagnosis of ophthalmic diseases from 2012 to 2021.

Rank	Title of citing documents	DOI	Times cited	Interpretation of the findings	Research limitations
7	A Cross-Modality Learning Approach for Vessel Segmentation in Retinal Images (Li et al., 2016)	10.1109/TMI.2015.2457891	330	A novel supervised vascular segmentation method for retinal images was presented, which has potential applications in retinal image diagnostic systems	1. There are specific requirements for the quality of the images to be diagnosed. 2. Special algorithms that simultaneously predict all pixel labels in one retinal image block remain unknown.
8	Automatic Segmentation of Nine Retinal Layer Boundaries in OCT Images of Non-Exudative AMD Patients using Deep Learning and Graph Search (Fang et al., 2017)	10.1364/BOE.8.002732	274	A new framework combining convolutional neural network and pattern search method was proposed for automatic segmentation of nine-layer boundaries of retinal optical coherence tomography image	The framework was validated in only subjects with non-exclusive age-related macular degeneration.
9	Joint Optic Disc and Cup Segmentation Based on Multi-Label Deep Network and Polar Transformation (Fu et al., 2018)	10.1109/TMI.2018.2791488	277	This study proposed a deep learning architecture called M-net, which jointly solved the problem of the optic disc and cup segmentation in fundus images in a single-stage multi-label system, and developed a function for glaucoma screening	The image data sets selected for verification were limited and included only ORIGA and SCES datasets.
10	Efficacy of a Deep Learning System for Detecting Glaucomatous Optic Neuropathy Based on Color Fundus Photographs (Li et al., 2018)	10.1016/j.ophtha.2018.01.023	272	This study proposed a deep learning system for detecting referable glaucomatous optic neuropathy with high sensitivity and specificity.	The ophthalmic images used in the study were only collected from Chinese hospitals, resulting in limitations associated with the image data

TABLE 6 | Top ten diseases mentioned in the published literature from 2020 to 2021.

Rank	Disease	Counts	Rank	Disease	Counts
1	Diabetic Retinopathy	340	6	Cataract	54
2	Glaucoma	294	7	Retinopathy of Prematurity	35
3	Age-related Macular Degeneration	128	8	Ophthalmic Tumor	31
4	Corneal Disease	71	9	Myopia	31
5	Diabetic Macular Edema	64	10	Intraocular Pressure	26

highly cited articles. The top five research institutions in terms of the number of publications are in the United States and the United Kingdom. From the perspective of the h-index, the national unity of Singapore had a strong impact. This was observed in the analysis results for national document issuance. From the analysis of the research field of the journal, it is evident that in recent years, research focused on the use of computer engineering technology combined with a knowledge base of ophthalmology to develop more suitable ophthalmic disease detection systems. AI is widely used to identify ophthalmic diseases, which is typically based on the analysis of ophthalmic images (Xu et al., 2021a; Wan et al., 2021b; Xu et al., 2021b). In addition, this research also includes the detection of genes related to ophthalmic diseases (Saikia and Nirmala, 2022), ocular metabolites (Myer et al., 2020), and pathology ocular metabolites (Nezu et al., 2020). Areas of active interest and the research frontiers of AI in ophthalmic disease diagnosis can be identified based on the clustering timeline of emerging keywords

and co-cited references. The titles and abstracts of 936 articles published in 2020 and 2021 were examined.

Table 6 lists the top ten diseases in the recent 2 years, among it we can see that the hottest disease with the ophthalmic diagnosis using AI technology is “diabetic retinopathy”. A classic study in 2016 was that Gulshan, V and others developed a deep machine learning algorithm based on 128,175 retinal images, which has high sensitivity and specificity in detecting diabetes retinopathy (Gulshan et al., 2016). In 2017, Ting, DSW and others obtained high sensitivity and specificity when using the deep learning system to evaluate the diagnostic images of patients with diabetes retinopathy and related eye diseases from multiple ethnic groups (Ting et al., 2017). Li, SC and others pointed out that the conditions for using artificial intelligence system to replace ophthalmologists are not mature (Li et al., 2022). Therefore, using AI technology to diagnose diabetes retinopathy or other ophthalmic diseases requires more research.

Hot Knowledge Base in the Start Period

According to the results of the cluster analysis of CO cited references, it is not difficult to determine during the early stage of the sharp increase in the number of studies, the most important knowledge base is “Brownian motion.”

Previous studies have shown that using fractional Brownian motion to model medical examination images can provide better global texture indicators than traditional texture feature-based measurement methods (McGarry and Deriche, 1997). Early detection of glaucoma is important in the prevention of blindness. Yun, WL et al. used digital fundus images to extract texture features based on fractal dimension and Brownian motion. Specifically, they performed two-dimensional two-level discrete wavelet transform on the images, extracted energy and entropy data, and finally developed a highly specific and sensitive early glaucoma diagnosis model (Yun et al., 2014b). They also proposed a final stage of automatic detection of diabetic retinopathy using Brownian motion characteristics, namely, proliferative diabetic retinopathy (Yun et al., 2014a). Earlier literature also confirmed that the Brownian motion model can be used to classify normal and abnormal ultrasound liver images (Wu et al., 1992).

Research Hotspots

The research hotspots can be identified based on an analysis of emerging keywords. The emergent keywords in different periods represent different research hotspots.

The emerging keywords from 2012 to 2015 were “Machine Learning Classifier,” “artificial neural network,” and “nerve fiber layer.” This suggests that the performance of different intelligent algorithms was under investigation for application to ophthalmic disease diagnosis. A subfield of artificial intelligence technology is machine learning. It employs algorithms in a systematic manner to synthesize the potential relationship between data and information (Awad and Khanna, 2015). Andersson, S et al. used the visual field print output of 99 glaucoma patients and 66 healthy people to compare the sensitivity and specificity of the results obtained for a glaucoma diagnosis system based on artificial neural network and direct diagnosis by ophthalmologists. This study confirmed that an artificial neural network has higher specificity and sensitivity and fewer classification errors compared to doctors (Andersson et al., 2013). Yousefi, S et al. compared the detection of glaucoma progression using different machine learning classifiers based on longitudinal structure data sequences extracted from retinal nerve fiber layer thickness measurement and visual function data obtained from standard automatic visual field examination and evaluated the performance of these classifiers (Yousefi et al., 2014). To improve the effectiveness of treating open-angle glaucoma, Ein Oh et al. investigated the application of a screening method to distinguish open-angle glaucoma from suspected glaucoma without visual field testing. They used five open-angle glaucoma risk prediction models that were created based on 8,958 subjects (including patients with suspected open-angle glaucoma) using an artificial neural network. It was established that the artificial neural network method was a cost-effective

screening tool for distinguishing between patients with open-angle glaucoma and glaucoma suspect subjects (Oh et al., 2015).

The emerging keywords from 2018 to 2019 were “retinal layer,” “head,” “macular degeneration,” and “cup.” This indicates that the research focus transitioned to the study of various ophthalmic diseases and anatomical structures. Color fundus photography facilitates the examination of the optic disc to determine the cup-to-disc ratio, which is important in the diagnosis of glaucoma. Al-Bander et al. proposed a new method based on deep learning, which used the combination of a convolution network and DenseNet to segment optical discs and optical cups. Four data sets for image detection were then used to evaluate its effectiveness (Al-Bander et al., 2018). Although the image quality of optical coherence tomography (OCT) needs to be improved and the scanning duration leads to patient discomfort, this imaging modality has become an established clinical routine for *in vivo* imaging of optic nerve head tissue, which is very important in the diagnosis of various ophthalmic diseases (Du et al., 2014). Devalla, SK et al. developed a customized deep learning method to remove the noise in a single frame OCT B-scan. The network proposed in this study performs denoising in less than 20 milliseconds (Devalla et al., 2019). Based on the analysis of chorioretinal OCT images, clinicians and researchers have a better understanding of the diagnosis of a series of ophthalmic diseases under different conditions (Bussel et al., 2014). In practical applications, choroidal boundary segmentation usually requires manual segmentation, which is time-consuming. Kugelman, J et al. proposed several depth learning methods based on complete convolution to accurately determine the location of the choroidal boundary of interest. Artificial intelligence technology was compared with manual boundary segmentation and standard image analysis technology as part of the study. Furthermore, the investigation established the advantage of deep learning methods in chorioretinal boundary analysis and the segmentation of OCT images (Kugelman et al., 2019).

The emerging keywords from 2020 to 2021 were “system,” “disease,” and “model,” which indicate that researchers have begun to develop various systematic diagnostic models for the study of ophthalmic diseases. The proportion of doctors and patients in China is unbalanced, and the regional distribution of medical capital is uneven (National Health Commission, 2020). To minimize these biases, Zheng, B et al. designed five intelligent models for the diagnosis of fundus diseases using transfer learning. These models can detect normal eyes and four common fundus diseases including retinal vein occlusion, high myopia, glaucoma, and diabetic retinopathy (Zheng et al., 2021). However, the limitation of this study is that the models can only diagnose four common fundus diseases, which may be misdiagnosed in the case of other ophthalmic diseases. Ahn, H used machine-learning artificial intelligence to develop a model to classify the severity of emerging ophthalmic diseases, with an accuracy of nearly 100% (Ahn, 2020). The authors reported that the relative lack of data set samples was a major limitation of the study. To prevent vision loss caused by corneal diseases and to improve the early diagnosis of corneal diseases, Elsayy, A et al.

proposed a deep learning network based on corneal OCT images, Fuchs' cochlear dystrophy, and keratoconus. The developed algorithm was then used to evaluate the data set of 16721 OCT images. It was determined that the algorithm was superior to other network learning procedures (Elsawy and Abdel-Mottaleb, 2021).

As the adoption of artificial intelligence increases and the technology is continually applied to a wide array of medical fields, more intelligent detection methods will be required for ophthalmic diseases diagnosis.

Limitations in Citing Articles

By summarizing the limitations of the top ten cited literature, it was determined that the constraints of AI in ophthalmic disease diagnosis can be divided into the following five categories: 1) The clinical examination standard is highly subjective, which leads to difficulties in the design of intelligent auxiliary diagnosis system; 2) Limited detectability of ophthalmic diseases in intelligent auxiliary diagnosis systems; 3) The data set used in most training models included a limited examination population; 4) The diagnosis of artificial intelligence of ophthalmic diseases is still in the stage of auxiliary diagnosis, and requires the use of traditional clinical examination tools; 5) The scope limitations of validating intelligent auxiliary diagnosis systems.

To develop a more robust and usable diagnostic system, it is necessary to obtain more types and larger data sets. For example, the collection of ophthalmic examination data from different races, countries, or regions (Bellemo et al., 2019; Raumviboonsuk et al., 2019; Al Turk et al., 2020). More disease types should also be included in these studies, such as pterygium, familial amyloidosis, and thyroid-associated ophthalmopathy (Kessel et al., 2020; Zamani et al., 2020; Xu W. et al., 2021; Song et al., 2021). In addition, more ophthalmologists with different levels of training should participate in the screening stage of the data set and the examination stage of the algorithm to obtain clinically-based diagnoses. Finally, by increasing the number of clinical cases of the validation system and utilizing statistical approaches to achieve high sensitivity and specificity, the utilization rate of artificial intelligence models can be further improved.

CONCLUSION

In summary, the training of intelligent algorithms based on the analysis of images is of growing interest. There is ongoing worldwide research on the use of AI in ophthalmic diagnosis.

REFERENCES

- Abramoff, M. D., Lavin, P. T., Birch, M., Shah, N., and Folk, J. C. (2018). Pivotal Trial of an Autonomous AI-Based Diagnostic System for Detection of Diabetic Retinopathy in Primary Care Offices. *NPJ Digit. Med.* 1, 39. doi:10.1038/s41746-018-0040-6
- Abramoff, M. D., Lou, Y., Erginay, A., Clarida, W., Amelon, R., Folk, J. C., et al. (2016). Improved Automated Detection of Diabetic Retinopathy on a Publicly Available Dataset through Integration of Deep Learning. *Invest. Ophthalmol. Vis. Sci.* 57, 5200–5206. doi:10.1167/iops.16-19964
- Ahn, H. (2020). Artificial Intelligence Method to Classify Ophthalmic Emergency Severity Based on Symptoms: a Validation Study. *Bmj Open* 10, e037161. doi:10.1136/bmjopen-2020-037161
- Al Turk, L., Wang, S., Krause, P., Wawrzynski, J., Saleh, G. M., Alsawadi, H., et al. (2020). Evidence Based Prediction and Progression Monitoring on Retinal Images from Three Nations. *Transl. Vis. Sci. Technol.* 9, 44. doi:10.1167/tvst.9.2.44
- In particular, the United States is the most influential country in this research field. The application of artificial intelligence technology to ophthalmic diagnosis has revolutionized the clinical landscape of ophthalmologists and patients. This technology facilitates more accurate diagnosis and remote diagnosis services. However, there are limitations associated with these approaches. For example, the credibility of the training model is questionable and is often not recognized by institutions for practical clinical work, even if it has been shown to have high sensitivity and specificity. In addition, contemporary research is focused on several relatively well-known diseases, whereas the number of studies on other diseases is small, and a mature diagnostic system has not been developed. At present, the research focus has shifted from the development of artificial intelligence algorithms and the analysis of the abnormal ocular physiological structure to research on ophthalmic disease diagnosis systems. To address the existing limitations, it is necessary to obtain more national and ethnic ophthalmic data to train and test the algorithm. This is a huge task. In addition to computer engineering experts who primarily develop algorithms, ophthalmologists from different regions and with different levels of experience need to participate in this endeavor.

DATA AVAILABILITY STATEMENT

The original contributions presented in the study are included in the article/Supplementary Material, further inquiries can be directed to the corresponding authors.

AUTHOR CONTRIBUTIONS

JZ and YL conceived and designed the analysis, performed the analysis, and wrote the manuscript; SZ performed the analysis and wrote the manuscript; WY, QJ and KL designed the research, acquired the article information, and revised the manuscript. All authors contributed to the article and approved the submitted version.

FUNDING

This research was funded by the Nanjing Enterprise Expert Team Project and, Medical Science and Technology Development Project Fund of Nanjing (Grant No. YKK21262) and Medical Big Data Clinical Research Project of Nanjing Medical University.

- Al-Bander, B., Williams, B. M., Al-Nuaimy, W., Al-Taei, M. A., Pratt, H., and Zheng, Y. L. (2018). Dense Fully Convolutional Segmentation of the Optic Disc and Cup in Colour Fundus for Glaucoma Diagnosis. *Symmetry-Basel* 10, 16. doi:10.3390/sym10040087
- Andersson, S., Heijl, A., Bizios, D., and Bengtsson, B. (2013). Comparison of Clinicians and an Artificial Neural Network Regarding Accuracy and Certainty in Performance of Visual Field Assessment for the Diagnosis of Glaucoma. *Acta Ophthalmol.* 91, 413–417. doi:10.1111/j.1755-3768.2012.02435.x
- Araújo, T., Aresta, G., Mendonça, L., Penas, S., Maia, C., Carneiro, A., et al. (2020). DR|GRADUATE: Uncertainty-Aware Deep Learning-Based Diabetic Retinopathy Grading in Eye Fundus Images. *Med. Image Anal.* 63, 101715. doi:10.1016/j.media.2020.101715
- Asaoka, R., Murata, H., Hirasawa, K., Fujino, Y., Matsuura, M., Miki, A., et al. (2019). Using Deep Learning and Transfer Learning to Accurately Diagnose Early-Onset Glaucoma from Macular Optical Coherence Tomography Images. *Am. J. Ophthalmol.* 198, 136–145. doi:10.1016/j.ajo.2018.10.007
- Awad, M., and Khanna, R. (2015). *Efficient Learning Machines: Theories, Concepts, and Applications for Engineers and System Designers*. Springer nature.
- Balyen, L., and Peto, T. (2019). Promising Artificial Intelligence-Machine Learning-Deep Learning Algorithms in Ophthalmology. *Asia Pac J. Ophthalmol. (Phila)* 8, 264–272. doi:10.22608/APO.2018479
- Bellema, V., Lim, Z. W., Lim, G., Nguyen, Q. D., Xie, Y., Yip, M. Y. T., et al. (2019). Artificial Intelligence Using Deep Learning to Screen for Referable and Vision-Threatening Diabetic Retinopathy in Africa: a Clinical Validation Study. *Lancet Digit. Health* 1, E35–E44. doi:10.1016/S2589-7500(19)30004-4
- Boudry, C., Al Hajj, H., Arnould, L., and Mouriaux, F. (2022). Analysis of International Publication Trends in Artificial Intelligence in Ophthalmology. *Graefes Arch. Clin. Exp. Ophthalmol.* 260, 1779–1788. doi:10.1007/s00417-021-05511-7
- Bourouis, A., Feham, M., Hossain, M. A., and Zhang, L. (2014). An Intelligent Mobile Based Decision Support System for Retinal Disease Diagnosis. *Decis. Support Syst.* 59, 341–350. doi:10.1016/j.dss.2014.01.005
- Bussell, I., Wollstein, G., and Schuman, J. S. (2014). OCT for Glaucoma Diagnosis, Screening and Detection of Glaucoma Progression. *Br. J. Ophthalmol.* 98 Suppl 2, ii15–9. doi:10.1136/bjophthalmol-2013-304326
- Dai, Q., Liu, X., Lin, X., Fu, Y., Chen, C., Yu, X., et al. (2021). A Novel Meibomian Gland Morphology Analytic System Based on a Convolutional Neural Network. *Ieee Access* 9, 23083–23094. doi:10.1109/access.2021.3056234
- Devalla, S. K., Subramanian, G., Pham, T. H., Wang, X., Perera, S., Tun, T. A., et al. (2019). A Deep Learning Approach to Denoise Optical Coherence Tomography Images of the Optic Nerve Head. *Sci. Rep.* 9, 14454. doi:10.1038/s41598-019-51062-7
- Dong, Y., Liu, Y. L., Yu, J. G., Qi, S. X., and Liu, H. J. (2021). Mapping Research Trends in Diabetic Retinopathy from 2010 to 2019 A Bibliometric Analysis. *Medicine* 100, 12. doi:10.1097/md.00000000000023981
- Du, Y., Liu, G., Feng, G., and Chen, Z. (2014). Speckle Reduction in Optical Coherence Tomography Images Based on Wave Atoms. *J. Biomed. Opt.* 19, 056009. doi:10.1117/1.JBO.19.5.056009
- Elsawy, A., and Abdel-Mottaleb, M. (2021). A Novel Network with Parallel Resolution Encoders for the Diagnosis of Corneal Diseases. *IEEE Trans. Biomed. Eng.* 68, 3671–3680. doi:10.1109/TBME.2021.3082152
- Fang, L., Cunefare, D., Wang, C., Guymer, R. H., Li, S., and Farsiu, S. (2017). Automatic Segmentation of Nine Retinal Layer Boundaries in OCT Images of Non-exudative AMD Patients Using Deep Learning and Graph Search. *Biomed. Opt. Express* 8, 2732–2744. doi:10.1364/BOE.8.002732
- Fu, H., Cheng, J., Xu, Y., Wong, D. W. K., Liu, J., and Cao, X. (2018). Joint Optic Disc and Cup Segmentation Based on Multi-Label Deep Network and Polar Transformation. *IEEE Trans. Med. Imaging* 37, 1597–1605. doi:10.1109/TMI.2018.2791488
- Gargeya, R., and Leng, T. (2017). Automated Identification of Diabetic Retinopathy Using Deep Learning. *Ophthalmology* 124, 962–969. doi:10.1016/j.ophtha.2017.02.008
- Giardini, M. E., and Livingstone, I. A. T. (2020). “Extending the Reach and Task-Shifting Ophthalmology Diagnostics through Remote Visualisation,”. *Biomedical Visualisation*. Editor P. M. Rea (Cham: Springer International Publishing Ag), Vol. 8. doi:10.1007/978-3-030-47483-6_9
- Grzybowski, A., and Brona, P. (2021). Analysis and Comparison of Two Artificial Intelligence Diabetic Retinopathy Screening Algorithms in a Pilot Study: IDx-DR and Retalyze. *J. Clin. Med.* 10, 8. doi:10.3390/jcm10112352
- Gulshan, V., Peng, L., Coram, M., Stumpe, M. C., Wu, D., Narayanaswamy, A., et al. (2016). Development and Validation of a Deep Learning Algorithm for Detection of Diabetic Retinopathy in Retinal Fundus Photographs. *JAMA* 316, 2402–2410. doi:10.1001/jama.2016.17216
- Hamet, P., and Tremblay, J. (2017). Artificial Intelligence in Medicine. *Metabolism* 69S, S36–S40. doi:10.1016/j.metabol.2017.01.011
- Hemalakhshi, G., Santhi, D., R. S. Mani, V., Geetha, A., and B. Prakash, N. (2020). Deep Residual Network Based on Image Priors for Single Image Super Resolution in FFA Images. *Cmes-Computer Model. Eng. Sci.* 125, 125–143. doi:10.32604/cmes.2020.011331
- Hirsch, J. E. (2005). An Index to Quantify an Individual's Scientific Research Output. *Proc. Natl. Acad. Sci. U. S. A.* 102, 16569–16572. doi:10.1073/pnas.0507655102
- Juneja, M., Singh, S., Agarwal, N., Bali, S., Gupta, S., Thakur, N., et al. (2020). Automated Detection of Glaucoma Using Deep Learning Convolution Network (G-Net). *Multimed. Tools Appl.* 79, 15531–15553. doi:10.1007/s11042-019-7460-4
- Kessel, K., Mattila, J., Linder, N., Kivelä, T., and Lundin, J. (2020). Deep Learning Algorithms for Corneal Amyloid Deposition Quantitation in Familial Amyloidosis. *Ocul. Oncol. Pathol.* 6, 58–65. doi:10.1159/000500896
- Koh, B. M. Q. R., Banu, R., Nusinovi, S., and Sabanayagam, C. (2021). 100 Most-Cited Articles on Diabetic Retinopathy. *Br. J. Ophthalmol.* 105, 1329–1336. doi:10.1136/bjophthalmol-2020-316609
- Kora, P., Ooi, C. P., Faust, O., Raghavendra, U., Gudigar, A., Chan, W. Y., et al. (2022). Transfer Learning Techniques for Medical Image Analysis: A Review. *Biocybern. Biomed. Eng.* 42, 79–107. doi:10.1016/j.bbe.2021.11.004
- Kugelman, J., Alonso-Caneiro, D., Read, S. A., Hamwood, J., Vincent, S. J., Chen, F. K., et al. (2019). Automatic Choroidal Segmentation in OCT Images Using Supervised Deep Learning Methods. *Sci. Rep.* 9, 13298. doi:10.1038/s41598-019-49816-4
- Li, Q., Feng, B., Xie, L., Liang, P., Zhang, H., and Wang, T. (2016). A Cross-Modality Learning Approach for Vessel Segmentation in Retinal Images. *IEEE Trans. Med. Imaging* 35, 109–118. doi:10.1109/TMI.2015.2457891
- Li, S., Zhao, R., and Zou, H. (2022). Artificial Intelligence for Diabetic Retinopathy. *Chin. Med. J.* 135, 253–260. doi:10.1097/cm9.0000000000001816
- Li, Z., He, Y., Keel, S., Meng, W., Chang, R. T., and He, M. (2018). Efficacy of a Deep Learning System for Detecting Glaucomatous Optic Neuropathy Based on Color Fundus Photographs. *Ophthalmology* 125, 1199–1206. doi:10.1016/j.ophtha.2018.01.023
- Liskowski, P., and Krawiec, K. (2016). Segmenting Retinal Blood Vessels with Deep Neural Networks. *IEEE Trans. Med. Imaging* 35, 2369–2380. doi:10.1109/TMI.2016.2546227
- Mcgarry, G., and Deriche, M. (1997). “Modelling Mammographic Images Using Fractional Brownian Motion,” in IEEE Region 10 Annual Conference on Speech and Image Technologies for Computing and Telecommunications (IEEE TENCON 97), Brisbane, Australia, Dec 02–04 1997, 299–302.
- Metha, P., Peterson, C. A., Wen, J. C., Banitt, M. R., Chen, P. P., Bojikian, K. D., et al. (2021). Automated Detection of Glaucoma with Interpretable Machine Learning Using Clinical Data and Multimodal Retinal Images. *Am. J. Ophthalmol.* 231, 154–169.
- Miller, R. A. (1994). Medical Diagnostic Decision Support Systems-Ppast, Present, and Future: a Threaded Bibliography and Brief Commentary. *J. Am. Med. Inf. Assoc.* 1, 8–27. doi:10.1136/jamia.1994.95236141
- Myer, C., Abdelrahman, L., Banerjee, S., Khattri, R. B., Merritt, M. E., Junk, A. K., et al. (2020). Aqueous Humor Metabolite Profile of Pseudoexfoliation Glaucoma Is Distinctive. *Mol. Omics* 16, 425–435. doi:10.1039/c9mo00192a
- National Health Commission (2020). Transcript of the Regular Press Conference of the National Health Commission. Available at <http://www.nhc.gov.cn/xcs/s3574/202006/1f519d91873948d88a77a35a427c3944.shtml>.2020.6.5.
- Nezu, N., Usui, Y., Asakage, M., Shimizu, H., Tsubota, K., Narimatsu, A., et al. (2020). Distinctive Tissue and Serum MicroRNA Profile of IgG4-Related Ophthalmic Disease and MALT Lymphoma. *J. Clin. Med.* 9, 18. doi:10.3390/jcm9082530
- Oh, E., Yoo, T. K., and Hong, S. (2015). Artificial Neural Network Approach for Differentiating Open-Angle Glaucoma from Glaucoma Suspect without a

- Visual Field Test. *Invest. Ophthalmol. Vis. Sci.* 56, 3957–3966. doi:10.1167/iov.15-16805
- President, E. O. T., Holdren, J. P., and Smith, M. (2016). *Preparing for the Future of Artificial Intelligence*. Washington: National Science and Technology Council.
- Ran, A. R., Tham, C. C., Chan, P. P., Cheng, C. Y., Tham, Y. C., Rim, T. H., et al. (2021). Deep Learning in Glaucoma with Optical Coherence Tomography: a Review. *Eye (Lond)* 35, 188–201. doi:10.1038/s41433-020-01191-5
- Raumviboonsuk, P., Krause, J., Chotomwongse, P., Sayres, R., Raman, R., Widner, K., et al. (2019). Deep Learning versus Human Graders for Classifying Diabetic Retinopathy Severity in a Nationwide Screening Program. *NPJ Digit. Med.* 2, 25. doi:10.1038/s41746-019-0099-8
- Ruiz Hidalgo, I., Rozema, J. J., Saad, A., Gatinel, D., Rodriguez, P., Zakaria, N., et al. (2017). Validation of an Objective Keratoconus Detection System Implemented in a Scheimpflug Tomographer and Comparison with Other Methods. *Cornea* 36, 689–695. doi:10.1097/ICO.0000000000001194
- Saeed, A. Q., Abdullah, S., Che-Hamzah, J., and Ghani, A. T. A. (2021). Accuracy of Using Generative Adversarial Networks for Glaucoma Detection: Systematic Review and Bibliometric Analysis. *J. Med. Internet Res.* 23, 32. doi:10.2196/27414
- Saikia, S. J., and Nirmala, S. R. (2022). Identification of Disease Genes and Assessment of Eye-Related Diseases Caused by Disease Genes Using JMFC and GDLNN. *Comput. Methods Biomech. Biomed. Engin* 25, 359–370. doi:10.1080/10255842.2021.1955358
- Song, X., Liu, Z., Li, L., Gao, Z., Fan, X., Zhai, G., et al. (2021). Artificial Intelligence CT Screening Model for Thyroid-Associated Ophthalmopathy and Tests under Clinical Conditions. *Int. J. Comput. Assist. Radiol. Surg.* 16, 323–330. doi:10.1007/s11548-020-02281-1
- Szeskin, A., Yehuda, R., Shmueli, O., Levy, J., and Joskowicz, L. (2021). A Column-Based Deep Learning Method for the Detection and Quantification of Atrophy Associated with AMD in OCT Scans. *Med. Image Anal.* 72, 12. doi:10.1016/j.media.2021.102130
- Ting, D. S. W., Cheung, C. Y., Lim, G., Tan, G. S. W., Quang, N. D., Gan, A., et al. (2017). Development and Validation of a Deep Learning System for Diabetic Retinopathy and Related Eye Diseases Using Retinal Images from Multiethnic Populations with Diabetes. *JAMA* 318, 2211–2223. doi:10.1001/jama.2017.18152
- Ting, D. S. W., Pasquale, L. R., Peng, L., Campbell, J. P., Lee, A. Y., Raman, R., et al. (2019). Artificial Intelligence and Deep Learning in Ophthalmology. *Br. J. Ophthalmol.* 103, 167–175. doi:10.1136/bjophthalmol-2018-313173
- Wan, C., Li, H., Cao, G. F., Jiang, Q., and Yang, W. H. (2021a). An Artificial Intelligent Risk Classification Method of High Myopia Based on Fundus Images. *J. Clin. Med.* 10, 13. doi:10.3390/jcm10194488
- Wan, C., Wu, J., Li, H., Yan, Z., Wang, C., Jiang, Q., et al. (2021b). Optimized-Unet: Novel Algorithm for Parapapillary Atrophy Segmentation. *Front. Neurosci.* 15, 10. doi:10.3389/fnins.2021.758887
- Wan, C., Zhou, X., You, Q., Sun, J., Shen, J., Zhu, S., et al. (2021c). Retinal Image Enhancement Using Cycle-Constraint Adversarial Network. *Front. Med. (Lausanne)* 8, 16.
- Wu, C. M., Chen, Y. C., and Hsieh, K. S. (1992). Texture Features for Classification of Ultrasonic Liver Images. *IEEE Trans. Med. Imaging* 11, 141–152. doi:10.1109/42.141636
- Xu, J., Shen, J., Wan, C., Jiang, Q., Yan, Z., and Yang, W. (2022). A Few-Shot Learning-Based Retinal Vessel Segmentation Method for Assisting in the Central Serous Chorioretinopathy Laser Surgery. *Front. Med. (Lausanne)* 9, 821565. doi:10.3389/fmed.2022.821565
- Xu, J., Wan, C., Yang, W., Zheng, B., Yan, Z., and Shen, J. (2021b). A Novel Multimodal Fundus Image Fusion Method for Guiding the Laser Surgery of Central Serous Chorioretinopathy. *Math. Biosci. Eng.* 18, 4797–4816. doi:10.3934/mbe.2021244
- Xu, J., Shen, J., Jiang, Q., Wan, C., Yan, Z., and Yang, W. (2021a). Research on the Segmentation of Biomarker for Chronic Central Serous Chorioretinopathy Based on Multimodal Fundus Image. *Dis. Markers* 2021, 11. doi:10.1155/2021/1040675
- Xu, W., Jin, L., Zhu, P. Z., He, K., Yang, W. H., and Wu, M. N. (2021c). Implementation and Application of an Intelligent Pterygium Diagnosis System Based on Deep Learning. *Front. Psychol.* 12, 759229. doi:10.3389/fpsyg.2021.759229
- Yousefi, S., Goldbaum, M. H., Balasubramanian, M., Jung, T. P., Weinreb, R. N., Medeiros, F. A., et al. (2014). Glaucoma Progression Detection Using Structural Retinal Nerve Fiber Layer Measurements and Functional Visual Field Points. *IEEE Trans. Biomed. Eng.* 61, 1143–1154. doi:10.1109/TBME.2013.2295605
- Yun, W. L., Mookiah, M. R. K., and Koh, J. E. W. (2014a). Automated Detection of Proliferative Diabetic Retinopathy Using Brownian Motion Features. *J. Med. Imaging Hlth Inf.* 4, 250–254. doi:10.1166/jmihi.2014.1248
- Yun, W. L., Mookiah, M. R. K., and Koh, J. E. W. (2014b). Glaucoma Classification Using Brownian Motion and Discrete Wavelet Transform. *J. Med. Imaging Hlth Inf.* 4, 621–627. doi:10.1166/jmihi.2014.1299
- Zamani, N. S. M., Zaki, W. M. D. W., Huddin, A. B., Hussain, A., Mutalib, H. A., and Ali, A. (2020). Automated Pterygium Detection Using Deep Neural Network. *Ieee Access* 8, 191659–191672. doi:10.1109/access.2020.3030787
- Zheng, B., Jiang, Q., Lu, B., He, K., Wu, M. N. A., Hao, X. L., et al. (2021). Five-Category Intelligent Auxiliary Diagnosis Model of Common Fundus Diseases Based on Fundus Images. *Transl. Vis. Sci. Technol.* 10, 10. doi:10.1167/tvst.10.7.20
- Zhou, Y., Li, G., and Li, H. (2020). Automatic Cataract Classification Using Deep Neural Network with Discrete State Transition. *IEEE Trans. Med. Imaging* 39, 436–446. doi:10.1109/TMI.2019.2928229

Conflict of Interest: The authors declare that the research was conducted in the absence of any commercial or financial relationships that could be construed as a potential conflict of interest.

Publisher's Note: All claims expressed in this article are solely those of the authors and do not necessarily represent those of their affiliated organizations, or those of the publisher, the editors and the reviewers. Any product that may be evaluated in this article, or claim that may be made by its manufacturer, is not guaranteed or endorsed by the publisher.

Copyright © 2022 Zhao, Lu, Zhu, Li, Jiang and Yang. This is an open-access article distributed under the terms of the Creative Commons Attribution License (CC BY). The use, distribution or reproduction in other forums is permitted, provided the original author(s) and the copyright owner(s) are credited and that the original publication in this journal is cited, in accordance with accepted academic practice. No use, distribution or reproduction is permitted which does not comply with these terms.



Network-Based Pharmacological Study on the Mechanism of Guishao-Liujun Decoction in the Treatment of Gastric Cancer

Xiaoqing Qian^{1,2†*}, Lingle Zhang^{3†}, Feng Xie^{4†}, Yingsheng Cheng^{5*} and Daxiang Cui^{2*}

¹School of Biomedical Engineering, Shanghai Jiao Tong University, Shanghai, China, ²Institute of Nano Biomedicine and Engineering, Shanghai Engineering Research Centre for Intelligent Diagnosis and Treatment Instrument, Department of Instrument Science and Engineering, School of Electronic Information and Electrical Engineering, School of Sensing Science and Engineering, Shanghai Jiao Tong University, Shanghai, China, ³College of Fisheries and Life Science, Shanghai Ocean University, Shanghai, China, ⁴Department of Thoracic Surgery, Renji Hospital, School of Medicine, Shanghai Jiao Tong University, Shanghai, China, ⁵Department of Radiology, Shanghai Jiao Tong University Affiliated Sixth People's Hospital, Shanghai, China

OPEN ACCESS

Edited by:

Yuanpeng Zhang,
Nantong University, China

Reviewed by:

Song Li,
Naval Medical University, China
Yang Yinliang,
Liaocheng University, China

*Correspondence:

Xiaoqing Qian
aibiomedqxq@163.com
Yingsheng Cheng
chengyingsheng@hotmail.com
Daxiang Cui
dxcui@sjtu.edu.cn

[†]These authors have contributed
equally to this work

Specialty section:

This article was submitted to
Experimental Pharmacology and Drug
Discovery,
a section of the journal
Frontiers in Pharmacology

Received: 06 May 2022

Accepted: 09 June 2022

Published: 05 July 2022

Citation:

Qian X, Zhang L, Xie F, Cheng Y and
Cui D (2022) Network-Based
Pharmacological Study on the
Mechanism of Guishao-Liujun
Decoction in the Treatment of
Gastric Cancer.
Front. Pharmacol. 13:937439.
doi: 10.3389/fphar.2022.937439

Objective: The aim of the study was to use a network pharmacological method to examine the mechanism of Guishao-Liujun decoction against gastric cancer (GC).

Methods: The traditional Chinese medicine systems pharmacology database and analysis platform (TCMSP) and the Traditional Chinese Medicine Integrated Database (TCMID) were used to obtain the chemical composition and targets of all the drugs of Guishao-Liujun decoction, and the targets of GC were screened using GeneCards and Online Mendelian Inheritance in Man (OMIM) databases. The obtained targets were imported into Cytoscape 3.7.2 software by using the R language to take the intersection for a Venn analysis to construct active ingredient target networks, and they were imported into the STRING database to construct protein-protein interaction (PPI) networks, with the BisoGenet plugin in Cytoscape 3.7.2 being used for analyzing network topology. On the potential target of Guishao-Liujun decoction for GC, gene ontology (GO) enrichment analysis and Kyoto Encyclopedia of Genes and Genomes (KEGG) enrichment analysis were performed using the R-language bioconductor platform, and the outcomes were imported into Cytoscape 3.7.2 software to obtain the KEGG network map. The core targets were docked with the active components by the macromolecular docking software application AutoDock Vina.

Results: A total of 243 chemical components and 1,448 disease targets including 127 intersecting targets were discovered. AKT1, TP53, and GO functional analysis were mainly associated with ubiquitination and oxidase reduction activity. In GC treatment, the KEGG analysis revealed that Guishao-Liujun decoction mainly acted through the tumor necrosis factor (TNF), interleukin 17 (IL-17), and cancer-related signaling pathways, with the best binding performance with TP53, as indicated by the outcomes of macromolecular docking.

Conclusion: In the treatment of GC, Guishao-Liujun decoction works with a variety of components and targets, establishing the groundwork for further research into its mechanism of action.

Keywords: network pharmacology, macromolecular docking, mechanism of action, GC, Guishao-Liujun decoction

INTRODUCTION

Over the past 40 years, China has experienced rapid demographic and epidemiological changes. Rapid industrialization, urbanization, aging, and lifestyle changes have shifted the burden of the disease spectrum from infectious to non-infectious diseases. With a large population, China plays an important role in the global cancer burden (He et al., 2021). Gastric cancer is common all over the world. One in 78 women and one in 33 men have gastric cancer for their whole life (GBD 2017 Causes of Death Collaborators, 2018). According to GBD 2019, the DALYs in China accounted for 44.21% of the total number (GBD 2019 Diseases and Injuries Collaborators, 2020). The causes of GC are relatively complicated and are closely linked to dietary conditions and geographical environments along with infection by *Helicobacter pylori* (*H. pylori*) and genetic factors. GC is relatively insidious, and most of the affected people are diagnosed in the middle and late stages. Presently, the key treatment of GC is still surgery, but patients face many problems post-surgery including immune dysfunction and the slow recovery of digestive tract function, which has a serious impact on the life quality and clinical efficacy of patients (Disbrow et al., 1993). Research has revealed that Guishao-Liujun decoction improves gastrointestinal function in a better manner and enhances the immune function of GC patients (Zhou et al., 2022).

The ingredients of Guishao-Liujun decoction include *Poria cocos* (Schw.) Wolf, *Codonopsis* Radix, *Herba Hedyotis diffusa*, Largehead Atractylodes Rhizome, *Salvia chinensis* Benth., *Radix Aucklandiae*, *Angelica sinensis*, *Pinellia ternata*, *Sparganium stoloniferum* (Graebn.) Buch. -Ham. ex Juz., *Paeonia lactiflora* Pall., *Curcuma phaeocaulis* Valetton., *Citrus reticulata* Blanco., *Amomum villosum* Lour., *Roasted Licorice*, and *Radix Glycyrrhizae Preparata*, which nourish the qi and blood, treat the deficiencies of the spleen and stomach, and improve swelling and abdominal fullness. At present, most reports have studied Guishao-Liujun decoction's mechanism of action in the treatment of GC through clinical observation, and pharmacological studies are lacking on the use of Guishao-Liujun decoction for the treatment of GC as a result of the diversity of GC genes and the complexity of herbal components (Zhang et al., 2019a). Furthermore, this research has used a network of pharmacological methods to examine the mechanism of action of Guishao-Liujun decoction in the treatment of GC.

MATERIALS AND METHODS

Screening of Target Components of Guishao-Liujun Decoction

The TCMSP and TCMID pharmacology platform of the traditional Chinese medicine system was used to search for

the active chemical components of the Chinese herbs (*Poria cocos* (Schw.) Wolf, *Codonopsis* Radix, *Herba Hedyotis diffusa*, Largehead Atractylodes Rhizome, *Salvia chinensis* Benth., *Radix Aucklandiae*, *Angelica sinensis*, *Pinellia ternata*, *Sparganium stoloniferum* (Graebn.) Buch. -Ham. ex Juz., *Paeonia lactiflora* Pall., *Curcuma phaeocaulis* Valetton., *Citrus reticulata* Blanco., *Amomum villosum* Lour., *Roasted Licorice* and *Radix Glycyrrhizae Preparata*) in Guishao-Liujun decoction. For screening purposes, the TCMSP was set with an oral bioavailability (OB) $\geq 30\%$ and drug-likeness (DL) ≥ 0.18 (Zhang et al., 2019b), the TCMID was screened in SwissADME, and screening conditions were set as follows: gastrointestinal (GI) absorption was enhanced in pharmacokinetics and more than two yeses in drug-likeness to filter out ineffective components and collect the active ingredients in Guishao-Liujun decoction. The SwissTargetPrediction database was used to explore the possible protein targets with the screening condition probability set at ≥ 0.1 . The UniProt database was used to convert screened protein targets into standardized gene names.

Screening of GC-Related Targets

To find target genes linked to GC, the term "gastric cancer" was searched on the OMIM and GeneCards databases. Because of a large number of targets in the GeneCards database, the targets were filtered according to their score value. The higher the score value, the stronger will be the link between the target and the disease, and the target with a score higher than the median is usually set as a potential disease target, leaving the genes with a score higher than five in the GeneCards to be combined and de-weighted with the OMIM database, which is the target associated with GC.

Acquisition of Effective Targets and Drawing of the Venn Diagram

A Venn diagram was used to obtain an intersection of the target points of Guishao-Liujun decoction and GC's target points, and the intersection of the two targets was indicated to be the effective target of Guishao-Liujun decoction for GC treatment.

Active Ingredient-Active Target Network Construction Analysis

The active components and effective target genes were imported into Cytoscape 3.7.2 (Zhang et al., 2019a) software for developing a network and to carry out a visualization analysis to get a drug-active ingredient-target network diagram, and the importance of the active component and its target of action were assessed using analyzing network topological parameters such as degree values.

Construction of Protein Networks

We imported the effective targets of Guishao-Liujun decoction and GC into the STRING database; then we constructed a protein interaction network and selected data with confidence ≥ 0.900 . The results were imported into Cytoscape 3.7.2 software (Martin et al., 2010) in tab-separated value (TSV) format so that we can analyze and visualize them. The PPI data were imported with R software to obtain the number of connection points of core genes, and the graph was obtained for the histogram's top 30 core genes.

Enrichment Analysis of Target Functions and Pathways

We collected gene IDs (entrezID) of potential targets using the R software (<https://www.r-project.org/>) and its backend database org. Hs.eg.db. The GO function enrichment analysis of the possible targets was conducted with the Disease Ontology Semantic and Enrichment analysis (DOSE), cluster profile, and path view package (Bioconductor), comprising the following three aspects: biological process (BP), cellular component (CC), and molecular function (MF), set to p -value cutoff = 0.05 and q -value cutoff = 0.05.

The GO enrichment analysis was categorized into three main groups, namely, biological process (BP), molecular function (MF), and cellular component (CC). Each group was ranked by significance, and bar and bubble charts were used to illustrate the top 10 enrichment entries.

Macromolecular Docking of the Main Active Ingredients and Targets of Guishao-Liujun Decoction

The targets of Guishao-Liujun decoction working on GC were found in the Protein Data Bank (PDB) database, and we saved the data in the PDB format. The mol2 format was used to save ligands with the top two compounds in terms of degree value after topological analysis. We carried out molecular docking between the potential targets of Guishao-Liujun decoction in GC and the main compounds in Guishao-Liujun decoction using AutoDockTools-1.5.6.

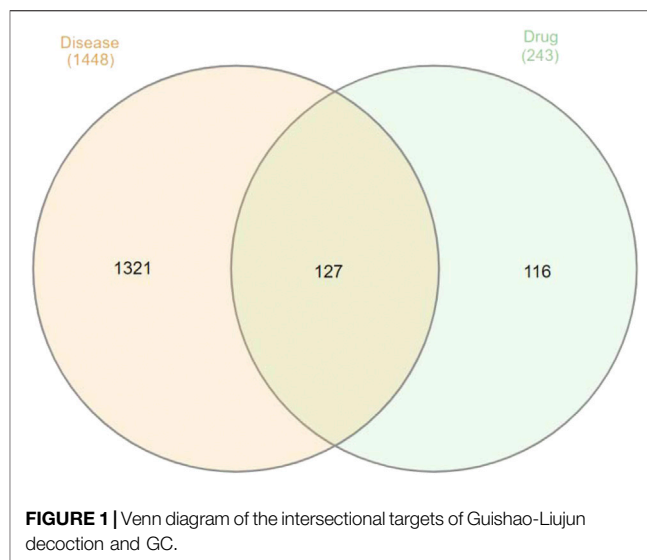
RESULTS

Acquisition of Active Ingredients and Related Targets of Guishao-Liujun Decoction

With OB 30% and DL 0.18, GI absorption as high in pharmacokinetics, and more than two yeses in drug-likeness as screening conditions, a total of 181 active ingredients in Guishao-Liujun decoction were obtained in the TCMSP and TCMID, respectively, and some of the active ingredients are listed in **Supplementary Table S1**. The TCMSP and TCMID gave us with 243 TCM targets.

Acquisition of GC-Related Targets

GeneCards and OMIM provided the affected genes, and targets with scores higher than the median were picked as prospective



disease targets empirically. A total of 1,448 GC-related targets were obtained after combining the relevant targets retrieved from the OMIM database, merging, and deleting duplicate values.

Venn Drawing

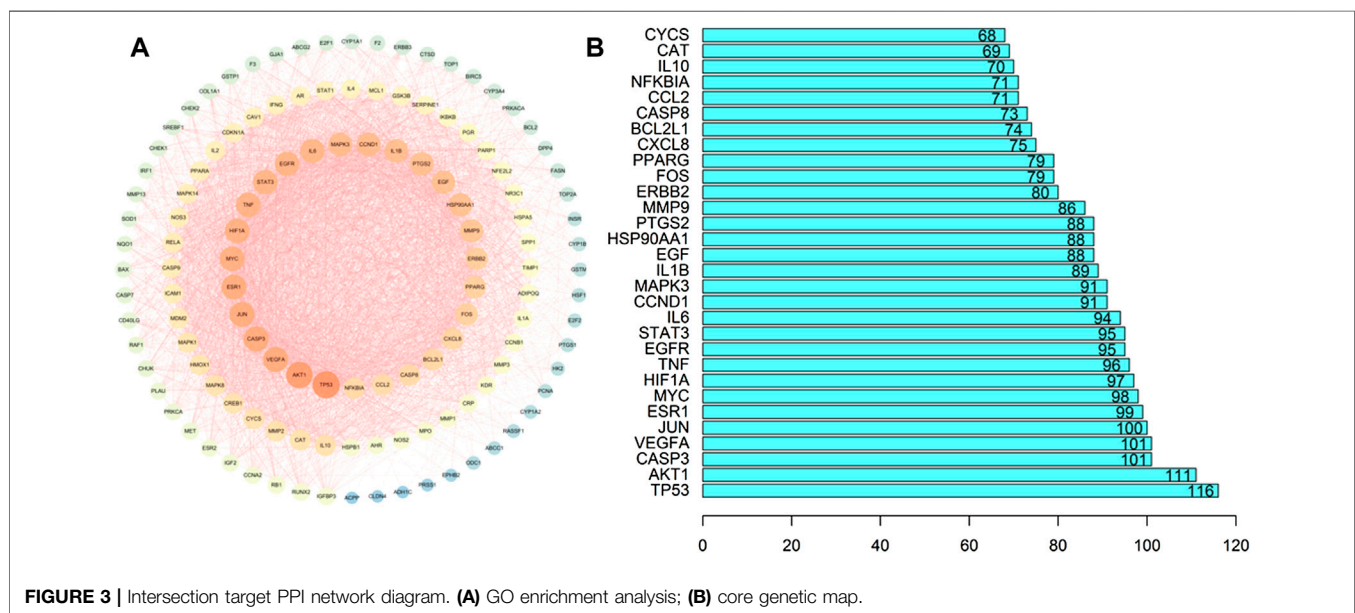
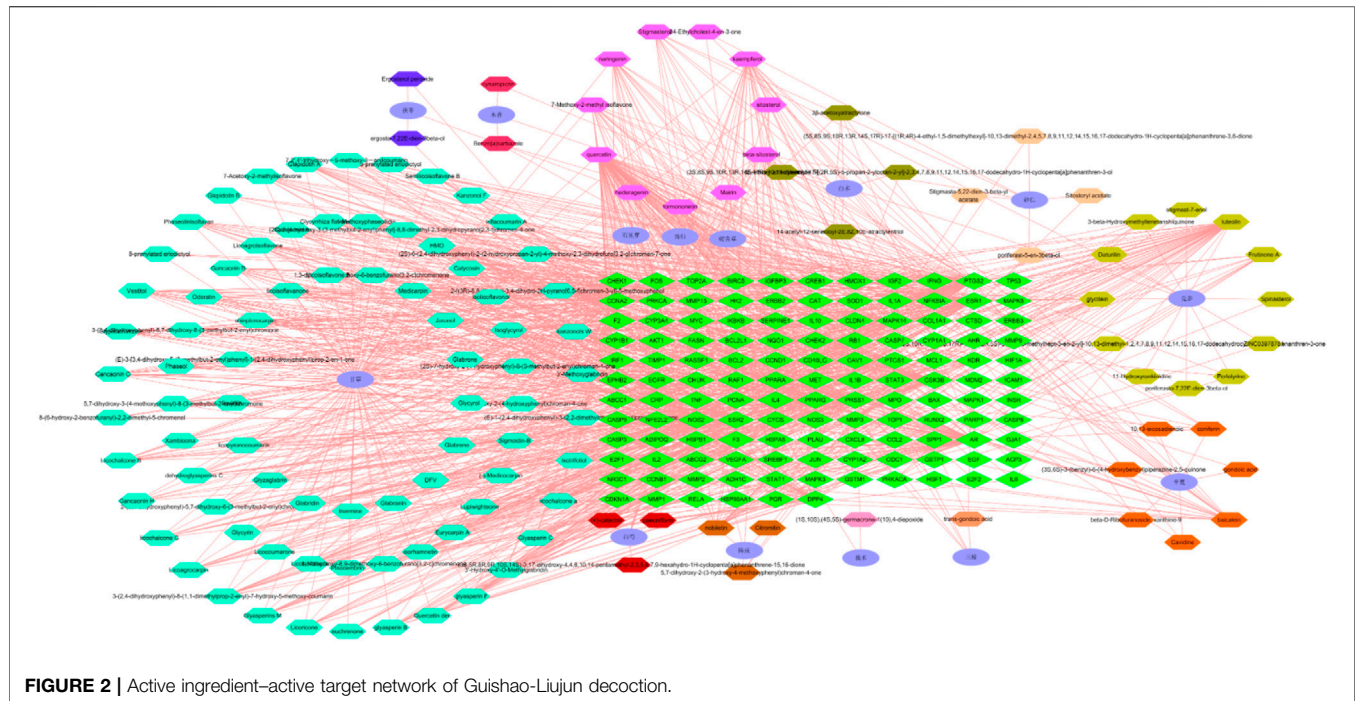
A total of 127 intersection targets of the aforementioned were obtained using the Venn diagram tool to take the intersection of Guishao-Liujun decoction and GC targets, and the results are illustrated in **Figure 1**.

Construction of the Active Ingredient–Effective Target Network Diagram of Guishao-Liujun Decoction

The network of active ingredients and effective targets of Guishao-Liujun decoction was built using Cytoscape 3.7.2, which is shown in **Figure 2**. Its topological parameters for GC were measured by the software, which were used to assess the significance of the active components and targets of action. The findings demonstrated that the active ingredients such as kaempferol, quercetin, luteolin, and decursinol angelate had the potential to act on more than one target, and they might be the active ingredients of Guixia Shao Liujun Tang that play a major role in GC treatment.

Construction of Protein Networks

Using the Venn tool in TBtools (**Figure 1**), the intersection of the targets of Guishao-Liujun decoction and the targets of GC were obtained and the intersection targets were uploaded to the STRING database with a confidence level of ≥ 0.9 to obtain the PPI network diagram of the targets. Then the existing data were imported into Cytoscape 3.7.2 to plot protein network relationships; the larger the node, the larger will be the degree value. The location in the network was judged on the basis of the degree value. As shown in **Figure 3**, the targets in the center of the network are TP53, AKT1, Caspase-3 (CASP3), vascular endothelial growth factor A (VEGFA), etc., which are



supposed to be the significant targets for GC treatment using Guishao-Liujun decoction.

Results of Enrichment Analysis of Target Functions and Pathways

R was used for the GO annotation analysis of the effective targets. We picked the top 20 BP, CC, and MF results, and found that these BP targets were mostly involved in oxidative stress and cellular

oxidative stress, metal ion response, antibiotic response, etc. MF was primarily involved in the binding of ubiquitinated protein ligase, cytokine response, and phosphorylase. CC was mostly involved in the membrane micro-domain, membrane rafts, transcription factor complexes, chromatin, etc. The results are shown in **Figure 4A**.

KEGG enriched 179 signaling pathways such as the TNF signaling pathway, P13K-Akt, IL-17 signaling pathway, mitogen-activated protein kinase 8 (MAPK8), etc. The top 20 pathways were visualized, and the results are shown in **Figure 4B**.

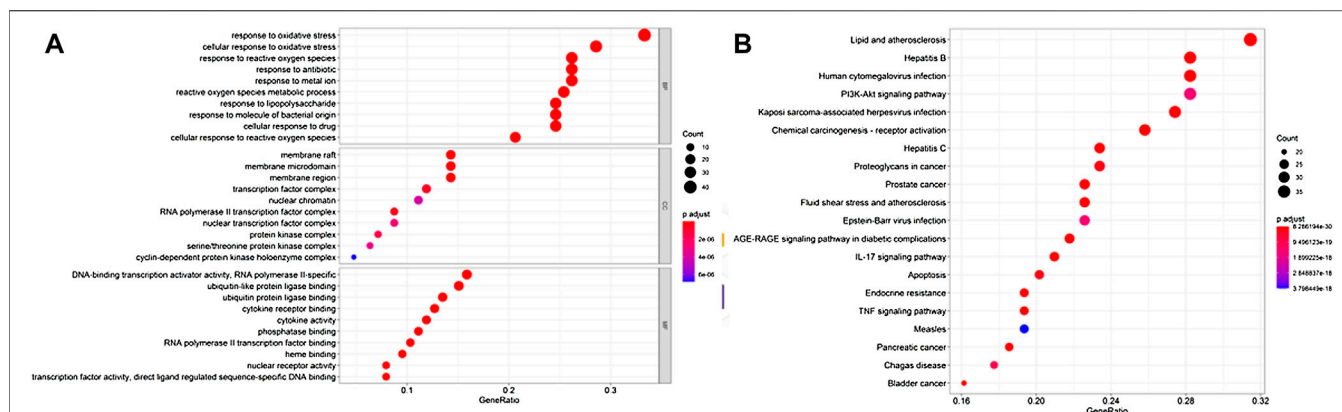


FIGURE 4 | Enrichment analysis of Guishao-Liujun decoction for GC. **(A)** GO enrichment analysis; **(B)** KEGG enrichment analysis.

Macromolecular Docking Results of the Active Ingredients of Guishao-Liujun Decoction

The potential targets of Guishao-Liujun decoction acting on GC were macromolecularly docked with the main compounds of Guishao-Liujun decoction calculated by the topological analysis using AutoDockTools-1.5.6, and the more stable the ligand-receptor binding confirmation was, the more likely the action occurred. Serine/threonine-protein kinase (AKT1) and tumor protein p3 (TP53) were chosen as the top two main targets based on the degree value. AutoDock Vina was used for macromolecular docking of the components, binding energies of -4.25 kcal/mol indicate some binding activity between the ligand small molecule and the receptor protein; binding energies of -5.0 kcal/mol indicate good binding activity between the two; binding energies of -7.0 kcal/mol indicate that the ligand and the receptor have strong conjugation activity (Hsin et al., 2013), and the binding energies of quercetin and the two core targets were -6.7 and -7.7 (kcal/mol), respectively. The specific docking results are shown in Figure 5.

DISCUSSION

TCM has exceptional anti-cancer properties, and in recent years, its anti-tumor mechanism has been of strong research interest. The etiology of GC in TCM is the deficiency in origin and excess in superficiality, that is, deficiency of the spleen is the origin, and heat, dampness, stagnation of qi, and blood stasis are in excess. Guishao-Liujun decoction is not only effective in nourishing the qi and blood, treating spleen, and stomach deficiency but also has a very significant function as an anti-tumor agent. In recent years, with the rise in the combination of TCM and Western medicine, many herbal medicines are playing a significant role in cancer treatment.

Through the collection and screening of the active components of Guishao-Liujun decoction, it was found that they mostly comprise eight compounds including kaempferol,

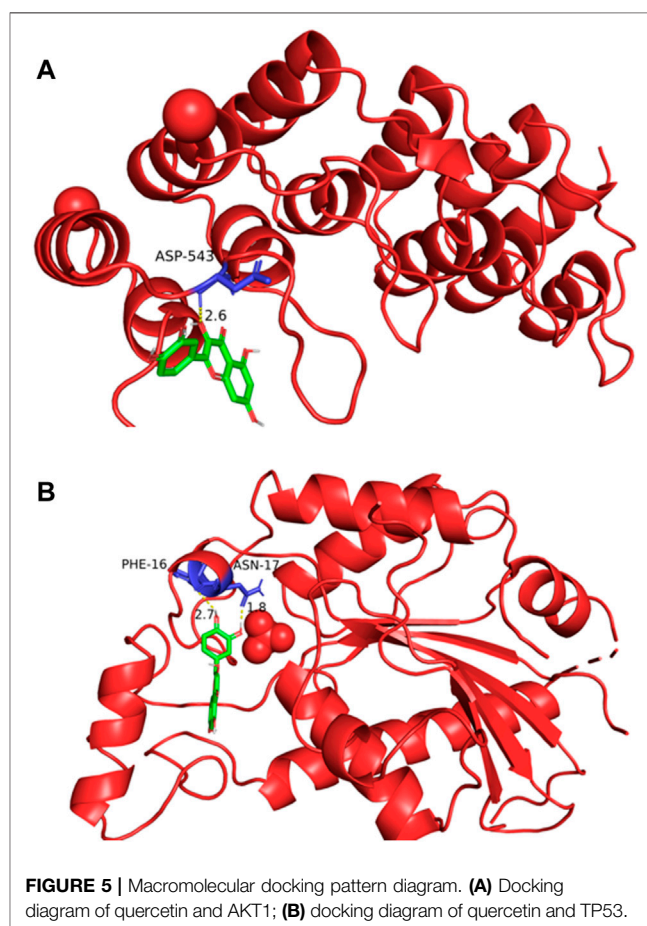


FIGURE 5 | Macromolecular docking pattern diagram. **(A)** Docking diagram of quercetin and AKT1; **(B)** docking diagram of quercetin and TP53.

quercetin, luteolin, etc. These components with their effective medicinal properties are the material basis of Guishao-Liujun decoction for GC treatment.

The major targets of Guishao-Liujun decoction for GC treatment are IL-17, AKT1, TP53, and TNF, as derived from

the analysis of the protein interaction network (Kumar et al., 2021). Serine/threonine-protein kinase (AKT1) has a role in cancer cell proliferation, inhibition of apoptosis, tumor angiogenesis, and energy metabolism (Chen et al., 2020); IL-17 is closely linked to gastric mucosal atrophy, gastric precancerous lesions, and the degree of intestinal epithelial hyperplasia (Li et al., 2021); TP53, a common tumor suppressor gene, is involved in apoptosis or the regulation of cell cycle and is related to lymph node metastasis, tissue differentiation, and infiltration depth of GC (Wen et al., 2021); TNF is also one of the pro-inflammatory factors; and TNF- α can induce apoptosis through the nuclear factor kappa-B (NF- κ B)-activated signaling pathway, caspase-mediated signaling pathway, and c-Jun N-terminal kinase (JNK) signaling pathway and it regulates the immune system to control the proliferation and apoptosis of tumor cells. By upregulating the serum TNF- α level and downregulating the TGF- α level, quercetin can increase the immune function of the body resulting in the suppression of tumors (Zhang, 2022), which is similar to the findings of the present study that the TNF signaling pathway is enriched. Nuclear factor κ B (NF- κ B) is a ubiquitous transcription factor of the NF- κ B/Rel protein family with the ability to mediate immune stress and inflammatory response, etc. Recent research demonstrated that NF- κ B is expressed highly in different tumor types, and its expression has a role in apoptosis inhibition, cell proliferation, invasive behavior, and angiogenesis (Sack, 2002; Ashrafizadeh et al., 2021; Huang et al., 2022). The molecular mechanism of anti-apoptosis in GC after NF- κ B signaling activation involves the direct regulation of downstream target genes' expression, such as through the regulation of B-cell lymphoma-2 (Bcl2) family proteins and caspase family proteins to exert anti-apoptotic effects. Moreover, NF- κ B plays role in all phases of the inflammatory response by causing gene expression and stimulating cytokines' release. The NF- κ B pathway is a crucial connection between inflammation and GC (Gurevitch et al., 1997). It has been discovered that baicalin can exert its biological effects using different signaling pathways and has the potential to inhibit the inflammatory response by suppressing the TLR4/NF- κ B signaling pathway. Toll-like receptors (TLR) are not only correlated with tumor growth and immunosuppression but are also involved in apoptosis and immune system activation, and the detection of molecules related to this signaling pathway may become a reference indicator for GC prognosis (Echizen et al., 2016; Susi et al., 2019; Zargari et al., 2022).

According to the aforementioned results, the active components in Guishao-Liujun decoction have effective binding activities with IL-17, TP53, AKT1, and TNF, but further validation is required for the bio-functionality of its compounds for the treatment of GC.

There are certain limitations to network pharmacology research: 1) the effective ingredient information sources in the traditional Chinese medicine database are limited, and cannot fully and timely reflect the substances found in traditional Chinese medicine. 2) Because the dosage of each medicine prescribed in Chinese medicine has a varied effect, the efficacy and concentration of Chinese medicine's active substances are strong or weak. However, the most present research chooses beneficial

compounds based on oral availability and drug-like qualities of chemical substances and rarely takes into account the dose-effect connection of Chinese medicine ingredients (Newman, 2020). 3) Traditional Chinese medicine comprises a complicated chemical composition system rather than a random assortment of substances. Its effect could be the overall effect of a set of effective components comprising numerous chemical components or the effect of its metabolites once they enter the body. As a result, it is unscientific to equate effective components, targets, and pathways with diseases, and it is vital to evaluate the holistic view of traditional Chinese medicine and the metabolic process *in vivo* from a clinical standpoint (Chen et al., 2022; Mei et al., 2022). 4) When existing network pharmacology analyzes the action targets of pharmaceutical ingredients, it can only predict using energy matching and compound geometric characteristics matching, but not the combined action type of the two, such as the target's activation or inactivation state, the drug's agonist or antagonist, and so on. 5) Traditional Chinese medicine (TCM) uses the concepts of "harmony between man and nature" and "therapy based on syndrome distinction" to treat ailments. The existing database of disease targets focuses primarily on the names of diseases in western medicine, rather than TCM syndromes, making it difficult to accurately reflect the internal relationship between TCM diseases and syndromes, and the theoretical foundation of TCM prescription construction (Wu et al., 2021). 6) The protein-protein interaction database is biased because it is based on a single source. Many academics, for example, frequently use STRING for online analysis, producing false positive or false-negative results. 7) Typically, research begins with a target protein that is shared by traditional Chinese medicine and diseases, and rarely considers drug ingredients in combination with other biological functional molecules, such as Chinese medicine ingredients-metabolites, Chinese medicine ingredients-lncRNA, Chinese medicine ingredients-circRNA, and so on. As a result, traditional Chinese medicine network pharmacology research has to be standardized and enlarged.

CONCLUSION

In conclusion, this study explores the mechanism of action of Guishao-Liujun decoction in the treatment of GC by network pharmacology and assessed that Guishao-Liujun decoction works through a variety of targets and components in GC treatment. As an emerging field, network pharmacology is useful for drug development and clinical guidance, but there are many ambiguities in the process of target collection and investigation; therefore, a protein model is required to validate the experiments, and cellular and animal experiments are needed to improve the conclusions.

DATA AVAILABILITY STATEMENT

The original contributions presented in the study are included in the article/**Supplementary Material**; further inquiries can be directed to the corresponding authors.

AUTHOR CONTRIBUTIONS

XQ, YC, and DC designed and directed the study; LZ and XQ conducted the data analysis and wrote the manuscript; FX helped with statistical analysis. All authors read and approved the final manuscript.

FUNDING

This work was supported by grants from the National Key Research and Development Program of China (Nos.

2017YFA0205301 and 2017YFA0205304), the National Natural Science Foundation of China (Nos. 81903169, 82072767, 81770145, and 81602192), and the Shanghai Sailing Program (No. 19YF1422300).

SUPPLEMENTARY MATERIAL

The Supplementary Material for this article can be found online at: <https://www.frontiersin.org/articles/10.3389/fphar.2022.937439/full#supplementary-material>

REFERENCES

- Ashrafizadeh, M., Rafiei, H., Mohammadinejad, R., Farkhondeh, T., and Samarghandian, S. (2021). Anti-tumor Activity of Resveratrol against Gastric Cancer: a Review of Recent Advances with an Emphasis on Molecular Pathways. *Cancer Cell Int.* 21, 66. doi:10.1186/s12935-021-01773-7
- Chen, W., Li, J., Li, C., Fan, H. N., Zhang, J., and Zhu, J. S. (2020). Network Pharmacology-Based Identification of the Antitumor Effects of Taraxasterol in Gastric Cancer. *Int. J. Immunopathol. Pharmacol.* 34, 2058738420933107. doi:10.1177/2058738420933107
- Chen, Y., Miao, Z., Sheng, X., Li, X., Ma, J., Xu, X., et al. (2022). Sesquiterpene Lactones-Rich Fraction from Aucklandia Lappa Decne. Alleviates Dextran Sulfate Sodium Induced Ulcerative Colitis through Co-regulating MAPK and Nrf2/Hmox-1 Signaling Pathway. *J. Ethnopharmacol.* 295, 115401. doi:10.1016/j.jep.2022.115401
- Disbrow, E. A., Bennett, H. L., and Owings, J. T. (1993). Effect of Preoperative Suggestion on Postoperative Gastrointestinal Motility. *West J. Med.* 158, 488–492.
- Echizen, K., Hirose, O., Maeda, Y., and Oshima, M. (2016). Inflammation in Gastric Cancer: Interplay of the COX-2/prostaglandin E2 and Toll-like receptor/MyD88 Pathways. *Cancer Sci.* 107, 391–397. doi:10.1111/cas.12901
- GBD 2017 Causes of Death Collaborators (2018). Global, Regional, and National Age-sex-specific Mortality for 282 Causes of Death in 195 Countries and Territories, 1980–2017: a Systematic Analysis for the Global Burden of Disease Study 2017. *Lancet* 392 (10159), 1736–1788. doi:10.1016/S0140-6736(18)32203-7
- GBD 2019 Diseases and Injuries Collaborators (2020). Global Burden of 369 Diseases and Injuries in 204 Countries and Territories, 1990–2019: a Systematic Analysis for the Global Burden of Disease Study 2019. *Lancet* 396, 1204–1222. doi:10.1016/S0140-6736(20)30925-9
- Gurevitch, J., Frolkis, I., Yuhas, Y., Lifschitz-Mercer, B., Berger, E., Paz, Y., et al. (1997). Anti-tumor Necrosis Factor-Alpha Improves Myocardial Recovery after Ischemia and Reperfusion. *J. Am. Coll. Cardiol.* 30, 1554–1561. doi:10.1016/s0735-1097(97)00328-8
- He, Y., Wang, Y., Luan, F., Yu, Z., Feng, H., Chen, B., et al. (2021). Chinese and Global Burdens of Gastric Cancer from 1990 to 2019. *Cancer Med.* 10, 3461–3473. doi:10.1002/cam4.3892
- Hsin, K. Y., Ghosh, S., and Kitano, H. (2013). Combining Machine Learning Systems and Multiple Docking Simulation Packages to Improve Docking Prediction Reliability for Network Pharmacology. *PLoS One* 8 (12), e83922. PMID: 24391846; PMCID: PMC3877102. doi:10.1371/journal.pone.0083922
- Huang, Y., Zhang, G., Liang, H., Cao, Z., Ye, H., and Gao, Q. (2022). Inhibiting Ferroptosis Attenuates Myocardial Injury in Septic Mice: the Role of Lipocalin-2. *Nan Fang Yi Ke Da Xue Xue Bao* 42, 256–262. doi:10.12122/j.issn.1673-4254.2022.02.13
- Kumar, V., Sood, A., Munshi, A., Gautam, T., and Kulharia, M. (2021). Geometrical and Electro-Static Determinants of Protein-Protein Interactions. *Bioinformation* 17, 851–860. doi:10.6026/97320630017851
- Li, L., Jin, X. J., Li, J. W., Li, C. H., Zhou, S. Y., Li, J. J., et al. (2021). Systematic Insight into the Active Constituents and Mechanism of Guiqi Baizhu for the Treatment of Gastric Cancer. *Cancer Sci.* 112, 1772–1784. doi:10.1111/cas.14851
- Martin, A., Ochagavia, M. E., Rabasa, L. C., Miranda, J., Fernandez-de-Cossio, J., and Bringas, R. (2010). BisoGenet: a New Tool for Gene Network Building, Visualization and Analysis. *BMC Bioinforma.* 11, 91. PMID: 20163717; PMCID: PMC3098113. doi:10.1186/1471-2105-11-91
- Mei, R., Chen, D., Zhong, D., Li, G., Lin, S., Zhang, G., et al. (2022). Metabolic Profiling Analysis of the Effect and Mechanism of Gushiling Capsule in Rabbits with Glucocorticoid-Induced Osteonecrosis of the Femoral Head. *Front. Pharmacol.* 13, 845856. doi:10.3389/fphar.2022.845856
- Newman, D. J. (2020). Modern Traditional Chinese Medicine: Identifying, Defining and Usage of TCM Components. *Adv. Pharmacol.* 87, 113–158. doi:10.1016/bs.apha.2019.07.001
- Sack, M. (2002). Tumor Necrosis Factor-Alpha in Cardiovascular Biology and the Potential Role for Anti-tumor Necrosis Factor-Alpha Therapy in Heart Disease. *Pharmacol. Ther.* 94, 123–135. doi:10.1016/s0163-7258(02)00176-6
- Susi, M. D., Lourenço Caroline, M., Rasmussen, L. T., Payão, S. L. M., Rossi, A. F. T., Silva, A. E., et al. (2019). Toll-like Receptor 9 Polymorphisms and *Helicobacter pylori* Influence Gene Expression and Risk of Gastric Carcinogenesis in the Brazilian Population. *World J. Gastrointest. Oncol.* 11, 998–1010. doi:10.4251/wjgo.v11.i11.998
- Wen, Q.-C., Lu, S.-Z., and Zhang, W.-L. (2021). LncRNA TP53TG1 Regulates the Resistance of Gastric Cancer Cells to 5-FU via miR-96/TPM1 axis [J]. *J. Clin. Exp. Med.* 20 (23), 2492–2496.
- Wu, C. W., Chen, H. Y., Yang, C. W., and Chen, Y. C. (2021). Deciphering the Efficacy and Mechanisms of Chinese Herbal Medicine for Diabetic Kidney Disease by Integrating Web-Based Biochemical Databases and Real-World Clinical Data: Retrospective Cohort Study. *JMIR Med. Inf.* 9, e27614. doi:10.2196/27614
- Zargari, S., Bahari, A., Goodarzi, M. T., Mahmoodi, M., and Valadan, R. (2022). TLR2 and TLR4 Signaling Pathways and Gastric Cancer: Insights from Transcriptomics and Sample Validation. *Iran. Biomed. J.* 26, 36–43. doi:10.52547/ibj.26.1.36
- Zhang, H., Liu, S., Gao, H., and Gong, L. (2019). Research Progress of Network Pharmacology Method of Compound Traditional Chinese Medicine [J]. *Eval. Analysis Drug-Use Hosp. China* 19 (10), 1270–1273+1276. doi:10.14009/j.issn.1672-2124.2019.10.035

- Zhang, K. (2022). Acupuncture for Quality of Life in Gastric Cancer Patients: Methodological Issues. *J. Pain Symptom Manage* 63, e447–e448. doi:10.1016/j.jpainsymman.2021.12.016
- Zhang, M., Li, L., and Yan, X. (2019). Professor Yan Xin's Clinical Experience in Using Guishao Liujun Decoction [J]. *Shanghai J. Traditional Chin. Med.* 53 (02), 26–29. doi:10.16305/j.1007-1334.2019.02.007
- Zhou, W., Zhang, H., Wang, X., Kang, J., Guo, W., Zhou, L., et al. (2022). Network Pharmacology to Unveil the Mechanism of Moluodan in the Treatment of Chronic Atrophic Gastritis. *Phytomedicine* 95, 153837. doi:10.1016/j.phymed.2021.153837

Conflict of Interest: The authors declare that the research was conducted in the absence of any commercial or financial relationships that could be construed as a potential conflict of interest.

Publisher's Note: All claims expressed in this article are solely those of the authors and do not necessarily represent those of their affiliated organizations, or those of the publisher, the editors, and the reviewers. Any product that may be evaluated in this article, or claim that may be made by its manufacturer, is not guaranteed or endorsed by the publisher.

Copyright © 2022 Qian, Zhang, Xie, Cheng and Cui. This is an open-access article distributed under the terms of the Creative Commons Attribution License (CC BY). The use, distribution or reproduction in other forums is permitted, provided the original author(s) and the copyright owner(s) are credited and that the original publication in this journal is cited, in accordance with accepted academic practice. No use, distribution or reproduction is permitted which does not comply with these terms.



OPEN ACCESS

EDITED BY

Yuanpeng Zhang,
Nantong University, China

REVIEWED BY

Tongguang Ni,
Changzhou University, China
Xiongtao Zhang,
Huzhou University, China

*CORRESPONDENCE

Feng Yuan,
wqdyu_yf@163.com
Zhifeng Xiao,
zux2@psu.edu

[†]These authors have contributed equally to this work and share first authorship

SPECIALTY SECTION

This article was submitted to
Experimental Pharmacology and Drug
Discovery,
a section of the journal
Frontiers in Pharmacology

RECEIVED 27 April 2022

ACCEPTED 29 June 2022

PUBLISHED 22 July 2022

CITATION

Wang W, Jiang R, Cui N, Li Q, Yuan F and
Xiao Z (2022), Semi-supervised vision
transformer with adaptive token
sampling for breast
cancer classification.
Front. Pharmacol. 13:929755.
doi: 10.3389/fphar.2022.929755

COPYRIGHT

© 2022 Wang, Jiang, Cui, Li, Yuan and
Xiao. This is an open-access article
distributed under the terms of the
[Creative Commons Attribution License](https://creativecommons.org/licenses/by/4.0/)
(CC BY). The use, distribution or
reproduction in other forums is
permitted, provided the original
author(s) and the copyright owner(s) are
credited and that the original
publication in this journal is cited, in
accordance with accepted academic
practice. No use, distribution or
reproduction is permitted which does
not comply with these terms.

Semi-supervised vision transformer with adaptive token sampling for breast cancer classification

Wei Wang^{1†}, Ran Jiang^{2†}, Ning Cui³, Qian Li³, Feng Yuan^{1*} and
Zhifeng Xiao^{4*}

¹Department of Breast Surgery, Hubei Provincial Clinical Research Center for Breast Cancer, Hubei Cancer Hospital, Tongji Medical College, Huazhong University of Science and Technology, Wuhan, Hubei, China, ²Department of Thyroid and Breast Surgery, Maternal and Child Health Hospital of Hubei Province, Wuhan, Hubei, China, ³Department of Ultrasound, Hubei Cancer Hospital, Tongji Medical College, Huazhong University of Science and Technology, Wuhan, Hubei, China, ⁴School of Engineering, Penn State Erie, The Behrend College, Erie, PA, United States

Various imaging techniques combined with machine learning (ML) models have been used to build computer-aided diagnosis (CAD) systems for breast cancer (BC) detection and classification. The rise of deep learning models in recent years, represented by convolutional neural network (CNN) models, has pushed the accuracy of ML-based CAD systems to a new level that is comparable to human experts. Existing studies have explored the usage of a wide spectrum of CNN models for BC detection, and supervised learning has been the mainstream. In this study, we propose a semi-supervised learning framework based on the Vision Transformer (ViT). The ViT is a model that has been validated to outperform CNN models on numerous classification benchmarks but its application in BC detection has been rare. The proposed method offers a custom semi-supervised learning procedure that unifies both supervised and consistency training to enhance the robustness of the model. In addition, the method uses an adaptive token sampling technique that can strategically sample the most significant tokens from the input image, leading to an effective performance gain. We validate our method on two datasets with ultrasound and histopathology images. Results demonstrate that our method can consistently outperform the CNN baselines for both learning tasks. The code repository of the project is available at <https://github.com/FeiYee/Breast-area-TWO>.

KEYWORDS

semi-supervised learning, breast cancer detection, vision transformer, adaptive token sampling, data enhancement

1 Introduction

Breast cancer (BC) has been the most common cancer type for women. The 2020 report of the World Cancer Research Fund shows that there were more than 2 million newly diagnosed BC cases in 2018 (Bray et al., 2018). Such worrying numbers highlight the significance of properly using present technological advancements to undertake efficient BC detection in its early stage. In particular, a recent development in artificial intelligence (AI) that explores the usage of deep learning models in a wide spectrum of health care applications presents a promising direction toward building a more effective computer-aided diagnosis (CAD) system for BC detection (Hu et al., 2020; Mewada et al., 2020; Moon et al., 2020; Boumaraf et al., 2021; Eroğlu et al., 2021; Mishra et al., 2021).

A variety of imaging techniques can be used for BC detection and diagnosis, including X-rays (mammograms) (Abdelrahman et al., 2021), ultrasound (sonography) (Moon et al., 2020; Mishra et al., 2021), thermography (Singh and Singh, 2020), magnetic resonance imaging (MRI) (Mann et al., 2019), and histopathology imaging (Benhammou et al., 2020). Ultrasound has been a widely adopted, low-cost, non-invasive, and non-radioactive imaging modality in the procedure of BC diagnosis and is usually followed by histopathological analysis. The latter applies biopsy techniques to collect cell/tissue samples that are placed on a microscope slide and then stained for microscopic examination. With a high degree of confidence, histopathological diagnosis has become the gold standard for almost all cancer types (Das et al., 2020). However, in spite of the usage of various imaging modalities, it requires radiologists or pathologists to perform a visual inspection, which is time-consuming and in need of a high degree of radiological/pathological expertise. In addition, it has been shown by several studies that a high percentage of inter-observer variability exists when the same set of images are read by different experts (Kaushal et al., 2019). An AI-powered system has the potential to eliminate this assessment discrepancy caused by different experiences, analytical methodology, and knowledge between human beings, providing a more accurate diagnostic result to support clinical decision-making (Hamed et al., 2020).

Recent advances in AI, especially in deep learning, have been extensively investigated in the health care industry (Beam and Kohane, 2018; Li and Xiao, 2022; Qu and Xiao, 2022). The number of use cases of deep learning in BC detection has also been increasing (Hamed et al., 2020). Our literature investigation shows that prior efforts in breast cancer image classification share two common characteristics. First, the learning models are mostly based on the convolutional neural network (CNN), including existing deep CNN architectures, custom CNNs, and hybrid models with a CNN as a component. Despite the effectiveness of CNN-based classification models, recent advances have witnessed the rise of a novel vision model, namely, the Vision Transformer (ViT) (Dosovitskiy et al.,

2020), which has been shown to be more accurate in multiple public benchmarks. Few studies have investigated the usage of the ViT in BC detection (Gheflati and Rivaz, 2021), and the potential of the ViT has not been fully explored in this area. Second, most existing studies are based on supervised learning, which requires a full annotation for all image samples in the dataset. The procedure of annotation is time-consuming and requires domain expertise. Semi-supervised learning (SSL) (Van Engelen and Hoos, 2020), on the other hand, only requires annotation on a small subset of training data and combines a larger subset of unlabeled data during training. SSL can effectively reduce the efforts of annotation. However, SSL has not been extensively used in present studies of BC detection.

Our study aims to address these methodological gaps. Specifically, we propose a ViT-based BC classification learning pipeline that combines both supervised learning and SSL. We use an adaptive token sampling (ATS) technique (Fayyaz et al., 2021) that allows the original ViT model to dynamically choose the most critical image tokens. Moreover, we present a custom consistency training (CT) strategy (Xie et al., 2020) to unify supervised and unsupervised learning with image augmentation. The CT-based SSL, when combined with an ATS-ViT (namely, ViT with ATS), can effectively boost the model performance. The proposed method has been validated on two datasets, including the dataset of breast ultrasound images (BUSI) (Al-Dhabyani et al., 2020) and the Breast Cancer Histopathological Image Classification (BreakHis) dataset (Spanhol et al., 2016). The results of our method have been promising and superior compared to the CNN models. The project is released under the MIT License and is available at <https://github.com/FeiYee/Breast-area-TWO>.

The rest of this study is organized as follows. We provide a literature review for relevant studies in Section 2. Section 3 describes the datasets used in this study and the details of the proposed model. In Section 4, several experiments are conducted to evaluate the effectiveness of the proposed model. Finally, in Section 5, we conclude the study and provide future work.

2 Related work

This section reviews the prior studies in two aspects, including DNN-based BC detection methods and SSL applied in biomedical image classification.

2.1 Deep neural network-based breast cancer detection

Numerous existing and custom deep CNN models have been used on both ultrasound and histopathology images for breast tumor classification. Compared to feature-based learning models that require hand-crafted features (Mishra et al., 2021), deep

neural network (DNN) models such as CNNs can learn discriminative patterns with automatically extracted features to represent an image sample (Li et al., 2021). For ultrasound imaging, Masud et al. (2020) proposed a custom CNN model compared with several existing CNN models, including AlexNet (Krizhevsky et al., 2012), Darknet19 (Redmon et al., 2016), GoogleNet (Szegedy et al., 2015), MobileNet (Howard et al., 2017), ResNet18 (He et al., 2016), ResNet50, VGG16 (Simonyan and Zisserman, 2014), and Xception (Chollet, 2017). In addition to single models, ensemble learning has also been used. Moon et al. (2020) aggregated three CNN models, including VGGNet, ResNet, and DenseNet (Huang et al., 2017) by fusing the image representations. Similarly, Eroglu et al. (2021) adopted a concatenation of features generated by Alexnet, MobilenetV2 (Sandler et al., 2018), and Resnet50, followed by a Minimum Redundancy Maximum Relevance-based feature selection strategy to choose a set of the most valuable features that were used to train a feature-based classifier [e.g., support vector machine (SVM) (Pisner and Schnyer, 2020), k-nearest neighbors (KNNs) (Peterson, 2009)]. As for histopathology imaging, prior studies have adopted CNN models with improvements in several aspects. Alom et al. (2019) proposed an Inception Recurrent Residual Convolutional Neural Network (IRRCNN) to combine the predictive power of the recurrent CNN, ResNet, and the Inception network. Wang et al. developed FE-BkCapsNet that integrates the CNN and CapsNet (Sabour et al., 2017) with deep feature fusion and enhanced routing. Mewada et al. (2020) proposed the use of both the spatial features of a CNN and the spectral features of a wavelet transform to address the convergence issue during training. In addition to the improvements in models, novel training strategies have also been developed. Boumaraf et al. (2021) used a block-wise fine-tuning method, allowing the last few residual blocks in the CNN to be more domain-specific. Despite the extensive studies of DNN-based models for BC detection, other model types have not been fully explored. The ViT, as a recently developed and highlighted vision model, has received significant attention in a wide range of tasks. It is desirable to validate the effect of the ViT in imaging-based BC detection. Our study is such an attempt.

2.2 Semi-supervised learning-based biomedical image classification

SSL has been an effective training technique to reduce the number of training examples required for a fully supervised learning procedure. Obtaining a data point in the biomedical domain could be time-consuming, especially in the field of cancer research, where it could take months or even years to determine a patient's final status (Zemmal et al., 2016). Thus, prior studies have adopted SSL to use the unlabeled data. Zemmal et al. (2016) adopted a Semi-Supervised Support Vector Machine (S3VM) with hand-crafted features for BC detection. Jaiswal et al. (2019)

TABLE 1 Three classes in the DBUI dataset.

Class	# Images per class
Benign	487
Malignant	210
Normal	133
Total	780

used pseudo labels on the PatchCamelyon-level to detect metastasized cancer cells in histopathology diagnosis. Shi and Zhang (2011) used low-density separation, an SSL method, to conduct gene expression-based outcome prediction for cancer recurrence. Ma and Zhang (2018) developed an SSL model that combines affinity network fusion and a neural network to implement few-shot learning, significantly improving the model's learning ability with fewer training data. Other applications of SSL include cancer survival analysis (Liang et al., 2016), skin cancer diagnosis (Masood et al., 2015), bladder cancer grading (Wenger et al., 2022), and colorectal cancer detection (Yu et al., 2021). To our best knowledge, prior studies have not explored CT for BC detection, and our research aims to fill this gap.

3 Materials and methods

3.1 Dataset

Two datasets are used to validate the proposed method, including the dataset of breast ultrasound images (BUSI) (Al-Dhabyani et al., 2020) and the Breast Cancer Histopathological Image Classification (BreakHis) dataset (Spanhol et al., 2016) that represent non-invasive and invasive BC detection methods, respectively. Also, the choice of these two datasets allows our model to be trained and validated using images from diverse sources, which can be used to evaluate a model's robustness.

3.1.1 Breast ultrasound images dataset

Table 1 shows the three classes of BUSI and the number of image samples for each class. Typically, ultrasound images are in grayscale. The images were gathered at the Baheya hospital, saved in DICOM format, and converted to PNG format afterward. Data collection and annotation took around 1 year to complete. The total number of images acquired at the start of the project was 1,100, which decreased to 780 after preprocessing to eliminate images with unimportant information. The LOGIQ E9 and the LOGIQ E9 Agile ultrasound systems were used in the scanning procedure, producing images with a resolution of 1280×1024 . Figure 1 shows two example samples per class, totaling six samples, in which (a) and (d) are benign, (b) and (e)

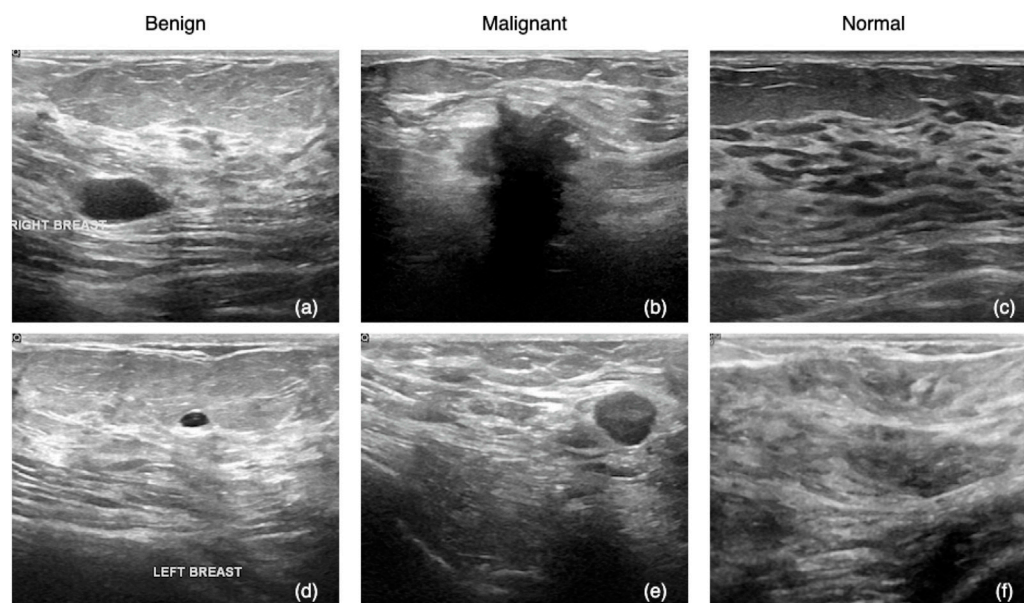


FIGURE 1
BUSI samples: (A,D) are benign tumor samples, (B,E) are malignant, and (C,F) are normal.

TABLE 2 Stats of the BreakHis dataset.

Magnification	Benign	Malignant	Total
x40	625	1,370	1,995
x100	644	1,437	2,081
x200	623	1,390	2,013
x400	588	1,232	1,820
Total	2,480	5,429	7,909
# Patients	24	58	82

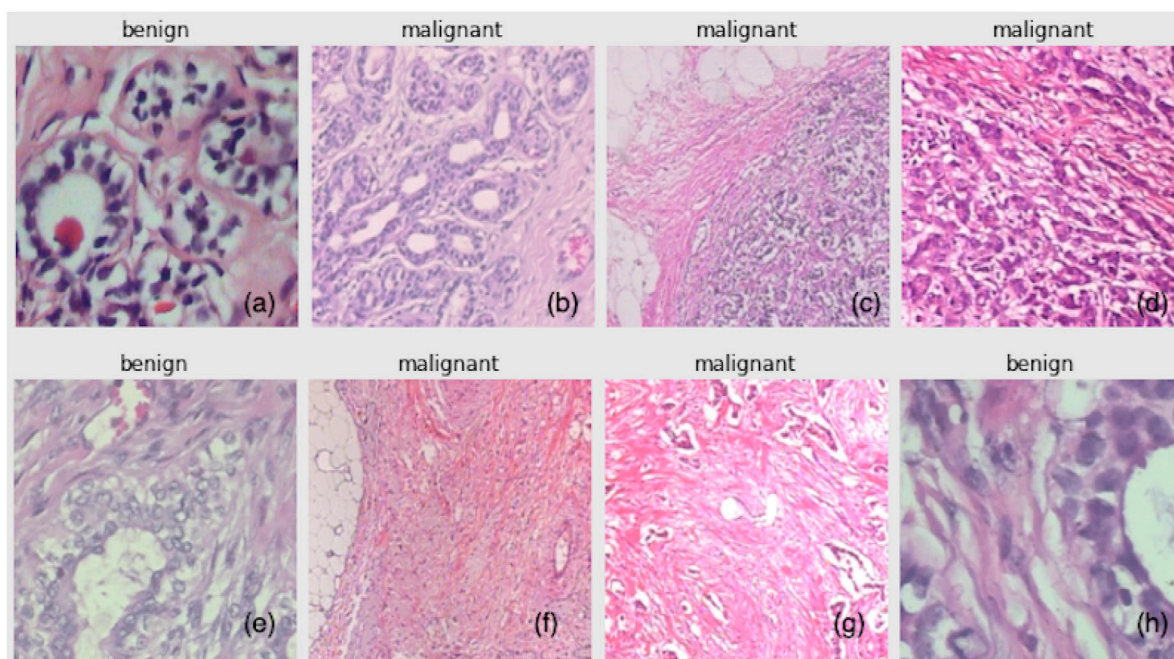
are malignant, and (c) and (f) are normal. An experienced radiologist reads an ultrasound image based on a set of standard criteria that involve mass size, echo nodule, tumor borders and morphology, calcification, blood flow, and so on. These criteria can be regarded as discriminative features allowing a trained human being to determine the class of an image. Traditional feature-based models encode these criteria into hand-crafted features to represent an image, while DNN-based models can automatically extract discriminative patterns and yield a higher accuracy (Shaheen et al., 2016; Han et al., 2017).

3.1.2 BreakHis dataset

The BreakHis dataset contains 7,909 microscopic images of breast tumor tissue, including 2,480 benign and 5,429 malignant

samples, collected from 82 patients by the P&D Laboratory-Pathological Anatomy and Cytopathology, Parana, Brazil. These images are with four magnifying factors, namely, $\times 40$, $\times 100$, $\times 200$, and $\times 400$. All of the samples are of 700×460 pixels with 3-channel RGB and 8-bit depth in each channel, stored in PNG format. A histologically benign sample does not meet any malignancy criteria such as mitosis, basement membranes disruption, metastasize, etc. In other words, benign tumors grow slowly and stay localized. On the contrary, the malignant ones have locally invasive lesions that can disrupt adjacent structures and lead to metastasis to distant sites of the human body. Table 2 shows a stats summary of the BreakHis dataset.

The breast tissue slides are imaged digitally using an Olympus BX-50 system microscope equipped with a 3.3x relay lens and a Samsung SCC-131AN digital color camera. The collected slides are then stained with hematoxylin and eosin (HE). The samples are obtained through surgical (open) biopsy (SOB), which is then processed for histological examination and labeled by pathologists from the P&D Laboratory. The standard paraffin method, which is widely used in clinical routine, was used in the preparation of the samples in this study. The primary purpose is to keep the original tissue structure and molecular composition, which allows it to be observed under a light microscope in its natural state. After staining, the anatomopathologists visually examine the tissue samples with a microscope to determine whether or not there are any cancerous lesions present in each slide. Experienced pathologists make the final diagnosis

**FIGURE 2**

BreakHis samples: (A,E,H) are benign, and (B–D,F,G) are malignant.

in each case, which is then confirmed by additional tests such as immunohistochemistry (IHC) analysis. Figure 2 shows a set of samples from the BreakHis dataset, in which the subfigures (a), (e), and (h) are benign samples, and the rest are all malignant.

3.2 Overview of the learning framework

Figure 3 shows the overall workflow of the proposed method. The core model to be trained is the ATS-ViT. The training procedure comprises two parts, namely, supervised and consistency training. The former aims to improve the model's predictive ability, and the latter improves its generalization. Both parts are unified *via* an end-to-end training procedure (described in Algorithm 1). It should be noted that the parameters of the ATS-ViT are shared across both parts of training. Also, three types of losses are combined to guide the optimization of the neural network via gradient descent. The training details are covered in Subsection 3.6.

3.3 Transformer

A transformer (Vaswani et al., 2017) is a neural architecture that uses an attention mechanism to mine and capture the semantic meanings and relations among the input tokens for sequential modeling problems. One of the benefits of the transformer is

that it allows parallelization since tokens passing through its architecture can be processed independently rather than sequentially, presenting a unique advantage over recurrent models such as long short term memory (LSTM) (Kim et al., 2016) and recurrent gated unit (GRU) (Chung et al., 2014). The transformer was originally designed for machine translation in natural language processing (NLP) and showed superior performance. Moreover, recent advances have explored applications of the transformer in a wide spectrum of NLP tasks and developed a rich set of pre-training techniques, making it one of the most influential works in AI in the past 5 years.

A transformer adopts an encoder-decoder structure. The encoder module comprises a stack of transformer encoders; similarly, the decoder module is a stack of transformer decoders. Each transformer encoder includes a self-attention layer with multiple attention heads to capture the semantic interaction among the input tokens. Specifically, each attention head calculates a tensor of scores to express how each token is affected (attended) by every other token. The outputs of these attention heads are aggregated, normalized, and passed to a feed-forward layer to generate a set of embeddings, which are the output of the present encoder. The subsequent encoder takes as input the embeddings generated from its previous encoder and repeats the process. A transformer decoder, on the other hand, comprises three layers, including a multi-head self-attention layer, an encoder-decoder attention layer, and a feed-forward layer. At each time step, a

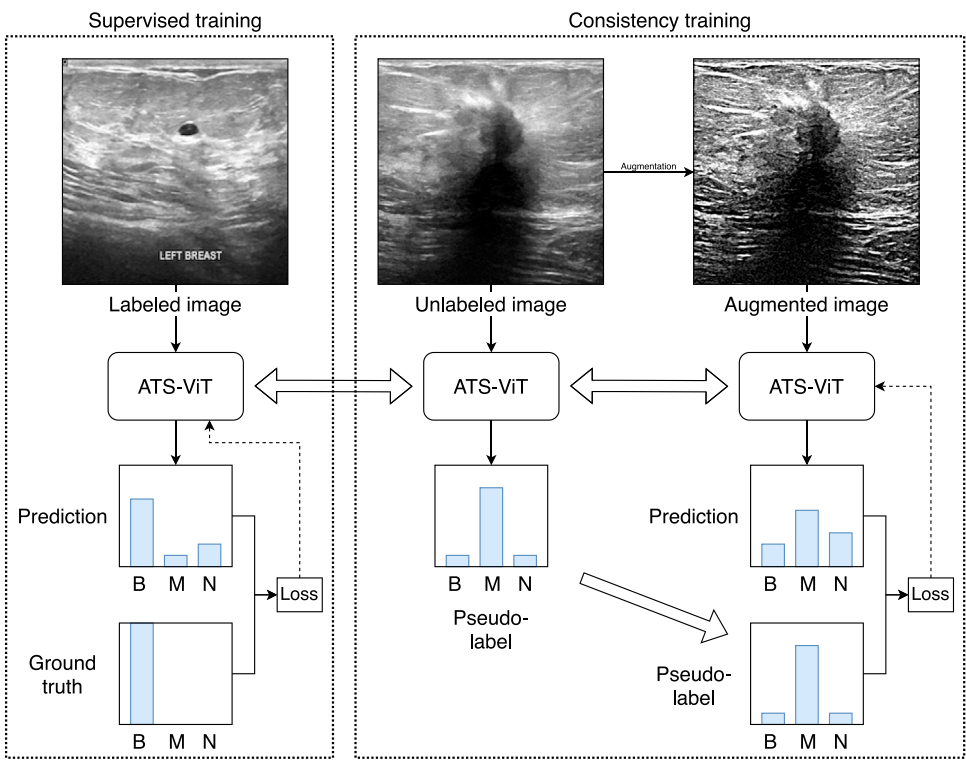


FIGURE 3 Overview of the proposed learning framework. The framework comprises supervised and consistency training unified via an end-to-end training procedure. For simplicity, the figure only uses image samples from the BUSI dataset. The method has been validated on both datasets used in this study.

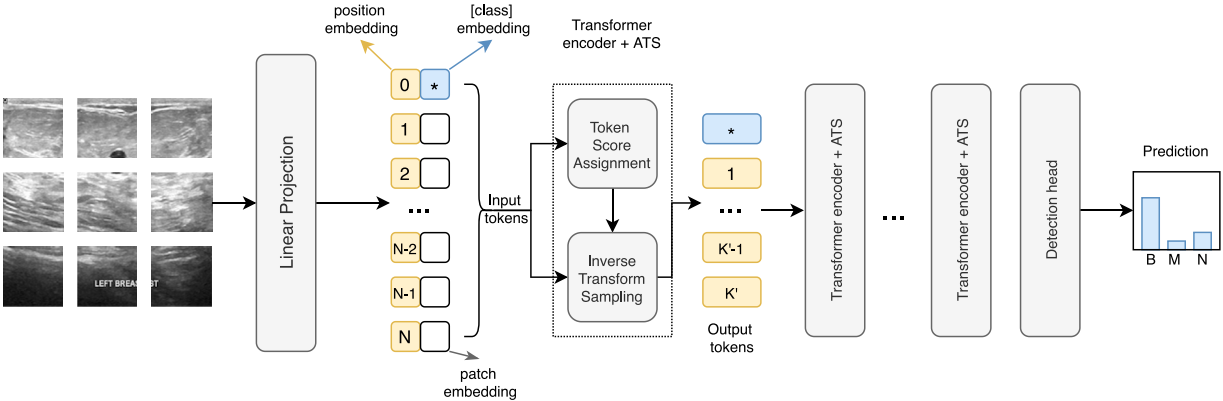


FIGURE 4 Architecture of the ATS-ViT. The ATS module can be integrated into each transformer block to perform two steps, including token score assignment and inverse transform sampling. The ATS can identify the most informative tokens that are passed to the subsequent layers, effectively reducing the computational cost and improving the classification accuracy.

transformer decoder takes as input two intermediate tensors generated by the last encoder layer, the embeddings from its previous decoder (it would be the output of the decoder module

at the previous time step for the first decoder); these data are fed through a stack of decoders, followed by a linear and a softmax layer to produce the prediction result.

3.4 Vision transformer

The wide success of a transformer in NLP tasks inspired researchers to explore its potential in computer vision. The ViT has been one of the first efforts. The ViT adopts the same structure as the original transformer with the following changes to the input. An image is chunked into a set of image patches to meet the input requirement of the transformer. The so-called image patch embedding operation is essentially a linear transformation, that is, a fully connected layer. Specifically, if an input image of size $H \times W \times C$ is split into N patches (i.e., tokens), each of size $P \times P \times C$, then we can determine that $N = \frac{HW}{P^2}$. Then, each patch is spread out into a vector of size D . Thus, the input is transformed into a 2D tensor of size $N \times D$. In addition, a special [CLS] token is inserted into the first position of the token sequence to encode the information used for classification. This strategy has been commonly seen in other pre-training strategies such as the Bidirectional Encoder Representations from Transformers (BERT) (Devlin et al., 2018). Furthermore, to maintain the relative position relationship between different patches, a position encoding vector is added to each patch embedding, generating a token embedding used by the first layer of the transformer encoder.

3.5 Adaptive token sampler

The ViT is computationally expensive since the computing cost rises quadratically with the number of tokens. CNNs reduce the resolution inside the network with different pooling operations. However, because the tokens are permutation invariant, using pooling in the ViT is not feasible. Thus, we adopt an adaptive token sampler (ATS), a technique that allows the model to dynamically choose significant tokens from the input tokens to reduce computational cost. Figure 4 shows the network structure of ViT with ATS.

An ATS works by assigning a score to each of the N input tokens to determine which ones to keep. The score indicates a token's contribution to the final prediction. Let K be the maximum number of retained tokens, and a sampling strategy is adopted as follows. Let \mathcal{K} , \mathcal{Q} , and \mathcal{V} be the query, key, and value vectors, respectively, in the standard self-attention layer of the transformer. The attention matrix \mathcal{A} can be computed via Eq. 1.

$$\mathcal{A} = \text{Softmax}\left(\frac{\mathcal{Q}\mathcal{K}^T}{\sqrt{d}}\right). \quad (1)$$

Thus, \mathcal{A} is $(N+1) \times (N+1)$ (with the [CLS] token counted) and sums up to 1 after the softmax operation. The output tokens, before sampling, are given by Eq. 2.

$$\mathcal{O} = \mathcal{A}\mathcal{V}. \quad (2)$$

Let $\mathcal{A}_{i,j}$ denote the element at row i and column j in \mathcal{A} , the significance score of token j can be calculated by Eq. 3.

$$\mathcal{S}_j = \frac{\mathcal{A}_{1,j}\|\mathcal{V}_j\|}{\sum_{i=2} \mathcal{A}_{1,i}\|\mathcal{V}_i\|}. \quad (3)$$

Only the first row of the attention matrix \mathcal{A} is used since each element $\mathcal{A}_{1,j}$ represents the importance of token j to token 1, namely, the [cls] token. With a significance score calculated for each input token, the inverse transform sampling strategy is used for token sampling. First, the cumulative distribution function of \mathcal{S} can be calculated via Eq. (4).

$$\text{CDF}_i = \sum_{j=2}^{i-1} \mathcal{S}_j. \quad (4)$$

It is noted that the first token is excluded since it is used to encode the classification information, and thus, is not needed for the calculation of the CDF. The sampling function, denoted by $\Upsilon(k)$, can now be obtained via the inverse function of the CDF, which is given by Eq. 5.

$$\Upsilon(k) = \text{CDF}^{-1}(k). \quad (5)$$

To obtain K' samples ($K' \leq K$), $\Upsilon(\cdot)$ is run K' times from uniform distribution $U[0, 1]$, which generates K' real numbers that are rounded to the nearest integers and used as the sampling indices. The selected K' output tokens should carry more informative patterns and are passed to the next transformer block.

3.6 Semi-supervised learning

SSL is a training paradigm that explores both labeled and unlabeled data to enhance the robustness of a model. Also, SSL is a popular strategy when the number of training samples is limited because of high annotation costs. In this study, we assume that similar images should belong to the same class, which is referred to as the smoothness assumption and has been adopted by many SSL training systems (Chen and Wang, 2010). CT is a typical SSL method used in prior studies (Xie et al., 2020; Lee and Cho, 2021). CT allows a model to be trained to yield consistent results for an image and its augmented versions with various perturbations such as crop, contrast, flip, jittering, etc. The proposed CT method is described in detail as follows.

First, we divide the original training set X into two sets X_l and X_u , treated as labeled and unlabeled datasets during CT, respectively. Second, a set of image augmentation algorithms $\{h_i\}_{i=1}^m$ are defined. An unlabeled sample x_u is fed into algorithm h_i to generate an augmented image denoted by $z_{u,i}$. Let F denote the ViT model. The training objective of our SSL algorithm is three-fold.

- First, the supervised loss should be minimized to improve the predictive ability of model F . For our study, the binary cross-entropy loss is used, denoted by L_{CE} . For a batch of m labeled samples $\{(x_l, y_l)\}_{l=1}^m$, we can calculate L_{CE} based on Eq. 6

$$L_{CE} = -\frac{1}{m} \sum_{l=1}^m y_l \log \mathbf{F}(x_l). \quad (6)$$

- Second, the pseudo-label loss should be minimized to encourage the model to produce consistent results for an image and its augmented versions with perturbations. For each image x_u in a batch of m unlabeled data, a random augmentation algorithm is selected from $\{h_i\}_{i=1}^m$ and applied to the image x_u to generate an augmented image z_u . Let $\mathbf{F}(x_u)$ be a pseudo-label, and we can then calculate pseudo-label loss using the mean squared error based on Eq. 7.

$$L_{MSE} = \frac{1}{m} \sum_{u=1}^m (\mathbf{F}(x_u) - \mathbf{F}(z_u))^2. \quad (7)$$

- Last, to ensure the consistency of the whole process, we also need to measure the intermediate result of unlabeled data and its augmented version, and since the intermediate result of the ViT is a one-dimensional sequence, we use Earth Mover's distance (Rubner et al., 2000), noted as L_{EM} , which is used to describe the degree of similarity of two distributions. Given two sets of distributions p_1, p_2, \dots, p_m and q_1, q_2, \dots, q_m , we need to find a way to arrange q in such a way that the EML loss is minimized. The loss can be given by Eq. 8.

$$L_{EM}(p, q) = \min_{q \in Q} \sum_i l(q_i, p_i), \quad (8)$$

where Q is the set of all possible permutations of q and l stands for the measurement, here, we choose it as L2 loss.

Aggregating the three aforementioned individual losses yields the following overall loss function, which is our final optimization objective.

$$L = L_{CE} + L_{MSE} + L_{EM}. \quad (9)$$

When we ask the model to obtain similar features for data before and after adding multiple joint perturbations, we can force the model to learn what does not change with perturbation, and the information that remains constant before and after perturbation is more relevant to the classification result, and such a strategy will lead to stronger generalization ability. Therefore, we can confirm that combining data augmentation strategies with semi-supervised learning can give better results.

Algorithm 1. SSL algorithm.

```

1: Initialize model  $\mathbf{F}$  parameterized by  $\Theta$ 
2: for epoch in range(1, N) do
3:   Sample a batch of  $m$  labeled data  $\{(x_l, y_l)\}_{l=1}^m$ , where  $x_l \in X_L, y_l \in Y_L$ .
4:   Obtain supervised loss  $L_{CE}$  based on Equation 6.
5:   Sample a batch of  $m$  unlabeled data  $\{x_u\}_{u=1}^m$ , where  $x_u \in X_U$ .
6:   Apply a random augmentation algorithm  $h_i$  to each  $x_u$  to obtain  $z_u$ , i.e.,  $z_u = h_i(x_u)$ .
7:   Obtain pseudo-label loss  $L_{MSE}$  based on Equation 7.
8:   Obtain the earth mover's distance based on Equation 8.
9:   Obtain the overall loss  $L = L_{CE} + L_{MSE} + L_{EM}$ .
10:  Perform one-step optimization, i.e.,  $\Theta \leftarrow \Theta - \alpha \Delta L$ .
11: end for
12: return Trained model  $\mathbf{F}$  with parameter  $\Theta$ 

```

4 Results

Codes in this study have been written in Python 3.6.10 and using PyTorch 1.8.0 as the deep learning framework. All experiments were run on a workstation with a Windows 10 operating system, an i7-10875h CPU, and an Nvidia GTX2080TI 12G graphic card.

4.1 Evaluation metrics

Since the classes for both datasets are imbalanced, accuracy (Acc) is not sufficient to reflect the true performance of a model. Therefore, in addition to ACC, we also use precision (Pre), recall (Rec), and F1 scores for performance evaluation. These indicators are defined in Eqs 10–13.

$$Acc = \frac{TP + TN}{TP + TN + FP + FN}, \quad (10)$$

$$Pre = \frac{TP}{TP + FP} \times, \quad (11)$$

$$Rec = \frac{TP}{TP + FN} \times, \quad (12)$$

$$F1 = 2 \times \frac{Pre \times Rec}{Pre + Rec}, \quad (13)$$

where TP, TN, FP, and FN refer to the number of true positives, true negatives, false positives, and false negatives, respectively. Pre reflects the ratio of false alarms. The higher the pre, the fewer false alarms the model has. Meanwhile, Rec reflects the quantity of missed positive samples. In other words, the higher the Rec, the fewer positive samples that have been missed. F1 represents the harmonic mean of Pre and Rec, presenting a more suitable metric than Acc for a classification task with an imbalanced dataset.

4.2 Baselines

Four models have been chosen as the baselines in this study, namely, the VGG16, ResNet101, DenseNet201, and ViT. All four models have been extensively used in a variety of image classification tasks and served as solid baselines.

- The VGG16 network comprises a sequence of five blocks, each with two or three convolutional layers for feature extraction, followed by a pooling layer for downscale sampling. The last block is further followed by three fully connected layers and a softmax layer to generate a normalized vector as the prediction result. The VGG neural architecture extensively uses small (3×3) convolutional filters, which is the basis for building a deep and accurate network.

TABLE 3 Training setting.

Hyperparameter	Value
Learning rate	2e-5
Eps	1e-8
Batch size	64
Epochs	300
Input image size	256 × 256
ATS # tokens	[256, 128, 64, 32, 16, 8]

- The ResNet neural architecture stacks a sequence of residual blocks, each of which facilitates the learning of an identity function *via* a shortcut connection by feeding the input of a block directly into the output. This way, an identity function can be easily learned, allowing a network with more layers to be trained more effectively without diminishing returns. ResNet101 contains a series of repeated residual blocks followed by a dense and a softmax layer, with a total of 101 layers.
- DenseNet is a variant of ResNet with two differences. First, DenseNet uses a concatenation instead of a summation (used in ResNet) to aggregate the layer output and the shortcut data within each block. Second, DenseNet introduces a transition layer placed between two dense blocks. Each transition layer comprises a 1×1 convolutional layer and an average pooling layer with a stride of two to control the model complexity.
- The ViT has been covered in [Section 3.4](#).

4.3 Training setting

The main hyperparameters used for training are shown in [Table 3](#). We adopted Adam as the optimizer with a learning rate of 2e-5. We set $\text{eps} = 1\text{e-}08$ to prevent the denominator from being 0. A batch size of 64 was chosen. The loss function was the binary cross entropy with logits. All evaluated models were trained with 300 epochs. For the ViT, each input image was re-scaled to a fixed size of 256×256 and split into 16 patches. The ViT model used in the study comprises six encoders. In the ATS procedure, the numbers of tokens kept in each layer were 256, 128, 64, 32, 16, and 8, which was the default setting from the original paper of the ATS. These parameters were obtained based on empirical results. It is noted that we tried a variety of token sample numbers in addition to the default setting and did not observe a significant difference in results, which was because of the fact that the sampling strategy of the ATS ensures that the model focuses on key regions, but does not completely discard the information of some outlier data, so it can adjust the pattern extraction ability of the model for different types of data according to the input.

TABLE 4 Results on BUSI.

Model	Acc	Pre	Rec	F1
VGG19	93.02	92.3	92.07	92.19
ResNet101	94.95	94.29	95.23	94.76
DenseNet201	93.62	92.88	93.71	93.29
ViT	93.38	93.02	93.37	93.43
ViT + ATS	94.45	94.29	94.78	94.47
CT + ViT + ATS (ours)	95.29	96.29	96.01	96.15

The highest scores of each metric are in bold.

Both datasets are split into training, validation, and test sets in the ratio of 7:1:2. In addition, the training set is further split in the ratio of 8:2; 80% of the data in the training set participate in the supervised training to learn an ATS-ViT model, and the rest 20% are treated as unlabeled data used for CT.

4.4 Results

[Table 4](#) presents a performance comparison between the proposed method and the chosen baselines. Also, an ablation study has been conducted to evaluate the efficacy of the ATS and CT. Specifically, we used the ViT as a base model and added the ATS and CT to form the ViT + ATS model and the CT + ViT + ATS model. For each evaluated model, four metrics defined in [Section 3.1](#) have been reported, including Acc, Pre, Rec, and F1. We provide the result interpretation as follows.

- It is observed that the CNN models, namely, VGG19, ResNet101, and DenseNet201, can achieve similar performance compared with the ViT base model. In particular, ResNet101 presents the highest Acc (95.59%) and F1 (94.76%) among the four baselines.
- The ViT base model does not perform better in our experiments than the CNN models. In the original study on the ViT, it has been validated to outperform the CNN models on several image classification tasks such as ImageNet ([Deng et al., 2009](#)). In our experiment, the ViT achieves an Acc of 93.38% and an F1 of 93.43%, ranked the third and second places among the four baselines. The reason why the ViT does not outperform all CNN models may be because of the training configuration or the hyperparameter setting that has not been sufficiently optimized.
- The addition of the ATS to the ViT has improved the Acc and F1 by 1.07 and 1.04%, respectively. However, the ViT + ATS is still not as good as ResNet101. The performance gain is mainly due to the sampling strategy that can effectively select a subset of tokens that contribute the most to the classification task.

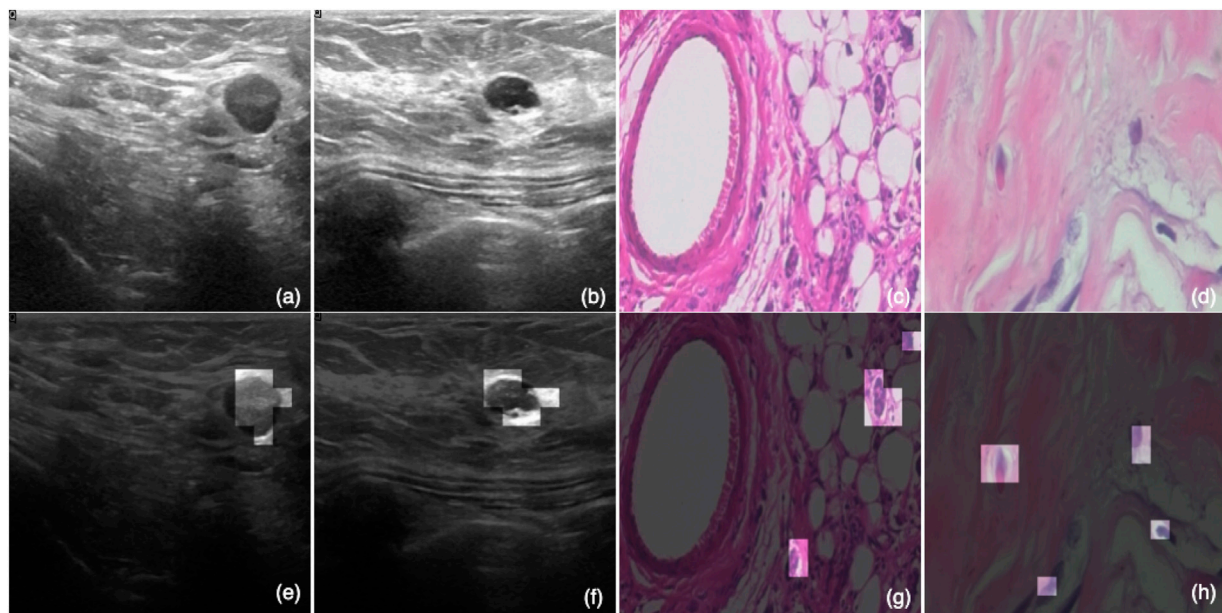


FIGURE 5

Visualized effect of the ATS. Subfigures (A,B) are ultrasound images; and (C,D) are histopathology samples. Meanwhile, (E–H) are the same images as (A–D) with the eight most significant tokens (image patches) kept for each image.

TABLE 5 Results on BreakHis.

Model	Acc	Pre	Rec	F1
VGG19	96.41	96.45	95.88	96.16
ResNet101	95.53	95.54	94.38	94.96
DenseNet201	97.42	93.98	97.89	95.6
ViT	95.68	95.67	95.7	95.69
ViT + ATS	96.98	96.85	95.68	96.26
CT + ViT + ATS (ours)	98.12	98.17	98.65	98.41

The highest scores of each metric are in bold.

- Our best model, namely, CT + ViT + ATS, achieves the best results on all four metrics with 95.29% Acc, 96.29% Pre, 96.01% Rec, and 95.15% F1, outperforming the second-best scores by 0.34, 2, 0.78, and 1.39%, respectively. Compared with the ViT + ATS model, the four scores have improved by 0.84, 2, 1.23, and 1.86%. The performance gains are mainly due to the training procedure that combines both supervised and unsupervised training so that the model can experience more diversified samples via data augmentation during consistency training.

Table 5 shows the results of the validated models on BreakHis. The same set of models has been evaluated, and the results are similar to the ones on BUSI. We highlight the observations as follows.

- Among the four baseline models, DenseNet201 shows the highest Acc of 97.42%, while VGG19 presents the highest F1 of 96.16%. The ViT base model posts an Acc of 95.68% and an F1 of 95.69%, ranked the third and second places, respectively. Again, the ViT does not stand out on this classification task.
- The addition of the ATS improves the Acc and F1 by 1.3 and 0.57%, respectively, lifting the model to the top place in F1 (96.26), with CT + ViT + ATS excluded. This improvement shows that the ATS can effectively locate the image tokens with the most informative parts, allowing the model to learn more distinguishable patterns to boost accuracy. The result shows that the ATS presents the desired effect and has been consistent across both classification tasks.
- CT + ViT + ATS, on the other hand, achieves the best performance for all four metrics with an Acc of 98.12%, a Pre of 98.17%, a Rec of 98.65%, and an F1 of 98.41%. This result shows that CT can bring consistent performance boost on both datasets and is a promising strategy to improve a model's generalization ability.

Figure 5 shows the effect of the ATS on the four samples, with two from each dataset. In this, Figures 5A,B are ultrasound images; and Figures 5C,D are histopathology samples. Meanwhile, Figures 5E–H are the same images as Figures 5A–D with the eight most significant tokens (image patches) kept for each image. These eight tokens are obtained from the last transformer block, which is closer to the detection head, and

thus, is more expressive for the classification result. It is observed that these tokens can accurately identify the regions of interest that are more indicative of the actual classes. Instead of looking at the whole image, an ATS-enabled model can reduce the amount of global information and pinpoint the most critical areas that contribute the most to the prediction results, which explains the effectiveness of the ATS.

5 Discussion

This study presents CT + ViT + ATS, a ViT model trained *via* CT and boosted *via* ATS. The proposed model has been validated on two BC imaging datasets and shown superior performance compared to three representative CNN baseline models. The results have demonstrated the efficacy of both the ATS and CT. The former allows the learning algorithm to identify the regions of interest that provide significant patterns for the classification task, and the latter unifies both supervised and unsupervised training to improve the generalization ability of the model. The proposed model, with the validated results, can serve as a credible benchmark for future research.

There are several notable findings from this study. Our experimental results show that the original ViT model does not present superior performance compared to its CNN competitors. On the BUSI dataset, the ViT is on a par with the CNN models, whereas on the BreakHis dataset, the ViT is slightly worse but still comparable. This could be because of the BC detection task, in which the images may contain subtle patterns hard to capture even with the self-attention mechanism used by the ViT. To discover these subtle patterns and improve detection accuracy, we adopt the ATS and CT as two boosting modules, which turn out to be effective. The gains, in Acc and F1, brought by the ATS and CT, have been notable and consistent on both datasets. Although the ATS was originally developed to reduce computational costs, we demonstrate that it also improves the detection accuracy since the model is encouraged to focus more on the critical image tokens and learn more subtle patterns. CT, on the other hand, exploits the existing training resources *via* a weakly-supervised training paradigm that effectively improves the robustness of the model. The two boosting modules refine the original ViT in three aspects: model, data, and training procedure. These joint efforts have been consistent for our task and have the potential to be used for other biomedical computer vision tasks.

The proposed CT + ViT + ATS method can be a core functional module of a CAD system for BC detection. It offers two merits. First, the ATS component allows the system to highlight the most informative image patches, which can help physicians quickly pinpoint the critical areas for precise and personalized diagnosis. Second, the backend of the CAD system can be easily modified to be a continuous learning system once

new images are available. Since CT is semi-supervised, only a portion of the newly added data needs to be labeled, significantly reducing the labor cost for annotation.

The proposed method can be extended in the following directions. First, we mainly compared CNN models and the ViT, while an ensemble of the two or feature-level aggregation can be another model design option that may bring together the strengths of both neural architectures. Given that the underlying designs of the CNN and the ViT are fundamentally different, the former adopts multiple filters to capture multi-scale features, while the latter explores semantic relations between each pair of tokens; a combination of the two could present superior performance compared to any single model. Second, a generative model such as a generative adversarial network (GAN) can be used to perform data augmentation in CT. Since a GAN captures the distribution of images belonging to a class, a well-trained GAN can generate synthetic images that look similar to real ones. These generated images can enhance the quantity and diversity of the training samples during CT, potentially leading to a more robust model. Lastly, the proposed method can be applied to a wider range of BC imaging datasets with additional image modalities such as X-ray, MRI, and thermography that are not considered in this study. It would be interesting to evaluate the proposed method on a multi-modal BC imaging dataset that offers multi-dimensional feature representations.

Data availability statement

The datasets presented in this study can be found in online repositories. The names of the repository/repositories and accession number(s) can be found at: <https://www.kaggle.com/datasets/aryashah2k/breast-ultrasound-images-dataset> (accessed on 20 November 2021) and <http://web.inf.ufpr.br/vri/breast-cancer-database> (accessed on 25 November 2021).

Author contributions

Conceptualization and methodology, WW, RJ, ZX, NC, QL, and FY; data analysis, software, validation, and original draft preparation, WW and RJ; review and editing, and supervision, ZX, QL, and FY. All authors have read and agreed to the published version of the manuscript.

Conflict of interest

The authors declare that the research was conducted in the absence of any commercial or financial relationships that could be construed as a potential conflict of interest.

Publisher's note

All claims expressed in this article are solely those of the authors and do not necessarily represent those of their affiliated

References

- Abdelrahman, L., Al Ghamdi, M., Collado-Mesa, F., and Abdel-Mottaleb, M. (2021). Convolutional neural networks for breast cancer detection in mammography: A survey. *Comput. Biol. Med.* 131, 104248. doi:10.1016/j.combiomed.2021.104248
- Al-Dhabyani, W., Gomaa, M., Khaled, H., and Fahmy, A. (2020). Dataset of breast ultrasound images. *Data Brief* 28, 104863. doi:10.1016/j.dib.2019.104863
- Alom, M. Z., Yakopcic, C., Nasrin, M. S., Taha, T. M., and Asari, V. K. (2019). Breast cancer classification from histopathological images with inception recurrent residual convolutional neural network. *J. Digit. Imaging* 32, 605–617. doi:10.1007/s10278-019-00182-7
- Beam, A. L., and Kohane, I. S. (2018). Big data and machine learning in health care. *Jama* 319, 1317–1318. doi:10.1001/jama.2017.18391
- Benhammou, Y., Achchab, B., Herrera, F., and Tabik, S. (2020). BreakHis based breast cancer automatic diagnosis using deep learning: Taxonomy, survey and insights. *Neurocomputing* 375, 9–24. doi:10.1016/j.neucom.2019.09.044
- Boumaraf, S., Liu, X., Zheng, Z., Ma, X., and Ferkous, C. (2021). A new transfer learning based approach to magnification dependent and independent classification of breast cancer in histopathological images. *Biomed. Signal Process. Control* 63, 102192. doi:10.1016/j.bspc.2020.102192
- Bray, F., Ferlay, J., Soerjomataram, I., Siegel, R. L., Torre, L. A., Jemal, A., et al. (2018). Global cancer statistics 2018: GLOBOCAN estimates of incidence and mortality worldwide for 36 cancers in 185 countries. *Ca. Cancer J. Clin.* 68, 394–424. doi:10.3322/caac.21492
- Chen, K., and Wang, S. (2010). Semi-supervised learning via regularized boosting working on multiple semi-supervised assumptions. *IEEE Trans. Pattern Anal. Mach. Intell.* 33, 129–143. doi:10.1109/TPAMI.2010.92
- Chollet, F. (2017). "Xception: Deep learning with depthwise separable convolutions," in Proceedings of the IEEE Conference on Computer Vision and Pattern Recognition, 1251–1258.
- Chung, J., Gulcehre, C., Cho, K., and Bengio, Y. (2014). Empirical evaluation of gated recurrent neural networks on sequence modeling. *arXiv Prepr. arXiv:1412.3555*.
- Das, A., Nair, M. S., and Peter, S. D. (2020). Computer-aided histopathological image analysis techniques for automated nuclear atypia scoring of breast cancer: A review. *J. Digit. Imaging* 33, 1091–1121. doi:10.1007/s10278-019-00295-z
- Deng, J., Dong, W., Socher, R., Li, L. J., Li, K., and Fei-Fei, L. (2009). "Imagenet: A large-scale hierarchical image database," in 2009 IEEE conference on computer vision and pattern recognition (Miami, FL, USA: IEEE), 248–255.
- Devlin, J., Chang, M. W., Lee, K., and Toutanova, K. (2018). Bert: Pre-training of deep bidirectional transformers for language understanding. *arXiv Prepr. arXiv:1810.04805*.
- Dosovitskiy, A., Beyer, L., Kolesnikov, A., Weissenborn, D., Zhai, X., Unterthiner, T., et al. (2020). An image is worth 16x16 words: Transformers for image recognition at scale. *arXiv Prepr. arXiv:2010.11929*.
- Eroglu, Y., Yildirim, M., and Çinar, A. (2021). Convolutional Neural Networks based classification of breast ultrasonography images by hybrid method with respect to benign, malignant, and normal using mRMR. *Comput. Biol. Med.* 133, 104407. doi:10.1016/j.combiomed.2021.104407
- Fayyaz, M., Kouhpayegani, S. A., Jafari, F. R., Sommerlade, E., Joze, H. R. V., Pirsiavash, H., et al. (2021). Ats: Adaptive token sampling for efficient vision transformers. *arXiv:2111.15667 [cs]*.
- Gheflati, B., and Rivaz, H. (2021). Vision transformer for classification of breast ultrasound images. *arXiv Prepr. arXiv:2110.14731*.
- Hamed, G., Marey, M. A. E. R., Amin, S. E. S., and Tolba, M. F. (2020). "Deep learning in breast cancer detection and classification," in The International Conference on Artificial Intelligence and Computer Vision (Berlin, Germany: Springer), 322–333.
- Han, Z., Wei, B., Zheng, Y., Yin, Y., Li, K., Li, S., et al. (2017). Breast cancer multi-classification from histopathological images with structured deep learning model. *Sci. Rep.* 7, 4172. doi:10.1038/s41598-017-04075-z
- He, K., Zhang, X., Ren, S., and Sun, J. (2016). "Deep residual learning for image recognition," in Proceedings of the IEEE Conference on Computer Vision and Pattern Recognition, 770–778.
- Howard, A. G., Zhu, M., Chen, B., Kalenichenko, D., Wang, W., Weyand, T., et al. (2017). Mobilenets: Efficient convolutional neural networks for mobile vision applications. *arXiv Prepr. arXiv:1704.04861*.
- Hu, Q., Whitney, H. M., and Giger, M. L. (2020). A deep learning methodology for improved breast cancer diagnosis using multiparametric MRI. *Sci. Rep.* 10, 10536. doi:10.1038/s41598-020-67441-4
- Huang, G., Liu, Z., Van Der Maaten, L., and Weinberger, K. Q. (2017). "Densely connected convolutional networks," in Proceedings of the IEEE Conference on Computer Vision and Pattern Recognition, 4700–4708.
- Jaiswal, A. K., Panshin, I., Shulkin, D., Aneja, N., and Abramov, S. (2019). Semi-supervised learning for cancer detection of lymph node metastases. *arXiv Prepr. arXiv:1906.09587*.
- Kaushal, C., Bhat, S., Koundal, D., and Singla, A. (2019). Recent trends in computer assisted diagnosis (CAD) system for breast cancer diagnosis using histopathological images. *Irbm* 40, 211–227. doi:10.1016/j.irbm.2019.06.001
- Kim, J., Kim, J., Thu, H. L. T., and Kim, H. (2016). "Long short term memory recurrent neural network classifier for intrusion detection," in 2016 international conference on platform technology and service (PlatCon) (Jeju, South Korea: IEEE), 1–5.
- Krizhevsky, A., Sutskever, I., and Hinton, G. E. (2012). Imagenet classification with deep convolutional neural networks. *Adv. neural Inf. Process. Syst.* 25.
- Lee, J., and Cho, S. (2021). Semi-supervised image classification with grad-CAM consistency. *arXiv:2108.13673*. doi:10.48550/arXiv.2108.13673
- Li, G., and Xiao, Z. (2022). Transfer learning-based neuronal cell instance segmentation with pointwise attentive path fusion. *IEEE Access*.
- Li, Z., Liu, F., Yang, W., Peng, S., and Zhou, J. (2021). A survey of convolutional neural networks: Analysis, applications, and prospects. *IEEE Trans. Neural Netw. Learn. Syst.* 2021, 1–21. doi:10.1109/TNNLS.2021.3084827
- Liang, Y., Chai, H., Liu, X. Y., Xu, Z. B., Zhang, H., Leung, K. S., et al. (2016). Cancer survival analysis using semi-supervised learning method based on Cox and AFT models with L1/2 regularization. *BMC Med. Genomics* 9, 11. doi:10.1186/s12920-016-0169-6
- Ma, T., and Zhang, A. (2018). Affinity network fusion and semi-supervised learning for cancer patient clustering. *Methods* 145, 16–24. doi:10.1016/j.ymeth.2018.05.020
- Mann, R. M., Kuhl, C. K., and Moy, L. (2019). Contrast-enhanced MRI for breast cancer screening. *J. Magn. Reson. Imaging* 50, 377–390. doi:10.1002/jmri.26654
- Masood, A., Al-Jumaily, A., and Anam, K. (2015). "Self-supervised learning model for skin cancer diagnosis," in 2015 7th International IEEE/EMBS Conference on Neural Engineering (NER), 1012–1015. doi:10.1109/NER.2015.7146798
- Masud, M., Eldin Rashed, A. E., and Hossain, M. S. (2020). Convolutional neural network-based models for diagnosis of breast cancer. *Neural Comput. Appl.* doi:10.1007/s00521-020-05394-5
- Mewada, H. K., Patel, A. V., Hassaballah, M., Alkinani, M. H., and Mahant, K. (2020). Spectral-spatial features integrated convolution neural network for breast cancer classification. *Sensors* 20, 4747. doi:10.3390/s20174747
- Mishra, A. K., Roy, P., Bandyopadhyay, S., and Das, S. K. (2021). Breast ultrasound tumour classification: A machine learning—radiomics based approach. *Expert Syst.* 38, e12713. doi:10.1111/exsy.12713
- Moon, W. K., Lee, Y. W., Ke, H. H., Lee, S. H., Huang, C. S., Chang, R. F., et al. (2020). Computer-aided diagnosis of breast ultrasound images using ensemble learning from convolutional neural networks. *Comput. Methods Programs Biomed.* 190, 105361. doi:10.1016/j.cmpb.2020.105361
- Peterson, L. E. (2009). K-nearest neighbor. *Scholarpedia* 4, 1883. doi:10.4249/scholarpedia.1883
- Pisner, D. A., and Schnyer, D. M. (2020). *Support vector machine. Machine Learning*. Amsterdam, Netherlands: Elsevier, 101–121.

- Qu, R., and Xiao, Z. (2022). An attentive multi-modal cnn for brain tumor radiogenomic classification. *Information* 13, 124. doi:10.3390/info13030124
- Redmon, J., Divvala, S., Girshick, R., and Farhadi, A. (2016). "You only look once: Unified, real-time object detection," in Proceedings of the IEEE Conference on Computer Vision and Pattern Recognition, 779–788.
- Rubner, Y., Tomasi, C., and Guibas, L. J. (2000). The Earth mover's distance as a metric for image retrieval. *Int. J. Comput. Vis.* 40, 99–121. doi:10.1023/a:1026543900054
- Sandler, M., Howard, A., Zhu, M., Zhmoginov, A., and Chen, L. C. (2018). "Mobilenetv2: Inverted residuals and linear bottlenecks," in Proceedings of the IEEE Conference on Computer Vision and Pattern Recognition, 4510–4520.
- Sabour, S., Frosst, N., and Hinton, G. E. (2017). Dynamic routing between capsules. *Adv. neural Inf. Process. Syst.* 30.
- Shaheen, F., Verma, B., and Asafuddoula, M. (2016). "Impact of automatic feature extraction in deep learning architecture," in 2016 International conference on digital image computing: techniques and applications (DICTA) (Gold Coast, QLD, Australia: IEEE), 1–8.
- Shi, M., and Zhang, B. (2011). Semi-supervised learning improves gene expression-based prediction of cancer recurrence. *Bioinformatics* 27, 3017–3023. doi:10.1093/bioinformatics/btr502
- Simonyan, K., and Zisserman, A. (2014). Very deep convolutional networks for large-scale image recognition. *arXiv Prepr. arXiv:1409.1556*.
- Singh, D., and Singh, A. K. (2020). Role of image thermography in early breast cancer detection-Past, present and future. *Comput. Methods Programs Biomed.* 183, 105074. doi:10.1016/j.cmpb.2019.105074
- Spanhol, F. A., Oliveira, L. S., Petitjean, C., and Heutte, L. (2016). A dataset for breast cancer histopathological image classification. *IEEE Trans. Biomed. Eng.* 63, 1455–1462. doi:10.1109/TBME.2015.2496264
- Szegedy, C., Liu, W., Jia, Y., Sermanet, P., Reed, S., Anguelov, D., et al. (2015). "Going deeper with convolutions," in Proceedings of the IEEE Conference on Computer Vision and Pattern Recognition, 1–9.
- Van Engelen, J. E., and Hoos, H. H. (2020). A survey on semi-supervised learning. *Mach. Learn.* 109, 373–440. doi:10.1007/s10994-019-05855-6
- Vaswani, A., Shazeer, N., Parmar, N., Uszkoreit, J., Jones, L., Gomez, A. N., et al. (2017). Attention is all you need. *Adv. neural Inf. Process. Syst.* 30.
- Wenger, K., Tirdad, K., Dela Cruz, A., Mari, A., Basheer, M., Kuk, C., et al. (2022). A semi-supervised learning approach for bladder cancer grading. *Mach. Learn. Appl.* 9, 100347. doi:10.1016/j.mlwa.2022.100347
- Xie, Q., Dai, Z., Hovy, E., Luong, T., and Le, Q. (2020). Unsupervised data augmentation for consistency training. *Adv. Neural Inf. Process. Syst.* 33, 6256–6268.
- Yu, G., Sun, K., Xu, C., Shi, X. H., Wu, C., Xie, T., et al. (2021). Accurate recognition of colorectal cancer with semi-supervised deep learning on pathological images. *Nat. Commun.* 12, 6311. doi:10.1038/s41467-021-26643-8
- Zemmal, N., Azizi, N., Dey, N., and Sellami, M. (2016). Adaptive semi supervised support vector machine semi supervised learning with features cooperation for breast cancer classification. *J. Med. Imaging Health Inf.* 6, 53–62. doi:10.1166/jmihi.2016.1591



OPEN ACCESS

EDITED BY

Yuanpeng Zhang,
Nantong University, China

REVIEWED BY

Yimei Du,
Huazhong University of Science and
Technology, China
Changfu Liu,
Sixth Medical Center of PLA General
Hospital, China

*CORRESPONDENCE

Jing Zhang,
Zhang115614@163.com
Ruiyun Peng,
Ruiyunpeng18@126.com

SPECIALTY SECTION

This article was submitted to
Experimental Pharmacology and Drug
Discovery,
a section of the journal
Frontiers in Pharmacology

RECEIVED 28 April 2022

ACCEPTED 28 June 2022

PUBLISHED 22 July 2022

CITATION

Xu X, Yin Y, Li D, Yao B, Zhao L, Wang H,
Wang H, Dong J, Zhang J and Peng R
(2022), Vicious LQT induced by a
combination of factors different from
hERG inhibition.
Front. Pharmacol. 13:930831.
doi: 10.3389/fphar.2022.930831

COPYRIGHT

© 2022 Xu, Yin, Li, Yao, Zhao, Wang,
Wang, Dong, Zhang and Peng. This is an
open-access article distributed under
the terms of the [Creative Commons
Attribution License \(CC BY\)](https://creativecommons.org/licenses/by/4.0/). The use,
distribution or reproduction in other
forums is permitted, provided the
original author(s) and the copyright
owner(s) are credited and that the
original publication in this journal is
cited, in accordance with accepted
academic practice. No use, distribution
or reproduction is permitted which does
not comply with these terms.

Vicious LQT induced by a combination of factors different from hERG inhibition

Xinping Xu, Yue Yin, Dayan Li, Binwei Yao, Li Zhao, Haoyu Wang,
Hui Wang, Ji Dong, Jing Zhang* and Ruiyun Peng*

Beijing Institute of Radiation Medicine, Beijing, China

Clinically, drug-induced torsades de pointes (TdP) are rare events, whereas the reduction of the human ether-à-go-go-related gene (hERG) current is common. In this study, we aimed to explore the specific factors that contribute to the deterioration of hERG inhibition into malignant ventricular arrhythmias. Cisapride, a drug removed from the market because it caused long QT (LQT) syndrome and torsade de pointes (TdP), was used to induce hERG inhibition. The effects of cisapride on the hERG current were evaluated using a whole-cell patch clamp. Based on the dose-response curve of cisapride, models of its effects at different doses (10, 100, and 1,000 nM) on guinea pig heart *in vitro* were established. The effects of cisapride on electrocardiogram (ECG) signals and QT interval changes in the guinea pigs were then comprehensively evaluated by multi-channel electrical mapping and high-resolution fluorescence mapping, and changes in the action potential were simultaneously detected. Cisapride dose-dependently inhibited the hERG current with a half inhibitory concentration (IC₅₀) of 32.63 ± 3.71 nM. The complete hERG suppression by a high dose of cisapride (1,000 nM) prolonged the action potential duration (APD), but not early after depolarizations (EADs) and TdP occurred. With 1 μ M cisapride and lower Mg²⁺/K⁺, the APD exhibited triangulation, dispersion, and instability. VT was induced in two of 12 guinea pig hearts. Furthermore, the combined administration of isoproterenol was not therapeutic and increased susceptibility to ventricular fibrillation (VF) development. hERG inhibition alone led to QT and ERP prolongation and exerted an anti-arrhythmic effect. However, after the combination with low concentrations of magnesium and potassium, the prolonged action potential became unstable, triangular, and dispersed, and VT was easy to induce. The combination of catecholamines shortened the APD, but triangulation and dispersion still existed. At this time, VF was easily induced and sustained.

KEYWORDS

cisapride, QT prolongation, optical mapping, TDP, triangulation, dispersion, instability

Introduction

Drug-induced long QT syndrome (LQT) is generally considered to be proarrhythmic and is often associated with torsade de pointes (TdP) arrhythmias and sudden death (De Bruin et al., 2005; Sanguinetti and Mitcheson, 2005; Hoffmann and Warner, 2006; Vandenberg et al., 2012). Human ether-à-go-go-related gene (hERG) blockade can cause LQT, and many drugs have been identified to pose a risk for arrhythmia because of hERG inhibition and prolongation of the action potential duration (APD) (De Bruin et al., 2005; Sanguinetti and Mitcheson, 2005; Gintant et al., 2006; Dennis et al., 2012). Previous evidence supports this correlation between anti-hERG activity and pro-arrhythmic risk (De Bruin et al., 2005). In fact, many drugs, such as cetirizine, loratadine, and ranolazine (Shenasa et al., 2016) which cause QT and APD prolongation or hERG inhibition, are non-proarrhythmic. Since these typical cases still need case-by-case investigations, it is inaccurate to use QT prolongation and hERG inhibition to determine the pro-arrhythmic risk of drugs (Hondeghem, 2008; Friedman et al., 2021). Meanwhile, hERG inhibition has a beneficial class III anti-arrhythmic effect. Consequently, other factors which differentiate hERG inhibition as benign and vicious should be taken into consideration but not hERG inhibition per se.

Cisapride, a gastrointestinal motility drug, has been removed from the market because of causing LQT and inducing TdP (Wysowski and Bacsanyi, 1996; Drolet et al., 1998; Di Diego et al., 2003a). Clinical evidence suggests that TdP occurs in approximately 1.5% of the patients taking cisapride. Significantly, however, patients who developed arrhythmia events induced by cisapride generally had a history of heart disease (e.g., atrial fibrillation, coronary heart disease, etc.), electrolyte disturbances, renal insufficiency, or long-term use of the drug in combination with other medicines that may cause arrhythmias or prolong QT intervals (Wysowski and Bacsanyi, 1996). Hence, we hypothesized that in normal hearts, QT prolongation induced by hERG inhibition, such as that caused by cisapride alone does not induce TdP and that pathogenic changes in QT or the action potential may occur because of the action of certain other factors.

Taking cisapride as an example, in our present study, we investigated the changes in the action potential, especially changes in the ventricular repolarization, in isolated guinea pig hearts after treatment with cisapride alone or in combination with the action of other factors. The action potential or ventricular repolarization can be described precisely by its APD triangulation, instability, and dispersion. Optical mapping can be applied for the visual detection of changes in the ventricular action potential, which can provide an important evaluation index for the cardiac safety evaluation of drugs (Niu et al., 2021; Wang et al., 2021).

Materials and methods

Experimental animals

Guinea pigs (weighing 200–250 g, male or female) were purchased from SPF (Beijing) Biotechnology Co., Ltd. Each cage contained five of these animals fed normally in an SPF-grade animal facility, with *ad libitum* access to food and water. They were kept at 20–25°C, under good ventilation and a humidity of 50% ± 5%. The ethics approval number of this study is SGLL220305018 (Henan, Henan Province, China).

Drug preparation

Cisapride powder (Sigma, United States) was dissolved in a DMSO solution to prepare a 10 μM stock solution, which was stored at –20°C for 2–4 weeks until use. The working solution was diluted with extracellular or KH solutions with a final DMSO concentration of less than 3%.

Cell culture

In this study, HEK293 cells stably expressing hERG were provided by Henan Scope Research Institute of Electrophysiology. The cells were cultured in a complete medium (DMEM medium plus 10% fetal bovine serum) in an incubator at 37°C and 5% CO₂. After 2–3 days of adherent cell growth, when the cell density reached approximately 90% of the culture flask, the cells were digested with trypsin digestion solution for 1–2 min, gently blown, and centrifuged. Then, 2–3 ml of DMEM complete culture medium was used to disperse the cell precipitate. A volume of 20–50 μl of the mixture was next taken and placed on a sterile slide of a prepared Petri dish. Furthermore, 1 ml of the mixture was placed in the cell incubator for patch-clamp recording.

Patch-clamp testing

The channel current was recorded in HEK293 cells stably expressing the hERG channel protein by the voltage-clamp technique with an Axon 700A patch-clamp amplifier (Molecular Devices, San Jose, CA, United States). The microelectrode was made of borosilicate hard glass blank, and the glass electrode was drawn by a puller. The following extracellular solution component concentrations (mM) in the K⁺ channel were used: NaCl 140, KCl 5.4, MgCl₂ 1, CaCl₂ 2, glucose 10, and HEPES 10, and the pH was adjusted to 7.4 with NaOH. The intracellular solution component concentrations (mM) used were KCl 140, Mg-ATP 4, MgCl₂ 1, EGTA 5, and HEPES 10, and the pH was adjusted to 7.2 with KOH. All

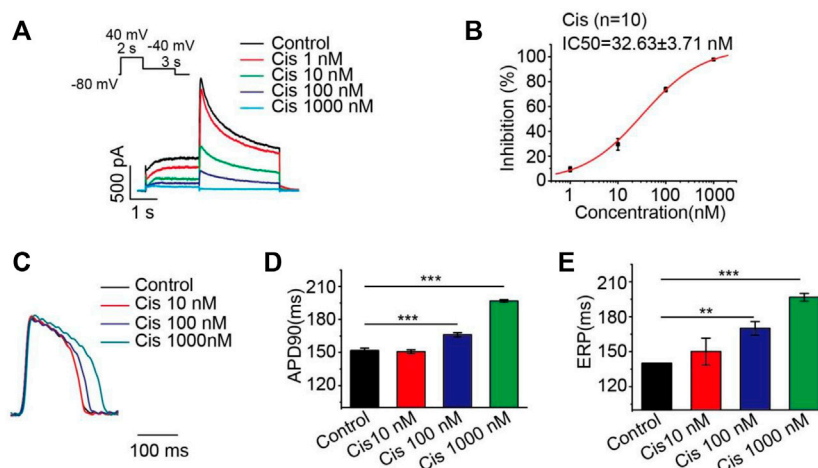


FIGURE 1

Cisapride dose-dependently inhibited the hERG current and increased APD and ERP. (A) Representative diagram of the concentration-dependent inhibition of the hERG channel by cisapride; (B) dose-response curve for the inhibition of the hERG channel by cisapride ($n = 10$); (C) representative graph of cisapride concentration-dependently increase APD; (D) APD and (E) ERP in the absence of different concentrations of cisapride (10, 100, and 1,000 nM) ($n = 8$).

reagents were purchased from Sigma (Budapest, Hungary). The electrode resistance was 2–4 MΩ after filling the electrode solution. In the experiment, the slides pre-plated with cells were placed in a bath, single cells were selected, and a clear field of view was obtained by adjustment. A microelectrode manipulator was used to fill the electrode into the liquid for liquid potential compensation. The electrode was given negative pressure after contacting the cells. After the negative pressure was maintained for several seconds, the electrode tip formed a GΩ sealing connection with the surface of the cell membrane. Then, to compensate for the electrode capacitance, the negative pressure was applied to suck up the cell membrane. The series resistance and cell membrane capacitance were compensated. The electrophysiological recording was further performed at room temperature. The sampling rate was 10 kHz and the rate of Bessel filtering was 6 kHz. The experimental process was controlled by pCLAMP10 software and Axoclamp700A software equipped with an amplifier. The digital-to-analog converter completed the generation of stimulation signals and fed back the acquisition of signals.

Optical mapping

Guinea pigs were intraperitoneally injected with heparin (3125 U/kg) and sacrificed approximately 15 min later (after isoflurane gas anesthesia). Inverted T-shaped thoracotomy was performed, and the heart was placed in a glass Petri dish filled with precooled bench-top solution. Then, the aorta was quickly

found, and the excess tissue was cut off. Next, the aorta was carefully sleeved at the bottom of the cardiac cannula using forceps, tied with surgical sutures, and pre-prepared KH solution in a syringe was gently pushed into the heart to pump out the residual blood of the heart, followed by Langendorff perfusion at a perfusion rate of 8 ml/min and a perfusion temperature of $37 \pm 0.5^\circ\text{C}$. A KH solution was used as the perfusion solution, which contained the following compounds (mM): NaCl 119, KCl 4, CaCl₂ 1.8, MgCl₂ 1, NaH₂PO₄ 1.2, NaHCO₃ 25, and D-Glucose 10. The lower Mg²⁺/K⁺ perfusion solution contained 2 mM KCl and 0.5 mM MgCl₂, with the other components unchanged. The experiment was performed after the heart returned to a normal rhythm and remained stabilized for 15 min. Then, 100 ml of KH solution was added to a circulating perfusion tank, 300 μl of 1 mg/ml Blebbistatin (Abcam, United Kingdom) was added to the dosing port to arrest the heart, and 50 μl of Pluronic F127 (Invitrogen, United States) was added to the circulating perfusion tank for 10 min. Later, 100 μl of 1 mg/ml voltage-sensitive dye RH237 (Santa Cruz Biotechnology, United States) was successively added to the dosing port and circulated for 15 min. The dye-loaded heart was then moved to the imaging perfusion chamber, and a stimulating electrode was inserted at the apex for pacing stimulation. The ECG electrodes were attached to the RA and LV of the heart, respectively. The action potential of normal hearts was recorded using the OMS-PICE-2002 system (MappingLab, United Kingdom) with EMapRecord 5.0 (MappingLab, United Kingdom). Cisapride was then perfused sequentially at 10 nM, 100 nM, and 1,000 nM, and the drug effect was measured 10 min after drug perfusion. Data

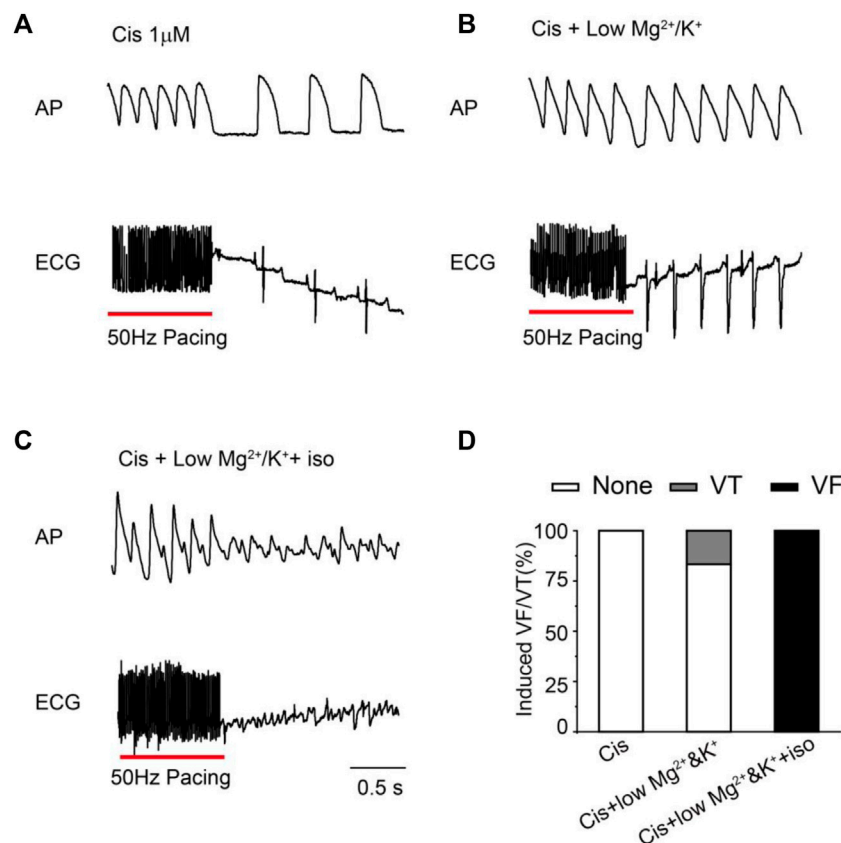


FIGURE 2

Representative traces and statistical graph of induced VF/VT under different conditions. (A) High-frequency stimulation induced VT/VF with 1 μM Cis ($n = 18$); (B) VT/VF was induced by high-frequency stimulation of 1 μM Cis + low Mg²⁺/K⁺ ($n = 12$); (C) high-frequency stimulation induced VT/VF with 1 μM Cis + low Mg²⁺/K⁺ + iso ($n = 7$); (D) statistical chart of VT/VF induction rate under different conditions.

analysis was performed using a commercially available analysis program (EMapScope5.7, MappingLab, United Kingdom). The activation time was presented as an iso-chronogram (Lee, et al., 2012; Liao, et al., 2020).

Statistical analyses

All patch-clamp recorded data were analyzed using Clampfit 10.6 (Molecular Devices, United States), OriginPro 8.0 (Origin Lab, United States), and Adobe Illustrator 10 (Adobe, United States). The concentration-response curve was fitted by the logistic equation $y = A_2 + (A_1 - A_2) / (1 + (x/x_0)^p)$, where x is the drug concentration and p is the Hill coefficient. All data were expressed as means ± SEM. One-way ANOVA, followed by a multiple-comparison test, was used to evaluate multiple test treatments. A value of $p < 0.05$ was considered to indicate statistically significant differences. IC₅₀ denotes the concentration determined for half-maximal inhibitory effects. In the figures, the

designations for the p -values are: * $p < 0.05$, ** $p < 0.01$, and *** $p < 0.001$, respectively.

Results

Dose-dependence of cisapride effect on the hERG current and overall cardiac action potential duration

Many studies have shown that cisapride-induced QT prolongation may be related to the block of potassium current, which prolongs the action potential repolarization in cardiomyocytes (Qian and Guo, 2010; Liang, et al., 2013). In this experiment, HEK293 cells stably expressing the hERG protein were studied, and it was found that cisapride dose-dependently inhibited the hERG current with an IC₅₀ of 32.63 ± 3.71 nM (Figure 1B), and a high dose (1,000 nM) caused 100% inhibition of the hERG current (Figure 1A). Action potentials were recorded at a pacing rate of 4 Hz. In the whole heart, the

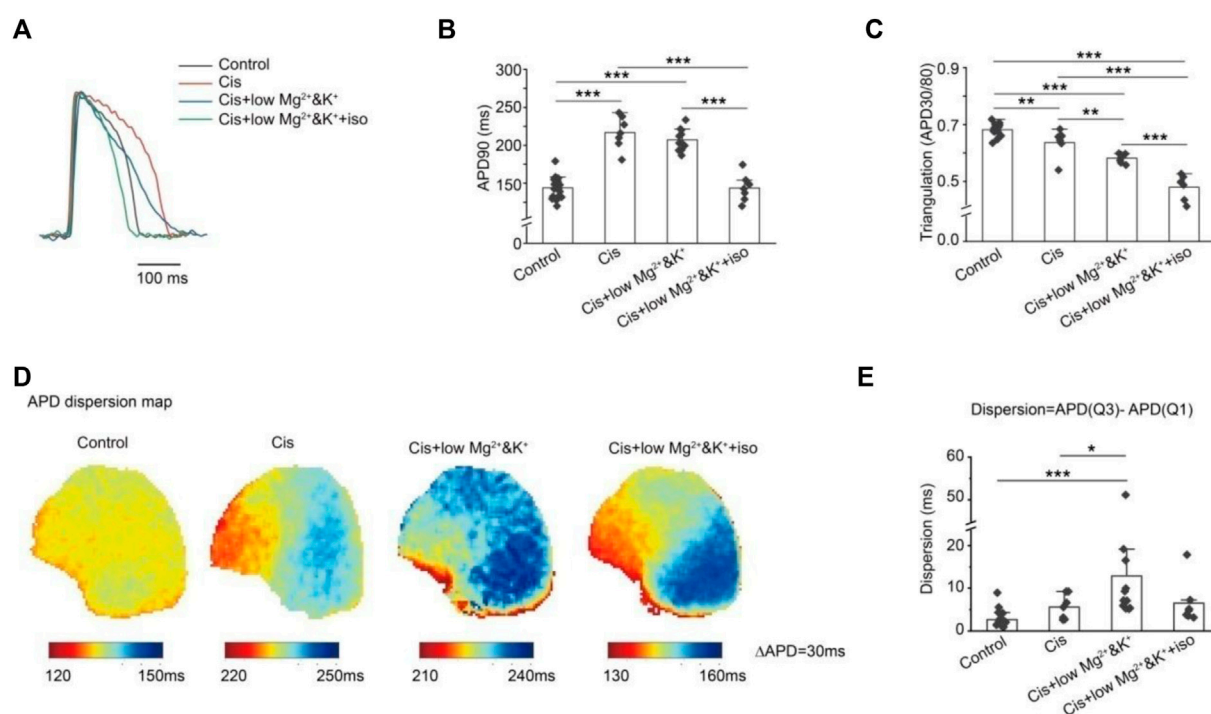


FIGURE 3

Effects of different conditions on AP morphology and dispersion. (A) Effects of different conditions on AP morphology; (B) quantitative statistics of APD prolongation under different conditions; (C) quantitative statistics of AP triangulation under different conditions. The APD30/APD80 ratio was used to quantify the AP triangular morphology under different conditions. A smaller ratio was associated with more significant AP triangular morphology; (D) optical mapping of ventricular AP under different conditions; (E) quantitative statistics of ventricular AP dispersion under different conditions were expressed by APD (Q3)-APD (Q1). We found that under low-magnesium and -potassium conditions, the dispersion of AP was significantly increased by cisapride (* $p < 0.05$; ** $p < 0.01$; and *** $p < 0.001$).

maximum APD prolongation was achieved at 1,000 nM (Figures 1C,D), with no significant difference between 1,000 nM and the increased concentration of 3,000 nM (not displayed). Ventricular effective refractory period (ERP) analysis of the recorded results revealed that cisapride could dose-dependently increase the ERP, similar to APD90 (Figure 1E). However, based on these data alone, it is hard to discriminate whether cisapride has an arrhythmia-inducing effect.

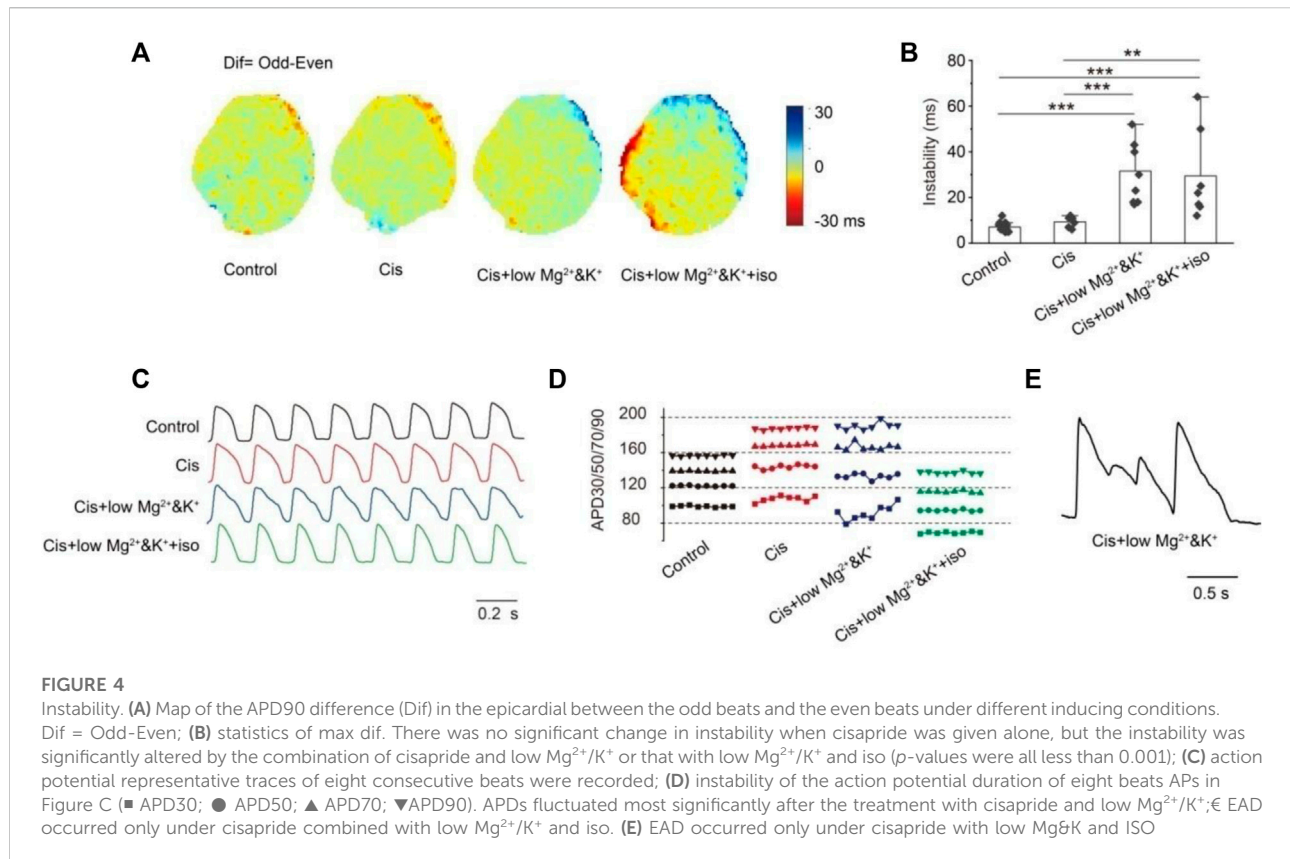
Arrhythmias (EAD/DAD/VT/VF) induced by high-frequency stimulation (50 Hz)

To further investigate the pro-arrhythmic risk of cisapride, we attempted to induce arrhythmias (EAD/DAD/VT/VF) with high-frequency stimulation (50 Hz) under different conditions (cisapride 1 μ M alone, combined with lower Mg²⁺/K⁺ or continued with isoproterenol 0.5 μ M) in Langendorff-perfusion guinea pig hearts. Using 1 μ M cisapride alone hardly induced VT/VF by high-frequency stimulation ($n = 18$, Figure 2A). With the combination of 1 μ M cisapride and lower Mg²⁺/K⁺, 2 of 12 guinea pig hearts induced VT but was not

sustained and was reversible (Figure 2B). Furthermore, VF was observed in 100% of the hearts of the guinea pigs treated with 1 μ M cisapride in combination with lower Mg²⁺/K⁺ and 0.5 μ M isoproterenol. All VFs induced were continuous and irreversible ($n = 7$, Figure 2C). The probability of induced VF/VT was compared under different conditions (Figure 2D). The results showed that using cisapride 1 μ M alone induced no VT/VF, whereas its combination with lower Mg²⁺/K⁺ or continued with 0.5 μ M isoproterenol had different levels of pro-arrhythmic risk.

Triangulation and dispersion changes after cisapride treatment or other factors added

We compared the graphics of the action potentials under different conditions (Figure 3A). The action potential duration was significantly prolonged at 1 μ M cisapride alone or its combination with lower Mg²⁺/K⁺, but it was shortened after isoproterenol was continued (Figure 3B). The APD30/APD80 ratio was used to represent the trend of triangulation. A smaller ratio indicated increased triangulation AP morphology. We found that the triangulation was more



significant when 1 μM cisapride was given or combined with lower Mg^{2+}/K^{+} or the combination was continued with isoproterenol (Figure 3C). Meanwhile, we compared the APD90 dispersion map of the anterior ventricular wall in Langendorff-perfusion guinea pig hearts (Figure 3D) and conducted a statistical analysis on its dispersion (Q3-Q1). We established that the dispersion of cisapride alone did not increase significantly compared with that in the control group, but the dispersion increased dramatically under the condition of lower Mg^{2+}/K^{+} (Figure 3E). Elevated dispersion might be a major risk of arrhythmias.

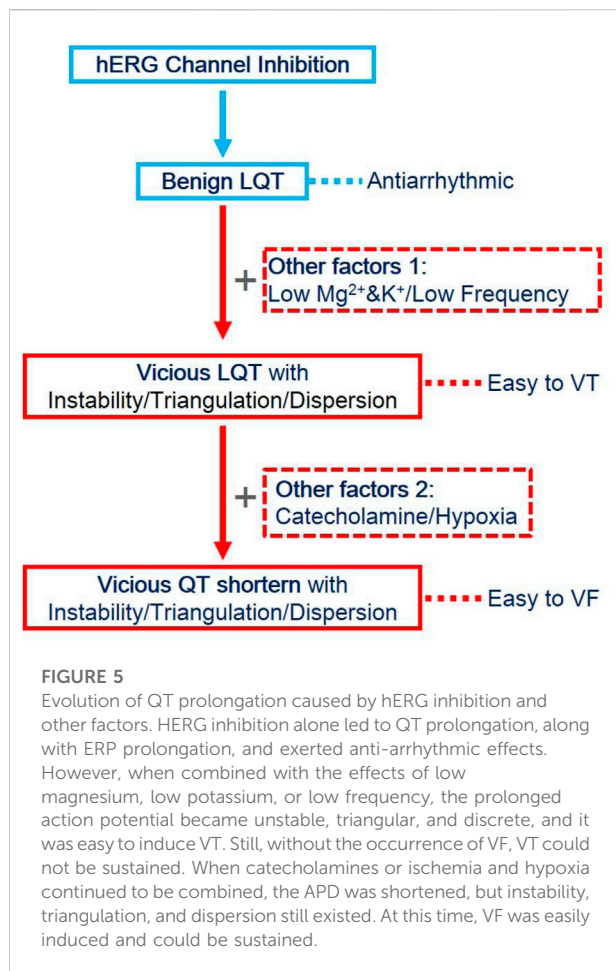
Instability changes after cisapride treatment or other factors added

The instability of consecutive APs provides the substrate for the development of severe arrhythmias. We analyzed the changes in APD instability in the control and in the group with perfusion of 1 μM cisapride alone or combined with lower Mg^{2+}/K^{+} or continued combined with isoproterenol. Figure 4A shows the optical maps of APD90 of the odd and even beats under the four conditions tested. As can be seen, it reflects the differences between different beats directly. In this study, the absolute value of the maximum APD90 difference (Max Δ APD90) between the odd and even

beats (Instability = $|\text{APD90Odd} - \text{APD90Even}|_{\text{Max}}$) was analyzed (Figure 4B). The instability of the APD was similar to that in the control when cisapride was perfused alone (con: 7.12 ± 0.46 ms, $n = 17$ vs. cis: 9.33 ± 0.99 ms, $n = 6$). In the 1 μM cisapride treatment combined with lower Mg^{2+}/K^{+} and continued combined with isoproterenol, the APD instability increased significantly (Cis + low Mg^{2+}/K^{+} : 31.56 ± 4.42 ms, $n = 9$, $p < 0.001$; Cis + low Mg^{2+}/K^{+} + iso: 19.43 ± 7.45 ms, $n = 7$, $p < 0.001$). Figures 4C,D show the morphology of the recorded consecutive APs and corresponding APD30/50/70/90 with 4 Hz stimulation under the four conditions. As can be seen, the treatment with 1 μM cisapride combined with lower Mg^{2+}/K^{+} led to greater instability. In addition, during the experiment, we found that the spontaneous heart rhythm slowed down, and EAD occasionally occurred when cisapride was combined with lower Mg^{2+}/K^{+} (Figure 4E).

Discussion

In the present study, we established the relationship between hERG channel inhibition alone or combined with other factors. Cisapride dose-dependently prolonged QT/APD and increased the ERP by the inhibition of the hERG channel. Increased ERP is described as a dominant mechanism of the anti-arrhythmic effect (Hondeghem et al., 2001). When the hERG current was thoroughly



inhibited by 1 μM cisapride alone, no EAD/DAD/VT/VF occurred spontaneously or was induced. If LQT exists, ERP begins to increase without instability/triangulation/dispersion and it is less likely to induce arrhythmia, but when LQT exists combined with other factors, such as lower $\text{Mg}^{2+}/\text{K}^{+}$ and low heart rate, it might be to induce arrhythmia and tend to be EAD and VT. Although choosing catecholamine as one of the medicines based on the LQT, the APD was shortened, instability, triangulation, and increased dispersion still existed, which could easily induce VF and persist (Figure 5).

First of all, researchers found that the addition of the action potential is one of the electrophysiological mechanisms for inducing arrhythmias according to a dose-dependent study of cisapride inhibiting the hERG channel and prolonging QT/APD. When hERG currents were completely inhibited by cisapride 1 μM alone, the AP increased without significant changes in dispersion, and no spontaneous or induced EAD/DAD/VT/VF occurred. But when additional experimental factors such as relatively low levels of $\text{Mg}^{2+}/\text{K}^{+}$ and heart rate were considered during the research, the dispersion increased and it is likely to induce arrhythmia (EAD and VT). Second, presently, isoproterenol is recommended as the preferred drug for the treatment of TdP because it could increase

the basic heart rate and shorten the QT interval. The research showed that when combined with isoproterenol, the APD was shortened and the dispersion was increased, and it was also easy to induce VF and persistent VT. In conclusion, isoproterenol also has a risk of causing cardiac arrhythmias.

In 1996, Wysowski and Bacsanyi (1996) reported that LQT and TdP occurred in 57 patients treated with cisapride. Nevertheless, it should be noted that all these patients had combinations with other risk factors, such as coronary disease, arrhythmia (especially atrial fibrillation), renal insufficiency or renal failure, electrolyte imbalance, and long-term intake of medications associated with the prolongation of QT intervals or arrhythmia. In our study, we also confirmed this view that more attention should be paid to other factors in addition to cisapride itself. Here, only the combination of 1 μM cisapride with other factors (such as low magnesium and potassium levels) induced EAD and VT, with a relatively low induction rate.

Isoproterenol is clinically recommended for TdP therapy because it can increase the basal heart rate and shorten the QT interval (Suarez, et al., 2018). However, the pro-arrhythmic risk of isoproterenol has also recently attracted increasing research attention. Wataru Shimizu et al. explained why isoproterenol makes the occurrence of TdP easier in acquired or inherited LQT1/LQT2. Isoproterenol lengthens the APD of M cells, shortens the APD of epi and endo cells, and increases the transmural repolarization dispersion of the AP of ventricular myocytes (Shimizu and Antzelevitch, 2000). However, after isoproterenol was administered in our experiment, the APD was shortened, and dispersion decreased while the triangulated form of the action potential became more serious and more likely to induce ventricular fibrillation. Meanwhile, the risks associated with shortening QT with isoproterenol may be even greater than those associated with TdP, which is only 15–20% likely to progress to ventricular fibrillation^[22]. The cardiac wavelength (conduction velocity * ERP) is an important concept for the development of arrhythmias. Increased λ could impede re-entry and vice versa. Shortening QT and triangulation might be the major reason for VF development. Therefore, the clinical application of isoproterenol for TdP therapy should be reexamined.

As for indicators of drug cardiac safety, QT prolongation and hERG inhibition may cause false-positive results, which may result in the blind screening of many valuable drugs (Zang, et al., 2012; Lu, et al., 2019). The findings of our present study show that in addition to hERG inhibition and QT prolongation, combined with changes in instability, triangulation, and dispersion may be a more comprehensive method to evaluate drug cardiotoxicity.

Previous results showed that cisapride (200 μM) caused the largest TDR and induced TdP (2 in 6) in dog left ventricular wedges; however, it should be noted that the stimulation frequency BCL = 2000 ms was far below the normal heart rhythm, and such a frequency only can be induced from epicardial (Di Diego, J. M. et al., 2003b). Differently, we did not observe TdP induction at any concentration in the

Langendorff-perfusion whole heart of a guinea pig without the action of other factors. EAD and VT would occur in combination with low magnesium and low potassium, but the probability was low. In our previous experiments, TdP was not induced when E-4031, cisapride, or sotalol were used alone. However, when combined with low magnesium, low potassium, and isoproterenol, VF was easily induced (Shimizu and Antzelevitch, 2000; Di Diego, J. M. et al., 2003b).

Limitations

First, the ion channel expression of guinea pig ventricular myocytes was different from that of humans, so the experiment on guinea pig heart cannot explain the effect on the human myocardium (Guo. et al., 2009; Horvath. et al., 2020). It has been reported that there is no Ito current in guinea pig cardiomyocytes, and the expression level of hERG is lower than that of humans. Second, cisapride slowed conduction at high concentrations, suggesting that it was not only the hERG channel which was affected by cisapride but other ion channels as well. However, according to $\lambda = \text{conduction velocity} \times \text{ERP}$, deceleration of the conduction velocity would lead to a higher heart safety risk. Nevertheless, no EAD/DAD/VT/VF occurred spontaneously or was induced by 1 μM cisapride alone. Third, after the addition of isoproterenol, the signal of the edge was not good because of the incomplete stop motivation. Thus, there was a large SE of instability after the perfusion of isoproterenol.

Data availability statement

The original contributions presented in the study are included in the article/Supplementary Material; further inquiries can be directed to the corresponding author.

Ethics statement

The animal study was reviewed and approved by Scope Research Institute of Electrophysiology. Written informed consent was obtained from the owners for the participation of their animals in this study.

References

- De Bruin, M. L., Pettersson, M., Meyboom, R. H., Hoes, A. W., and &Leufkens, H. G. (2005). Anti-HERG activity and the risk of drug-induced arrhythmias and sudden death. *Eur. Heart J.* 26, 590–597. doi:10.1093/eurheartj/ehi092
- Dennis, A. T., Wang, L., Wan, H., Nassal, D., Deschenes, I., &Ficker, E., et al. (2012). Molecular determinants of pentamidine-induced hERG trafficking inhibition. *Mol. Pharmacol.* 81, 198–209. doi:10.1124/mol.111.075135

Author contributions

XX, RP, and JZ designed the experimental procedure. XX and JZ performed the data acquisition, analysis, and interpretation. XX, YY, and DL conducted the mapping experiment and analysis. JZ, XX, LZ, HaW, HuW, JD, and BY participated in the development of the animal model. XX wrote the manuscript. RP and JZ provided suggestions for this manuscript and RP ensured the necessary laboratory space. All authors contributed substantially to the work described in this manuscript, read the final version of the manuscript, and agreed to publish it.

Funding

This research was financed by the Major Logistics Research Program (AWS17J006) and the Comprehensive Research (JK20211A040601).

Conflict of interest

The authors declare that the research was conducted in the absence of any commercial or financial relationships that could be construed as a potential conflict of interest.

Publisher's note

All claims expressed in this article are solely those of the authors and do not necessarily represent those of their affiliated organizations, or those of the publisher, the editors, and the reviewers. Any product that may be evaluated in this article, or claim that may be made by its manufacturer, is not guaranteed or endorsed by the publisher.

Supplementary material

The Supplementary Material for this article can be found online at: <https://www.frontiersin.org/articles/10.3389/fphar.2022.930831/full#supplementary-material>

- Di Diego, J. M., Belardinelli, L., and Antzelevitch, C. (2003a). Cisapride-induced transmural dispersion of repolarization and torsade de pointes in the canine left ventricular wedge preparation during epicardial stimulation. *Circulation* 108, 1027–1033. doi:10.1161/01.CIR.0000085066.05180.40

- Di Diego, J. M., and Antzelevitch, C. (2003b). Cellular Basis for ST-Segment Changes Observed During Ischemia. *J. Electrocardiol.* 36Suppl, 1–5. doi:10.1016/j.jelectrocard.2003.09.001

- Drolet, B., Khalifa, M., Daleau, P., Hamelin, B. A., and Turgeon, J. (1998). Block of the rapid component of the delayed rectifier potassium current by the prokinetic agent cisapride underlies drug-related lengthening of the QT interval. *Circulation* 97, 204–210. doi:10.1161/01.cir.97.2.204
- Friedman, A., Miles, J., Liebelt, J., Christia, P., Engstrom, K., Thachil, R., et al. (2021). QT dispersion and drug-induced torsade de Pointes. *Cureus* 13, e12895. doi:10.7759/cureus.12895
- Gintant, G. A., Su, Z., Martin, R. L., and Cox, B. F. (2006). Utility of hERG assays as surrogate markers of delayed cardiac repolarization and QT safety. *Toxicol. Pathol.* 34, 81–90. doi:10.1080/01926230500431376
- Guo, L., Dong, Z., and Guthrie, H. (2009). Validation of a Guinea pig Langendorff heart model for assessing potential cardiovascular liability of drug candidates. *J. Pharmacol. Toxicol. Methods* 60, 130–151. doi:10.1016/j.vascn.2009.07.002
- Hoffmann, P., and Warner, B. (2006). Are hERG channel inhibition and QT interval prolongation all there is in drug-induced torsadogenesis? A review of emerging trends. *J. Pharmacol. Toxicol. Methods* 53, 87–105. doi:10.1016/j.vascn.2005.07.003
- Hondeghem, L. M., Carlsson, L., and Duker, G. (2001). Instability and triangulation of the action potential predict serious proarrhythmia, but action potential duration prolongation is anti-arrhythmic. *Circulation* 103, 2004–2013. doi:10.1161/01.cir.103.15.2004
- Hondeghem, L. M. (2008). QT and TdP: QT: An unreliable predictor of proarrhythmia. *Acta Cardiol.* 63, 1–7. doi:10.2143/AC.63.1.2025324
- Horvath, B., Hezso, T., Szentandrássy, N., Kistamas, K., Arpadffy-Lovas, T., Varga, R., et al. (2020). Late sodium current in human, canine and Guinea pig ventricular myocardium. *J. Mol. Cell. Cardiol.* 139, 14–23. doi:10.1016/j.yjmcc.2019.12.015
- Lee, P., Taghavi, F., Yan, P., Ewart, P., Ashley, E. A., Loew, L. M., et al. (2012). *In situ* optical mapping of voltage and calcium in the heart. *PLoS One* 7, e42562. doi:10.1371/journal.pone.0042562
- Liang, P., Lan, F., Lee, A. S., Gong, T., Sanchez-Freire, V., Wang, Y., et al. (2013). Drug screening using a library of human-induced pluripotent stem cell-derived cardiomyocytes reveals disease-specific patterns of cardiotoxicity. *Circulation* 127, 1677–1691. doi:10.1161/CIRCULATIONAHA.113.001883
- Liao, J., Wu, Q., Qian, C., Zhao, N., Zhao, Z., Lu, K., et al. (2020). TRPV4 blockade suppresses atrial fibrillation in sterile pericarditis rats. *JCI Insight* 5, 137528. doi:10.1172/jci.insight.137528
- Lu, H. R., Zeng, H., Kettenhofen, R., Guo, L., Kopljár, I., van Ammel, K., et al. (2019). Assessing drug-induced long QT and proarrhythmic risk using human stem-cell-derived cardiomyocytes in a Ca²⁺ imaging assay: Evaluation of 28 CiPA compounds at three test sites. *Toxicol. Sci.* 170, 345–356. doi:10.1093/toxsci/kfz102
- Niu, H. L., Liu, Y. N., Xue, D. Q., Dong, L. Y., Liu, H. J., Wang, J., et al. (2021). Inhibition of Nav1.7 channel by a novel blocker QLS-81 for alleviation of neuropathic pain. *Acta Pharmacol. Sin.* 42, 1235–1247. doi:10.1038/s41401-021-00682-9
- Qian, J. Y., and Guo, L. (2010). Altered cytosolic Ca²⁺ dynamics in cultured Guinea pig cardiomyocytes as an *in vitro* model to identify potential cardiotoxicants. *Toxicol. Vitro* 24, 960–972. doi:10.1016/j.tiv.2009.12.027
- Sanguinetti, M. C., and Mitcheson, J. S. (2005). Predicting drug-hERG channel interactions that cause acquired long QT syndrome. *Trends Pharmacol. Sci.* 26, 119–124. doi:10.1016/j.tips.2005.01.003
- Shenasa, M., Assadi, H., Heidary, S., and Shenasa, H. (2016). Ranolazine: Electrophysiologic effect, efficacy, and safety in patients with cardiac arrhythmias. *Card. Electrophysiol. Clin.* 8, 467–479. doi:10.1016/j.ccep.2016.02.011
- Shimizu, W., and Antzelevitch, C. (2000). Differential effects of beta-adrenergic agonists and antagonists in LQT1, LQT2 and LQT3 models of the long QT syndrome. *J. Am. Coll. Cardiol.* 35, 778–786. doi:10.1016/s0735-1097(99)00582-3
- Suarez, K., Mack, R., Hardegree, E. L., Chiles, C., Banchs, J. E., Gonzalez, M. D., et al. (2018). Isoproterenol suppresses recurrent torsades de pointes in a patient with long QT syndrome type 2. *Hear. Case Rep.* 4, 576–579. doi:10.1016/j.hrcr.2018.08.013
- Vandenberg, J. I., Perry, M. D., Perrin, M. J., Mann, S. A., Ke, Y., Hill, A. P., et al. (2012). hERG K(+) channels: Structure, function, and clinical significance. *Physiol. Rev.* 92, 1393–1478. doi:10.1152/physrev.00036.2011
- Wang, G., Lu, C. J., Trafford, A. W., Tian, X., Flores, H. M., Maj, P., et al. (2021). Electrophysiological and proarrhythmic effects of hydroxychloroquine challenge in Guinea-pig hearts. *ACS Pharmacol. Transl. Sci.* 4, 1639–1653. doi:10.1021/acspsci.1c00166
- Wysowski, D. K., and Bacsanyi, J. (1996). Cisapride and fatal arrhythmia. *N. Engl. J. Med.* 335, 290–291. doi:10.1056/NEJM199607253350416
- Zang, J., Wu, S., Tang, L., Xu, X., Bai, J., Ding, C., et al. (2012). Incidence and risk of QTc interval prolongation among cancer patients treated with vandetanib: A systematic review and meta-analysis. *PLoS One* 7, e30353. doi:10.1371/journal.pone.0030353



OPEN ACCESS

EDITED BY

Khin Wee Lai,
University of Malaya, Malaysia

REVIEWED BY

Md. Solaiman Mia,
Green University of Bangladesh,
Bangladesh
Fa Zhu,
Nanjing Forestry University, China

*CORRESPONDENCE

Saleem Sanatan Kujur,
salim.kujur@gmail.com

SPECIALTY SECTION

This article was submitted to
Experimental Pharmacology and Drug
Discovery,
a section of the journal
Frontiers in Pharmacology

RECEIVED 21 May 2022

ACCEPTED 27 June 2022

PUBLISHED 05 August 2022

CITATION

Kujur SS and Sahana SK (2022), Medical
image registration utilizing tissue
P systems.
Front. Pharmacol. 13:949872.
doi: 10.3389/fphar.2022.949872

COPYRIGHT

© 2022 Kujur and Sahana. This is an
open-access article distributed under
the terms of the [Creative Commons
Attribution License \(CC BY\)](#). The use,
distribution or reproduction in other
forums is permitted, provided the
original author(s) and the copyright
owner(s) are credited and that the
original publication in this journal is
cited, in accordance with accepted
academic practice. No use, distribution
or reproduction is permitted which does
not comply with these terms.

Medical image registration utilizing tissue P systems

Saleem Sanatan Kujur* and Sudip Kumar Sahana

Department of Computer Science and Engineering, Birla Institute of Technology Mesra, Ranchi, India

The tissue P system (TPS) possesses intrinsic attributes of parallel execution in comprehensive data and instruction space, which provides fast convergence during the transition from local to global optima. Method- In this study, we have proposed and built a TPSysIR framework using the TPS for image registration that optimizes upon the mutual information (MI) similarity metric to find a global solution. Result- The model was tested on single- and multimodal brain MRI scans and other prominent optimization-based image registration techniques. Conclusion- Results show that, among all methods, TPSysIR provides better MI values with minimum deviation in a range of experiment setups conducted iteratively.

KEYWORDS

P systems, MRI, TPS, optimization, medical image registration

Introduction

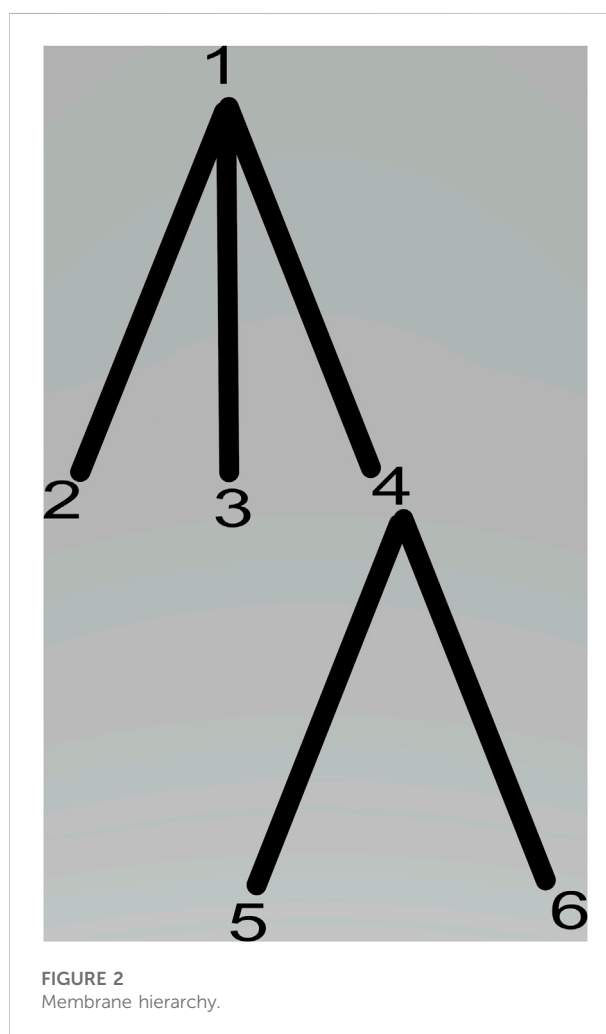
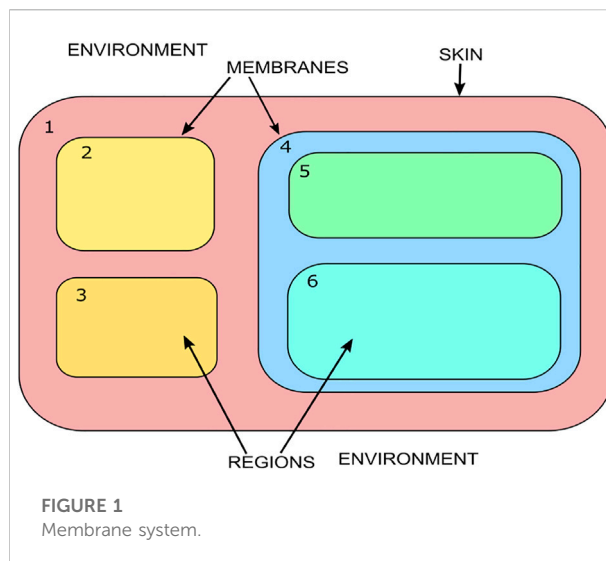
Medical image registration involves processing image data from multiple sources, each having a different coordinate system. These sources often have different sensors and viewpoints, transforming the data collected into a single spatial coordinate system. Image registration requires optimized parameter values for the required transformation, translation, or rotation to be applied over the source images with respect to the reference image to achieve matching. Image registration has been utilized in many recent advances in image reconstruction (Prakash et al., 2019), land cover mapping (Wang et al., 2020), and weather prediction (Kakimoto et al., 2019). A large number of image registration methods are already available, which can be classified as single or multimodal, automatic vs. inter-active, spatial domain vs. frequency domain-based, intensity vs. feature-based, and transform-based. Image registration finds essential applicability in the areas of remote sensing and medical image processing. Image registration can be viewed as an optimization problem (Song et al., 2017) whose aim is to maximize the similarity or minimize the cost in the process. It takes single or multiple image data and transforms them according to the parameters to maximize the similarity to the target reference image. Various parameters which can be optimized are correlation ratio (Gong et al., 2019), mutual information (Ramamoorthy et al., 2010), energy of joint probability distribution (Susskind et al., 2011), normalized correlation (Lewis, 2001), and normalized mutual information (Knops et al., 2005).

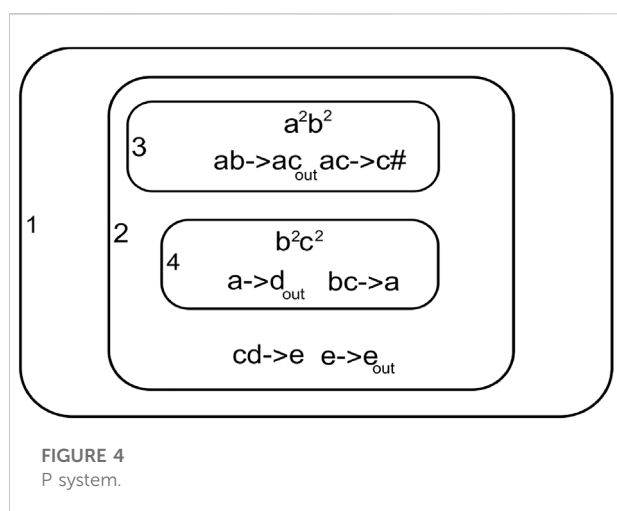
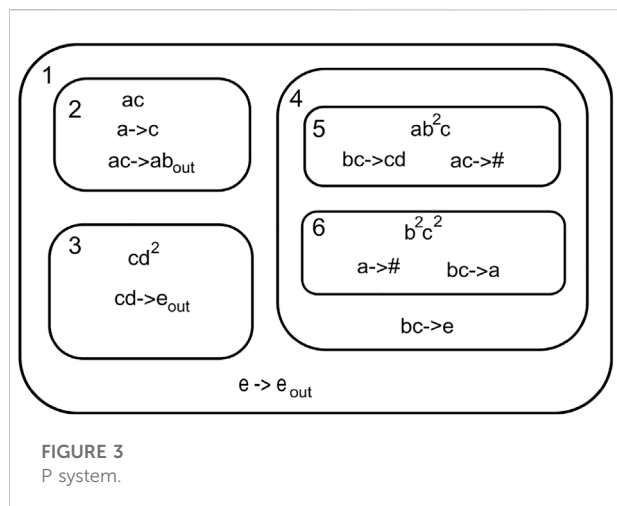
Optimization methods such as Powell's were among the earliest attempts to solve image registration problems. However, the algorithm provided local optimum results, and the objective search speed was also low. These shortcomings lead to the utilization of

nature-based optimization techniques for image registration as the next-generation solution. The genetic algorithm (GA)-based method has been proposed by Rouet, Jacq, and Roux (Rouet et al., 2000). Utilizing the local optima, LI Zuo-zhu (Zuo-zhu, 2007) applied GA on mutual information (MI) metric optimization to achieve an image registration solution. Rajapakse and Guojun (Rajapakse and Guojun, 1999) performed image registration by utilizing GA on time-series images. Still, the nonexistence of fine-tuning ability coupled with considerable execution time led researchers to explore better methods. Chen, Lin, and Mimori (Lin et al., 2012) utilized particle swarm optimization (PSO) on the image dataset, optimizing the MI measure. Wachowiak et al. (Wachowiak et al., 2004), Chel, and Nandi (Chel and Nandi, 2013) used hybrid PSO on 3-D medical images; similarly optimization was performed on normalized MI decreasing the overall execution time. Basset et al. (Abdel-Basset et al., 2017) utilized modified MI metric and PSO for image registration. This method fell into local maxima with increasing degrees of rotation. Zhang et al. (Zhang et al., 2010) integrated PSO with Powell to overcome these shortcomings and applied them to image registration.

In recent years, machine learning (Zhu et al., 2022) and deep learning (Zhu et al., 2021) have found applications in image processing and registration. Balakrishna et al. (Balakrishnan et al., 2019) used a convolutional neural network for 3D image registration. Ali and Rittscher (Ali and Rittscher, 2019) utilized concatenated convolutional layers for deformable image registration. Mansilla, Milone, and Ferrante (Mansilla et al., 2020) proposed the AC-RegNet architecture to achieve image registration.

Membrane computing (MC) (Paun, 2000) was introduced by Gheorghe Paun, inspired by the computational mechanisms of living cells or tissue systems. Biological and computational processes at the cellular and tissue level are performed in a maximally parallel and randomly distributed manner. These random processes and communications are triggered when appropriate compounds and catalyst inhibitors are present in the cellular environment. Membrane computing forms the computational model called P systems; these have been efficiently utilized to obtain solutions to many NP-complete (Paun, 2001) problems by creating a trade-off between time and space complexity. P systems are built upon low-level biological interactions or processes by equipping them to capture the computational essence of complex cell metabolism and information interchange. The P system may use any one of the following mechanism or mechanisms to create variants of the system: selective object recognition, controlled exchange of particles through protein channels, cytoplasmic metabolism or division, and dissolution of membranes. The P system has been proved computationally complete and is utilized to solve many optimization-based and NP-complete problems (Paun, 2001), such as subset sum (Jiménez and Núñez, 2005), TSP, and tricolor problems. Computation in a P system proceeds in a maximally

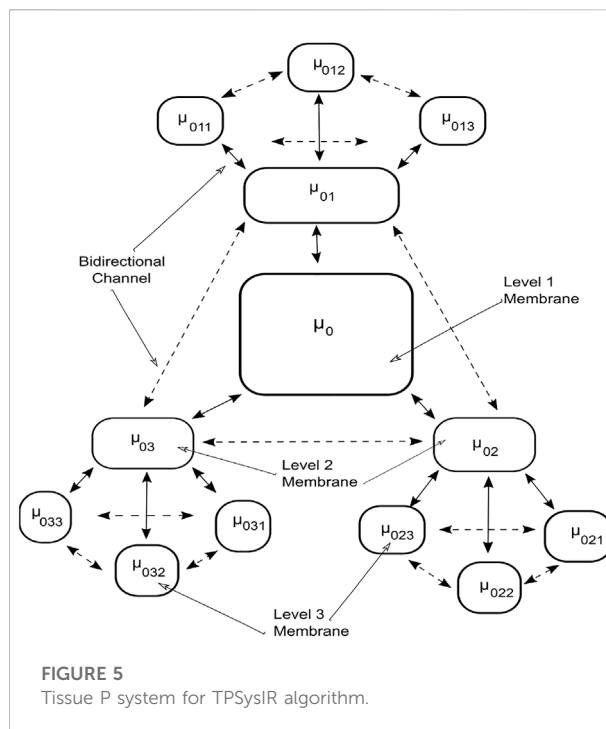




parallel and non-deterministic path, which can be tuned according to the execution model of the problem.

Membrane system

The membrane system shown in Figure 1 can be viewed as a hierarchically organized set of membranes existing inside an outer space called the environment. The tree in Figure 2 can represent the hierarchical organization of a membrane system in Figure 1. The tree's root is associated with the skin membrane, and the leaves are associated with the elementary membranes. The membranes at the same level can float around in the same membrane compartment. The hierarchical string expression 1) is written for Figure 2 membrane structure:



$$[1[2]2[3]3[4]5]5[6]6]4]1. \quad (1)$$

P systems

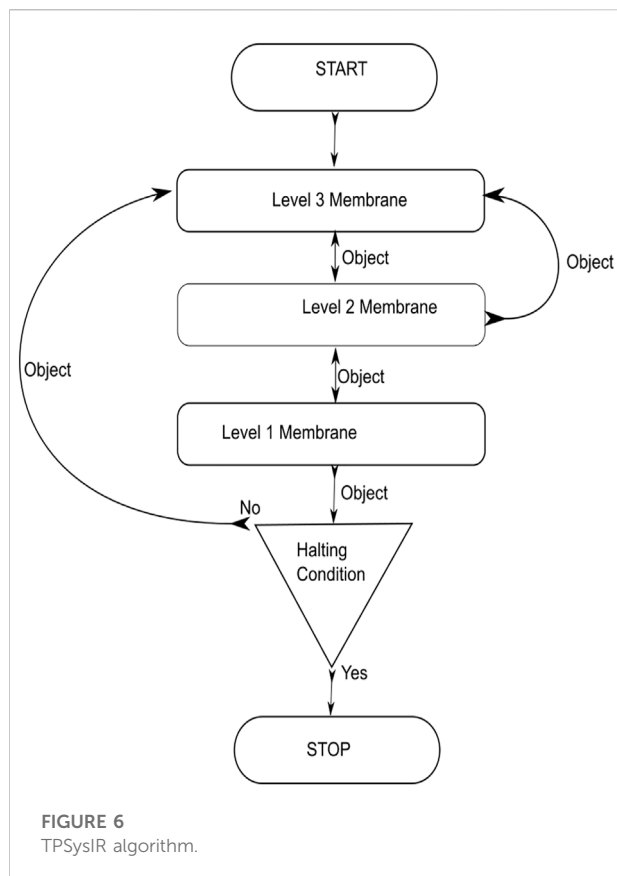
The operations of a P System can be visualized as an extended distributed computation machine that presents a range of solutions to a particular problem. The nature of the multiset solution present in the output environment or membrane varies, based on the halting condition associated with the problem. The distribution and transition of multisets in the membrane regions determine the generated languages and their related grammar. Formally a P system Π can be defined as

$$\Pi = (O, M, m_1, m_2, \dots, m_n, R_1, R_2, \dots, R_n, \delta_0). \quad (2)$$

Here, O is the finite set of objects. M is the set of membranes. m_i is the multiset of objects in the membrane. R_i is the rule inside the corresponding membrane. δ_0 is the set of output membrane.

A P System can be viewed as a hierarchical system comprising of a three-dimensional space referred environment containing membranes. The membranes contain a set of objects called multiset, coexisting with rules and other membranes. Figure 3 shows a P System.

The P System can be formally written as



$$\Pi = (\{a, b, c, d, e\}, \{1, 2, 3, 4, 5, 6\}, \{ac, cd^2, ab^2c, b^2c^2\}, \{e \rightarrow e_{out}, \{ac \rightarrow ab, a \rightarrow b_{out}, \{cd \rightarrow e_{out}, \{bc \rightarrow e_{out}, \{bc \rightarrow cd, ac \rightarrow \#, \{bc \rightarrow e_{out}, \{bc \rightarrow a, a \rightarrow \#\}, \{1\}\} \}. \quad (3)$$

Here, $O = \{a, b, c, d, e\}$, $M = \{1, 2, 3, 4, 5, 6\}$, and $m_i = \{ac, cd^2, ab^2c, b^2c^2\}$. $R_i = \{e \rightarrow e_{out}, \{ac \rightarrow ab, a \rightarrow b_{out}, \{cd \rightarrow e_{out}, \{bc \rightarrow e_{out}, \{bc \rightarrow cd, ac \rightarrow \#, \{bc \rightarrow a, a \rightarrow \#\}\}$. The rules in the membranes are represented as $x \rightarrow y$ or $x \rightarrow y\#$, with $x \in O^+$ and $y \in (O \times Tar)^*$, where $Tar = \{here; in; out\}$. Many forms of multiset rewriting and communicating rules have been utilized to convey more information about the state. There are mainly two types of rules: evolution and communication rules. The evolution rules govern the evolution of the membrane state, and communication rules facilitate communication, i.e., data transportation from one membrane to another. Evolution rules are of the form $l \rightarrow m$ or $l \rightarrow \#$; here, the occurrence of the $\#$ symbol leads to the dissolution of the membrane wherever the rule is executed, and all multisets currently existing inside it are passed onto its parent membrane. Communication rules are of form $w \rightarrow x_{out}y_{in}$; here the multiset w forms two multisets, x and y ; here, x moves

outside the membrane to the parent whereas y moves to the child existing inside the current membrane.

Computation process in a P system

Computation in a P system is performed in a non-deterministic and maximally parallel manner. The configuration changes from an initial state to the next state in an asynchronous manner, referred to as the transition of a P system. The computation is thus the continuous transition of the P system by applying the rules in a non-deterministic and maximally parallel manner until the system halts. The halting condition is achieved when no further rules can be applied and the output is obtained as the contents of the output membrane. A non-deterministic manner ensures that the rules are chosen at random. This randomness may lead to different transition paths. The order of application of rules is also an important aspect. Maximally parallel application of rules ensures that all possible rules are executed simultaneously in every transition step of the computation. The rules rewrite the multiset content inside a membrane. The execution of $u \rightarrow v$ rules is dependent mainly on the availability of the multiset composing the left side of the membrane u , which transforms into the right side multiset v .

Figure 4 shows a simple P System with four membranes 1, 2, 3, and 4. Membrane one is the outermost membrane that holds the output on halting. The system can transit through multiple process paths due to the non-deterministic nature of the computation.

Example steps of computation

- Step 1: Observing the initial configuration in membranes three and four Figure 4

$m_3, R_3 = \{a^2b^2\}, \{ab \rightarrow ac, ac \rightarrow c\# \}$ ab is assigned to rule $ab \rightarrow ac$
 $m_4, R_4 = \{b^2c^2\}, \{bc \rightarrow a, a \rightarrow d_{out}\}$ bc is assigned to rule $bc \rightarrow a$.

- Step 2: After transition in step 1 we have

$m_3, R_3 = \{a^2c^2\}, \{ac \rightarrow c\# \}$ ac is assigned to rule $ac \rightarrow c\#$ $\#$ dissolves membrane three and multiset ac^2 moves into membrane two

$m_4, R_4 = \{a^2\}, \{a \rightarrow d_{out}\}$ a is assigned to rule $a \rightarrow d_{out}$ d^2 is passed out of membrane four and no more transitions can happen in it.

- Step 3: After step 2 we have the membrane possible for transition

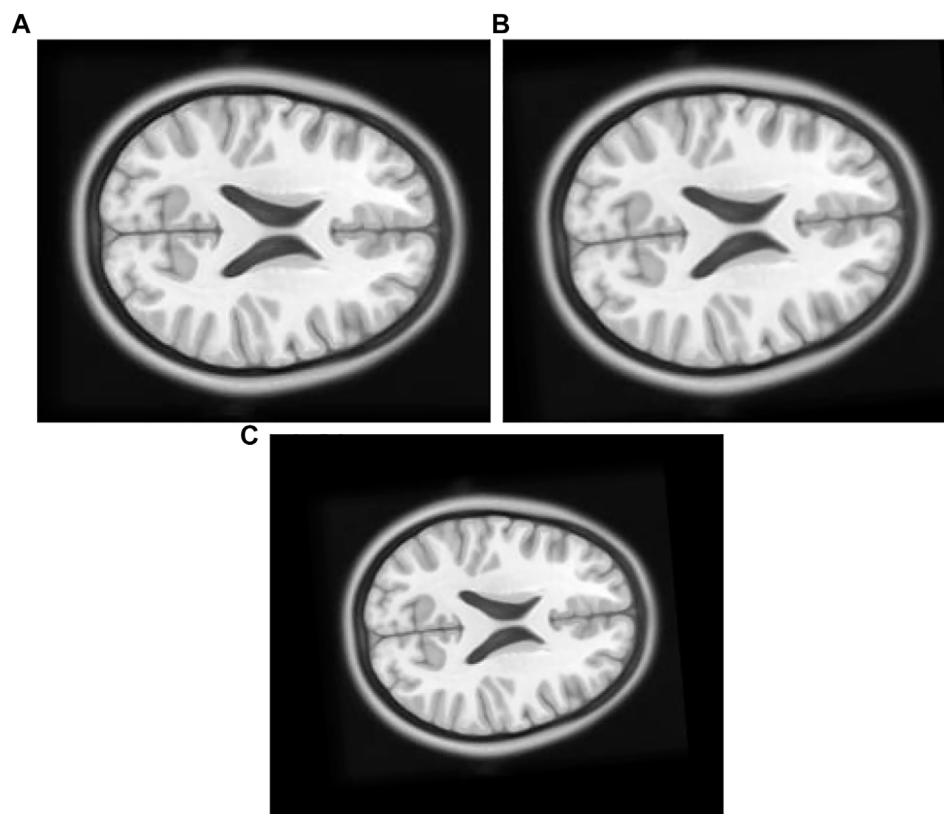


FIGURE 7

(A) Original Image: row first left. (B) Float Image Unscaled: row first right. (C) Float Image Scaled: second row center.

$m_2, R_2 = \{ac^2d^2\}, \{cd \rightarrow e, e \rightarrow e_{out}\}$ cd is assigned to rule $cd \rightarrow e$.

- Step 4: After step 3 membrane two new state

$m_2, R_2 = \{ae^2\}, \{e \rightarrow e_{out}\}$ e is assigned by $e \rightarrow e_{out}$ e^2 is passed out to membrane one.

- membrane one is the output membrane so the computation halts here

$m_1, R_1 = \{e^2\}$

The computation halts since no more rules can be executed.

Mutual Information

Mutual information measures the statistical dependency between two sets of data (here the image data sets) independent of the intensity values of images. The MI value between two images or voxels is maximum when the geometrical

alignment between them is good. MI measures two sets of image data, A and B, obtained as follows:

$$MI(A, B) = \sum_{a,b} Prob(a, b) \log \frac{Prob(a, b)}{Prob(a)Prob(b)}. \quad (4)$$

Here, $Prob(a, b)$ is the joint probability of $a \in A$ and $b \in B$. $Prob(a)$ and $Prob(b)$ are the independent probabilities.

Methods

Tissue P system

Tissue P system (Pan and Perez-Jim'enez, 2010) can be viewed as the graph of P system membranes connected with bidirectional protein channels (Freund et al., 2005). The protein channels facilitate the communication (transportation) of multisets of objects between the membranes. The communication can be performed in a replicative manner where a copy of the multiset can be sent to all adjacent membranes attached to the communication channel (protein

channel) or in a non-replicative manner where only one copy of the membrane is communicated to a particular membrane. Mathematically, the tissue P system (Bernardini and Gheorghe, 2005) of degree (number of membranes) n can be defined as

$$\Gamma = (O, \mu_1, \mu_2, \dots, \mu_n, comm, \mu_{out}). \quad (5)$$

Here,

1. O is a finite set of objects (alphabets)
2. $comm \subseteq \{1, 2, 3, \dots, n\} \times \{1, 2, 3, \dots, n\}$
3. $\mu_{out} = \{\mu_1, \mu_2, \dots, \mu_n\}$ is the output membrane
4. $\{\mu_1, \mu_2, \dots, \mu_n\}$ are the membranes of form $\mu_1 = \{s_{i,0}, mul_{i,0}, Rule_i\}$
 - (a) $s_{i,0}$ is initial state of i^{th} membrane
 - (b) $mul_{i,0}$ multiset of i^{th} membrane
 - (c) $Rule_i$ set of rules in i^{th} membrane

The tissue P system in Figure 5 is organized in the form of a multilevel membrane structure, with levels one and two having three membranes as child membranes. The output membrane or level 1 membrane is labeled using μ_0 . It contains three child membranes labeled by μ_{01} , μ_{02} , and μ_{03} respectively; these form level two in the system. The level two membranes further contain three child membranes each. Child membranes are labelled as μ_{ab} where a is the parent node and b is the child membrane. The system is interconnected with a bidirectional transportation channel that facilitates the transportation or communication of objects between the membranes. Each membrane contains multisets of objects along with the rules governing the evolution and communication of objects. The algorithm searches for the optimal solution among the floating image objects configured with the transform parameters inside the membranes. The objects in the solution space continuously evolve by utilizing the rules and are examined for the existence of a better optimized solution.

The objects

The object in the solution space can be represented as the set of transformation parameters:

$$Obj_{rs} = x_{rs}, y_{rs}, \theta_{rs}, Z_{rs}. \quad (6)$$

1. $r = 1 \dots n$ and $s = 1 \dots m$
2. n is the membrane count of tissue P system
3. m is the object count in membrane r
4. θ_{rs} is the degree of rotation
5. Z_{rs} is the image scaling factor
6. x_{rs} is the displacement in x axis
7. y_{rs} is the displacement in y axis

The algorithm utilizes the MI metric as the optimization function to measure and maximize the similarity of the parameters in the evolved objects. The object evolves inside the membranes, and the local best is selected for each level 3 membrane. This local best value is communicated to the neighboring membrane and level 2 membranes through the bidirectional channel. The level 2 membranes communicate between themselves and their children to search for the global best solution. This solution is then transferred to the level 1 output membrane, thus representing the final solution.

The evolution rules

The evolution rules govern the evolution of float image object configurations inside the membrane; the evolution is performed so as to achieve the optimal best object according to the optimization criteria. Each level 3 membrane contains three optimal objects; $Obj_{ab}^{t,best}$, the local optimal best object obtained at the t^{th} moment inside the ab^{th} membrane, $Obj_{ab,n}^{t,best}$, one of the optimal best object randomly selected among all the optimal objects received from the neighbors to the ab^{th} membrane, and $Obj_{ab,u}^{t,best}$, the optimal best object transferred from the parent level 2 membrane u to ab^{th} child membrane.

The PSO (particle swarm optimization) technique is utilized here to govern the formation and execution of $rule_1$ and $rule_2$, and its velocity position equation is modified to define the evolution rules. These rules evolve the objects according to the position (configuration) and time.

$$v_{k,ab}^{t+1} = \omega^t v_{k,ab}^t + l_0 z_0 (Obj_{ab}^{t,best} - Obj_{k,ab}^t) + l_1 z_1 (Obj_{ab,n}^{t,best} - Obj_{k,ab}^t) + l_2 z_2 (Obj_{ab,u}^{t,best} - Obj_{k,ab}^t), \quad (7)$$

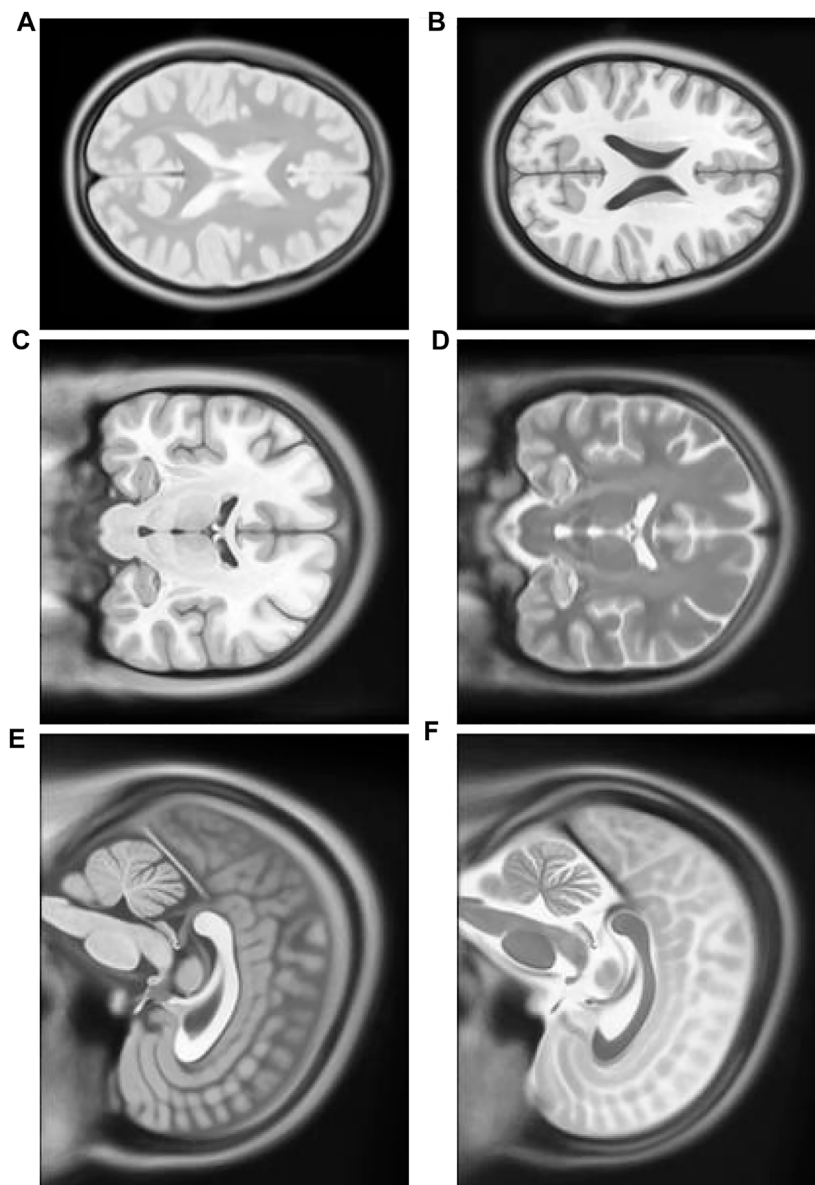
$$Obj_{k,ab}^{t+1} = Obj_{k,ab}^t + v_{k,ab}^{t+1}, \quad (8)$$

$$rule_1 \equiv [Obj_{k,ab}^t]_{ab}^t \leftrightarrow [Obj_{k,ab}^{t+1}]_{ab}^{t+1}, \quad (9)$$

$$Obj_{ab}^{t+2,best} = \max\{\{MI(Obj_{k,ab}^{t+1})\} \cup MI(Obj_{ab}^{t,best})\}, \quad (10)$$

$$rule_2 \equiv [Obj_{ab}^{t,best}]_{ab}^{t+1} \leftrightarrow [Obj_{ab}^{t+2,best}]_{ab}^{t+2}. \quad (11)$$

The velocity component is updated using (7) ω^t is the weight balancing factor which gradually decreases; l_0, l_1 , and l_2 are the learning factor; z_0, z_1 , and z_2 are the random numbers between 0 and 1. $Obj_{k,ab}^t$ is the k^{th} float object in ab^{th} membrane having a configuration of the floating image. This is updated by $rule_1$ in Eqs. 8, 9. This updates the new configuration of each object inside the membrane. The local best object of the membrane is selected by utilizing Eq 10, and the old one is replaced by the new local best utilizing $rule_2$ at Eq 11.

**FIGURE 8**

(A) Multimodal Experiment 1 T2: row first left. (B) Multimodal Experiment 1 T1: row first right. (C) Multimodal Experiment 2 T1: row second left. (D) Multimodal Experiment 1 T2: row second right. (E) Multimodal Experiment 3 T1: row third left. (F) Multimodal Experiment 1 T2: row third right.

The communication rules

The communication (Paun and Paun, 2002) rules facilitate the transportation of objects between the membranes at inter- or intra-level utilizing the bidirectional channel connecting them.

Intra-level object communication rule

The local optimal object $Obj_{ab}^{t,best}$ is updated during the evolution stage inside each membrane at level 3. These objects are further communicated to every neighboring

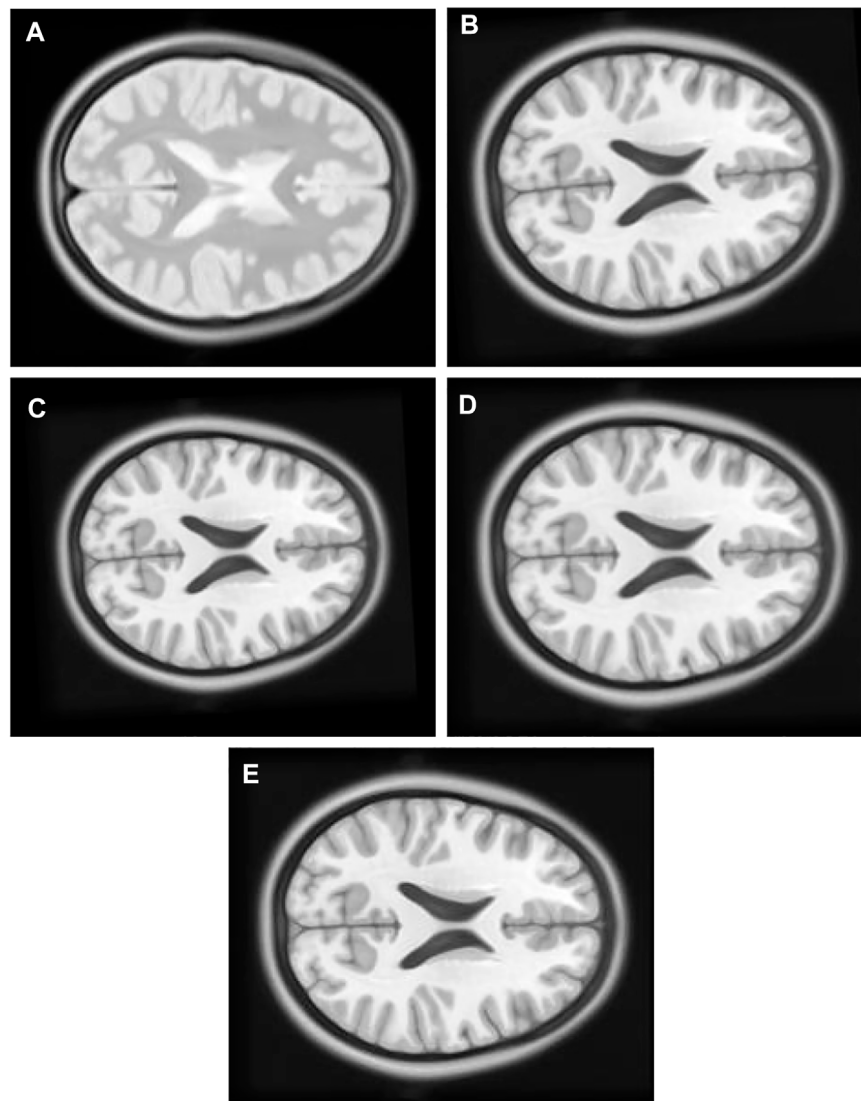


FIGURE 9

(A) Multi Modal Experiment 1 Float: row first left. (B) Multi Modal Experiment 1 GA output: row first right. (C) Multi Modal Experiment 1 PSO output: row second left. (D) Multi Modal Experiment 1 PSO and Powell Output: row second right. (E) Multi Modal Experiment 1 TPSysIR Output: row third center.

membrane under the shared parent membrane. This process involves the creation of a duplicate copy of the local optimal object $Obj_{ab}^{t,best}$ in each membrane, exchanging it with every other membrane under the common parent. The intracommunication rule is described as follows:

$$rule_3 \equiv [Obj_{aj}^{t,best}]_{ai}^t \leftrightarrow [Obj_{ai}^{t,best}]_{aj}^t. \quad (12)$$

In Eq 12 $rule_3$ the objects $Obj_{aj}^{t,best}$ and $Obj_{ai}^{t,best}$ are the local optimal bests in membranes aj and ai , respectively. Both are located at level 3 under the same parent membrane. The objects are exchanged and $rule_3$ is executed in Eq 12.

Inter-level object communication rule

The copy of the local optimal object $Obj_{ab}^{t,best}$ is updated during the evolution stage in each membrane at level 3, and this object is also communicated to the parent membrane at level 2. All the membranes in the child level 3 receive a copy of $Obj_{u}^{t,best}$ optimal object updated at the parent level. This process involves simultaneous duplication and communication between a membrane at the parent and another at the child level. The intercommunication rule is described as

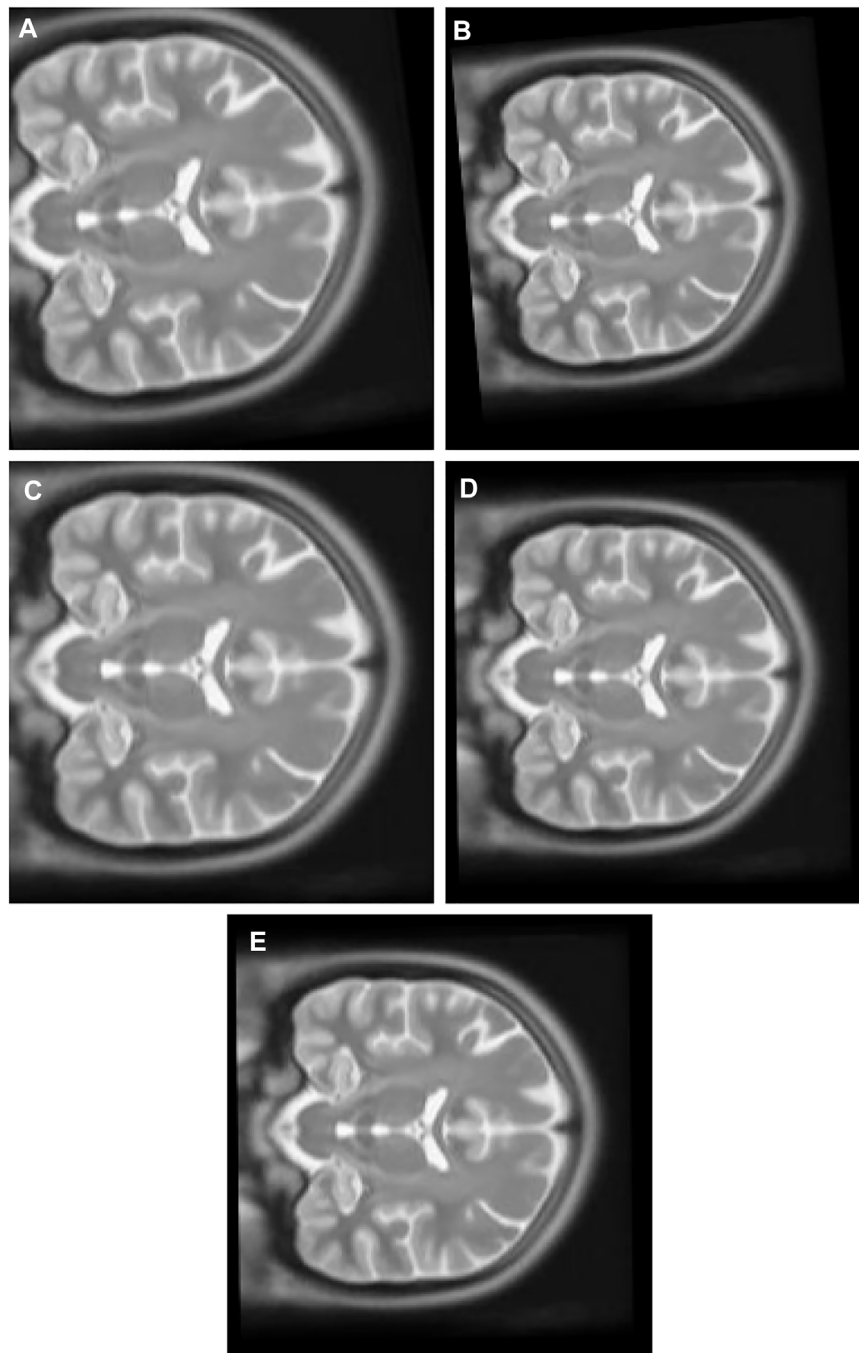


FIGURE 10

(A) Multi Modal Experiment 2 Float: row first left. (B) Multi Modal Experiment 2 GA output: row first right. (C) Multi Modal Experiment 2 PSO output: row second left. (D) Multi Modal Experiment 2 PSO and Powell Output: row second right. (E) Multi Modal Experiment 2 TPSysIR Output: row third center.

$$rule_4 \equiv [Obj_u^{t,best}]_{ab}^t \leftrightarrow [Obj_{ab}^{t,best}]_u^t, \quad (13)$$

$$rule_5 \equiv [Obj_u^{t,best}]_u^t \leftrightarrow [Obj_u^{t,best}]_0^t. \quad (14)$$

In (13), $rule_4$ exchanges the objects $Obj_{ab}^{t,best}$ and $Obj_u^{t,best}$ from membrane ab in level 3 and membrane u at level 2, respectively. The objects are first copied and are then exchanged between each child

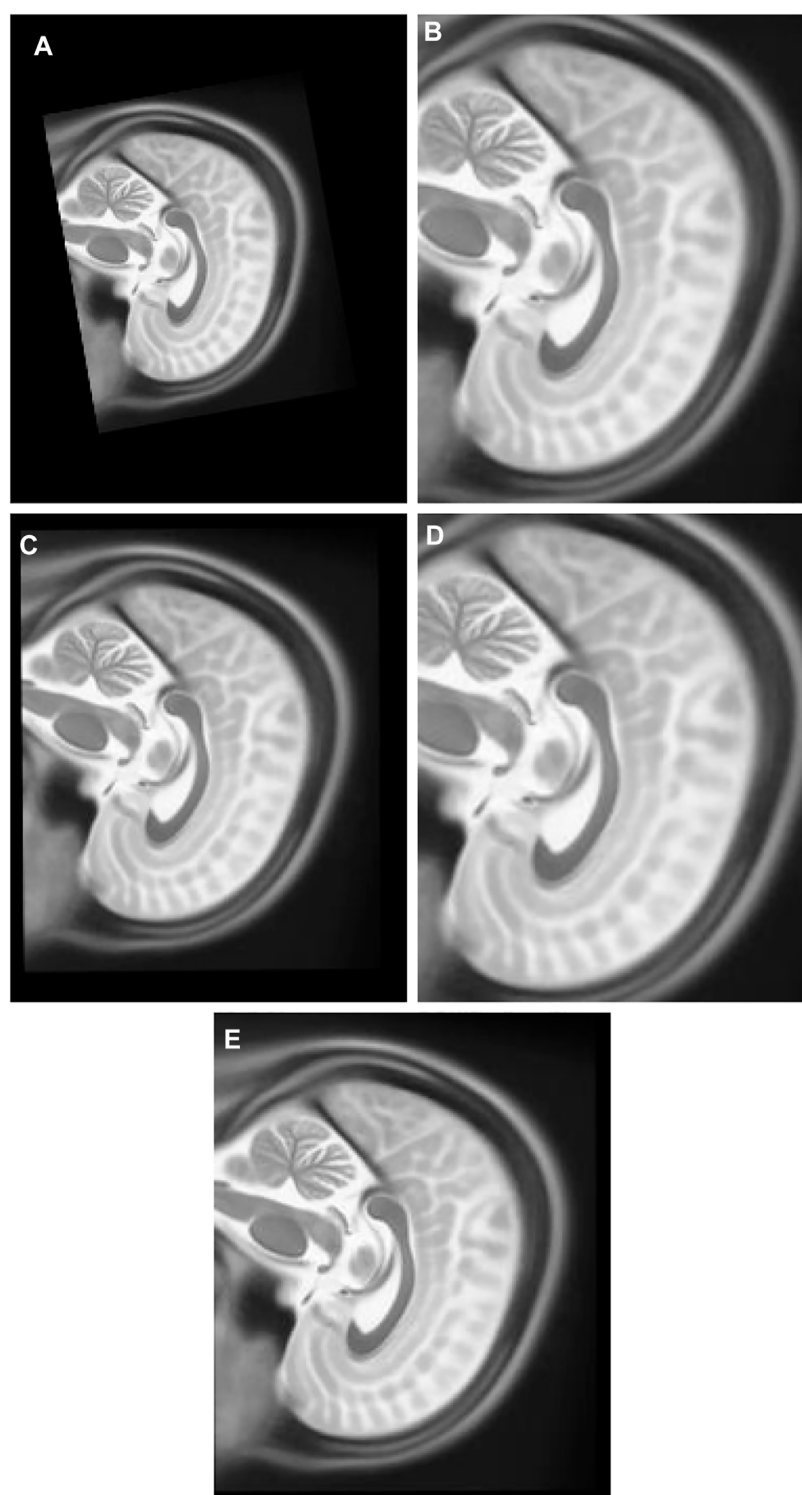


FIGURE 11

(A) Multi Modal Experiment 3 Float: row first left. (B) Multi Modal Experiment 3 GA output: row first right. (C) Multi Modal Experiment 3 PSO output: row second left. (D) Multi Modal Experiment 4 PSO and Powell Output: row second right. (E) Multi Modal Experiment 5 TPSysIR Output: row third center.

TABLE 1 Without scaling DATA.

Algorithm		$X - 8$	$Y - 6$	$\theta - 5$	MI
GA	Max	0.925	0.888	0.132	1.459
	Min	0.688	0.722	0.030	1.075
	Mean	0.806	0.805	0.081	1.267
	Δ	0.118	0.083	0.051	0.192
PSO	Max	0.679	0.741	0.111	1.232
	Min	0.490	0.607	0.073	0.962
	Mean	0.584	0.674	0.092	1.097
	Δ	0.094	0.067	0.019	0.135
PSO and POWELL	Max	0.530	0.496	0.072	1.569
	Min	0.493	0.465	0.055	1.356
	Mean	0.511	0.480	0.063	1.462
	Δ	0.018	0.015	0.008	0.106
TPSysIR	Max	0.511	0.508	0.058	1.712
	Min	0.470	0.484	0.036	1.669
	Mean	0.49	0.496	0.047	1.690
	Δ	0.020	0.012	0.011	0.021

and parent membrane, executing $rule_4$ for each child's membrane. The membrane at level 2 will have local optimal best objects from all its child membranes, and all its children will have a copy of the optimal object from its parent.

The (14) $rule_5$ communicates the object $Obj_u^{t,best}$ optimal best of membrane u at level 2 is copied and sent to output membrane at level 1 as the global best.

The selection and substitution rules

After the inter level object communication stage, the membrane at level 2 has n copies of the object from each of its child nodes. Level 2 membrane selects the best among all the objects received from the child membranes and compares it with its local optimal best. The MI metric is utilized to perform the selection between the two best optimal values. The maximal object obtained from the above process is substituted as the current local best of this membrane. The rule can be described as

$$Obj_{ab}^{t+2,best} = \max\{\{MI(Obj_{k,ab}^{t+1})\} \cup MI(Obj_{ab}^{t,best})\}, \quad (15)$$

$$rule_6 \equiv [Obj_u^{t,best}]_u^t \rightarrow [Obj_u^{t+1,best}]_u^{t+1}. \quad (16)$$

Eq. 15 examines the MI of all objects $Obj_{k,ab}^{t+1}$ received from the child membranes along with the MI of the current best object $Obj_u^{t,best}$ of membrane u for the maximum among all of them. This value is replaced as the new local best of membrane u by $rule_6$ in Eq 16.

The designed TPS utilizes the search capability of the PSO algorithm and explores the search space filled with floating image object solutions. The local object evolution is performed at the third level of the system; this generates local optimum objects.

The optimized objects then move to the neighboring membrane and higher level 2 membranes.

The halting condition

The system is executed in the manner of steps; it is halted after the desired number of steps are performed. The optimal object obtained at the output level 1 membrane at that instance is recorded as the best solution to the problem.

The TPSysIR algorithm

The algorithm is designed using the TPS framework in the form of three membrane levels; the algorithm is shown in Figure 6. The system utilizes each level for specific evolution and optimization objectives. The level 3 membranes are utilized to evolve the floating image objects to achieve local optimal values at their level inside each membrane. Communication of local optimal objects among membranes under a common parent is done to optimize the configuration object further. This optimal object, obtained from each child membrane at level 3, is communicated to the level 2 membranes to form the global optimal solution. Level 2 membranes examine the optimality of the received objects from the child membranes to create a global maximal. The optimal value of level 2 is sent to the level 1 output membrane. The copy of the optimal value of the level 2 membrane is also sent back to the children's membrane. The entire process, from the evolution of objects in the level 3 membrane to the transfer of global optima from level 2 to level 1, constitutes a step. The specified number of steps must be completed before the system halts; otherwise, the system restarts

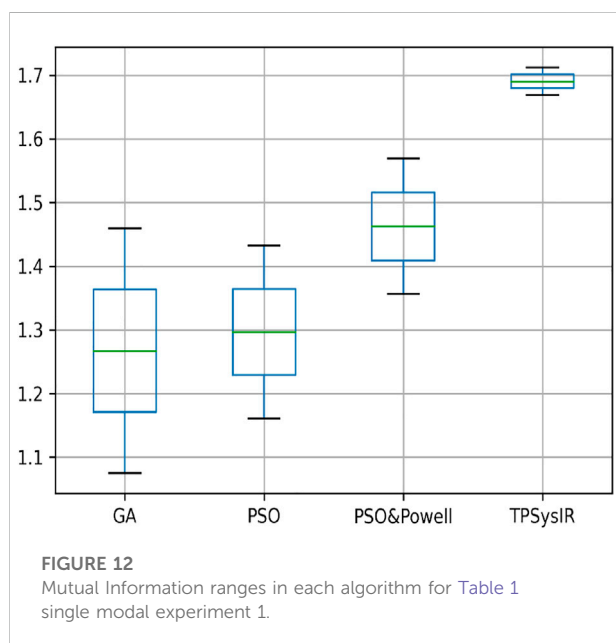
TABLE 2 With scaling DATA.

Algorithm		$X - 8$	$Y - 6$	$\theta - 5$	$S-1.25$	MI
Single multimodal experiment 2						
GA	Max	0.717	0.678	0.316	0.010	0.385
	Min	0.516	0.123	0.139	0.003	0.291
	Mean	0.616	0.400	0.227	0.006	0.324
	Δ	0.10	0.24	0.08	0.003	0.033
PSO	Max	0.845	0.507	0.234	0.006	0.445
	Min	0.633	0.039	0.132	0.002	0.402
	Mean	0.739	0.273	0.183	0.004	0.423
	Δ	0.106	0.234	0.051	0.002	0.021
PSO and POWELL	Max	0.567	0.461	0.189	0.005	0.519
	Min	0.421	0.055	0.143	0.003	0.477
	Mean	0.494	0.251	0.166	0.004	0.498
	Δ	0.073	0.196	0.023	0.001	0.021
TPSysIR	Max	0.459	0.362	0.189	0.004	0.551
	Min	0.400	0.049	0.123	0.002	0.532
	Mean	0.429	0.206	0.156	0.003	0.541
	Δ	0.029	0.156	0.033	0.001	0.019
Multimodal experiment 1						
GA	Max	0.98	0.48	0.50	0.025	0.0079
	Min	0.75	0.12	0.32	0.018	0.0013
	Mean	0.86	0.30	0.41	0.006	0.0046
	Δ	0.12	0.18	0.09	0.003	0.0033
PSO	Max	0.84	0.31	0.47	0.023	0.0100
	Min	0.62	0.03	0.16	0.019	0.0031
	Mean	0.73	0.17	0.31	0.004	0.0065
	Δ	0.11	0.14	0.11	0.002	0.0034
PSO and POWELL	Max	0.56	0.24	0.30	0.013	0.0112
	Min	0.42	0.05	0.18	0.011	0.0070
	Mean	0.49	0.14	0.24	0.004	0.0091
	Δ	0.07	0.10	0.06	0.001	0.0021
TPSysIR	Max	0.38	0.22	0.25	0.010	0.0136
	Min	0.31	0.03	0.21	0.008	0.0098
	Mean	0.35	0.13	0.23	0.003	0.0112
	Δ	0.03	0.09	0.02	0.001	0.0019
Multimodal experiment 2						
GA	Max	1.655	1.751	0.965	0.074	0.0191
	Min	1.295	1.591	0.074	0.018	0.0071
	Mean	1.475	1.671	0.854	0.062	0.0131
	Δ	0.180	0.80	0.111	0.012	0.0060
PSO	Max	1.126	1.506	0.751	0.060	0.0204
	Min	0.862	1.400	0.419	0.043	0.0115
	Mean	0.994	1.453	0.585	0.051	0.0160
	Δ	0.132	0.053	0.83	0.009	0.0045
PSO and POWELL	Max	0.850	1.118	0.452	0.023	0.0225
	Min	0.664	1.047	0.353	0.015	0.0147
	Mean	0.757	1.082	0.402	0.019	0.0186
	Δ	0.093	0.036	0.050	0.004	0.0039
TPSysIR	Max	0.503	0.643	0.324	0.012	0.0271
	Min	0.381	0.547	0.280	0.010	0.0221
	Mean	0.442	0.608	0.242	0.008	0.0246
	Δ	0.061	0.035	0.040	0.002	0.0024
Multimodal experiment 3						
GA	Max	1.122	1.990	0.965	0.617	0.0308
	Min	0.810	1.796	0.743	0.578	0.0071
	Mean	0.966	1.893	1.204	0.597	0.0235
	Δ	0.156	0.097	0.093	0.020	0.0162
PSO	Max	1.009	1.838	1.067	0.471	0.0387
	Min	0.739	1.445	0.982	0.424	0.0261
	Mean	0.874	1.641	0.984	0.447	0.0324
	Δ	0.135	0.197	0.083	0.023	0.0063

(Continued on following page)

TABLE 2 (Continued) With scaling DATA.

Algorithm		$X - 8$	$Y - 6$	$\theta - 5$	$S-1.25$	MI
PSO and POWELL	Max	0.598	0.523	0.708	0.163	0.0447
	Min	0.400	0.377	0.568	0.129	0.0147
	Mean	0.499	0.450	0.638	0.146	0.0401
	Δ	0.099	0.073	0.070	0.017	0.0355
TPSysIR	Max	0.323	0.361	0.531	0.088	0.0544
	Min	0.187	0.267	0.460	0.062	0.0476
	Mean	0.237	0.314	0.495	0.075	0.0510
	Δ	0.086	0.047	0.035	0.013	0.0034



the evolution process utilizing the previously obtained locally optimized solutions.

Experimental setup

All the experiments were conducted using python (Python Programming Language, 2021) and plingua (P Lingua Programming Language, 2021) on a platform with Intel i5 four-core CPU at 2.5 GHz each and 8 gigabytes of RAM. The image data consisting of standard brain atlas was obtained from the Montreal Neurological Institute (MNI) (McConnell Brain Imaging Centre, 2021). The data was utilized by different optimization-based methods, utilizing MI as an optimization metric for image registration. The experiments are divided into two sets; first set of two

experiments utilizes the single modal data and second set of three experiment utilizes the multimodal data.

Experiments with a single-modal image

1) Experiment 1: The float Figure 7B in this experiment is created by moving the original Figures 7A, 8 pixel units in x -axis up direction, six pixel units in y -axis in the left direction, and rotated 5° in a counterclockwise direction.

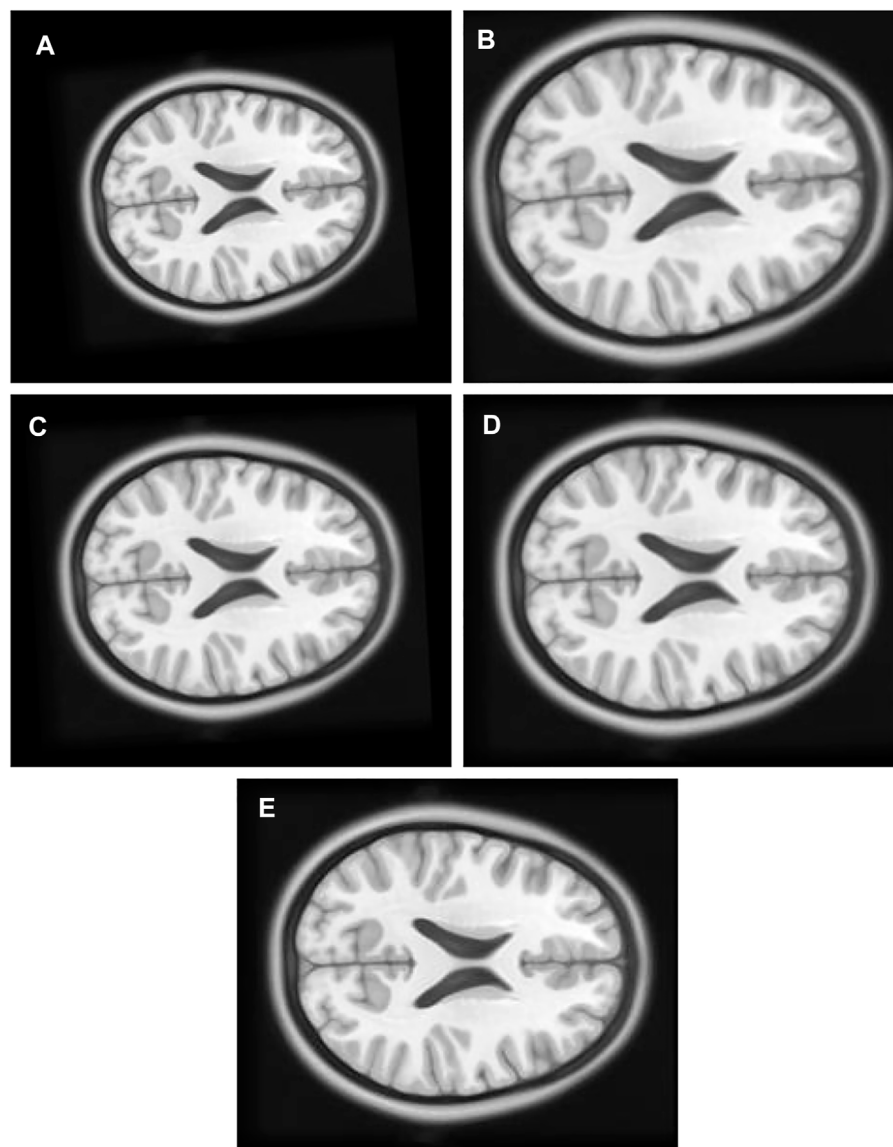
2) Experiment 2: The original Figure 7A in this experiment is moved eight pixel-units in x -axis up direction, six pixel-units in y -axis, rotated 5° in a counterclockwise direction, and scaled into 0.8 times of its original size to create float Figure 7C.

Experiment with multimodal images

1) Experiment 1: The multimodal image set one contains images from two different modes, cerebrospinal fluid (CSF) section T1-weighted MRI Figure 8B having low signal and T2-weighted Figure 8A having high signal in the CSF section. T1 in X-Y plane image was utilized to create the float image Figure 9A after it was panned eight pixel units in x axis in the upward direction, six pixel units in Y axis in the left direction, rotated 5° in a counter clockwise direction, and scaled into 0.8 of its original size.

2) Experiment 2: The multimodal image set two contains T1 Figure 8C and T2 Figure 8D in the X-Z plane. The float Figure 10A was created from T2 after it was panned 10 pixel units in X axis in the upward direction, 13 pixel units in Z axis in the left direction, rotated 7° in a counter clockwise direction, and scaled into 1.1 of its original size. T1 is the target image.

3) Experiment 3: The multimodal image set two contains T1 and T2 images in the Y-Z plane. T1 Figure 8E is the target image while T2 Figure 8F was utilized as the float image. Figure 11A was created after it was panned 12 pixel units in Y axis in the upward direction, nine pixel units in Z axis in the left

**FIGURE 13**

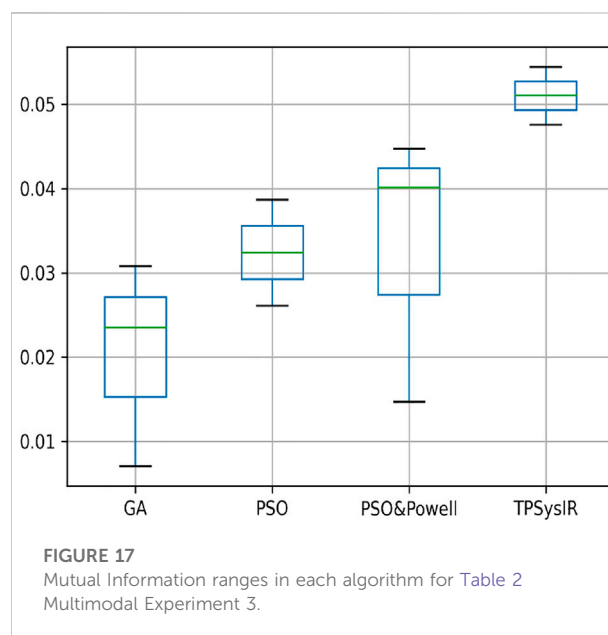
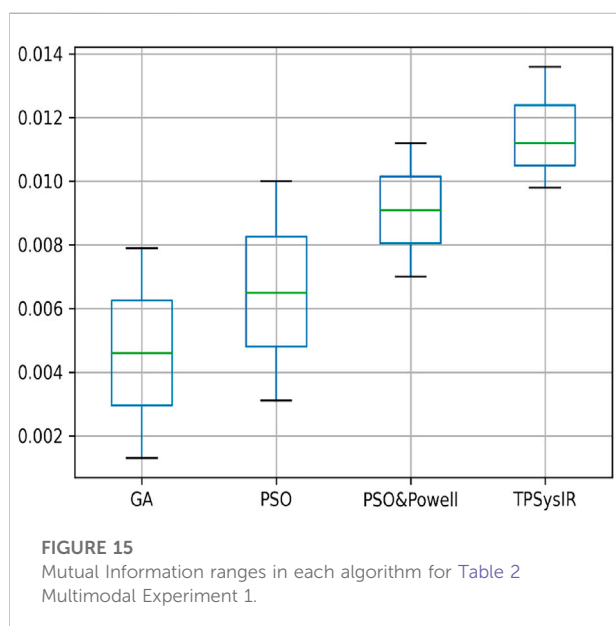
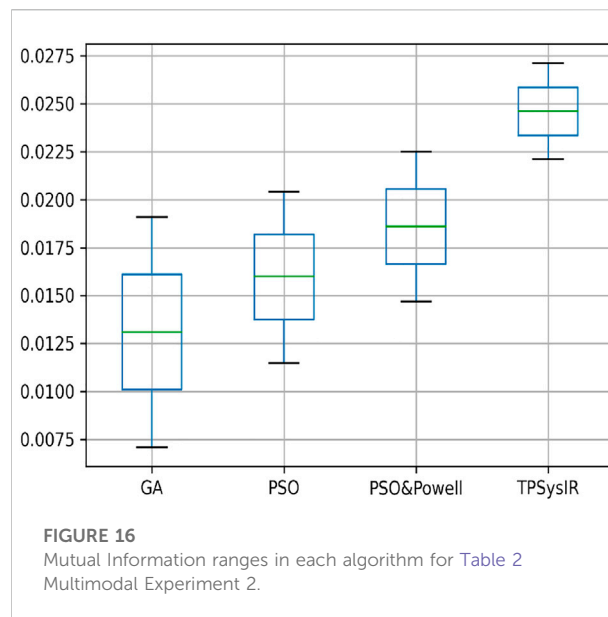
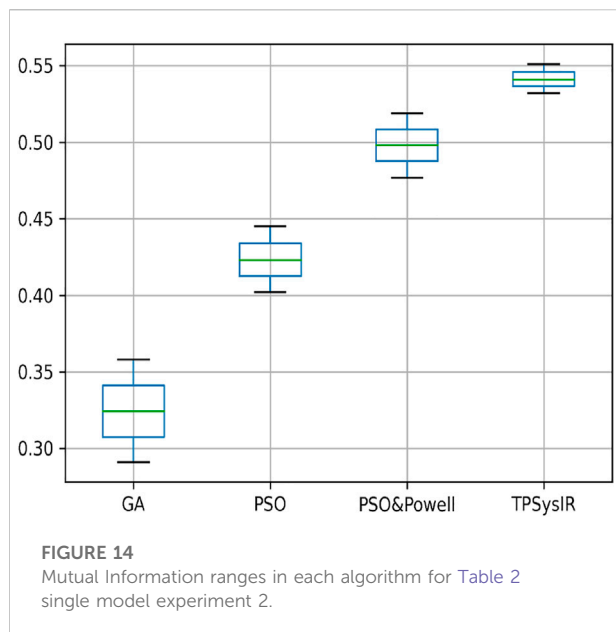
(A) Single Modal Experiment 2 Float: row first left. (B) Single Modal Experiment 2 GA output: row first right. (C) Single Modal Experiment 2 PSO output: row second left. (D) Single Modal Experiment 2 PSO and Powell Output: row second right. (E) Single Modal Experiment 2 TP SysIR Output: row third center.

direction, rotated 10° in a counter clockwise direction, and scaled into 0.7 of its original size.

Experimental results and analysis

The experiments designed above are applied to the proposed TP SysIR algorithm along with three other optimization-based algorithms, GA, PSO, PSO, and

POWELL. The experiments were repeated eight times for each method, and the maximum and minimum variance values were recorded and tabulated. MI value was also calculated for the output configuration on recorded data. The results for the variance along the X-axis and Y-axis and rotation angle(θ) are recorded in Table 1 for experiment 1, utilizing single modal images with no scaling factor. Table 2 shows that scaling factor variance S is considered for experiment 2 utilizing single modal image data with a



scaling factor. Table 2 with multimodal experiments 1, 2, and 3 utilizes multimodal images for the experiments, and all four variables are considered.

Table 1 results with no size scaling experiment show that PSO and POWELL have the lowest mean variance (Mean) and deviation(Δ) among the results in the Y-axis. TPSysIR has the lowest variance value on the X-axis and equals the deviation to PSO and POWELL. The mean rotation variance (θ) is the least in TPSysIR than all other algorithms including GA, PSO, and PSO and

POWELL. TPSysIR has the maximum values, in mutual information, of 1.76 and the slightest deviation 0.02. The boxplot Figure 12 shows that the range of MI values obtained by PSO and Powell and TPSysIR is better than other algorithms, but TPSysIR obtains the range of least deviation. The maximum MI results for TPSysIR has shown 17.93%, 19.58%, and 9.61% improvement against the corresponding maximum MI values of GA, PSO, and PSO and POWELL algorithms.

Table 2 single modal experiment 2 data includes the scaling factor along with all other parameters measured in experiment 1 to obtain

results from all four methods. Notably in this experiment 2, the overall MI is lower than the previous experiment 1 as the similarity between the original and output image has decreased. The deviation in the X-axis is least in the TPSysIR algorithm. The deviation angle of rotation varies from 0.08 to 0.02 for GA to PSO and POWELL and TPSysIR. TPSysIR has a deviation value of 0.03 but has a lower max value than PSO and POWELL. The results of the experiments are shown in Figure 13B–E. PSO and POWELL and TPSysIR did a better job on image scaling. Mutual interference values show slightly better results for TPSysIR than PSO and POWELL, whereas other algorithms such as GA and PSO have lower scores. Angular bias is present in the output configuration images for GA Figure 13B and PSO Figure 13C. The boxplot Figure 14 shows that all algorithms gave minimum deviation in the range of MI values, but the maximum value range was obtained by TPSysIR to obtain best alignment. The maximum MI results for TPSysIR have shown 57.14%, 25%, and 7.84% improvement against the corresponding maximum MI values of GA, PSO, and PSO and POWELL algorithms, respectively.

Table 2 multimodal experiment 1 data shows lower ranges of the MI values than in previous experiments, expressing further dissimilarity between the reference and the output image. The TPSysIR algorithm shows lower deviation values for X, Y, and rotation angle variance. The scalability factor deviation has relative range values for PSO and POWELL and TPSysIR, while MI values are best for TPSysIR. The boxplot Figure 15 shows that the ranges of MI values obtained by TPSysIR were the best. The maximum MI results for TPSysIR has shown 72.15%, 36%, and 21.42% improvement against corresponding maximum MI values of GA, PSO, and PSO and POWELL algorithms, respectively. The configuration results obtained for each method in the experiment for multimodal images are shown in Figure 9B–E.

Table 2 multimodal experiment 2 contains the data from the experiment performed over multimodal T1 and T2 images taken in the X-Z plane. The output in Figure 10B–E shows the output for the experiment. The table values for GA and PSO variance over X and Z have significantly higher values than PSO and Powell and TPSysIR. The MI value shows overlapping ranges for GA, PSO, and PSO and Powell while TPSysIR has higher ranges, as shown in the boxplot Figure 16. The TPSysIR has 29.52%, 24.72%, and 16.97% better MI values than GA, PSO, and PSO and Powell.

Table 2 multimodal experiment 3 data is obtained from the experiment performed over multimodal T1 and T2 images taken in the Y-Z plane. The output data for this experiment are shown in Figures 11B–E. The data shows the variance in Y of GA is the maximum of all other algorithms, and TPSysIR has the lowest. The MI range values of GA, PSO, and PSO and Powell show overlapping, while TPSysIR has a higher range of values. The same is confirmed in the boxplot in Figure 17. The TPSysIR MI values are 43.38%, 28.86%, and 17.83% are better than GA, PSO, and PSO and Powell respectively.

PSO and POWELL has good optimization capability due to its hybridization to acquire local and global search capabilities. The TPSysIR algorithm employs the TPS's parallel execution

capability, optimizing the local search and creating a globally optimal solution with faster convergence of results.

Conclusion

The method described in this paper utilizes the tissue P system's parallel and simultaneous execution feature to guide its velocity position model-based rules. The novelty of this work is the use of the TPS, which enables faster convergence and high MI with the parallel feature using an optimization-based model to obtain parameters for image registration and the use of the PSO technique to make the evolution rules. The algorithm is tested on multimodal and unimodal MRI image sets to verify its effectiveness. The results of the tests prove it to be a good optimization-based solution to the image registration problem compared to other state-of-the-art algorithms.

Data availability statement

The datasets presented in this study can be found in online repositories. The names of the repository/repositories and accession number(s) can be found at: McConnell Brain Imaging Centre. <https://www.bic.mni.mcgill.ca/ServicesAtlases/ICBM152Nlin2009>.

Author contributions

SK—methodology, original draft, writing and editing, algorithm design, and implementation. SS—guidance, approach, correction, editing, and review.

Acknowledgments

The work here was tested utilizing images from The. nii files mni_icbm152_t1_tal_nlin_asym_09a.nii and mni_icbm152_t2_tal_nlin_asym_09a.nii obtained from the mni non-linear templates archive hosted at (Paun and Paun, 2002). Above usage required the following license copy (here the word “software” is utilized for the above files): copyright (C) 1993–2004 louis collins, mcconnell brain imaging center, montreal neurological institute, McGill University. Permission to use, Copy, Modify and Distribute this Software and its Documentation for any Purpose and Without Fee is Here Granted, Provided That Above Copyright Notice Appear in all Copies the Authors and McGill University Make no Reperentations About The Suitability Of This Software For Any Purpose. It is Provided “as is” Without Express or Implied Warranty. The Authors are not Responsible for any Data Loss, Equipment Damage, Property Loss, or Injury To The

Subjects or Patients Resulting from Use or Misuse of this Software Package.

Conflict of interest

The authors declare that the research was conducted in the absence of any commercial or financial relationships that could be construed as a potential conflict of interest.

References

- Abdel-Basset, M., Fakhry, A. E., El-henawy, I., Qui, T., and Sangaiah, A. K. (2017). Feature and intensity based medical image registration using particle swarm optimization. *J. Med. Syst.* 41, 197. doi:10.1007/s10916-017-0846-9
- Ali, S., and Rittscher, J. (2019). *Conv2Warp: An unsupervised deformable image registration with continuous convolution and Warping10*. Available from: <https://arxiv.org/abs/1908.06194v1>.
- Balakrishnan, G., Zhao, A., Sabuncu, M. R., Guttag, J., and Dalca, A. V. (2019). VoxelMorph: A learning framework for deformable medical image registration. *IEEE Trans. Med. Imaging* 38, 1788–1800. doi:10.1109/TMI.2019.2897538
- Bernardini, F., and Gheorghe, M. (2005). Cell communication in tissue P systems: Universality results. *Soft Comput.* 9, 640–649. doi:10.1007/s00500-004-0393-4
- Chel, H. D., and Nandi, D. (2013). “Image registration in noisy environment using particle swarm optimization,” in *2013 IEEE second international conference on image information processing (ICIIP-2013)*, 458–463. doi:10.1109/ICIIP.2013.6707634
- Freund, R., Paun, G., and Perez-Jimenez, M. J. (2005). Tissue P systems with channel states. *Theor. Comput. Sci.* 330 (1), 101–116. doi:10.1016/j.tcs.2004.09.013
- Gong, L., Zhang, C., Duan, L., Du, X., Liu, H., Chen, X., et al. (2019). Nonrigid image registration using spatially region-weighted correlation Ratio and GPU-acceleration. *IEEE J. Biomed. Health Inf.* 23 (2), 766–778. doi:10.1109/JBHI.2018.2836380
- Jiménez, M. J. P., and Núñez, A. R. (2005). Solving the Subset-Sum problem by P systems with active membranes. *New Gener. comput.* 23, 339–356. doi:10.1007/BF03037637
- Kakimoto, M., Endoh, Y., Shin, H., Ikeda, R., and Kusaka, H. (2019). Probabilistic solar irradiance forecasting by conditioning joint probability method and its application to electric power trading. *IEEE Trans. Sustain. Energy* 10 (2), 983–993. doi:10.1109/TSTE.2018.2858777
- Knops, Z. F., Maintz, J. B., Viergever, M. A., and Pluim, J. P. (2005). Normalized mutual information based registration using k-means clustering and shading correction. *Med. Image Anal.* 10 (3), 432–439. doi:10.1016/j.media.2005.03.009
- Lewis, J. P. (2001). *Fast normalized cross-correlation*. Quebec City: Canadian Image Processing and Pattern Recognition Society.
- Lin, C., Mimori, A., and Chen, Y. (2012). Hybrid particle swarm optimization and its application to multimodal 3D medical image registration. *Comput. Intell. Neurosci.* (2012), 561406. Article 6. doi:10.1155/2012/561406
- Mansilla, L., Milone, D. H., and Ferrante, E. (2020). Learning deformable registration of medical images with anatomical constraints. *Neural Netw.* 269–279. doi:10.1016/j.neunet.2020.01.023
- McConnell Brain Imaging Centre (2021). *Services atlases*. Available from: <http://www.bic.mni.mcgill.ca/ServicesAtlases/ICBM152Nlin2009> (Accessed Nov 16, 2021).
- P Lingua Programming Language (2021). *Lingua Programming Language*. Available from: http://www.p-lingua.org/wiki/index.php/Main_Page (Accessed Nov 23, 2021).
- Pan, L., and Perez-Jiménez, M. J. (2010). Computational complexity of tissue-like P systems. *J. Complex.* 26 (3), 296–315. doi:10.1016/j.jco.2010.03.001
- Paun, A., and Paun, G. (2002). The power of communication: P systems with symport/antiport. *New Gener. comput.* 20, 295–305. doi:10.1007/BF03037362
- Paun, G. (2000). Computing with membranes. *J. Comput. Syst. Sci.* 61 (1), 108–143. doi:10.1006/jcss.1999.1693
- Paun, G. P. (2001). Systems with active membranes: Attacking NP complete problems. *J. Automata, Lang. Comb.* 6, 75–90.
- Prakash, J., Mandal, S., Razansky, D., and Ntziachristos, V. (2019). Maximum entropy based non-negative optoacoustic tomographic image reconstruction. *IEEE Trans. Biomed. Eng.* 66 (9), 2604–2616. doi:10.1109/TBME.2019.2892842
- Python Programming Language (2021). *python*. Available from: <https://www.python.org/> (Accessed Nov 16, 2021).
- Rajapakse, J. C., and Guojun, B. (1999). Functional MR image registration using a genetic algorithm, ICONIP'99. ANZIS'99 ANNES'99 ACNN'99. 6th international conference on neural information processing. *Proc. Cat. No.99EX378* 3, 922–927. doi:10.1109/ICONIP.1999.844660
- Ramamoorthy, S., Priyadharsini, K., and Rajaram, S. (2010). Intensity based image registration by maximization of mutual information. *Int. J. Comput. Appl.* 1, 1–7. doi:10.5120/432-637
- Rouet, J. M., Jacq, J. J., and Roux, C. (2000). Genetic algorithms for a robust 3-D MR-CT registration. *IEEE Trans. Inf. Technol. Biomed.* 4 (4), 126–136. doi:10.1109/4233.845205
- Song, G., Han, J., Zhao, Y., Wang, Z., and Du, H. (2017). A Review on medical image registration as an optimization problem. *Curr. Med. Imaging Rev.* 13 (3), 274–283. doi:10.2174/1573405612666160920123955
- Susskind, J., Memisevic, R., Hinton, G., and Pollefeys, M. (2011). Modeling the joint density of two images under a variety of transformations. *Proc. IEEE Comput. Soc. Conf. Comput. Vis. Pattern Recognit.*, 2793–2800. doi:10.1109/CVPR.2011.5995541
- Wachowiak, M. P., Smol'ikova, R., Zheng, Y., Zurada, J. M., and Elmaghraby, A. S. (2004). An Approach to multimodal biomedical image registration utilizing particle swarm optimization. *IEEE Trans. Evol. Comput.* 8 (8), 289–301. doi:10.1109/tevc.2004.826068
- Wang, P., Wang, L., Leung, H., and Zhang, G. (2020). Super-resolution mapping based on spatial-spectral correlation for spectral imagery. *IEEE Trans. Geosci. Remote Sens.* 59 (3), 2256–2268. doi:10.1109/TGRS.2020.3004353
- Zhang, Z., Huo, P., Teng, J., Xue, W., and Suhuan, W. (2010). “Medical image registration algorithm with generalized mutual information and PSO-Powell hybrid algorithm,” in *Advances in Swarm intelligence*. Editors Y. Tan, Y. Shi, and K. C. Tan (Berlin Heidelberg: Springer), 160–166. doi:10.1007/978-3-642-13495-1_20
- Zhu, F., Gao, J., Yang, J., and Ye, N. (2022). Neighborhood linear discriminant analysis. *Pattern Recognit.* 123, 108422. doi:10.1016/j.patcog.2021.108422
- Zhu, F., Ning, Y., Chen, X., Zhao, Y., and Gang, Y. (2021). On removing potential redundant constraints for SVOR learning. *Appl. Soft Comput.* 102, 106941. doi:10.1016/j.asoc.2020.106941
- Zuo-zhu, L. (2007). Based on genetic algorithm mutual information of medical image registration. *Artif. Intell. Identif. Technol.* 1 (1), 1121–1122.

Publisher's note

All claims expressed in this article are solely those of the authors and do not necessarily represent those of their affiliated organizations, or those of the publisher, the editors and the reviewers. Any product that may be evaluated in this article, or claim that may be made by its manufacturer, is not guaranteed or endorsed by the publisher.



TVGG Dental Implant Identification System

Jianbin Guo^{1*}, Pei-Wei Tsai², Xingsi Xue³, Dong Wu⁴, Qui Tran Van²,
Chanaka Nimantha Kaluarachchi², Hong Thi Dang² and Nikhitha Chintha²

¹Fujian Key Laboratory of Oral Diseases and Fujian Provincial Engineering Research Center of Oral Biomaterial and Stomatological Key Lab of Fujian College and University, School and Hospital of Stomatology, Fujian Medical University, Fuzhou, China, ²Department of Computing Technologies, Swinburne University of Technology, Hawthorn, VIC, Australia, ³Fujian Provincial Key Laboratory of Big Data Mining and Applications, Fujian University of Technology, Fuzhou, China, ⁴Institute of Stomatology and Research Center of Dental and Craniofacial Implants, School and Hospital of Stomatology, Fujian Medical University, Fuzhou, China

OPEN ACCESS

Edited by:

Khin Wee Lai,
University of Malaya, Malaysia

Reviewed by:

Wen Zhang,
Fuzhou University, China
Yinghong Zhou,
The University of Queensland,
Australia

*Correspondence:

Jianbin Guo
jianbin@fjmu.edu.cn

Specialty section:

This article was submitted to
Experimental Pharmacology and Drug
Discovery,
a section of the journal
Frontiers in Pharmacology

Received: 19 May 2022

Accepted: 09 June 2022

Published: 08 August 2022

Citation:

Guo J, Tsai P-W, Xue X, Wu D, Van QT,
Kaluarachchi CN, Dang HT and
Chintha N (2022) TVGG Dental Implant
Identification System.
Front. Pharmacol. 13:948283.
doi: 10.3389/fphar.2022.948283

Identifying the right accessories for installing the dental implant is a vital element that impacts the sustainability and the reliability of the dental prosthesis when the medical case of a patient is not comprehensive. Dentists need to identify the implant manufacturer from the x-ray image to determine further treatment procedures. Identifying the manufacturer is a high-pressure task under the scaling volume of patients pending in the queue for treatment. To reduce the burden on the doctors, a dental implant identification system is built based on a new proposed thinner VGG model with an on-demand client-server structure. We propose a thinner version of VGG16 called TVGG by reducing the number of neurons in the dense layers to improve the system's performance and gain advantages from the limited texture and patterns in the dental radiography images. The outcome of the proposed system is compared with the original pre-trained VGG16 to verify the usability of the proposed system.

Keywords: VGG, CNN, dental implant, radiography image, implant identification

1 INTRODUCTION

Oral radiography images are widely used in assisting dentists in making judgements on a patient's case, evaluating the conditions, and deciding on further treatment or operations that work the best for the patient. One of the essential steps in observing the oral radiography image is that the dentist needs to identify which manufacturer is the one who manufactured the particular implant that has been placed in the patient's mouth. Identifying the correct implant manufacturer is vital because different implant manufacturers have different operating procedures and corresponding accessories for their products. Using the right supplements and operating procedures ensures the dental prosthesis's sustainability and reliability. Thus, identifying the dental implant manufacturer from either the intraoral or the extraoral x-ray image is the key to ensuring the quality of the work.

An intraoral x-ray image is obtained by having a film positioned in the buccal cavity. Unlike the intraoral x-ray image, an extraoral x-ray image is obtained by positioning the patient between the x-ray source and the radiographic film. The intraoral technique produces images focusing on a local region of the mouth, but the extraoral approach provides panoramic x-ray images of the mouth. Either way, the dentist needs to identify the manufacturer by observing the implant's characteristics (Saghiri et al., 2020), shapes (Guarnieri et al., 2019), and patterns (Makary et al., 2019) from the x-ray image and judge from which manufacturer the implant should be. This can be a high-pressure task when a large volume of patients are pending in the queue for proper treatments. The chance of

humans making mistakes under a high-pressure scenario is much greater than average. Having a support system assisting the dentists in identifying the implant's manufacturer is ideal for lifting the burden on the dentists as a solution for this. Hence, many machine learning-based support systems for identifying the dental implant's manufacturer and related usability studies have been proposed in recent years.

The remaining of this article is organized as follows: the related works are discussed in **Section 2**, the proposed system model is revealed in **Section 3**, the experiments and results are summarized and discussed in **Section 4** and is followed by the conclusion in **Section 5**.

2 RELATED WORKS

Training a deep neural network from scratch is heavily resource consuming. To avoid getting the model with the hard way, using transfer learning to adjust the model based on a pre-trained model is a popular solution. For example, Kim et al. test a set of transfer learning-based systems for identifying the dental implant in 2020 (Kim et al., 2020). They conclude that the tested convolutional neural network (CNN) models can properly classify four dental implants from manufacturers of "Brånemark Mk TiUnite," "Dentium Implantium," "Straumann Bone Level," and "Straumann Tissue Level" with high accuracy. Some data augmentation techniques are applied to their collected data set for preventing overfitting. Their experimental results are produced by SqueezeNet (Iandola et al., 2016), GoogLeNet (Szegedy et al., 2015), ResNet (He et al., 2015), and MobileNet-v2 (Sandler et al., 2018). All models used in their work are pre-trained by ImageNet. However, image sources collected in ImageNet are natural images. The pattern and details contained in those images are very different from and much more complex than those in medical radiography images. Using a thinner network structure may already be sufficient for the dental implant identification task. The terminology "thinner" refers to a network layer with less neurons and thus the width of a layer is narrower. A thinner network structure can save much more resources and computational cost in training and model deployment.

Sukegawa et al. compare the dental implant classification results obtained by the basic CNN with three convolution layers, the VGG16 and the VGG19 models (Sukegawa et al., 2020). According to their findings, the classification accuracy before fine-tuning the VGG models is already higher than the basic CNN model. The accuracy is lifted to above 90% after the fine-tuning for both VGG16 and VGG19. This result shows the advantage of using VGG model over the conventional CNN. In 2015, Simonyan and Zisserman conclude that having up to 19 weight layers of the CNN structure is sufficient for the classification accuracy on the ImageNet challenge dataset (Simonyan and Zisserman, 2015). Nevertheless, fine-tuning a deep learning model is highly resource consuming. Lighten the model to accommodate the radiography images may be a more efficient solution.

In 2020, Almubarak et al. propose a two-stage mask R-CNN model for decomposing the object identification task into the object cropping task and the object classification task in a sequence (Almubarak et al., 2020). Their approach utilizes the bounding box and the semantic segmentation output from the mask R-CNN (He et al., 2020) to locate the target for cropping in the first stage. The cropped target is sent to the second stage as the input for classification. The drawback of this method is that it requires the annotation mask to indicate the ground truth for training. The annotation is highly labor demanded and thus is less preferred in many applications. Besides, the quality of the annotation is vital to the model accuracy. Keeping the annotation in the same quality level is also challenging.

Vuola et al. utilize the ensemble learning technique to aggregate the output from a mask R-CNN and a U-Net (Ronneberger et al., 2015) in the nuclei segmentation application (Vuola et al., 2019). Their finding indicate that the mask R-CNN and the U-Net models make mistakes in different parts of the input image. Thus, using ensemble learning to integrate their output provides a better result in the nuclei segmentation task. Although their experiment is carried out with the fluorescence and histology images, similar experience is potential to be taken in use in the dental implant application as well.

In 2022, Liu et al. use R-CNN to detect marginal bone loss around dental implants (Liu et al., 2022). They find that their model output performs similarly to the resident dentist but is less accurate than the experienced dentist. The reason could be that the model is yet fine-tuned. With proper fine-tuning and optimization, the model is expected to be improved. Moreover, R-CNN model has been improved from the original version to the fast R-CNN, the faster R-CNN, and the current state-of-the-art: the mask R-CNN. By using the more advanced model, the result should be lifted to the next level.

Summarizing the lesson learned from the related works, we notice that the radiography image has more minor features and patterns than the natural image. This implies that a thinner network structure may already be sufficient to complete the task. The observed knowledge inspired us to simplify the complexity of the VGG structure for our system.

3 PROPOSED METHOD

Our goal in this work is to create a support system for the dentist to quickly identify the dental implant manufacturers from the x-ray image automatically. With the output from the support system, the dentist only needs to verify whether the result is correct rather than identifying the manufacturer with no reference information. Furthermore, considering the x-ray image is relatively monotone than the natural image, we expect a thinner network structure can accommodate the given task. Thus, we build a thinner VGG16 network called TVGG16 with a reduced number of neurons in the dense layers to reduce the computational cost. **Figure 1** shows the diagram of the proposed dentist supporting system.

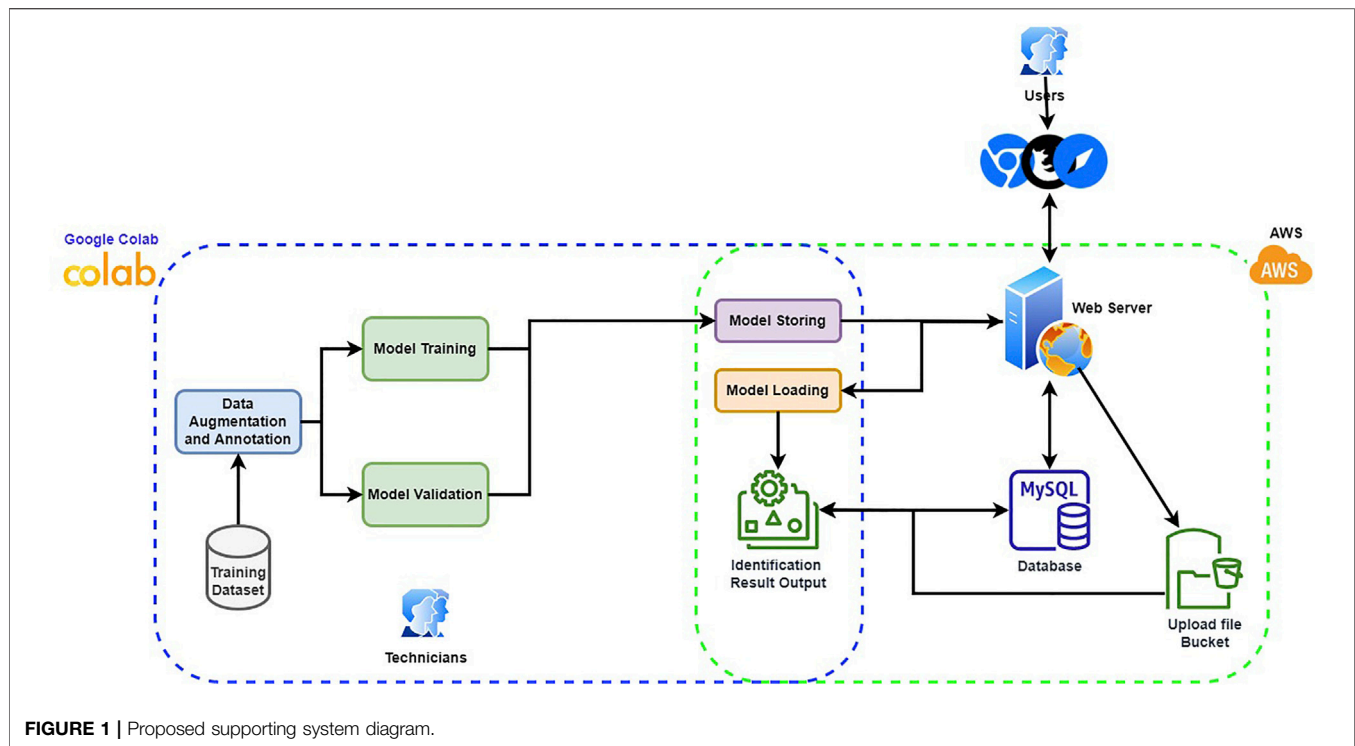


FIGURE 1 | Proposed supporting system diagram.

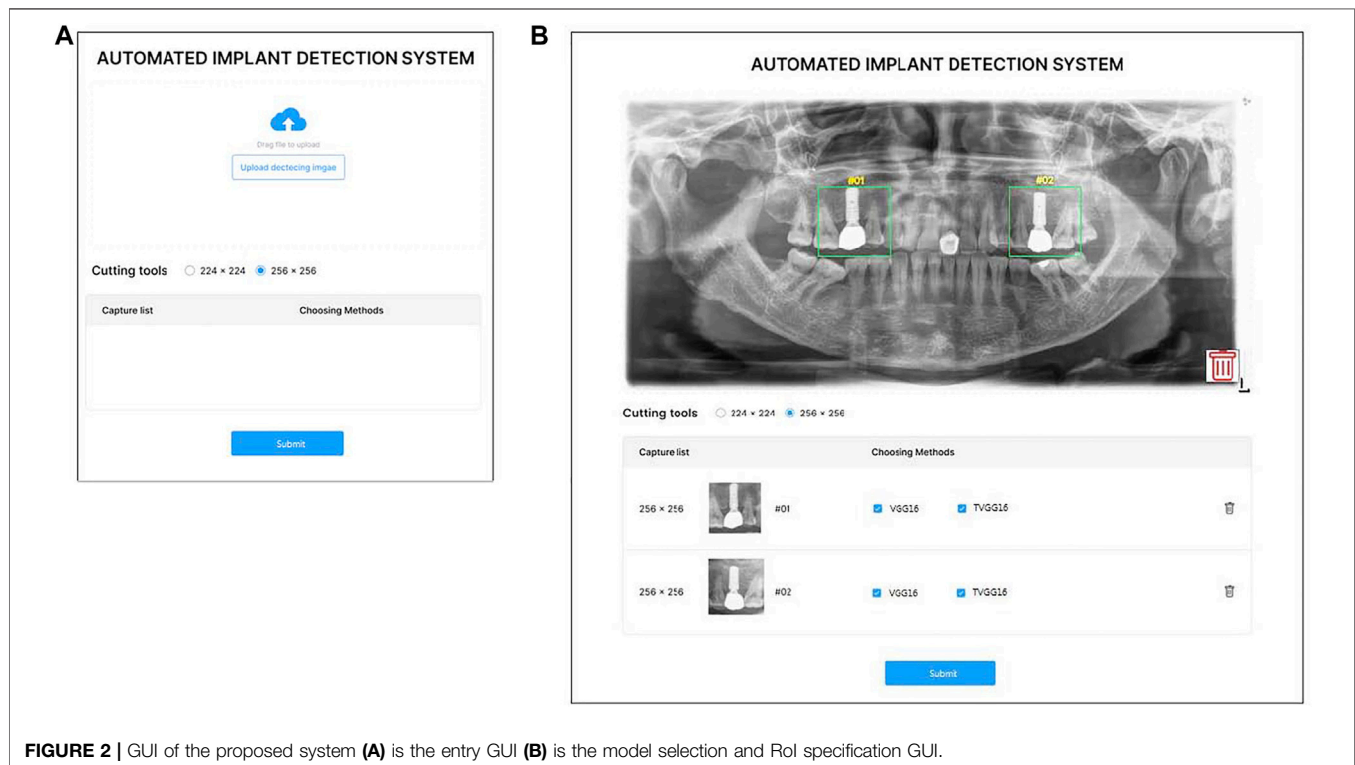
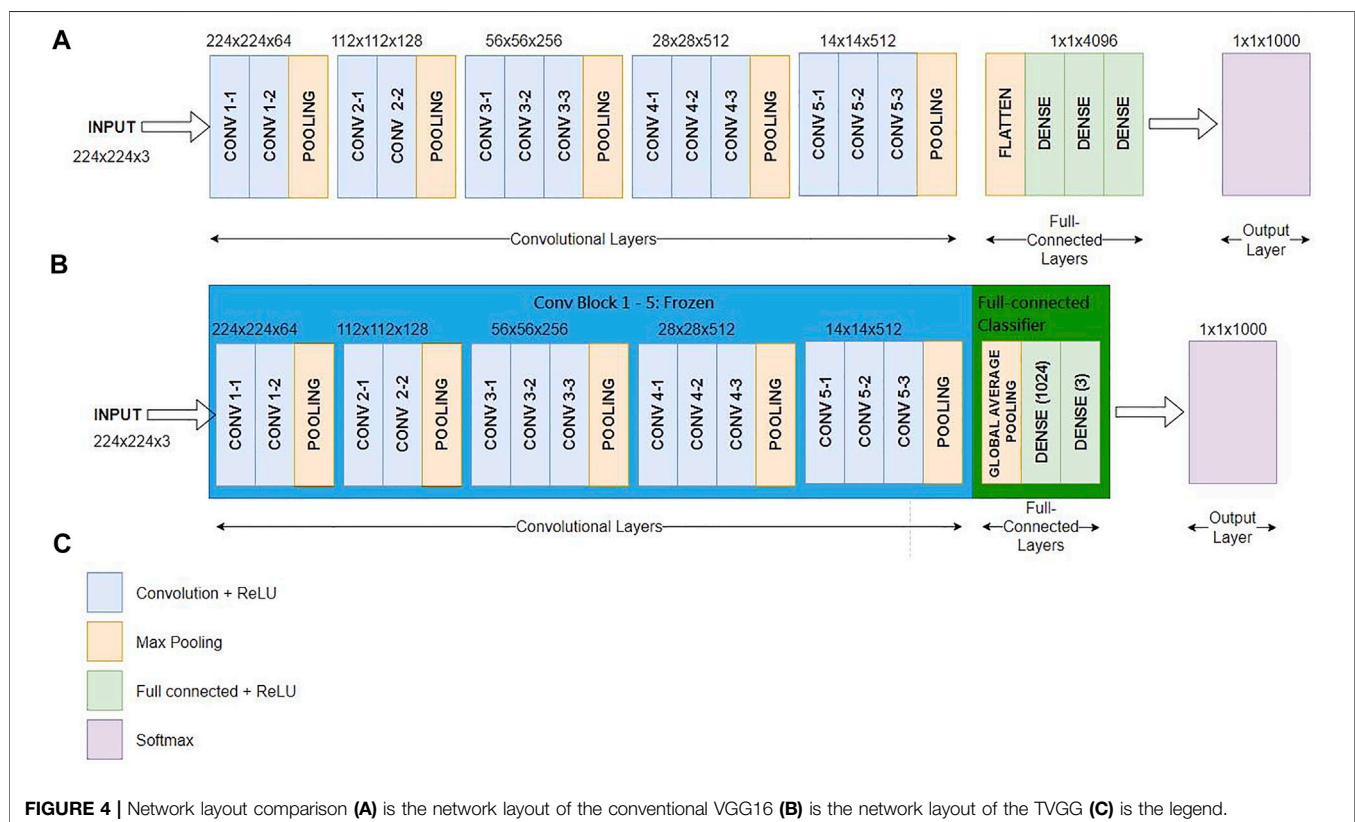
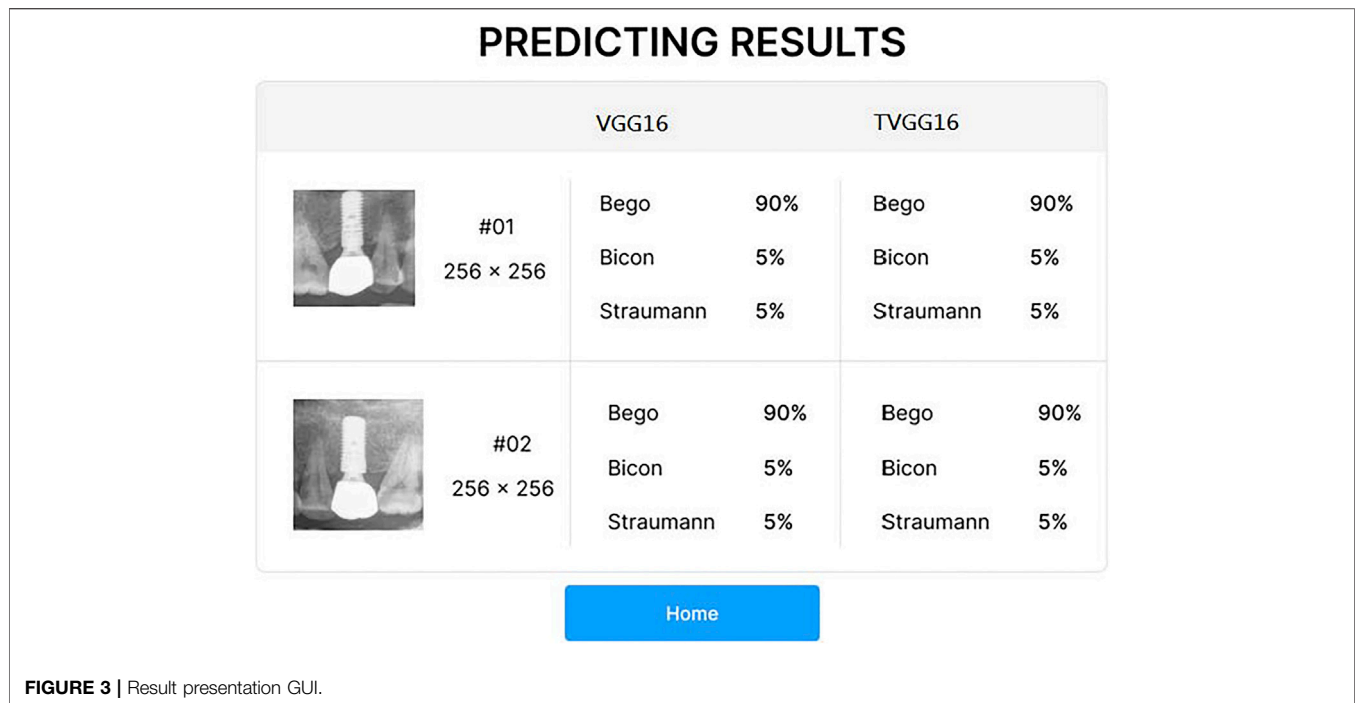


FIGURE 2 | GUI of the proposed system (A) is the entry GUI (B) is the model selection and RoI specification GUI.

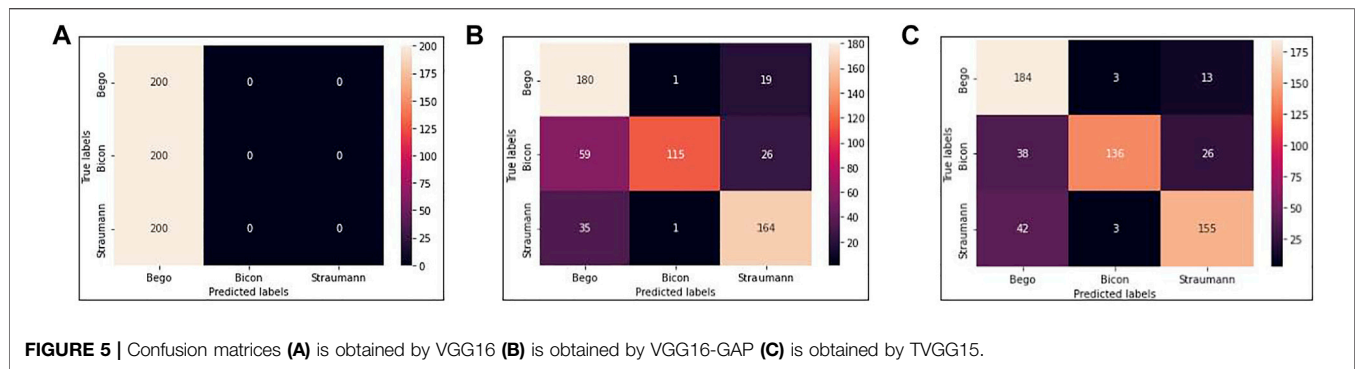
To make the system user friendly, the system is equipped with a graphical user interface (GUI), which is built by JavaScript with React plus the Flask API with Python. The model training is

completed offline. The trained model is stored and loaded on the server. When the user inputs a dental x-ray image, the GUI offers cropping boxes for users to pinpoint the region of interest (RoI).



The cropped image is further resized to fit the model's input and is uploaded from the client to the server for manufacturer identification. The identification results are collected from the

enabled models, stacked up as the final result, and returned to the user with probabilities corresponding to different manufacturers. The back-end, including model building, training and test, are

**TABLE 1 |** Evaluation matrices of all class.

Model	Bego			Bicon			Straumann		
	Precision	Recall	F ₁ -score	Precision	Recall	F ₁ -score	Precision	Recall	F ₁ -score
VGG16	0.33	1.00	0.50	0	0	0	0	0	0
VGG16-GAP	0.66	0.90	0.76	0.98	0.57	0.73	0.78	0.82	0.80
TVGG15	0.70	0.92	0.79	0.96	0.68	0.80	0.80	0.78	0.79

The bold values represents those presents the best across all methods.

processed via Python with Google Colab as the IDE. Amazon Web Services (AWS) is used to host the server and the database. The database stores the information about the RoIs and the information will be used if a user latches a ticket for correcting the identification result. The server is used to store the trained models and to process the user-input test image. Users can hook up to the system via any web browser and connect to the web server to pass the submitted test image to the back-end process. The GUI guides the user through the process of choosing the test images and the RoIs. The identification result will then be returned and displayed in the browser. Since the built-in models are treated as on-demand modules to be loaded depending on whether the user chooses to include them in the identification process, the designed system can be easily scaled up by integrating new models in the back-end. More details of the components in the proposed system are given in the following subsections.

3.1 Graphical User Interface

Considering the potential users of the proposed support system are not from the computer science background, a user-friendly interface is essential to lift the system's usability. Hence, the system is designed with a GUI instead of a command line-based interface. **Figure 2A** demonstrates the GUI of the system for users to upload the x-ray image, and select the size of the bounding box. **Figure 2B** shows the GUI for users to indicate the RoI and select models. Two standard sizes, e.g. 224×224 and 256×256 of the RoI are built into the system to match the input image size of the pre-trained models. After uploading the x-ray image, users can drag on the interface to draw the user-defined RoIs. Once the RoIs are drawn, the cropping function is triggered automatically and resizes the RoIs to fit in the model input size. Users can then tick the boxes to select which models are employed in the

TABLE 2 | Model training information.

	Precision	Recall	F ₁ -score
VGG16	0.11	0.33	0.17
VGG16-GAP	0.81	0.77	0.76
TVGG15	0.82	0.79	0.79

The bold values represents those presents the best across all methods.

identification process. Users can delete the RoIs or the uploaded image anytime before submitting them to the system by clicking the bin icon.

After the user clicks on the submission button, the RoIs are fed into the selected models on the server. After all models complete their prediction, the probabilities output from the selected models are returned for displaying on the system interface (see **Figure 3**). If the user clicks on the home button, the system returns to the entry page and stand-by to receive other dental x-ray images.

3.2 Thinner VGG (TVGG)

We choose VGG to be our base model for implementation because the existing study shows that VGG has more advantages in terms of energy consumption than other models (Canziani et al., 2017). As mentioned in **Section 2**, the monotone texture and patterns in the dental x-ray image caught our attention, and we assume that a simplified network structure is sufficient to cope with the implant manufacturer identification task. Nevertheless, adopting pre-trained models also has a strong point in reducing the training cost. If we remove layers in the model, we will need to start the training from scratch, which is much more resources and power-hungry than adopting the pre-trained model and performing fine-tuning. Aside from fine-tuning, we use the well-known dropout technique (Srivastava et al., 2014) as the tool to thinner the width of

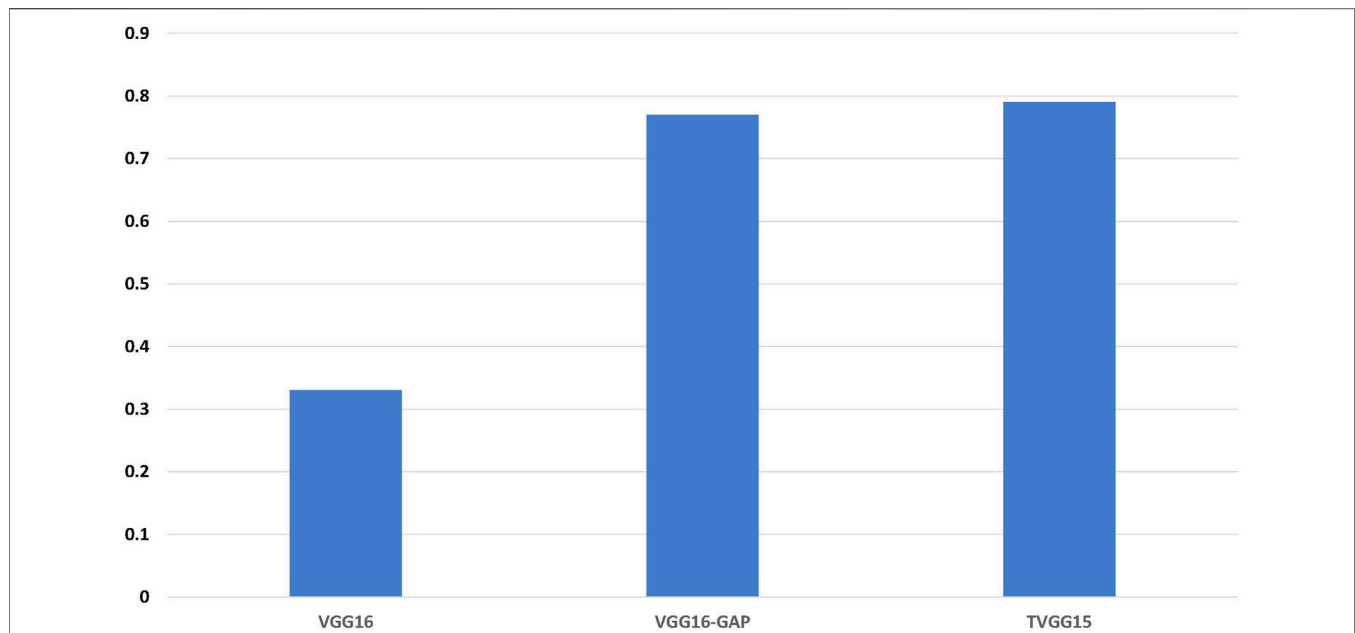


FIGURE 6 | Identification accuracy across all models.

TABLE 3 | Model training information.

	VGG16	VGG16-GAP	TVGG15
Occupied Storage	1.38 GB	272.4 MB	62.3 MB
Training Time (hours)	6.04	5.81	5.78
Best Training Accuracy	0.33	0.91	0.92
Best Validation Accuracy	0.33	0.88	0.89

The bold values represents those presents the best across all methods.

the dense layers. Dropout was originally proposed to prevent the network goes into overfitting. We adopt this technique but use its concept in removing neurons in the dense layers. Thus, this results in the dense layer in the modified VGG, e.g. the TVGG has much fewer neurons in the last few layers.

Figure 4A shows the conventional VGG16 layout (Simonyan and Zisserman, 2015), **Figure 4B** reveals our proposed TVGG layout, and **Figure 4C** presents the legend. Since the pre-trained VGG16 model is adopted as the base model, weights on the first-five convolution blocks are frozen in the training process. Only the weights on the full-connection layers are updated. Moreover, we replaced the original full connection layers from the flatten layer followed by three dense layers to the compact structure composed of the global average pooling and two dense layers. The dense layer size is also reduced by dropping out more than three-fourths of neurons.

4 EXPERIMENTS AND RESULT DISCUSSIONS

The experiments are conducted in Python with Google Colab. The training environment contains two virtual CPUs, 24GB

RAM, 150 GB storage space, and GPUs of K80, P100, and T4. Python libraries used in constructing the models include Tensorflow and Keras. Details of the experiment contents are described below.

4.1 Dataset

The dental x-ray images are collected at Fujian Medical University - Fujian Stomatological Hospital in P.R. China. It contains three classes of the dental implant manufacturer, namely, the Bego, the Bicon, and the Straumann, with 850, 892, and 527 x-ray images for the corresponding groups, respectively. This dataset is a hybrid of intraoral and extraoral x-ray images. Each of the classes contains both types of images. All collected x-ray images are containing implants from a single manufacturer. Mixture cases are not included in the collection.

4.2 Experiment Design

To ensure we have a balanced dataset across images from all manufacturers, data augmentation methods are used to expand the volume of the dataset to ensure all classes have the same quantity of data. Moreover, having data augmentation involved in the process helps avoid the overfitting issue. The methods used in the data augmentation process include a random rotation between $[-\frac{\pi}{9}, \frac{\pi}{9}]$ degrees, object shifting in both vertical and horizontal directions within a 20% range, cropping and zooming both within 20% range, and horizontal flipping. With the help of the data augmentation, our model is capable of adopting the implant facing multiple directions. Thus the RoIs are not rotated to a specific angle in the test phase of our design. In the end, we have 550, 185, and 200 images for training, validation, and test, respectively, for each class.

The structure of the conventional VGG16 and our proposed TVGG is described in **Section 3.2**. We add another VGG16 model for comparison but replace the flatten layer with the global-average-pooling to have more models for comparison. The Adam optimization is used in all models in the training phase.

4.3 Evaluation Criteria

The common evaluation criteria in classification, including precision, recall, f1-score, and accuracy, are used to quantify the experimental results. Let TP , FP , TN , and FN represent the true positive, false positive, true negative, and false negative, respectively; these matrices can be calculated by **Eqs 1–4**.

$$\text{Precision} = \frac{TP}{TP + FP} \quad (1)$$

$$\text{Recall} = \frac{TP}{TP + FN} \quad (2)$$

$$F_1 - \text{score} = \frac{TP}{TP + 0.5 \times (FP + FN)} \quad (3)$$

$$\text{Accuracy} = \frac{TP + TN}{TP + TN + FP + FN} \quad (4)$$

4.4 Experiment Results and Discussions

We use VGG16, VGG16-GAP, and TVGG15 to indicate the conventional VGG16 model, the conventional VGG16 but replacing the flatten layer with global-average-pooling, and the thinner VGG, respectively. **Figure 5** shows the confusion matrices from all models.

Our dataset size is relatively small compared to other studies. **Figure 5A** shows that using a small dataset to fine-tune the pre-trained VGG16 is not feasible because the training data volume is insufficient to support the tuning on a large scale of weights. Thus, we create the VGG16-GAP model to give the network a boost. From **Figure 5B**, the improvement is observable by the eye, and the correct classification results start to go across all classes. On the other hand, in the TVGG15 model, the correctly classified results (see **Figure 5C**) are getting higher than in the VGG16-GAP model.

Table 1 reveals the values from the evaluation matrices obtained by different implant manufacturers, namely, Bego, Bicon, and Straumann, respectively. The bold font marks the model performing the best in the column. It is observable that TVGG15 owns the most counts of achieving the best. The average performance across all classes is summarized in **Table 2**.

Figure 6 shows the accuracy calculated from the test results. TVGG15 presents the highest accuracy while VGG16-GAP achieves the second.

Table 3 shows the resource occupation, the training cost, and the training outcomes recorded by executing 200 epochs for each model. We can see that the TVGG15 model size is 2, 215 times less than VGG16 and 4.37 times less than VGG16-GAP. This compact characteristic gives TVGG15 an advantage in deploying the client-server internet environment. Moreover, by using the same resources for training the model, the training time of TVGG15 is reduced 4.3% than VGG16. The TVGG15 model also achieved the highest best training and validation accuracy.

5 CONCLUSION

In this work, we create a dentist supporting system for automatic dental implant manufacturer identification from the dental x-ray images. The proposed system uses the TVGG15 model, which is an improved version from the VGG16 model pre-trained by ImageNet. The experiment results indicate that the pre-trained VGG16 is too large to be fine-tuned with the available quantity of data in our study. However, the proposed TVGG15 presents a satisfactory result in the case that the available training data is limited. Moreover, the proposed model occupies 2, 215 times less storage resource for preserving the model parameters given that the structure is not only more compact but also much thinner than the conventional VGG16 model. To gain the advantage of using a pre-trained model, the modification is only applied to the full connection layers in the CNN structure.

The dataset used in the experiment contains dental implants from a single manufacturer in each x-ray image, and thus no mixture case is included. However, our proposed system crops images into multiple RoIs. Even if there is an x-ray image containing a mixture of dental implants from numerous manufacturers, the proposed system should also present its performance as stable on the same level as in the current experiments.

In terms of building an application system, we see the potential to adopt the ensemble learning structure into the system back-end to increase the number of available candidate models in the future work. Heterogeneous models are more preferred because they can discover different characteristics of the input data. Moreover, we plan to remove the option for selecting the RoI cropping size in the GUI and only keep the one to a greater extent. Although different pre-trained models may require other input image sizes, the smaller RoI can be obtained by applying proper down-sampling techniques in the back-end and automatically satisfying this need. Furthermore, we plan to use some intelligent optimization methods to extend the modifiable parameters from the dense layers to the convolutional layers. This is a potential way to further improve the performance of the models without retrain the whole models.

DATA AVAILABILITY STATEMENT

The datasets presented in this article are not readily available because the patients' data is not publicly accessible. Further inquiries can be directed to the corresponding author JG, jianbin@fjmu.edu.cn.

ETHICS STATEMENT

The studies involving human participants were reviewed and approved by Hospital of Stomatology, Fujian Medical University. Written informed consent for participation was not required for this study in accordance with the national legislation and the institutional requirements.

AUTHOR CONTRIBUTIONS

Data collection and ground truth establishment by JG and DW; System and framework design by JG, P-WT, XX; experiment data validation and check by JG and DW; GUI design by HD and NC; system implementation by QTV and CNK; experiment result validation by P-WT and XX; article writing by JG, P-WT, XX and DW.

REFERENCES

- Almubarak, H., Bazi, Y., and Alajlan, N. (2020). Two-Stage Mask-Rcnn Approach for Detecting and Segmenting the Optic Nerve Head, Optic Disc, and Optic Cup in Fundus Images. *Appl. Sci.* 10, 3833–3848. doi:10.3390/app10113833
- Canziani, A., Culurciello, E., and Paszker, A. (2017). An Analysis of Deep Neural Network Models for Practical Applications. *arXiv*. 1–12. doi:10.48550/arXiv.1605.07678
- Guarnieri, R., Di Nardo, D., Di Giorgio, G., Miccoli, G., and Testarelli, L. (2019). Clinical and Radiographics Results at 3 Years of Rct with Split-Mouth Design of Submerged vs. Nonsubmerged Single Laser-Microgrooved Implants in Posterior Areas. *Int. J. Implant Dent.* 5, 44–10. doi:10.1186/s40729-019-0196-0
- He, K., Gkioxari, G., Dollar, P., and Girshick, R. (2020). Mask R-Cnn. *IEEE Trans. Pattern Anal. Mach. Intell.* 42, 386–397. doi:10.1109/TPAMI.2018.2844175
- He, K., Zhang, X., Ren, S., and Sun, J. (2015). Deep Residual Learning for Image Recognition. *arXiv* 1–12. doi:10.48550/arXiv.1512.03385
- Iandola, F. N., Han, S., Moskewicz, M. W., Ashraf, K., Dally, W. J., and Keutzer, K. (2016). SqueezeNet: Alexnet-Level Accuracy with 50x Fewer Parameters and < 0.5mb Model Size. *arXiv*, 1–13. doi:10.48550/arXiv.1602.07360
- Kim, J. E., Nam, N. E., Shim, J. S., Jung, Y. H., Cho, B. H., and Hwang, J. J. (2020). Transfer Learning via Deep Neural Networks for Implant Fixture System Classification Using Periapical Radiographs. *J. Clin. Med.* 9, 1–11. doi:10.3390/jcm9041117
- Liu, M., Wang, S., Chen, H., and Liu, Y. (2022). A Pilot Study of a Deep Learning Approach to Detect Marginal Bone Loss Around Implants. *BMC Oral Health* 22, 1–8. doi:10.1186/s12903-021-02035-8
- Makary, C., Menhall, A., Zammari, C., Lombardi, T., Lee, S. Y., and Stacchi, C. (2019). Primary Stability Optimization by Using Fixtures with Different Thread Depth According to Bone Density: A Clinical Prospective Study on Early Loaded Implants. *Mater. (Basel)* 12, 1–15. doi:10.3390/ma12152398
- Ronneberger, O., Fischer, P., and Brox, T. (2015). “U-Net: Convolutional Networks for Biomedical Image Segmentation,” in *Medical Image Computing and Computer-Assisted Intervention – MICCAI 2015*. Editors N. Navab, J. Hornegger, W. M. Wells, and A. F. (Frangi (Germany: SpringerLink), 234–241. doi:10.1007/978-3-319-24574-4_28
- Saghiri, M. A., Asatourian, A., Kazerani, H., Gutmann, J. L., and Morgano, S. M. (2020). Effect of Thermocycling on the Surface Texture and Release of Titanium Particles from Titanium Alloy ($Ti_{6}Al_{4}V$) Plates and Dental Implants: An *In Vitro* Study. *J. Prosthet. Dent.* 124, 801–807. doi:10.1016/j.prosdent.2019.11.013

FUNDING

This work is supported by Fujian Provincial Natural Science Foundation (No. 2020J01646), Joint Funds for the Innovation of Science and Technology Fujian Province (No. 2020Y9031), Science and Technology Planning Project of Fujian Provincial Health Commission (No. 2021CXA035) and Fuzhou Science and Technology Planning Project (No. 2021-ZD-286).

- Sandler, M., Howard, A., Zhu, M., Zhmoginov, A., and Chen, L.-C. (2018). “Mobilenetv2: Inverted Residuals and Linear Bottlenecks,” in 2018 IEEE Conference on Computer Vision and Pattern Recognition (IEEE), 4510–4520. doi:10.1109/cvpr.2018.00474
- Simonyan, K., and Zisserman, A. (2015). “Very Deep Convolutional Networks for Large-Scale Image Recognition,” in The 3rd International Conference on Learning Representations (IEEE), 1–14.
- Srivastava, N., Hinton, G., Krizhevsky, A., Sutskever, I., and Salakhutdinov, R. (2014). Dropout: A Simple Way to Prevent Neural Networks from Overfitting. *J. Mach. Learn. Res.* 15, 1–30.
- Sukegawa, S., Yoshii, K., Hara, T., Yamashita, K., Nakano, K., Yamamoto, N., et al. (2020). Deep Neural Networks for Dental Implant System Classification. *Biomolecules* 10, 1–13. doi:10.3390/biom10070984
- Szegedy, C., Liu, W., Jia, Y., Sermanet, P., Reed, S., Anguelov, D., et al. (2015). “Going Deeper with Convolutions,” in 2015 IEEE Conference on Computer Vision and Pattern Recognition. Editors K. Grauman, E. Learned-Miller, A. Torralba, and A. Zisserman (IEEE), 1–9. doi:10.1109/cvpr.2015.7298594
- Vvola, A. O., Akram, S. U., and Kannala, J. (2019). “Mask-Rcnn and U-Net Ensembled for Nuclei Segmentation,” in 2019 IEEE 16th International Symposium on Biomedical Imaging (IEEE), 208–212.

Conflict of Interest: The authors declare that the research was conducted in the absence of any commercial or financial relationships that could be construed as a potential conflict of interest.

Publisher’s Note: All claims expressed in this article are solely those of the authors and do not necessarily represent those of their affiliated organizations, or those of the publisher, the editors and the reviewers. Any product that may be evaluated in this article, or claim that may be made by its manufacturer, is not guaranteed or endorsed by the publisher.

Copyright © 2022 Guo, Tsai, Xue, Wu, Van, Kaluarachchi, Dang and Chintha. This is an open-access article distributed under the terms of the Creative Commons Attribution License (CC BY). The use, distribution or reproduction in other forums is permitted, provided the original author(s) and the copyright owner(s) are credited and that the original publication in this journal is cited, in accordance with accepted academic practice. No use, distribution or reproduction is permitted which does not comply with these terms.



OPEN ACCESS

EDITED BY

Yuanpeng Zhang,
Nantong University, China

REVIEWED BY

Sun Lin,
Shandong University of Science and
Technology, China
Hongyi Fang,
Southeast University, China

*CORRESPONDENCE

Cai-Bin Huang,
hcbgmua@126.com

SPECIALTY SECTION

This article was submitted to
Experimental Pharmacology and Drug
Discovery,
a section of the journal
Frontiers in Pharmacology

RECEIVED 14 June 2022

ACCEPTED 07 July 2022

PUBLISHED 16 August 2022

CITATION

Guo D-F, Fan L-W, Le Q and Huang C-B
(2022), Transjugular intrahepatic
portosystemic shunt for the prevention
of rebleeding in patients with cirrhosis
and portal vein thrombosis: Systematic
review and meta-analysis.
Front. Pharmacol. 13:968988.
doi: 10.3389/fphar.2022.968988

COPYRIGHT

© 2022 Guo, Fan, Le and Huang. This is
an open-access article distributed
under the terms of the [Creative
Commons Attribution License \(CC BY\)](#).
The use, distribution or reproduction in
other forums is permitted, provided the
original author(s) and the copyright
owner(s) are credited and that the
original publication in this journal is
cited, in accordance with accepted
academic practice. No use, distribution
or reproduction is permitted which does
not comply with these terms.

Transjugular intrahepatic portosystemic shunt for the prevention of rebleeding in patients with cirrhosis and portal vein thrombosis: Systematic review and meta-analysis

Ding-Fan Guo¹, Lin-Wei Fan^{2,3}, Qi Le⁴ and Cai-Bin Huang^{1*}

¹Department of Gastroenterology, The First Affiliated Hospital of Gannan Medical University, Ganzhou, China, ²The First Clinical Medical School of Nanchang University, Nanchang, China, ³Key Laboratory of Jiangxi Province for Transfusion Medicine, The First Affiliated Hospital of Nanchang University, Nanchang, China, ⁴Department of General Surgery, The First Hospital of Lanzhou University, Lanzhou, China

Background: Transjugular intrahepatic portosystemic shunt (TIPS) has been performed on patients with cirrhosis and portal vein thrombosis (PVT) to prevent rebleeding; however, the associated evidence is scarce. Hence, the study aimed to evaluate the feasibility and efficacy of TIPS in patients with cirrhosis and PVT and promote personalized treatment in such patients.

Methods: Literature was systematically obtained from PubMed, EMBASE, Cochrane Library, and Web of Science. Data from the included studies were extracted, and meta-analyses by the random effects model were used to pool data across studies. Heterogeneity was assessed using Cochran's Q and I² statistics. The source of heterogeneity was explored using subgroup analyses and meta-regressions.

Results: A total of 11 studies comprising 703 patients with cirrhosis and portal vein thrombosis (PVT: complete, 32.2%; chronic, 90.2%; superior mesenteric vein or splenic vein involvement, 55.2%; cavernous transformation, 26.8%) were included. TIPS showed feasibility in 95% of the cases (95% confidence interval [CI]: 89%–99%) with heterogeneity (I² = 84%, $p < 0.01$) due to cavernous transformation. The pooled rebleeding rate was 13% (95% CI: 7%–20%) with heterogeneity (I² = 75%, $p < 0.01$) explained by chronic PVT and anticoagulation (AC) therapy. Hepatic encephalopathy occurred in 32% of patients. The survival rate, portal vein recanalization rate, and shunt patency rate were 80%, 82%, and 77%, respectively.

Abbreviations: AC, Anticoagulation; CTPV, Cavernous transformation of the portal vein; CI, Confidence interval; HE, Hepatic encephalopathy; MELD, Model for end-stage liver disease; NSBBs, Non-selective beta-blockers; PVT, Portal vein thrombosis; RCTs, Randomized clinical trials; LT, Liver transplantation; LWMH, Low-molecular-weight heparin; PV, Portal vein; PPG, Portosystemic pressure gradient; PH, Portal hypertension; SMV, Superior mesenteric vein; SV, Splenic vein; VB, Variceal bleeding; TJ, Transjugular; TH, Transhepatic; TS, Transsplenic; TIPS, Transjugular intrahepatic portosystemic shunts.

Conclusion: TIPS is feasible and effectively prevents rebleeding in patients with cirrhosis and PVT, regardless of cavernous transformation of the portal vein. Due to a potentially high risk of rebleeding and no apparent benefits of AC, post-TIPS AC must be employed cautiously.

Systematic Review Registration: [https://www.crd.york.ac.uk/PROSPERO/display_record.php?RecordID=258765], identifier [CRD42021258765].

KEYWORDS

transjugular intrahepatic portosystemic shunt, liver cirrhosis, portal vein thrombosis, meta-analysis, systematic review

Introduction

Non-neoplastic portal vein thrombosis (PVT) is a prevalent complication of liver cirrhosis, with incidence rates ranging from 10% to 23% (Qi et al., 2014; Harding et al., 2015). PVT raises portal vein pressure and reduces blood flow to the liver, worsening liver function, which is a hallmark of poor outcomes (Englesbe et al., 2010a; Werner et al., 2013). In addition, PVT increases mortality after liver transplantation and contraindicates the procedure when the thrombus extends to the superior mesenteric or splenic vein (Englesbe et al., 2010b). Variceal bleeding (VB) is a life-threatening complication with a 6-weeks mortality rate of 20% (Sarin et al., 2011). PVT increases the threat of VB and sometimes death by potentially increasing the portal vein pressure (Englesbe et al., 2010a).

At present, no consensus or guideline elucidates the optimal prophylactic treatment for patients with cirrhosis with VB and PVT. Standard treatments, including endoscopic treatments such as endoscopic band ligation and non-selective beta-blockers (NSBB), provide an effect to achieve immediate hemostasis and maximize the prevention of rebleeding (de Franchis, 2015). Transjugular intrahepatic portosystemic shunt (TIPS) is advised when patients fail to respond to endoscopic therapy and NSBB (de Franchis, 2015). Studies have reported that patients with cirrhosis and PVT require long time to achieve complete variceal eradication (Englesbe et al., 2010a; Dell'Era et al., 2014). Moreover, PVT may aggravate VB after endoscopic variceal ligation (Huang et al., 2020). Endoscopic treatments such as endoscopic band ligation are disconnection procedures that increase portal vein pressure. The side effects of NSBB treatment may lead to thrombus formation by reducing splanchnic blood flow (Groszmann et al., 2005). Hence, the standard treatments have limitations.

Recent advances in interventional radiological techniques and refinement of stent materials could facilitate the use of TIPS in complex cases, even with cavernous transformation of the portal vein (CTPV), which has been viewed as a contraindication in the past (Boyer and Haskal, 2010; Han et al., 2011). Studies have investigated the efficacy and safety of TIPS in patients with cirrhosis and PVT (Van Ha et al., 2006; Han et al., 2011; Luca et al., 2011; Luo et al., 2015; Wang et al., 2015; Lakhoo and Gaba, 2016; Qi et al., 2016; Wang et al., 2016; Luo et al., 2018; Lv et al.,

2018; Lv et al., 2021). Two randomized clinical trials (RCT) reported that TIPS placement effectively prevented recurrent VB in patients with cirrhosis and PVT (Luo et al., 2015; Lv et al., 2018).

However, implementation of TIPS in a clinical setting is low due to the lack of consensus on the details of TIPS in preventing rebleeding in patients with cirrhosis and PVT. Hence, the present study conducted a systematic review and meta-analysis on the feasibility and efficacy of TIPS in preventing rebleeding in patients with cirrhosis and PVT to facilitate personalized treatment.

Methods

This systematic review was conducted according to the Preferred Reporting Items for Systematic Reviews and Meta-Analyses statement and registered with PROSPERO (CRD 42021258765) (Page et al., 2021).

The following definitions were adopted in the study: Complete PVT was defined as an occlusion that occupied the entire crucial portal vein vessel lumen. Chronic PVT was defined as the presence of portal cavernoma, replacement of the original principal portal vein with a fibrotic cord, or a low intraluminal density on contrast-enhanced computed tomography (CT) (Lv et al., 2018). Post-TIPS anticoagulation (AC) was defined as a long-term AC (warfarin and other anticoagulant drugs for at least 6 months) after TIPS. Technical feasibility was defined as successful access to the portal vein, formation of an intrahepatic shunt between the hepatic and portal veins, and placement of stents. Recanalization was defined as the complete disappearance of the previous thrombosis.

Search strategy

PubMed, Cochrane Library, EMBASE, and Web of Science were searched systematically from the inception to October 2021. Search terms, such as liver cirrhosis, hepatic fibrosis, and portal vein thrombosis, were devised for the population, whereas TIPS and transjugular intrahepatic portosystemic shunt were devised for the intervention. The medical subject heading, Embase subject heading, and free text terms were used to maximize search sensitivity.

Study selection and data extraction

The inclusion and exclusion criteria were predefined to reduce the risk of bias. The inclusion criteria were as follows: 1) patients with cirrhosis and PVT diagnosed using imaging; 2) patients receiving TIPS to treat VB; and 3) reported rebleeding and clinical outcomes. The exclusion criteria were as follows: 1) letters, editorials, case reports, reviews, and animal experiments; 2) studies unavailable in English or Chinese; 3) patients with cancer or Budd–Chiari syndrome; 4) exclusively postoperative PVT; 5) follow-up period <6 months; and 6) insufficient outcome data. The articles with the highest number of cases or the most applicable information were selected in the case of studies with multiple publications. Two authors, D.F. Guo and L.W. Fan screened the titles and abstracts identified in the literature search and scrutinized the potentially eligible studies by reading full texts, extracting the following information: 1) Characteristics of the included studies and patient populations: first author, publication year, country, study design, and the number of patients, age, sex, etiology of cirrhosis, Child-Pugh classification, Model for end-stage liver disease score, and thrombosis characteristics; 2) characteristics of TIPS placement: indication for TIPS, approach to the portal vein, types of stents, related AC therapy, portosystemic pressure gradient (PPG) reduction, and additional procedures; and 3) clinical follow-up: the number and proportion of patients with rebleeding, hepatic encephalopathy (HE), survival, recanalization, shunt patency, and technical feasibility. Moreover, relevant information was obtained from the authors whose studies lacked critical information.

Most discrepancies in opinions were resolved through discussion between the two authors. If unresolved, the opinion of the third author (C.B. Huang) was sought.

Quality assessment

D.F. Guo and L.W. Fan independently assessed all the included articles. The quality assessments for non-randomized and randomized studies were conducted using the risk of bias in non-randomized studies of interventions tool (Sterne et al., 2016) and the Cochrane risk of bias 2.0 tool (Sterne et al., 2019), respectively.

Statistical analysis

A meta-analysis was performed to devise the pooled proportions and 95% confidence interval (CI), followed by Freeman–Tukey double arcsine transformation of the raw proportions (Barendregt et al., 2013). Assuming that heterogeneity was present among the participant studies, calculations were determined using the random effects model. Heterogeneity among studies was evaluated using the Cochran's Q test ($p < 0.1$ was considered significant) and I^2 statistic (values of 25%, 50%, and 75% indicated low, moderate, and high degrees of

heterogeneity, respectively) (Higgins et al., 2003; Huedo-Medina et al., 2006). Potential factors associated with the heterogeneity were examined using subgroup analysis and a meta-regression model. Several predefined potential confounders were considered in the subgroup analysis and meta-regression model: study design, the proportions of complete and chronic PVT, CTPV, superior mesenteric vein (SMV), or splenic vein (SV) involvement, covered stent, approach to PV, and post-TIPS AC. Publication bias was assessed using Egger's linear regression test and funnel plot (the number of included studies was ≥ 10). Statistical analysis was performed using the R software (version 4.1.0; R Foundation Inc.; <http://cran.r-project.org/>).

Results

Study selection and quality assessment

After the initial search, 1,439 citations were retrieved from the database. After removing the duplicate results, 986 records were selected for screening. Of these, 11 full-text articles followed the predefined criteria and were included in the meta-analysis (Van Ha et al., 2006; Han et al., 2011; Luca et al., 2011; Luo et al., 2015; Wang et al., 2015; Lakhoo and Gaba, 2016; Qi et al., 2016; Wang et al., 2016; Luo et al., 2018; Lv et al., 2018; Lv et al., 2021). A flowchart illustrating the study selection process is shown in Figure 1. The quality of the studies was estimated, and the risk of bias is shown in Supplementary Figure S1.

Characteristics of included studies and patients

As shown in Table 1, 11 studies (3 RCT and 8 observational studies) published over the last 15 years were included in the meta-analysis. Eight, two, and one studies were performed in China, America, and Italy, respectively. Many studies were excluded due to the inclusion of cancer or Budd–Chiari syndrome. Most studies reported that the leading etiology of cirrhosis is viral hepatitis. PVT was complete and chronic in 32.2% and 90.2% of cases, respectively, SMV or SV involvement was present in 55.2% of cases, and cavernous transformation was observed in 26.8% of cases.

Application of TIPS technique and its technical feasibility

As shown in Table 2, the main indication for TIPS was portal hypertension, a complication of cirrhosis. Two studies reported an additional indication of maintaining the portal vein patency before liver transplantation. All studies included patients with VB. Other complications, such as refractory ascites and

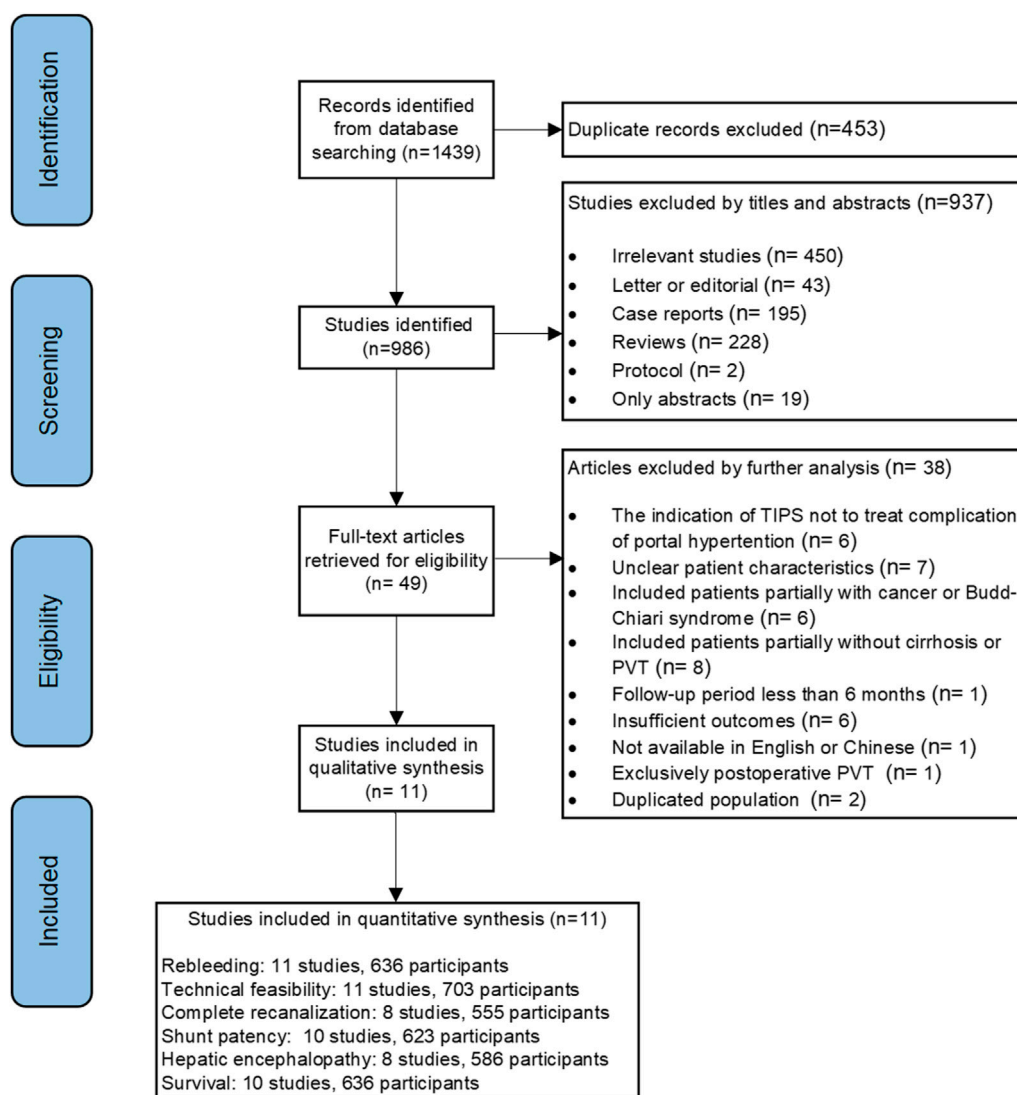


FIGURE 1

Flowchart showing the selection of studies for the present systematic review and meta-analysis.

refractory hydrothorax, were also observed. In five studies, the traditional transjugular approach to the portal vein was used, and in one study, the transhepatic approach was used. In the other five studies, the transhepatic/transsplenic approach to the portal vein was used when the traditional transjugular approach failed. In nine studies, concomitant variceal embolization and local thrombolysis were employed. In two studies, the bare-metal stents to complete shunt creation were employed, whereas, in nine studies, covered stents were employed. Different covered stents, including the viatorr, fluency, and unspecified expanded polytetrafluoroethylene stent grafts, were employed in the studies. In seven studies, post-TIPS AC was used. Anticoagulant methods included oral warfarin and low-

molecular-weight heparin. PPG reduction ranged from 10 to 19 mm Hg.

The forest plot showed the feasibility rate for each study and a pooled rate of 95% (95% CI: 89%–99%) with high heterogeneity ($I^2 = 84\%$, $p < 0.01$) (Figure 2). The rate in the studies that excluded patients with CTPV increased to 100% (95% CI: 98%–100%) without heterogeneity ($I^2 = 0\%$, $p = 0.94$). A similar result was found in five studies using only the transjugular approach, with the pooled rate of 100% (95% CI: 98%–100%) without heterogeneity ($I^2 = 0\%$, $p = 0.98$). The subgroup analyses are shown in Figure 3. Publication bias was not significant (Egger's test, $z = 1.02$, $p = 0.33$) (Supplementary Figure S2A).

TABLE 1 Characteristics of the included studies and patient populations.

Study	Country	Design	Patients number	Male (%)	Age	Etiology, viral/other	Child-pugh A/B/C	MELD score	Characteristics of PVT			
									Complete(%)	Chronic (%)	SMV or SV(%)	CTPV (%)
Lv et al. (2021)	China	Prospective	324	195 (60.2)	52.6	264/60	102/183/39	11.8	94/324 (29.0)	N/A	192/324 (59.3)	107/324 (33.0)
Luo et al. (2018)	China	Retrospective	24	19 (79.2)	44.6	17/7	7/14/3	10.7	24/24 (100.0)	24/24 (100.0)	3/24 (12.5)	N/A
Lv et al. (2018)	China	RCT	24	13 (54.2)	49.0 ^a	21/3	9/13/2	12.0 ^a	8/24 (33.3)	22/24 (91.7)	22/24 (91.7)	11/24 (45.8)
Wang et al. (2016)	China	RCT	64	38 (59.4)	54.8	53/11	24/32/8	10.8	N/A	61/64 (95.3)	24/64 (37.5)	4/64 (6.3)
Qi et al. (2016)	China	Prospective	51	31 (60.8)	51.5	35/16	8/34/9	8.1	23/51 (45.1)	N/A	N/A	24/51 (47.1)
Lakhoo and Gaba, (2016)	America	Retrospective	12	5 (41.7)	63.0 ^a	3/9	4/5/3	15.0 ^a	0/12 (0)	7/12 (58.3)	9/12 (75.0)	0/12 (0)
Wang et al. (2015)	China	Retrospective	25	22 (88.0)	47.3	22/3	3/20/2	12.0	2/25 (8.0)	25/25 (100.0)	4/25 (16.0)	0/25 (0)
Luo et al. (2015)	China	RCT	37	19 (51.4)	50.8	30/7	0/25/12	14.2	13/37 (35.1)	37/37 (100.0)	N/A	0/37 (0)
Luca et al. (2011)	Italy	Retrospective	70	47 (67.1)	55.0	43/27	17/42/11	11.6	24/70 (34.3)	52/70 (74.3)	52/70 (74.3)	2/70 (2.9)
Han et al. (2011)	China	Retrospective	57	20 (35.1)	50.0	40/17	25/26/6	N/A	14/57 (24.6)	57/57 (100.0)	N/A	30/57 (52.6)
Van Ha et al. (2006)	America	Retrospective	15	12 (80.0)	53.0 ^a	N/A	0/11/4	18.3	4/15 (26.7)	11/15 (73.3)	2/15 (13.3)	4/15 (26.7)

MELD, Model for End-Stage Liver Disease; PVT, portal vein thrombosis; SMV, superior mesenteric vein; SV, splenic vein; CTPV, cavernous transformation of portal vein; RCT, randomized controlled trial; N/A, not accessible.

^aData was expressed as median.

TABLE 2 Characteristics of TIPS placement.

Study	Indication for TIPS	Approach to PV	Additional procedure	Covered stents (%)	AC post-TIPS (%)	AC methods	PPG (mmHg)		
							Before TIPS	After TIPS	Reduction
Lv et al. (2021)	PH complication	TJ, TH, TS	Some used variceal embolization	285/285 (100.0)	197/285 (69.1)	Oral warfarin	23.0	8.3	15.7
Luo et al. (2018)	PH complication	TH	Some used variceal embolization	22/22 (100.0)	21/22 (95.5)	LMWH, oral warfarin	22.0	10.6	11.4
Lv et al. (2018)	PH complication	TJ, TH, TS	5 used local thrombolysis, 7 used variceal embolization	23/23 (100.0)	21/23 (91.3)	LMWH, oral warfarin	27.7	8.7	19.0
Wang et al. (2016)	PH complication	TJ	some used mechanical lysis with a balloon catheter	64/64 (100.0)	31/64 (48.4)	LMWH, oral warfarin	21.2	9.8	11.4
Qi et al. (2016)	PH complication	TJ, TH, TS		26/43 (60.5)	0/43 (0)		N/A	N/A	N/A
Lakhoo and Gaba, (2016)	PH complication, PV patency pre-LT	TJ	3 used variceal embolization	12/12 (100.0)	0/12 (0) ^a		18.0	8.0	10.0
Wang et al. (2015)	PH complication	TJ	some used variceal embolization	25/25 (100.0)	25/25 (100.0)	Oral warfarin	20.4	9.1	11.3
Luo et al. (2015)	PH complication	TJ	21 used variceal embolization	37/37(100.0)	37/37 (100.0)	LMWH, oral warfarin	27.5	10.4	17.1
Luca et al. (2011)	PH complication, PV patency pre-LT	TJ	1 used variceal embolization	57/70 (81.4)	0/70 (0)		20.8	8.5	12.3
Han et al. (2011)	PH complication	TJ, TH, TS		0/43 (0)	43/43 (100.0)	LMWH, oral warfarin	25.7	14.0	11.7
Van Ha et al. (2006)	PH complication	TJ, TH	1 used local thrombolysis	0/13 (0)	0/13 (0) ^a		20.0	8.0	12.0

TIPS, transjugular intrahepatic portosystemic shunt; PV, portal vein; AC, anticoagulation; PPG, portosystemic pressure gradient; PH, portal hypertension; TJ, transjugular; TH, transhepatic; TS, transsplenic; LT, liver transplantation; LMWH, low-molecular-weight heparin; N/A, not accessible.

^aAnticoagulant time was less than 6 months.

Rebleeding

All studies reported the overall rebleeding rate ranging from 0% to 27.9% (Table 3). The pooled rebleeding rate was 13% (95% CI: 7%–20%) with high heterogeneity ($I^2 = 75\%$, $p < 0.01$) (Figure 4). The rebleeding rate in four studies that exclusively included patients with chronic PVT increased to 23% (95% CI: 16%–31%) without heterogeneity ($I^2 = 0\%$, $p = 0.89$). Studies that involved not less than 90% of patients receiving AC showed an elevated pooled rebleeding rate of 23%. No heterogeneity was observed in this subgroup ($I^2 = 0\%$, $p = 0.96$). Other factors associated with the heterogeneity were not confirmed. The subgroup analyses are shown in Figure 5. Funnel plot and Egger's test ($z = 0.07$, $p = 0.94$) showed no significant publication bias (Supplementary Figure S2B).

Hepatic encephalopathy and survival

HE incidence was reported in 8 of 11 studies and varied among studies, ranging from 14% to 60.5% (Table 3). The

pooled rate was 32% (95% CI: 24%–42%) with moderate heterogeneity ($I^2 = 69\%$, $p < 0.01$) (Figure 6). The remaining studies, excluding those that included patients with chronic PVT, showed an HE incidence of 26% (95% CI: 19%–33%) with no heterogeneity ($I^2 = 0\%$, $p = 0.38$). Regarding the extent of PVT, the HE incidence was lower in studies that included 30% of patients with SMV or SV than that in the remaining studies (20% vs. 29%, respectively). Heterogeneity among these studies was not significant ($I^2 = 0\%$, $p = 0.87$). The HE incidence was 30% (95% CI: 22%–39%) in studies using post-TIPS AC with low heterogeneity ($I^2 = 10\%$, $p = 0.34$). These subgroup analyses are shown in Supplementary Figure S3. The publication bias was not examined due to the low number of studies.

All 11 studies were included in the meta-analysis of survival rates. The pooled survival rate for all studies was 80% (95% CI: 71%–87%) with high heterogeneity ($I^2 = 78\%$, $p < 0.01$) (Figure 7). In the studies using post-TIPS AC, the survival rate was similar (76%; 95% CI: 68%–84%) with low heterogeneity ($I^2 = 19\%$, $p = 0.31$). These subgroup analyses are shown in Supplementary Figure S4. Egger's test ($z = 0.30$,

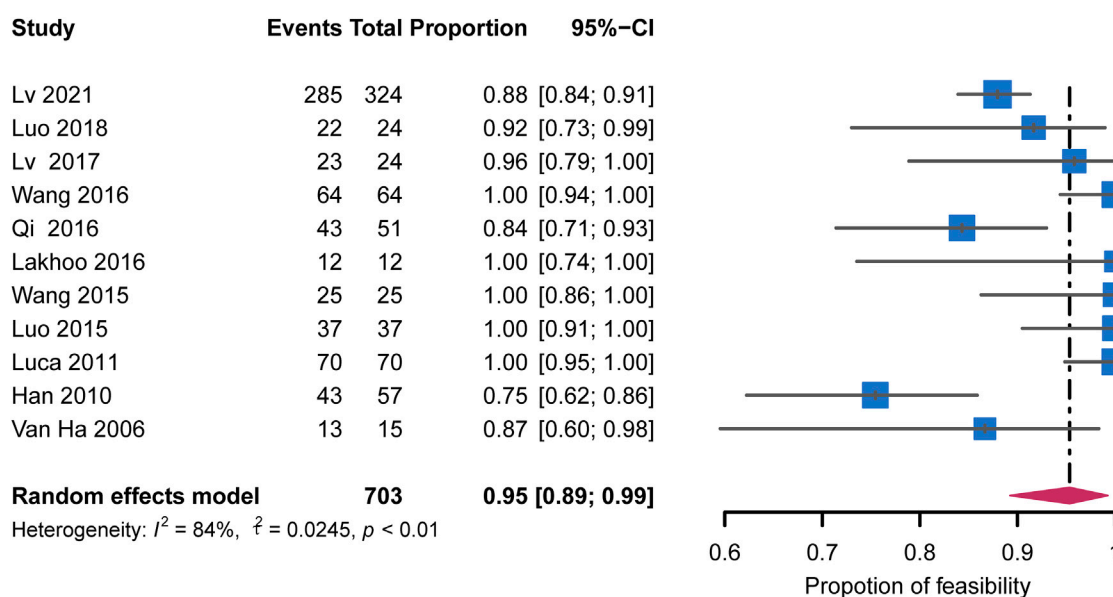


FIGURE 2
Forest plots for pooled rates of technical feasibility.

$p = 0.77$) showed no significant publication bias (Supplementary Figure S2C).

Portal vein recanalization and shunt patency

Eight studies reported data on complete recanalization. The recanalization rate ranged from 57.1 to 93.7%, with a pooled rate of 82% (95% CI: 67%–93%; $I^2 = 92\%$) (Supplementary Figure S5). The recanalization rate of studies involving at most 30% of patients with SMV or SV was 81% (95% CI: 71%–88%). Heterogeneity among these studies was not significant ($I^2 = 0\%$, $p = 0.38$). The subgroup analysis is shown in Supplementary Figure S6. The publication bias was not estimated since the number of studies was <10 .

Shunt patency rates were reported in 10 studies, and the pooled rate was 77% (95% CI: 69%–83%; $I^2 = 63\%$) (Supplementary Figure S7). Egger's test ($z = 0.22$, $p = 0.83$) showed no significant publication bias (Supplementary Figure S2D).

Subgroup analysis

The studies were divided into subgroups based on the distribution of observed characteristics, as shown in Figures 3, 5. All other subgroup analysis results, which have been discussed above, are provided in the Supplementary Figures.

Meta-regression analysis

Meta-regression was performed on technical feasibility, rebleeding, and survival. As shown in Table 4, a transhepatic/transsplenic approach to the portal vein was significantly associated with a decreased technical feasibility rate. In contrast, AC therapy post-TIPS was significantly associated with a higher rebleeding rate. Due to insufficient data, the meta-regression analysis was not conducted for other factors and outcomes.

Discussion

The present systematic review and meta-analysis comprehensively and strictly examined three RCT and eight non-RCT studies to evaluate the feasibility and efficacy of TIPS in preventing rebleeding in patients with cirrhosis and PVT. The pooled analyses revealed that TIPS implantation was significantly feasible in most cases (95%). Regarding the clinical outcome, the pooled rebleeding rate was 13%, HE incidence was 32%, survival rate was 80%, recanalization rate was 82%, and shunt patency rate was 77%. These results showed that TIPS was significantly associated with effective prevention of rebleeding and high survival rate.

A previous meta-analysis of 12 studies designed to investigate the outcome of TIPS in patients with cirrhosis and PVT suggested that portal hypertension-associated complications are indications for TIPS (Zhang et al., 2021). The present

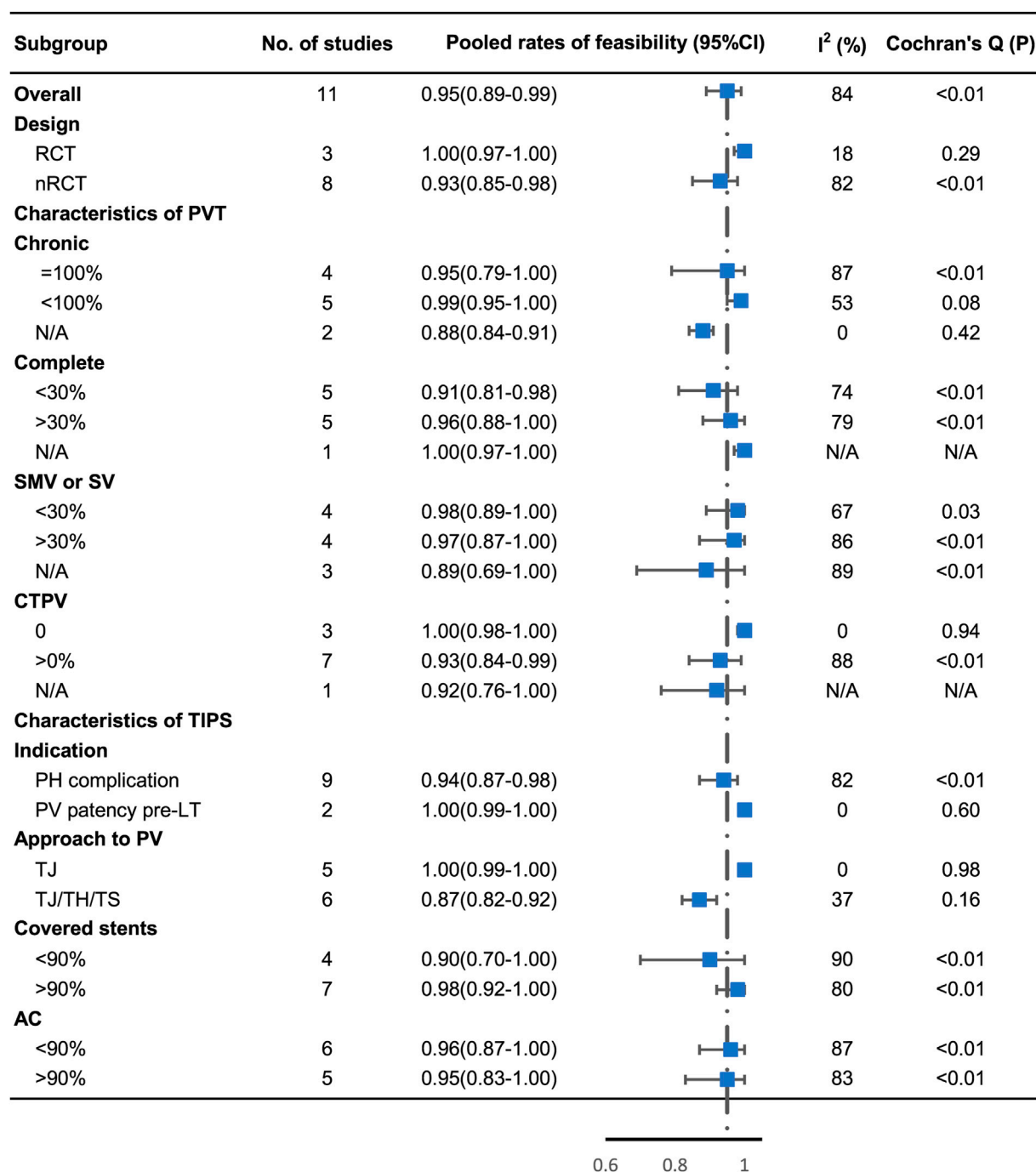


FIGURE 3

Subgroup analysis of technical feasibility by study design, proportion of complete and chronic PVT, proportion of CTPV, proportion of involvement of SMV or SV, indication of TIPS, approach to PV, proportion of covered stent, and proportion of post-TIPS AC.

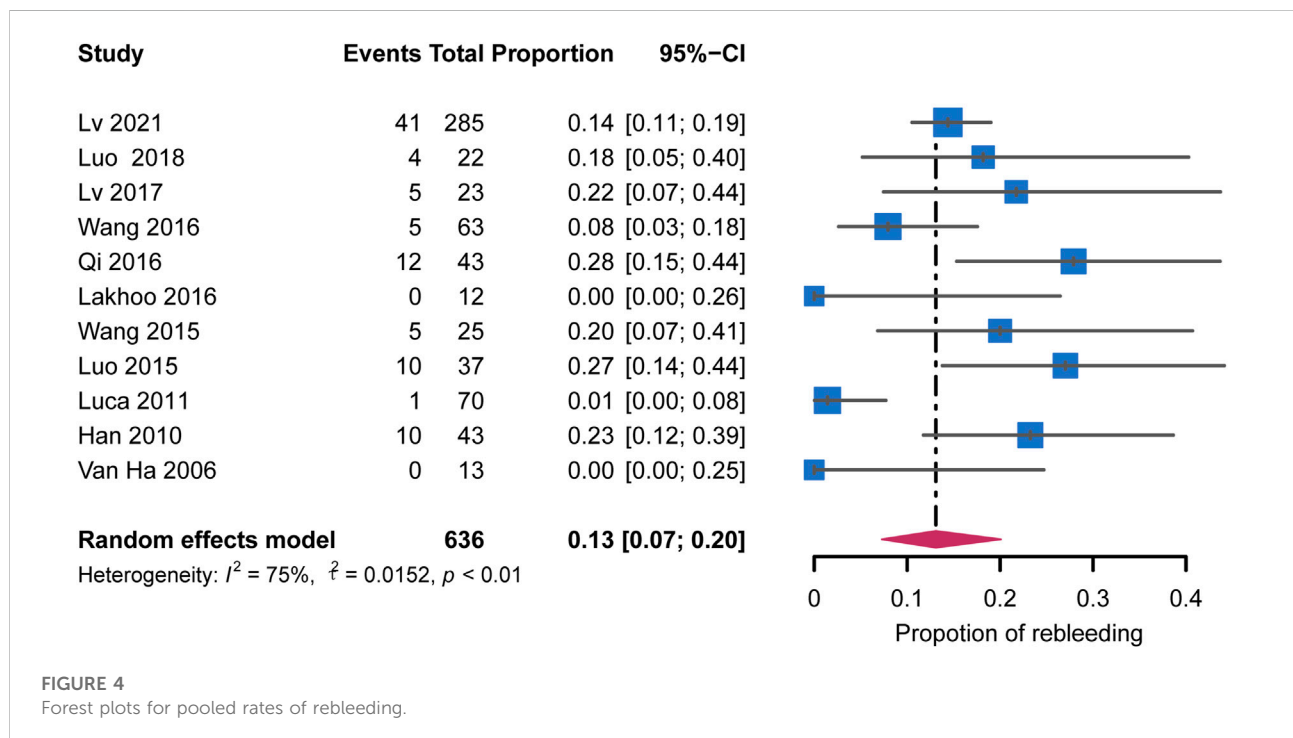
study had some limitations. First, the low number of records available through database search showed that a comprehensive literature search was not performed, potentially producing biased results. Second, high heterogeneity in several analyses may have hindered the robust conclusions and recommendations.

Unfortunately, the potential sources of heterogeneity and rebleeding-related clinical outcomes were not identified and discussed. Hence, further investigation is warranted to estimate the real benefit of TIPS before its widespread application.

TABLE 3 Clinical follow-up.

Study	Technical feasibility (%)	Rebleeding (%)	HE (%)	Survival (%)	Complete recanalization (%)	Shunt patency (%)	Follow-up time (months)
Lv et al. (2021)	285/324 (88.0)	41/285 (14.4)	82/285 (14.0)	210/285 (73.7)	267/285 (93.7)	217/285 (76.1)	>6.0
Luo et al. (2018)	22/24 (91.7)	4/22 (18.2)	4/22 (18.2)	19/22 (86.4)	N/A	17/22 (77.3)	34.0
Lv et al. (2018)	23/24 (95.8)	5/23 (21.7)	6/23 (26.1)	15/23 (65.2)	19/22 (86.4)	19/22 (86.4)	30.9 ^a
Wang et al. (2016)	64/64 (100.0)	5/63 (7.9)	13/63 (20.6)	62/63 (98.4)	49/63 (77.8)	58/63 (92.1)	12.0
Qi et al. (2016)	43/51 (84.3)	12/43 (27.9)	26/43 (60.5)	27/43 (62.8)	N/A	32/43 (74.4)	40.1 ^a
Lakhoo and Gaba, (2016)	12/12 (100.0)	0/12 (0)	N/A	9/12 (75.0)	7/12 (58.3)	N/A	15.0 ^a
Wang et al. (2015)	25/25 (100.0)	5/25 (20.0)	N/A	20/25 (80.0)	20/23 (87.0)	20/25 (80.0)	25.6
Luo et al. (2015)	37/37 (100.0)	10/37 (27.0)	15/37 (40.5)	25/37 (67.6)	24/37 (64.9)	25/37 (67.6)	22.8
Luca et al. (2011)	70/70 (100)	1/70 (1.4)	22/70 (31.4)	60/70 (85.7)	40/70 (57.1)	43/70 (61.4)	23.4 ^a
Han et al. (2011)	43/57 (75.5)	10/43 (23.3)	13/43 (30.2)	35/43 (81.4)	43/43 (100.0)	26/43 (60.5)	>6.0
Van Ha et al. (2006)	13/15 (86.7)	0/13 (0)	N/A	11/13 (84.6)	N/A	12/13 (92.3)	17.0 ^a

HE, hepatic encephalopathy; N/A, not accessible.

^aData was expressed as median.

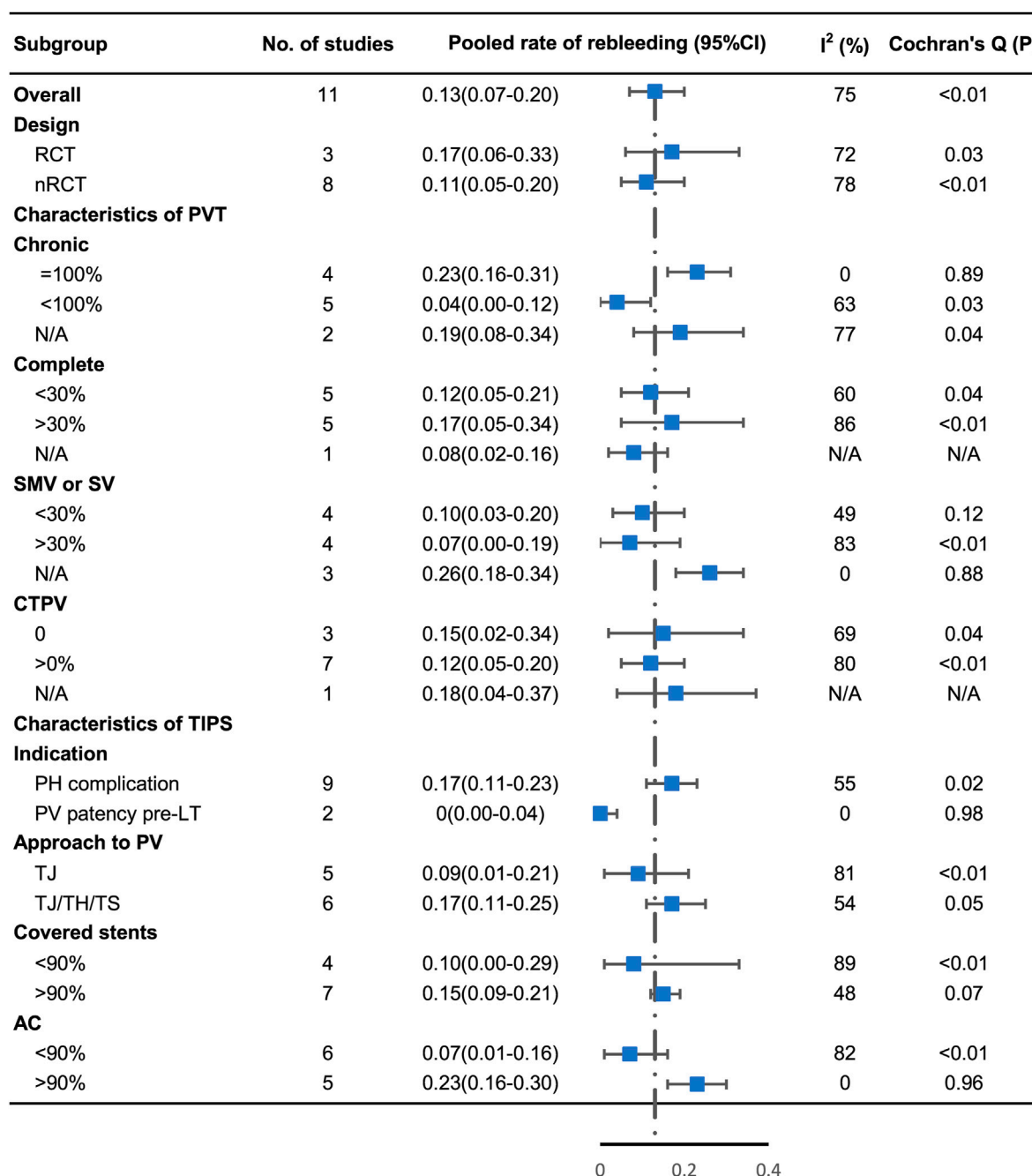


FIGURE 5

Subgroup analysis of rebleeding by study design, proportion of complete and chronic PVT, proportion of CTPV, proportion of involvement of SMV or SV, indication of TIPS, approach to PV, proportion of covered stent, and proportion of post-TIPS AC.

First, we evaluated the technical feasibility of TIPS. CTPV was the main barrier hindering the implementation of TIPS. However, the feasibility rate decreased slightly from 95% to 93%, indicating that TIPS remained successful despite the presence of cavernous transformation. The subgroup analyses suggested that these patients had good outcomes

after TIPS. Surprisingly, compared with the studies that used the traditional transjugular approach, advanced puncture techniques such as the transsplenic and transhepatic approaches did not improve the feasibility rate, perhaps since the two studies that employed the transsplenic and transhepatic approaches were published 10 years ago.

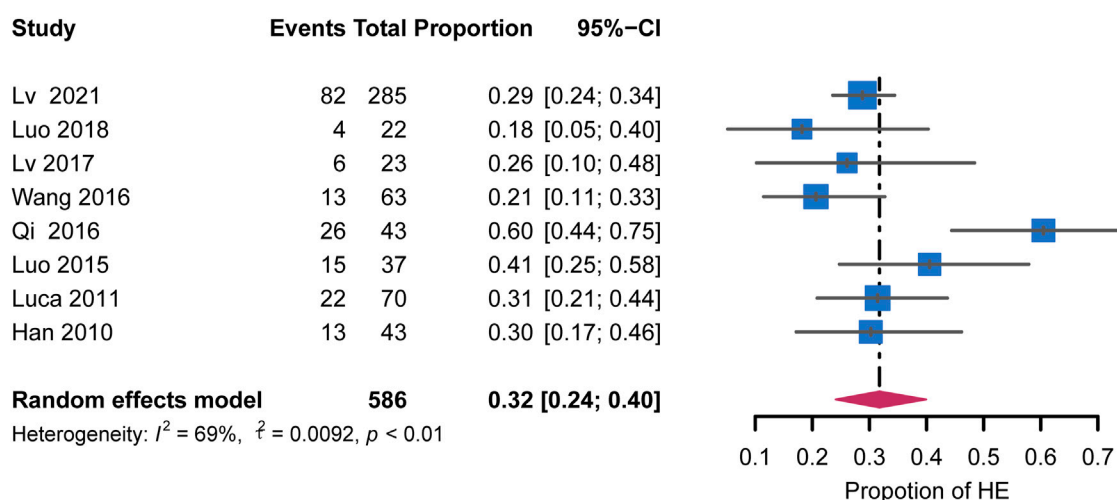


FIGURE 6
Forest plots for pooled rates of HE.

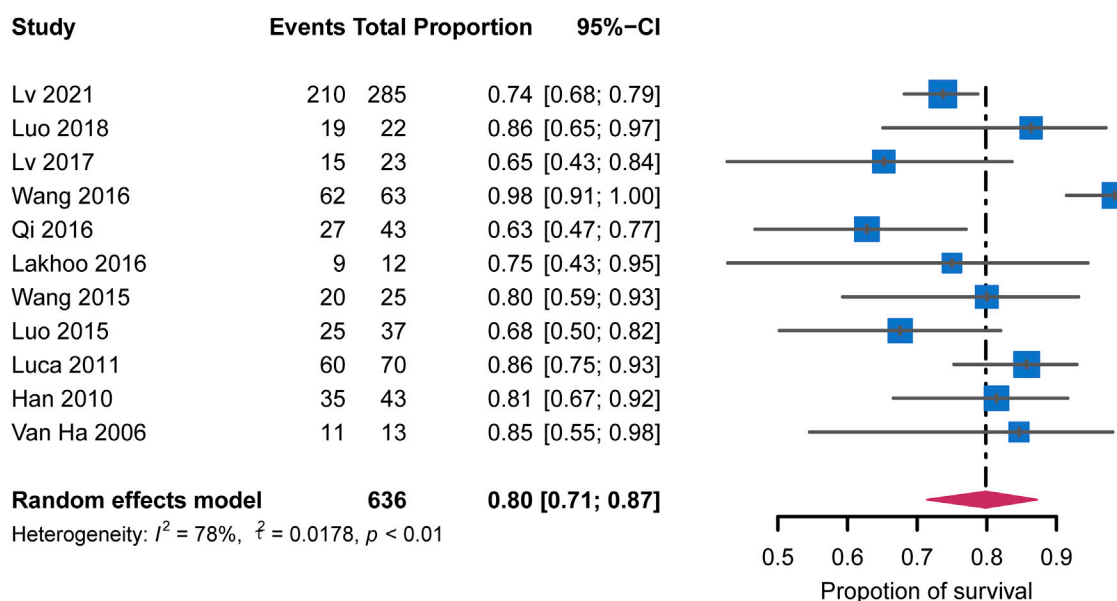


FIGURE 7
Forest plots for pooled rates of survival.

Therefore, the feasibility could be improved with increased technical experience.

One of the key findings of this meta-analysis is that post-TIPS AC treatment is not necessary for certain patients with cirrhosis and PVT. Although post-TIPS AC promoted recanalization in the subgroup analysis, it was associated with a higher rebleeding rate and a lower survival rate. Previous

studies concluded that TIPS alone effectively maintained the portal vein patency due to the high-velocity flow created by the shunt, not requiring AC treatment (Wang et al., 2016; Rodrigues et al., 2019). In addition, heterogeneity prevailed after subgroup analyses based on the AC treatment, indicating that AC is not a unique source of heterogeneity. A slightly lower shunt patency rate was observed in the subgroup analysis when the thrombus

TABLE 4 Meta-regression analysis according to outcomes.

Factors	Feasibility			Rebleeding			Survival		
	Coeff.	95%CI	P	Coeff.	95%CI	P	Coeff.	95%CI	P
Study characteristics									
RCT vs. non-RCT	0.176	−0.153 to 1.402	0.098	0.075	−0.136 to 0.286	0.489	0.046	−0.163 to 0.254	0.667
TIPS technical and treatment characteristics									
Approach to PV	−0.302	−0.383 to −0.222	<0.001	0.114	−0.063 to 0.292	0.206	−0.113	−0.287 to 0.060	0.200
Covered or bare metal stents	0.155	−0.082 to 0.393	0.200	0.058	−0.140 to 0.255	0.567	0.015	−0.198 to 0.228	0.891
Post-TIPS AC	−0.020	−0.249 to 0.208	0.861	0.198	0.035 to 0.360	0.017	−0.069	−0.270 to 0.133	0.506

Coeff., coefficient; HE, hepatic encephalopathy; PV, portal vein; TIPS, transjugular intrahepatic portosystemic shunt; RCT, randomised controlled trial; AC, anticoagulation.

extended to the SMV or SV. Hence, the extent of PVT should be considered to balance the risk of rebleeding and portal vein patency in the long-term clinical management of patients.

Another important aspect of our findings is that the covered stents for TIPS reduce HE incidence without decreasing the risk of rebleeding. Despite clinical heterogeneity, these results are crucial and may help advocate for covered stents (Bureau et al., 2007; Perarnau et al., 2014). A randomized multilevel study stated the superiority of 8-mm stents in decreasing the rate of spontaneous overt HE and severe and recurrent/persistent HE after TIPS (Wang et al., 2017). Further, the size of covered stents is essential. However, this meta-analysis showed that the post-TIPS HE incidence was high, a major post-TIPS complication yet (Han et al., 2011). In addition, improved shunt patency and recanalization were observed in the subgroup analyses based on the type of stent but with heterogeneity. This implies that recanalization and shunt patency are associated with the characteristics of PVT. The specific sources of heterogeneity were not found, as shunt patency and recanalization are dependent on multiple factors, including patient characteristics, stent sizes, types of stents, and operator expertise (Patidar et al., 2014; Tang et al., 2017).

Although TIPS and its associated materials and stents have been developed and refined over the last two decades, the placement of TIPS remains a rescue or second-line therapy in patients with cirrhosis and PVT. TIPS is performed when AC treatment is contraindicated or in patients with uncontrolled bleeding post endoscopic therapy. Therefore, there is a low utilization rate in the actual clinical setting, with only some patients with cirrhosis receiving the TIPS placement. Nevertheless, it is encouraging that TIPS has significant clinical benefits and may provide novel insights into treating patients with cirrhosis and PVT. Further studies are warranted to accumulate sufficient evidence to standardize operating procedures, associated adjuvant drug treatments, and periprocedural care, optimizing current treatment strategies.

The present systematic review and meta-analysis have a few shortcomings. First, technical methods, types, and manufacturers of stents might bring significant heterogeneity to this meta-analysis; however, these factors were not considered. Nevertheless, most heterogeneity could be explained using subgroup analysis with a random-effects model and meta-regression. Second, the included studies spanned 15 years during which the techniques and medical devices for TIPS have made swift advances. Nevertheless, the endpoints of previous and current studies were homogeneous; thus, these studies were included in the quantitative studies. Third, many related studies were excluded from our meta-analysis due to the lack of outcomes and full-text availability. However, an extensive search strategy was performed to collect all related information, and no evidence of publication bias was revealed. Lastly, a difference in the follow-up time was observed among the included studies, limiting the interpretation of some outcomes.

Conclusion

TIPS is feasible and effectively prevents rebleeding in patients with cirrhosis and PVT, including those with CTPV. Due to a potentially high risk of rebleeding and no apparent benefits of AC, post-TIPS AC must be used cautiously. Further, the characteristics of PVT should be considered before making decisions on the TIPS procedure and during long-term clinical management.

Data availability statement

The original contributions presented in the study are included in the article/Supplementary Material, further inquiries can be directed to the corresponding author.

Author contributions

(I) Conception and design: D-FG and CB-H; (II) Administrative support: C-BH; (III) Acquisition of data: D-FG and L-WF; (IV) Collection and assembly of data: D-FG; (V) Data analysis and interpretation: D-FG, L-WF, and QL; (VI) article writing: all authors; (VII) Final approval of article: all authors.

Conflict of interest

The authors declare that the research was conducted in the absence of any commercial or financial relationships that could be construed as a potential conflict of interest.

References

- Barendregt, J. J., Doi, S. A., Lee, Y. Y., Norman, R. E., and Vos, T. (2013). Meta-analysis of prevalence. *J. Epidemiol. Community Health* 67 (11), 974–978. doi:10.1136/jech-2013-203104
- Boyer, T. D., and Haskal, Z. J. (2010). The role of transjugular intrahepatic portosystemic shunt (TIPS) in the management of portal hypertension: Update 2009. *Hepatology* 51 (1), 306. doi:10.1002/hep.23383
- Bureau, C., Garcia Pagan, J. C., Layrargues, G. P., Metivier, S., Bellot, P., Perreault, P., et al. (2007). Patency of stents covered with polytetrafluoroethylene in patients treated by transjugular intrahepatic portosystemic shunts: Long-term results of a randomized multicentre study. *Liver Int.* 27 (6), 742–747. doi:10.1111/j.1478-3231.2007.01522.x
- de Franchis, R. (2015). Expanding consensus in portal hypertension: Report of the Baveno VI Consensus Workshop: Stratifying risk and individualizing care for portal hypertension. *J. Hepatol.* 63 (3), 743–752. doi:10.1016/j.jhep.2015.05.022
- Dell'Era, A., Iannuzzi, F., Fabris, F. M., Fontana, P., Reati, R., Grillo, P., et al. (2014). Impact of portal vein thrombosis on the efficacy of endoscopic variceal band ligation. *Dig. Liver Dis.* 46 (2), 152–156. doi:10.1016/j.dld.2013.08.138
- Englesbe, M. J., Kubus, J., Muhammad, W., Sonnenday, C. J., Welling, T., Punch, J. D., et al. (2010a). Portal vein thrombosis and survival in patients with cirrhosis. *Liver Transpl.* 16 (1), 83–90. doi:10.1002/lt.21941
- Englesbe, M. J., Schaubel, D. E., Cai, S., Guidinger, M. K., and Merion, R. M. (2010b). Portal vein thrombosis and liver transplant survival benefit. *Liver Transpl.* 16 (8), 999–1005. doi:10.1002/lt.22105
- Groszmann, R. J., Garcia-Tsao, G., Bosch, J., Grace, N. D., Burroughs, A. K., Planas, R., et al. (2005). Beta-blockers to prevent gastroesophageal varices in patients with cirrhosis. *N. Engl. J. Med.* 353 (21), 2254–2261. doi:10.1056/NEJMoa044456
- Han, G., Qi, X., He, C., Yin, Z., Wang, J., Xia, J., et al. (2011). Transjugular intrahepatic portosystemic shunt for portal vein thrombosis with symptomatic portal hypertension in liver cirrhosis. *J. Hepatol.* 54 (1), 78–88. doi:10.1016/j.jhep.2010.06.029
- Harding, D. J., Perera, M. T., Chen, F., Olliff, S., and Tripathi, D. (2015). Portal vein thrombosis in cirrhosis: Controversies and latest developments. *World J. Gastroenterol.* 21 (22), 6769–6784. doi:10.3748/wjg.v21.i22.6769
- Higgins, J. P., Thompson, S. G., Deeks, J. J., and Altman, D. G. (2003). Measuring inconsistency in meta-analyses. *Bmj* 327 (7414), 557–560. doi:10.1136/bmj.327.7414.557
- Huang, X. Q., Ni, L. Y., Jiang, S. Y., Xia, R. Q., Ma, L. L., Wang, J., et al. (2020). Zhonghua Gan Zang Bing Za Zhi 28 (9), 747–752. doi:10.3760/cma.j.cn501113-20200616-00326
- Huedo-Medina, T. B., Sánchez-Meca, J., Marín-Martínez, F., and Botella, J. (2006). Assessing heterogeneity in meta-analysis: Q statistic or I² index? *Psychol. Methods* 11 (2), 193–206. doi:10.1037/1082-989X.11.2.193
- Lakhoo, J., and Gaba, R. C. (2016). Outcomes of transjugular intrahepatic portosystemic shunt creation for flow-enabled dissolution of spleno-mesenterico-portal venous thrombosis. *Diagn. Interv. Imaging* 97 (11), 1085–1093. doi:10.1016/j.diii.2016.07.005
- Luca, A., Miraglia, R., Caruso, S., Milazzo, M., Sapere, C., Maruzzelli, L., et al. (2011). Short- and long-term effects of the transjugular intrahepatic portosystemic shunt on portal vein thrombosis in patients with cirrhosis. *Gut* 60 (6), 846–852. doi:10.1136/gut.2010.228023
- Luo, J., Li, M., Zhang, Y., Wang, H., Huang, M., Li, Z., et al. (2018). Percutaneous transhepatic intrahepatic portosystemic shunt for variceal bleeding with chronic portal vein occlusion after splenectomy. *Eur. Radiol.* 28 (9), 3661–3668. doi:10.1007/s00330-018-5360-z
- Luo, X., Wang, Z., Tsao, J., Zhou, B., Zhang, H., Li, X., et al. (2015). Advanced cirrhosis combined with portal vein thrombosis: A randomized trial of TIPS versus endoscopic band ligation plus propranolol for the prevention of recurrent esophageal variceal bleeding. *Radiology* 276 (1), 286–293. doi:10.1148/radiol.15141252
- Lv, Y., Bai, W., Li, K., Wang, Z., Guo, W., Luo, B., et al. (2021). Anticoagulation and transjugular intrahepatic portosystemic shunt for the management of portal vein thrombosis in cirrhosis: A prospective observational study. *Am. J. Gastroenterol.* 116 (7), 1447–1464. doi:10.14309/ajg.0000000000001194
- Lv, Y., Qi, X., He, C., Wang, Z., Yin, Z., Niu, J., et al. (2018). Covered TIPS versus endoscopic band ligation plus propranolol for the prevention of variceal rebleeding in cirrhotic patients with portal vein thrombosis: A randomised controlled trial. *Gut* 67 (12), 2156–2168. doi:10.1136/gutjnl-2017-314634
- Page, M. J., McKenzie, J. E., Bossuyt, P. M., Boutron, I., Hoffmann, T. C., Mulrow, C. D., et al. (2021). The PRISMA 2020 statement: An updated guideline for reporting systematic reviews. *Bmj* 372, n71. doi:10.1136/bmj.n71
- Patidar, K. R., Sydnor, M., and Sanyal, A. J. (2014). Transjugular intrahepatic portosystemic shunt. *Clin. Liver Dis.* 18 (4), 853–876. doi:10.1016/j.cld.2014.07.006
- Perarnau, J. M., Le Gouge, A., Nicolas, C., d'Altoche, L., Borentain, P., Saliba, F., et al. (2014). Covered vs. uncovered stents for transjugular intrahepatic portosystemic shunt: A randomized controlled trial. *J. Hepatol.* 60 (5), 962–968. doi:10.1016/j.jhep.2014.01.015
- Qi, X., Han, G., and Fan, D. (2014). Management of portal vein thrombosis in liver cirrhosis. *Nat. Rev. Gastroenterol. Hepatol.* 11 (7), 435–446. doi:10.1038/nrgastro.2014.36
- Qi, X., He, C., Guo, W., Yin, Z., Wang, J., Wang, Z., et al. (2016). Transjugular intrahepatic portosystemic shunt for portal vein thrombosis with variceal bleeding in liver cirrhosis: Outcomes and predictors in a prospective cohort study. *Liver Int.* 36 (5), 667–676. doi:10.1111/liv.12929
- Rodrigues, S. G., Sixt, S., Abalde, J. G., De Gottardi, A., Klinger, C., Bosch, J., et al. (2019). Systematic review with meta-analysis: Portal vein recanalisation and transjugular intrahepatic portosystemic shunt for portal vein thrombosis. *Aliment. Pharmacol. Ther.* 49 (1), 20–30. doi:10.1111/apt.15044
- Sarin, S. K., Kumar, A., Angus, P. W., Bajjal, S. S., Baik, S. K., Bayraktar, Y., et al. (2011). Diagnosis and management of acute variceal bleeding: Asian pacific association for study of the liver recommendations. *Hepatol. Int.* 5 (2), 607–624. doi:10.1007/s12072-010-9236-9

Publisher's note

All claims expressed in this article are solely those of the authors and do not necessarily represent those of their affiliated organizations, or those of the publisher, the editors and the reviewers. Any product that may be evaluated in this article, or claim that may be made by its manufacturer, is not guaranteed or endorsed by the publisher.

Supplementary material

The Supplementary Material for this article can be found online at: <https://www.frontiersin.org/articles/10.3389/fphar.2022.968988/full#supplementary-material>

- Sterne, J. A., Hernán, M. A., Reeves, B. C., Savović, J., Berkman, N. D., Viswanathan, M., et al. (2016). ROBINS-I: A tool for assessing risk of bias in non-randomised studies of interventions. *Bmj* 355, i4919. doi:10.1136/bmj.i4919
- Sterne, J. A. C., Savović, J., Page, M. J., Elbers, R. G., Blencowe, N. S., Boutron, I., et al. (2019). RoB 2: A revised tool for assessing risk of bias in randomised trials. *Bmj* 366, i4898. doi:10.1136/bmj.l4898
- Tang, Y., Zheng, S., Yang, J., Bao, W., Yang, L., Li, Y., et al. (2017). Use of concomitant variceal embolization and prophylactic antiplatelet/anticoagulative in transjugular intrahepatic portosystemic shunting: A retrospective study of 182 cirrhotic portal hypertension patients. *Med. Baltim.* 96 (49), e8678. doi:10.1097/MD.00000000000008678
- Van Ha, T. G., Hodge, J., Funaki, B., Lorenz, J., Rosenblum, J., Straus, C., et al. (2006). Transjugular intrahepatic portosystemic shunt placement in patients with cirrhosis and concomitant portal vein thrombosis. *Cardiovasc. Interv. Radiol.* 29 (5), 785–790. doi:10.1007/s00270-005-0090-4
- Wang, Q., Lv, Y., Bai, M., Wang, Z., Liu, H., He, C., et al. (2017). Eight millimetre covered TIPS does not compromise shunt function but reduces hepatic encephalopathy in preventing variceal rebleeding. *J. Hepatol.* 67 (3), 508–516. doi:10.1016/j.jhep.2017.05.006
- Wang, Z., Jiang, M. S., Zhang, H. L., Weng, N. N., Luo, X. F., Li, X., et al. (2016). Is post-TIPS anticoagulation therapy necessary in patients with cirrhosis and portal vein thrombosis? A randomized controlled trial. *Radiology* 279 (3), 943–951. doi:10.1148/radiol.2015150369
- Wang, Z., Zhao, H., Wang, X., Zhang, H., Jiang, M., Tsauo, J., et al. (2015). Clinical outcome comparison between TIPS and EBL in patients with cirrhosis and portal vein thrombosis. *Abdom. Imaging* 40 (6), 1813–1820. doi:10.1007/s00261-014-0320-9
- Werner, K. T., Sando, S., Carey, E. J., Vargas, H. E., Byrne, T. J., Douglas, D. D., et al. (2013). Portal vein thrombosis in patients with end stage liver disease awaiting liver transplantation: Outcome of anticoagulation. *Dig. Dis. Sci.* 58 (6), 1776–1780. doi:10.1007/s10620-012-2548-y
- Zhang, J. B., Chen, J., Zhou, J., Wang, X. M., Chen, S., Chu, J. G., et al. (2021). Systematic review and meta-analysis of trans-jugular intrahepatic portosystemic shunt for cirrhotic patients with portal vein thrombosis. *World J. Clin. Cases* 9 (19), 5179–5190. doi:10.12998/wjcc.v9.i19.5179



OPEN ACCESS

EDITED BY
Khairunnisa Hasikin,
University of Malaya, Malaysia

REVIEWED BY
Wei Hong Lim,
UCSI University, Malaysia
Jerline Sheebha Anni D,
KMCT College of Engineering for
Women, India

*CORRESPONDENCE
Kui Jiang,
kuij@ntu.edu.cn

[†]These authors have contributed equally
to this work.

SPECIALTY SECTION
This article was submitted to
Experimental Pharmacology and Drug
Discovery,
a section of the journal
Frontiers in Pharmacology.

RECEIVED 19 May 2022
ACCEPTED 28 June 2022
PUBLISHED 17 August 2022

CITATION
Ran X, Shi J, Chen Y and Jiang K (2022),
Multimodal neuroimage data fusion
based on multikernel learning in
personalized medicine.
Front. Pharmacol. 13:947657.
doi: 10.3389/fphar.2022.947657

COPYRIGHT
© 2022 Ran, Shi, Chen and Jiang. This is
an open-access article distributed
under the terms of the [Creative
Commons Attribution License \(CC BY\)](#).
The use, distribution or reproduction in
other forums is permitted, provided the
original author(s) and the copyright
owner(s) are credited and that the
original publication in this journal is
cited, in accordance with accepted
academic practice. No use, distribution
or reproduction is permitted which does
not comply with these terms.

Multimodal neuroimage data fusion based on multikernel learning in personalized medicine

Xue Ran[†], Junyi Shi[†], Yalan Chen and Kui Jiang^{*}

Department of Medical Informatics, Nantong University, Nantong, China

Neuroimaging has been widely used as a diagnostic technique for brain diseases. With the development of artificial intelligence, neuroimaging analysis using intelligent algorithms can capture more image feature patterns than artificial experience-based diagnosis. However, using only single neuroimaging techniques, e.g., magnetic resonance imaging, may omit some significant patterns that may have high relevance to the clinical target. Therefore, so far, combining different types of neuroimaging techniques that provide multimodal data for joint diagnosis has received extensive attention and research in the area of personalized medicine. In this study, based on the regularized label relaxation linear regression model, we propose a multikernel version for multimodal data fusion. The proposed method inherits the merits of the regularized label relaxation linear regression model and also has its own superiority. It can explore complementary patterns across different modal data and pay more attention to the modal data that have more significant patterns. In the experimental study, the proposed method is evaluated in the scenario of Alzheimer's disease diagnosis. The promising performance indicates that the performance of multimodality fusion *via* multikernel learning is better than that of single modality. Moreover, the decreased square difference between training and testing performance indicates that overfitting is reduced and hence the generalization ability is improved.

KEYWORDS

neuroimaging, personalized medicine, multimodal data fusion, multikernel learning, magnetic resonance imaging, positron emission tomography

1 Introduction

Neuroimaging technologies are currently the most widely used methods to study brain diseases, and they can directly or indirectly image the nervous system. Common neuroimaging techniques include structural magnetic resonance imaging (sMRI), which can provide rich morphological features of brain tissues; functional magnetic resonance imaging (fMRI), which not only provides anatomical information but also shows the response mechanism of the nervous system; positron emission tomography (PET), which is the only novel imaging technique that can display biomolecular metabolism, receptors,

and neuromediator activity *in vivo*; diffusion tensor imaging (DTI), which can reflect the structure of white matter fibrin in the brain, etc (Klöppel et al., 2012; Friston, 2009). Neuroimaging technologies play a very important role in the research of Alzheimer's disease (AD) (Bao et al., 2021; Karikari et al., 2021; Zhang et al., 2021). Previous studies on AD and mild cognitive impairment (MCI) were often based on a single neuroimaging technique (single modality data). However, single modality data have obvious defects; they can only provide information on local brain abnormalities, which will affect the diagnostic accuracy of AD and MCI. In recent years, many studies have found that multimodal data have the advantage of realizing information complementation (Zhang et al., 2022a). The features of multimodal data can be combined to obtain more comprehensive disease information, which is of great significance for the early diagnosis and treatment of AD. In particular, with the development of artificial intelligence (AI) technologies, multimodal fusion has been developed rapidly for AD diagnosis studies. For example, Kohannim et al. (2010) used support vector machines (SVMs) to classify AD. When using MRI as single-modal data for experiments, the classification accuracy of AD vs. normal control (NC) and that of MCI vs. NC were 79.07% and 71.21%, respectively. When experiments were performed after combining MRI, fluorodeoxyglucose-PET, and cerebrospinal fluid (CSF), the classification accuracy of AD vs. NC and that of MC vs. NC were 90.70% and 75.76%, respectively. Compared to single modality, the classification accuracy is improved by 5–10%. Zhang et al. (2011) combined MRI, PET, and CSF for AD classification. A multikernel SVM was taken as the classifier. The classification accuracy of AD vs. NC was 93.2%. Compared with using single-modal data, the accuracy was improved by 7–10%. The accuracy of MCI vs. NC was 76.4%, which was an improvement of 4.4–5% compared to using single modality data. Buvanewari and Gayathri (2021) combined the features extracted from DTI and fMRI into a multikernel SVM for AD classification, and the accuracy of AD vs. NC was 98.4%; however, when the two modalities were used alone for classification, the highest achieved accuracy was only 90.9%. The above research further verifies that in the classification of AD, compared with single-modal data, the use of multimodal data can obtain richer and more valuable features, and the classifier can obtain higher classification accuracy.

From existing studies regarding multimodality fusion, we found that classifiers based on multikernel learning were commonly used. This is because each modality can be mapped into the kernel space by a kernel function. Therefore, multikernel learning actually provides a natural framework for multimodality fusion. However, when multikernel learning is applied to practice, e.g., medical data analysis, overfitting often exists. Therefore, to overcome overfitting and to obtain promising prediction performance, in this study, according to regularized label relaxation linear regression (Fang et al., 2017),

we integrate label relaxation and compactness graph mechanisms into multikernel learning and propose a new multikernel learning algorithm for AD diagnosis.

The main differences with the existing studies can be summarized as follows.

- (1) Unlike the modality-consistent regularization used in previous studies (Jiang et al., 2016), the “all-single” fusion strategy is introduced so that every single feature and the possible combinations are all considered so that the complementary information can be fully explored.
- (2) We extend the compactness graph mechanism from the linear space to the multikernel space so that the overfitting problems can be reduced in the multikernel space.

The remaining article is organized into four sections. In Section 2, we will state some related work regarding AI-assisted AD diagnosis based on multimodality fusion. In Section 3, we will present our new method and its optimization. In Section 4, we will report our experimental results and in the last, we will conclude our study and indicate our future work.

2 Related work

Multimodality fusion strategies can be divided into three levels: pixel-level fusion, feature-level fusion, and decision-level fusion (Xia et al., 2020). Pixel-level fusion is to directly perform pixel-related fusion based on strict registration. Feature-level fusion refers to transforming different modal data into high-dimensional feature spaces and then merging them before or during modeling. Decision-level fusion is to use certain strategies, such as voting, to fuse the decision result of each modal, to obtain the globally optimal result. In Table 1, we summarize some representative previous works belonging to these three categories.

Strict registration plays a key role in pixel-level fusion. For example, Daneshvar et al. proposed a fusion strategy based on integrated intensity-hue-saturation and retina-inspired model to improve the fusion performance. The strategy often used in decision-level fusion is ensemble learning. In the early studies of AD diagnosis, the most commonly used learning components in ensemble learning were SVM (Shukla et al., 2020) and also linear classifiers (Jiang et al., 2020), Bayesian networks (Zhang et al., 2017), decision trees (Zhang et al., 2020), etc. For example, Fan et al. (2008) took the two-modal data of the bilateral hippocampus volume and the bilateral entorhinal cortex volume as core features and used SVM as the learning component. The accuracies of AD vs. MCI, AD vs. NC, and MCI vs. NC are 58.30%, 82.00%, and 76.00% respectively.

Feature-level fusion has been widely used in AD studies. For example, Suk et al. (2014) obtained high-level latent and shared

TABLE 1 Representative works of multimodality fusion.

Categories	Authors	Modalities	Methodologies
Pixel-level	Daneshvar and Hassan, (2010)	MRI, PET	A model based on integrated intensity-hue-saturation and retina-inspired model was proposed to improve the fusion performance
	Li and Wang, (2012)	SPECT, MRI	A method of multiscaled combination of MR and SPECT images based on variable-weight
	Bhatnagar et al. (2015)	MRI and PET	A novel framework for spatially registered multimodal medical image fusion based on nonsubsampling contourlet transform
Decision-level	Dimitriadis et al. (2018)	MRI	A random forest feature selection, fusion, and ensemble strategy was applied to the classification and prediction of AD
	Fan et al. (2008)	MRI and PET	An SVM-based ensemble method was proposed and two modal data of the bilateral hippocampus volume and the bilateral entorhinal cortex volume as core features were used for AD prediction
	Zeng et al. (2018)	sMRI, PET, and CSF	An SVM-based ensemble method was proposed and the combined features of sMRI, PET, and CSF were used to build an ensemble classification model for AD prediction
Feature-level	Zhang et al. (2020)	MRI and PET	A deep multimodal fusion network based on an attention mechanism, which was able to selectively extract deep features from MRI and PET was proposed to predict AD
	Suk et al. (2014)	MRI and PET	High-level latent and shared feature representations were extracted and fused from neuroimaging <i>via</i> deep network-confined Boltzmann machines
	Madusanka et al. (2019)	MRI and PET	Texture and morphological features were fused as a biomarker to diagnose AD. SVM was taken as the classifier

feature representations from neuroimaging *via* deep network-confined Boltzmann machines. In the binary classification of AD vs. NC and MCI vs. NC, maximum accuracies of 95.35% and 85.67% were finally obtained, respectively. Madusanka et al. (2019) used the fusion of texture and morphological features as a biomarker to diagnose AD and used SVM as the classifier. The classification accuracy reached 86.61%. Zhang et al. (2020) proposed a deep multimodal fusion network based on an attention mechanism, which was able to selectively extract deep features from MRI and PET, while suppressing irrelevant information. In the attention mechanism-based model, the fusion ratio of each modality is automatically assigned according to the importance of the modality. In addition, a hierarchical fusion method was adopted to ensure the effectiveness of multimodal data fusion. The final classification accuracies of NC vs. AD and SMCI vs. PMCI were 95.21% and 89.79%, respectively.

In this study, we also focus on feature-level fusion. From previous studies regarding feature-level fusion, we find that there are still some issues that should be addressed in the future.

- (1) Most of the previous studies only directly concatenate features from different modalities and then input them into a model for AD prediction. This strategy does not consider complementary patterns across different modalities.
- (2) Some multikernel-based studies achieved promising performance and also consider complementary patterns across different modalities. However, with a sparse or small training set, overfitting often occurs.

Therefore, to address the abovementioned issues, in this study, we will propose a novel multimodality fusion model at the feature-fusion level.

3 Data and methods

3.1 Data

The data (MRI and PET) used in this study were collected from Alzheimer's Disease Neuroimaging Initiative. There are 103 subjects in the dataset, where 51 subjects were organized into the NC group and 52 subjects were organized into the AD group. We used the following workflows (Zhang et al., 2021), as shown in Figure 1, to perform data preprocessing.

As can be seen from Figure 1A, the tissue probability map template was first used to segment the original MRI into white matter (WM), gray matter (GM), and other tissues. In particular, WM and GM tissues were mapped into the Montreal Neurological Institute (MNI) space during preprocessing. Second, diffeomorphic anatomical registration through exponentiated Lie algebra (DARTEL) was employed to create average templates for the obtained WM and GM tissues. In the last, GM was modulated to transform the density information into volume information. In addition, GM was smoothed (8 mm Gaussian) to avoid the influences caused by noises.

As can be seen from Figure 1B, SPM-12 was employed to fuse these PET images (one subject has 96 images) to construct a 3-D image that provides brain spatial information and the feature information between tissue structures was also retained. Moreover, head motion was corrected. After fusion alignment, MRI and PET of each subject were registered and affinely aligned. In the last, the average template data generated in Figure 1A were used to spatially normalize all PET images to the standard MNI space. PET images were also smoothed (8 mm Gaussian) to avoid the influences caused by noises.

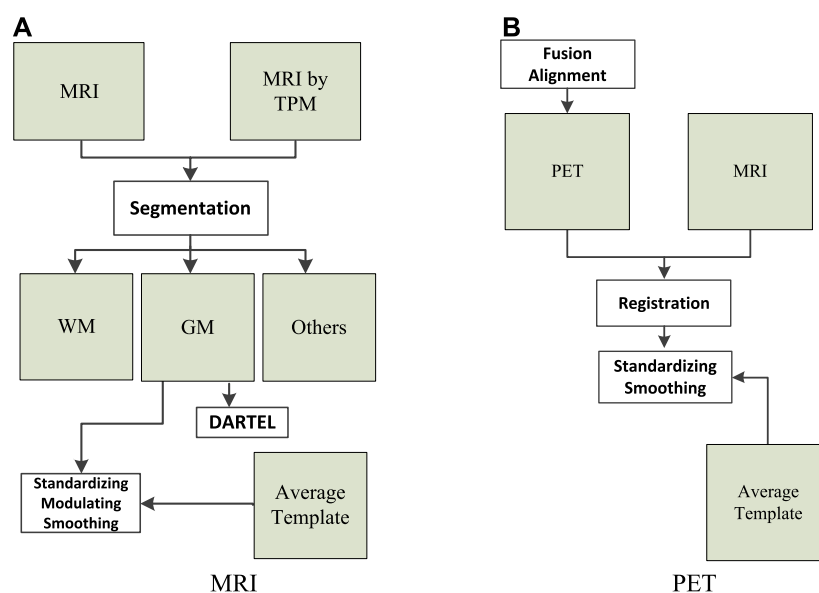


FIGURE 1

Data preprocessing: (A) magnetic resonance imaging (MRI) and (B) positron emission tomography (PET).

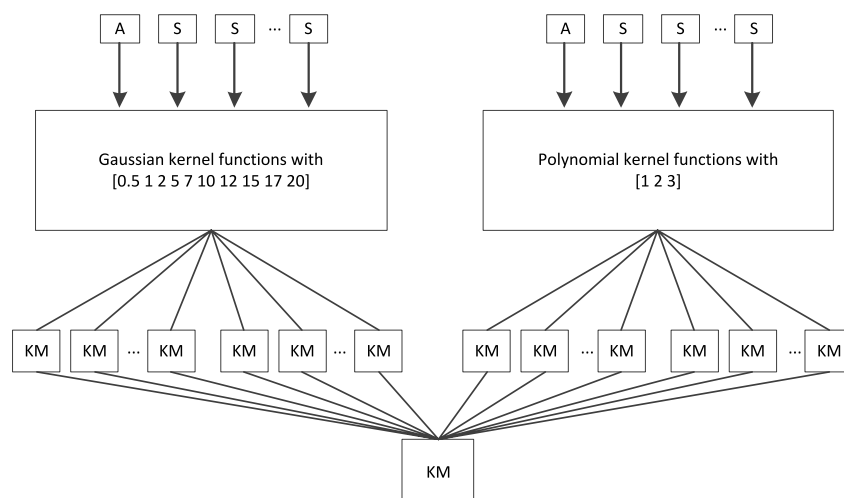


FIGURE 2

"All-single" fusion strategy.

3.2 Methods

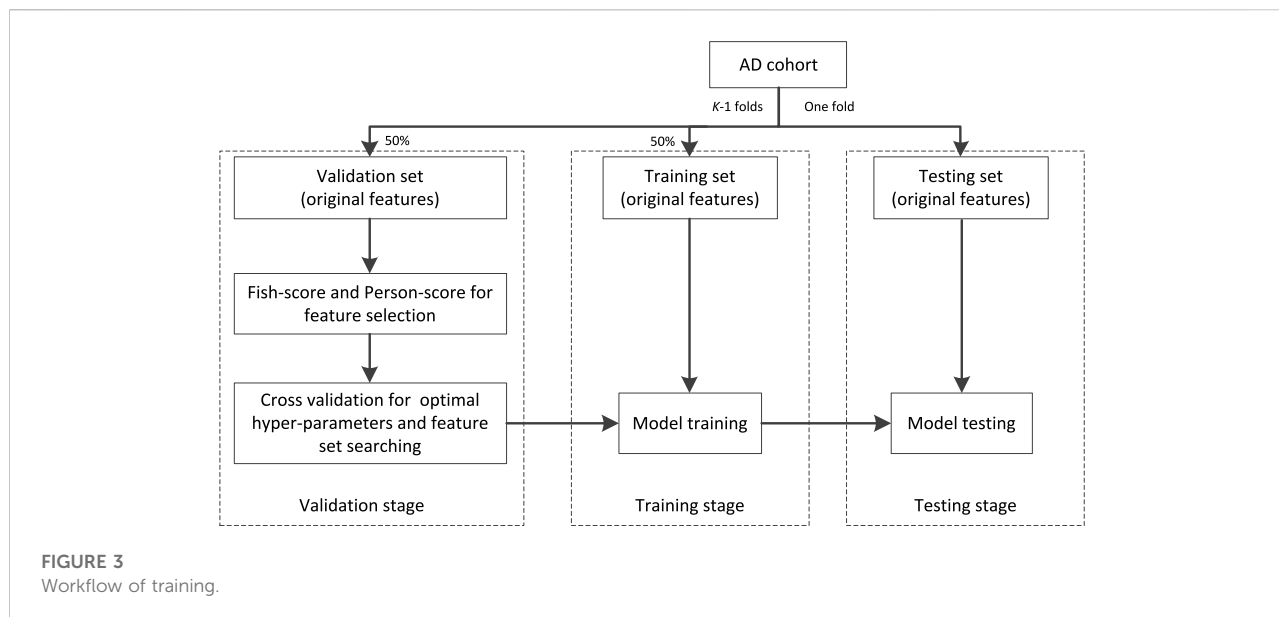
3.2.1 Kernelized regularized label relaxation

A regularized label relaxation (RLR) linear regression model was proposed to address the overfitting problem (Fang et al., 2017). The objective function is defined as follows:

$$\min_{\mathbf{A}, \mathbf{M}} \|\mathbf{X}\mathbf{A} - (\mathbf{Y} + \mathbf{B} \odot \mathbf{M})\|_F^2 + \lambda \text{tr}(\mathbf{A}^T \mathbf{X}^T \mathbf{L} \mathbf{X} \mathbf{A}) \quad (1)$$

$$\text{s.t. } \mathbf{M} \geq 0$$

where $\{\mathbf{X}, \mathbf{Y}\}$ represents the training set, \mathbf{B} represents a luxury matrix derived from \mathbf{Y} , \mathbf{A} represents the transformation matrix, \mathbf{M} represents a nonnegative label relaxation matrix, \mathbf{L} represents the Laplacian matrix, λ is a regularized parameter, $\text{tr}()$ represents



the trace of a matrix, and \odot is a Hadamard product operator. RLR can classify linear data well and restrain overfitting. However, in many real-world scenarios, especially in the medical field, many data are not linear, which may limit the application of RLR. Therefore, Fang et al. employed the kernel technique to further extend RLR to its nonlinear version, that is, kernelized RLR (KRLR). The objective function of KRLR is defined as follows:

$$\min_{\Theta, \mathbf{M}} \|\mathbf{K}\Theta - (\mathbf{Y} + \mathbf{B} \odot \mathbf{M})\|_F^2 + \lambda \text{tr}(\Theta^T \mathbf{K}^T \mathbf{L} \mathbf{K} \Theta) \quad (2)$$

s.t. $\mathbf{M} \geq 0$

where Θ can be considered the transformation matrix and the new \mathbf{K} is a positive semidefinite kernel Gram matrix in which each element can be calculated as follows:

$$\mathbf{K}_{ij} = [\langle \phi(\mathbf{X}_i), \phi(\mathbf{X}_j)^T \rangle]_{ij} = k(\mathbf{x}_i^T, \mathbf{x}_j^T). \quad (3)$$

In Eq. 3, $\phi(\mathbf{X}) = [\phi(\mathbf{x}_1)^T, \phi(\mathbf{x}_2)^T, \dots, \phi(\mathbf{x}_N)^T]^T$, $\phi: R^d \rightarrow \Gamma$ is a nonlinear function that maps the input data from the original feature space to the Hilbert space Γ . $k: R^d \times R^d \rightarrow R$ represents a kernel function in which the polynomial kernel, Gaussian kernel, and the hyperbolic tangent kernel are usually adopted.

3.2.2 Multikernel kernelized regularized label relaxation

We know that multikernel learning provides us a natural framework for multimodal data fusion (Wang et al., 2021). Therefore, we can extend KRLR to its multikernel version by adjusting the generation way of the kernel Gram matrix. In this study, a linear combination is used to generate the new kernel Gram matrix in the multikernel space, that is,

$$\mathbf{K} = \sum_{m=1}^M \alpha_m \mathbf{K}_m. \quad (4)$$

By substituting Eq. 4 into Eq. 2, we can obtain the objective function of multikernel KRLR,

$$\min_{\Theta, \mathbf{M}, \alpha_m} \left\| \sum_{m=1}^M \alpha_m \mathbf{K}_m \Theta - (\mathbf{Y} + \mathbf{B} \odot \mathbf{M}) \right\|_F^2 + \lambda \text{tr} \left(\Theta^T \left(\sum_{m=1}^M \alpha_m \mathbf{K}_m \right) \mathbf{L} \left(\sum_{m=1}^M \alpha_m \mathbf{K}_m \right) \Theta \right) \quad \text{s.t. } \mathbf{M} \geq 0, \sum_{m=1}^M \alpha_m = 1. \quad (5)$$

In Eq. 5, three components are required to be optimized; they are the transformation matrix Θ , the relaxation matrix \mathbf{M} , and the linear kernel combination coefficient α_m . Since the objective function in Eq. 6 is convex, an iterative updating strategy is adopted for optimization so that in each iteration a closed-form solution can be guaranteed (Xiang et al., 2012).

To devise the updating rule regarding the transformation matrix Θ , we suppose that the relaxation matrix \mathbf{M} and the linear kernel combination coefficient α_m have been fixed; thus, the optimization problem becomes

$$J(\Theta) = \min_{\Theta} \left\| \sum_{m=1}^M \alpha_m \mathbf{K}_m \Theta - (\mathbf{Y} + \mathbf{B} \odot \mathbf{M}) \right\|_F^2 + \lambda \text{tr} \left(\Theta^T \left(\sum_{m=1}^M \alpha_m \mathbf{K}_m \right) \mathbf{L} \left(\sum_{m=1}^M \alpha_m \mathbf{K}_m \right) \Theta \right) \quad (6)$$

By setting the derivation of Eq. 6 with respect to the transformation matrix Θ to 0, that is, $\partial J(\Theta)/\partial \Theta = 0$, we have

$$\Theta = \left(\left(\sum_{m=1}^M \alpha_m \mathbf{K}_m \right)^T \left(\sum_{m=1}^M \alpha_m \mathbf{K}_m \right) + \lambda \left(\sum_{m=1}^M \alpha_m \mathbf{K}_m \right)^T \mathbf{L} \left(\sum_{m=1}^M \alpha_m \mathbf{K}_m \right) \right)^{-1} \left(\sum_{m=1}^M \alpha_m \mathbf{K}_m \right)^T (\mathbf{Y} + \mathbf{B} \odot \mathbf{M}) \quad (7)$$

To devise the updating rule regarding the relaxation matrix \mathbf{M} , we suppose that the transformation matrix Θ and the linear kernel combination coefficient α_m have been fixed; thus, the optimization problem becomes

$$\min_{\Theta, \mathbf{M}, \alpha_m} \left\| \sum_{m=1}^M \alpha_m \mathbf{K}_m \Theta - (\mathbf{Y} + \mathbf{B} \odot \mathbf{M}) \right\|_F^2 \quad \text{s.t. } \mathbf{M} \geq 0 \quad (8)$$

The solution of \mathbf{M} can be finally obtained as follows:

$$\mathbf{M} = \max \left(\mathbf{B}, \sum_{m=1}^M \alpha_m \mathbf{K}_m \Theta - \mathbf{Y} \right). \quad (9)$$

To devise the updating rule regarding the kernel combination coefficient α_m , we suppose that the transformation matrix Θ and the relaxation matrix \mathbf{M} have been fixed; thus, the optimization problem becomes

$$J(\Theta) = \min_{\Theta} \left\| \sum_{m=1}^M \alpha_m \mathbf{K}_m \Theta - (\mathbf{Y} + \mathbf{B} \odot \mathbf{M}) \right\|_F^2 + \lambda \text{tr} \left(\Theta^T \left(\sum_{m=1}^M \alpha_m \mathbf{K}_m \right) \mathbf{L} \left(\sum_{m=1}^M \alpha_m \mathbf{K}_m \right) \Theta \right) \quad \text{s.t. } \sum_{m=1}^M \alpha_m = 1. \quad (10)$$

From Eq. 10, it can be seen that the analytical solution of α_m cannot be directly obtained. In this study, the reduced gradient method is used to obtain the optimal α_m (Rakotomamonjy et al., 2008). To be specific, when the gradient of Eq. 10 with respect to α_m is obtained, α_m can be updated along its decent direction D_m to ensure that the equality constraint and the nonnegativity constraints on α_m are satisfied. Let α_g be a nonzero entry of α , then $\nabla_{\text{reg}} J$, which represents the reduced gradient of Eq. 10, has components $[\nabla_{\text{reg}} J]_m$ and $[\nabla_{\text{reg}} J]_g$ that are defined as

$$[\nabla_{\text{reg}} J]_m = \frac{\partial J}{\partial \alpha_m} - \frac{\partial J}{\partial \alpha_g}, \forall m \neq g \quad (11)$$

$$[\nabla_{\text{reg}} J]_g = \sum_{m \neq g} \left(\frac{\partial J}{\partial \alpha_g} - \frac{\partial J}{\partial \alpha_m} \right) \quad (12)$$

where g is the index of the largest element in α . The positivity constraints have also to be taken into account in the descent direction. However, if there is an index m such that $\alpha_m = 0$ and $[\nabla_{\text{reg}} J]_m > 0$, using this direction would violate the positivity constraint for α_m . Hence, the descent direction for that component is set to 0. This gives the descent direction for update D_m as

$$D_m = \begin{cases} 0 & \text{if } \alpha_m > 0 \text{ and } \frac{\partial J}{\partial \alpha_m} - \frac{\partial J}{\partial \alpha_g} > 0 \\ -\frac{\partial J}{\partial \alpha_m} + \frac{\partial J}{\partial \alpha_g} & \text{if } \alpha_m > 0 \text{ and } m \neq g \\ \sum_{m \neq g} \left(\frac{\partial J}{\partial \alpha_g} - \frac{\partial J}{\partial \alpha_m} \right) & \text{if } m \neq g \end{cases} \quad (13)$$

3.3 Algorithm

Based on the solutions to the transformation matrix Θ , the relaxation matrix \mathbf{M} , and the kernel combination coefficient α_m , detailed algorithm steps were deduced as follows.

Algorithm 1.

Input: Multi-modal training data $\{\mathbf{x}_i^{(m)}, y_i\}$ and the regularized parameter λ .

Output: Transformation matrix Θ , relaxation matrix \mathbf{M} and kernel combination coefficient α_m Procedures:

Use “All-single” fusion strategy to obtain input data from $\{\mathbf{x}_i^{(m)}, y_i\}$. Initialize α by setting $\alpha_m = 1/M$.

Randomize \mathbf{M} .

Repeat

Update Θ by equation (7).

Update \mathbf{M} by equation (9).

Update $\partial J / \partial \alpha_m$ and D_m by equation (13).

Update $g = \arg \max \alpha_m$.

Set $J^\dagger = 0, \alpha^\dagger = \alpha, D^\dagger = D$.

Repeat

Update $\alpha = \alpha^\dagger, D = D^\dagger$.

Update $v = \arg \min -\alpha_m / D_m$.

Update $\beta_{\max}^{(m)D_m \leq 0} \alpha_v / D_v$.

Update $\alpha^\dagger = \alpha + \beta_{\max} D$.

Update $D_m^\dagger = D_m - D_v, D_v^\dagger = 0$.

Update J^\dagger by $\sum_{m=1}^M \alpha_m^\dagger \mathbf{K}_m$

Until ($J^\dagger \geq J$)

Until (convergence)

The time complexity of Algorithm 1 consists of 3 parts: the computation of Θ , the computation of \mathbf{M} , and the computation of α . From Eq. 7, it is easy to find that the time complexity of the computation of Θ is $O(N^3)$, and from Eqs. 9 and 13, we see that the computation of \mathbf{M} and α is $O(N^2)$. Therefore, the asymptotic time complexity of Algorithm 1 is $O(N^3)$.

4 Experimental results

4.1 Settings

The original features extracted from sMRI and PET images were represented in a very high-dimensional feature space. Therefore, the direct use of high-dimensional features for modeling will lead to the curse of dimensionality (Chandrashekar and Sahin, 2014). That is to say, samples become very sparse in the high-dimensional space, so the discriminability between samples will be significantly reduced. Therefore, before modeling, feature selection was performed to reduce the dimension of feature spaces. In this study, the *Fish score* was employed as the supervised method to reduce the

TABLE 2 Parameter settings.

Methods	Parameter settings
RR	The regularized parameter was searched from 0.0001 to 1
Our method	The regularized parameter λ was searched from 0.0001 to 1
MV-TSK-FS	We use the parameter settings recommended by the original references
simpleMKL	We use the parameter settings recommended by the original references
RFF-MKL	We use the parameter settings recommended by the original references
MV-L2-SVM	

irrelevant features to the outcome. In *Fish score*, we select the first 30 features with the highest-ranking values for the next unsupervised feature selection. *Person score* was employed as the unsupervised method to reduce the redundancy between features. In *Person score*, the threshold is set to 0.4.

Regarding multikernel learning, the “all-single” strategy, as shown in Figure 2, was adopted to fuse sMRI features and PET features. In Figure 3, “A” represents the combined features of sMRI and PET, “S” represents each sMRI or PET feature, and “KM” denotes the kernel matrix. Suppose we had a dataset $\chi = [x_{i1}^{(m)}, x_{i2}^{(m)}, x_{i3}^{(m)}]_{i=1,2,3,4,m=1,2}$ having 3 subjects, each subject has two modalities ($m = 1$ and 2), and each modality has 4 features ($i = 1, 2, 3$, and 4), then “A” in Figure 2 can be expressed as $[x_{i1}^{(1)}, x_{i2}^{(1)}, x_{i1}^{(2)}, x_{i2}^{(2)}, x_{i3}^{(2)}]_{i=1,2,3,4}$, and “S” can be expressed as $[x_{i1}^{(m)}, x_{i2}^{(m)}, x_{i3}^{(m)}]_{i=1,2,3,4,m=1,2}$. According to Rakotomamonjy et al., (2008), {0.5, 1, 2, 5, 7, 10, 12, 15, 17, 20} is taken as a Gaussian kernel parameter candidate set and {1, 3, 5} is taken as a

polynomial kernel parameter candidate set. Therefore, with such settings, 91 KMs were finally generated, and the goal of multikernel learning is to learn the coefficient of each KM.

The workflow chart of training is shown in Figure 3. The AD cohort is first partitioned into K ($K = 5$ in our study) folds, one is taken as the testing set and the remaining are taken as the validation set (50%) and training set (50%). At the stage of validation, the *Fish score* is employed as the supervised method to reduce the irrelevant features to the outcome. *Person score* is employed as the unsupervised method to reduce the redundancy between features. Then the cross-validation (5-CV) strategy is used to determine the optimal feature set and hyper parameters (the regularized parameter λ is searched from 0.0001 to 1) with respect to the proposed model. At the stage of training, with the optimal feature set and hyper parameters, the best model can be obtained. At the stage of testing, with the best model, we can obtain the corresponding testing results. The workflow shown in Figure 3 is repeated K times so that each fold has the opportunity to become the testing set.

To highlight the performance of our multimodality fusion method, a single modality model ridge regression (RR) and 4 multimodality fusion models, i.e., MV-TSK-FS (Jiang et al., 2016), simpleMKL (Rakotomamonjy et al., 2008), RFF-MKL (Liu et al., 2013), and MV-L2-SVM (Wang et al., 2015), are introduced for comparison study. Table 2 shows the parameter settings of RR and our method.

4.2 Result analysis

The experimental results were reported from three aspects, i.e., feature selection of every single modality, comparison

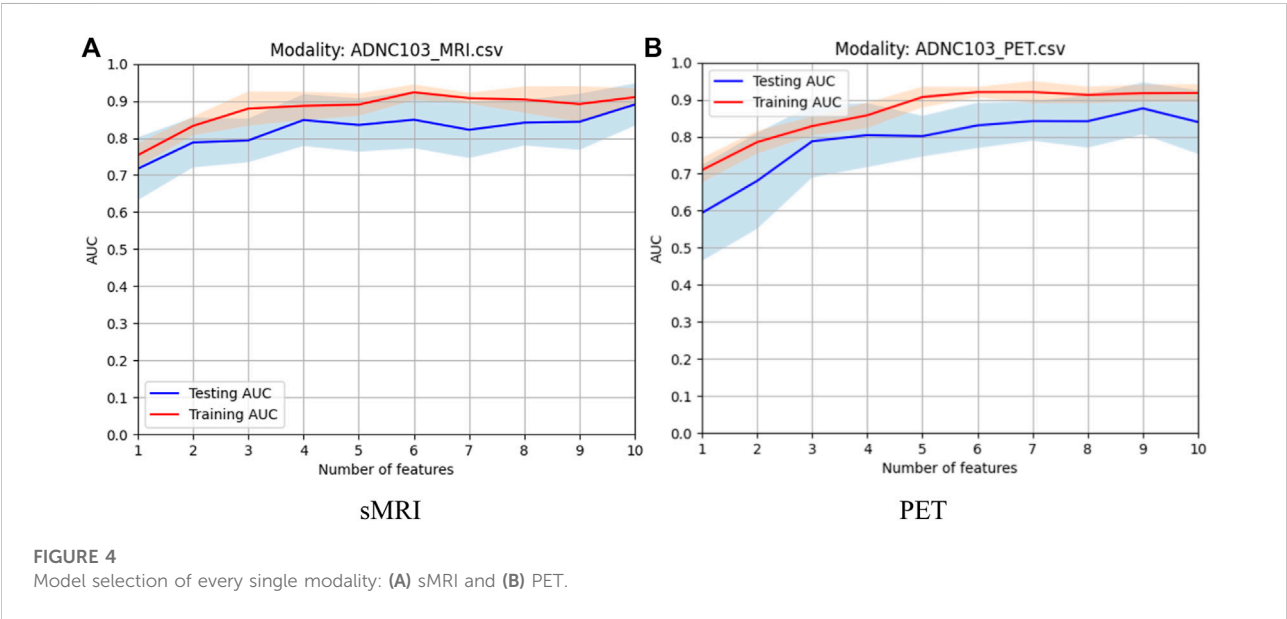
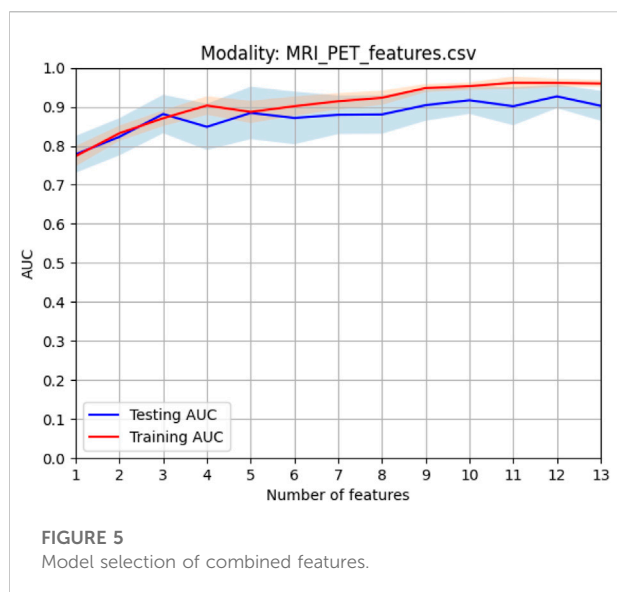


FIGURE 4 Model selection of every single modality: (A) sMRI and (B) PET.



between single modality and multimodality in terms of AUC, and overfitting analysis in terms of the discrepancy between training and testing.

4.2.1 Feature selection of every single modality

In this study, before modality fusion, we have to select the best model for every single modality. That is to say, we should

find an optimal feature subset for each modality. As we stated before, the *Fish score* was employed as the supervised method to reduce the irrelevant features to the outcome. *Person score* was employed as the unsupervised method to reduce the redundancy between features. After the two-step feature selection, we select the optimal feature set that deduces the best training AUC. As shown in Figure 4, for sMRI, it can be found that the first 6 features were selected for the following modality fusion, and for PET, the first 7 features were selected for the following modality fusion.

4.2.2 Comparison between single modality and multimodality

When the optimal feature sets of sMRI and PET were combined, feature redundancy between different modalities may also exist. Therefore, *Person score* was also employed as the unsupervised method to reduce the redundancy across different modalities. After this procedure, the best model can be obtained by finding the best training AUC. As shown in Figure 5, the first 12 features can generate the best model.

Figure 6 shows the comparison results in terms of the ROC curve of sMRI, PET, and their combination. It can be found that the testing AUC of multimodality fusion is 0.9188, which is better than that of every single modality. This is because each modality is mapped into the kernel space and multikernel learning can explore the complementary information

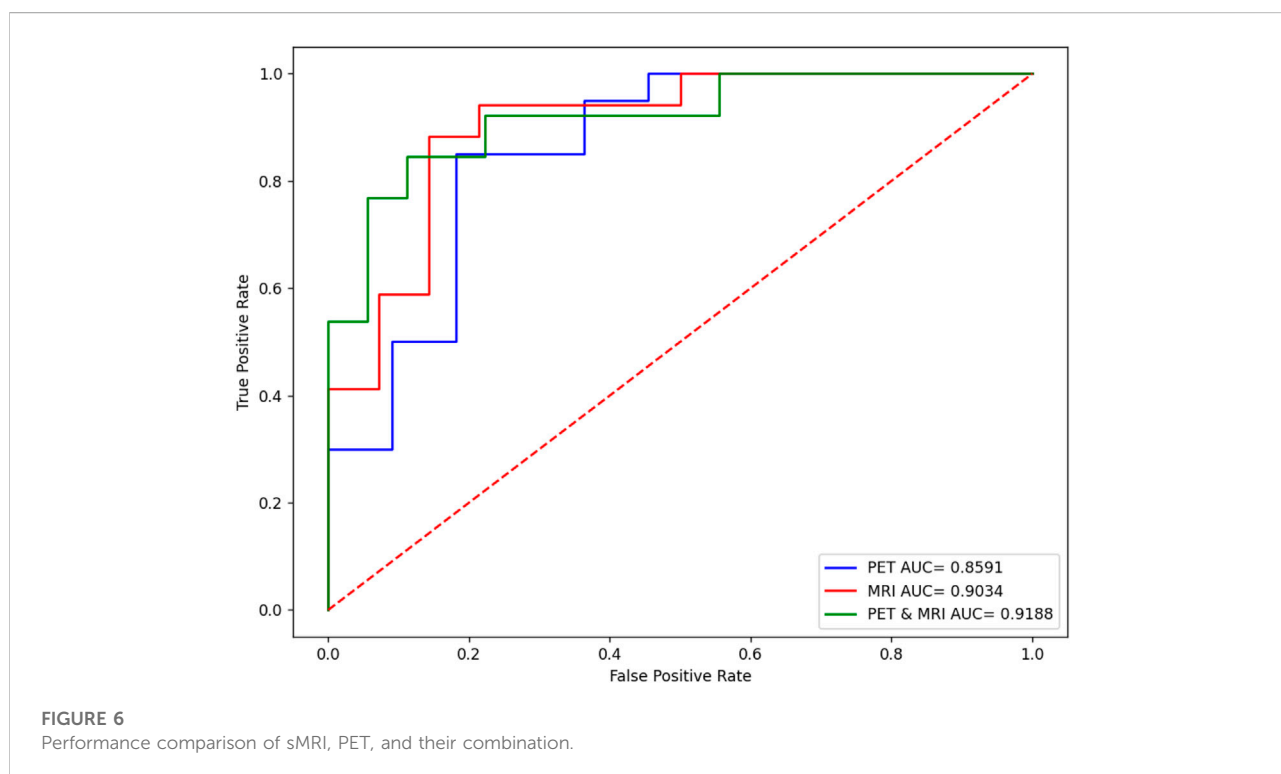
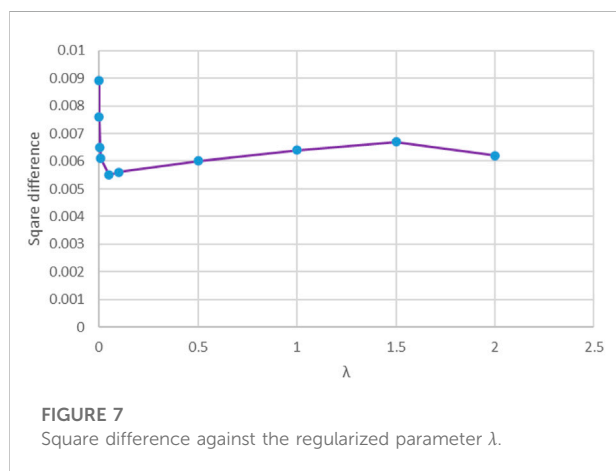


TABLE 3 Comparison with state-of-art multimodality methods in terms of accuracy and AUC.

Methods	Accuracy	AUC
MV-TSK-FS	0.9236 \pm 0.0058*	0.8897 \pm 0.0032*
simpleMKL	0.9454 \pm 0.0047*	0.9059 \pm 0.0063*
RFF-MKL	0.9402 \pm 0.0025*	0.8987 \pm 0.0036*
MV-L2-SVM	0.9489 \pm 0.0046*	0.9021 \pm 0.0047*
Our method	0.9586 \pm 0.0032	0.9188 \pm 0.0028

The bold means the best performance.



between the two modalities. In addition, from Eq. 10, we can see that the coefficient of the kernel matrix is sparse so that the modality which contains more patterns is endowed with more attention.

4.2.3 Comparison with state-of-art multimodality methods

To highlight the promising performance of the proposed method, we introduce 4 state-of-art multimodality fusion methods for comparison studies. In addition to AUC, *accuracy* is also introduced to measure the classification performance. Table 3 shows the comparison results in terms of both accuracy and AUC, where the best results are marked in bold, and “*” means that the difference between state-of-art methods and the proposed method is significant.

From Table 3, we can find that our method achieves the best performance. In particular, simpleMKL and RFF-MKL are also multikernel-based methods, but both of them perform worse than our method. This phenomenon indicates that label relaxation and compactness graph mechanisms are useful to

improve the classification performance. In addition, we see that MV-TSK-FS and MV-L2-SVM perform worse than multikernel-based methods. This is because MV-TSK-FS and MV-L2-SVM both used modality-consistent regularization to achieve multimodality fusion, which did not consider the complementary information across different modalities. With the “all-single” fusion strategy used in multikernel-based methods, every single feature and the possible combinations are all considered so that the complementary information can be fully explored.

4.2.4 Overfitting analysis

From Eq. 10, we can see that λ was used to control the contribution of the manifold regularization term. We know that the manifold regularization term can reduce overfitting; therefore, to quantificationally observe the overfitting, the square difference between training AUC and testing AUC was used. Figure 7 shows the square difference against the regularized parameter λ . From Figure 7, it can be found that from $\lambda = 0.001$ to $\lambda = 0.05$, the square difference between training AUC and testing AUC decreased gradually, which means that overfitting was reduced and the generalization ability was improved. This is because the manifold regularization term in the objective function assumes that when the training samples were transformed from the feature space to the label space, if two samples are in the same manifold in the feature space, they are also in the same class the label space (Fang et al., 2017). With this assumption, sparse samples, noisy samples, or outliers will be compressed into a compact class so that the hyperplane will not excessively fit these samples.

5 Conclusion

In the area of personalized medicine, multimodal neuroimage data fusion plays a significant role in brain disease diagnosis. Multikernel learning actually provides a natural framework for multimodality fusion. However, when multikernel learning is applied to practice, e.g., medical data analysis, overfitting often exists. Therefore, in this study, according to RLR linear regression, we integrate label relaxation and compactness graph mechanisms into multikernel learning and propose a new multikernel learning algorithm for AD diagnosis. In the experimental study, the proposed method is evaluated in the scenario of AD diagnosis. The promising performance indicates the advantages of our method. However, from Figure 2, we can find that there are many kernel matrices generated during model training, which

may consume a lot of CPU seconds and storage memory. Therefore, how to speed up the training and reduce storage memory is a hot topic in our future work.

Data availability statement

Publicly available datasets were analyzed in this study. The data are available on <http://adni.loni.usc.edu/about/>.

Author contributions

XR and JS contributed to coding and manuscript writing. YC contributed to data preprocessing. KJ supervised the whole study.

Funding

This work was partly supported by the Postgraduate Research & Practice Innovation Program of Jiangsu Province (No. KYCX21_3105).

References

- Bao, W., Xie, F., Zuo, C., Guan, Y., and Huang, Y. H. (2021). PET neuroimaging of Alzheimer's disease: radiotracers and their utility in clinical research. *Front. Aging Neurosci.* 13, 624330. doi:10.3389/fnagi.2021.624330
- Bhatnagar, Gaurav, Wu, Q. M. Jonathan, and Zheng, Liu (2015). A new contrast based multimodal medical image fusion framework. *Neurocomputing* 157, 143–152. doi:10.1016/j.neucom.2015.01.025
- Buvaneshwari, P. R., and Gayathri, R. (2021). Detection and Classification of Alzheimer's disease from cognitive impairment with resting-state fMRI. *Neural Comput. Appl.*, 1–16. doi:10.1007/s00521-021-06436-2
- Chandrashekar, G., and Sahin, F. (2014). A survey on feature selection methods. *Comput. Electr. Eng.* 40 (1), 16–28. doi:10.1016/j.compeleceng.2013.11.024
- Daneshvar, Sabalan, and Hassan, Ghassemian (2010). MRI and PET image fusion by combining IHS and retina-inspired models. *Inf. fusion* 11 (2), 114–123. doi:10.1016/j.inffus.2009.05.003
- Dimitriadis, Stavros I., Liparas, D., and Tsolaki, M. N. (2018). Random forest feature selection, fusion and ensemble strategy: Combining multiple morphological MRI measures to discriminate among healthy elderly, MCI, cMCI and Alzheimer's disease patients: From the Alzheimer's disease neuroimaging initiative (ADNI) database. *J. Neurosci. Methods* 302, 14–23. doi:10.1016/j.jneumeth.2017.12.010
- Fan, Y., Batmanghelich, N., Clark, C. M., and Davatzikos, C. (2008). Spatial patterns of brain atrophy in MCI patients, identified via high-dimensional pattern classification, predict subsequent cognitive decline. *Neuroimage* 39 (4), 1731–1743. doi:10.1016/j.neuroimage.2007.10.031
- Fang, X., Xu, Y., Li, X., Lai, Z., Wong, W. K., Fang, B., et al. (2017). Regularized label relaxation linear regression. *IEEE Trans. Neural Netw. Learn. Syst.* 29 (4), 1006–1018. doi:10.1109/TNNLS.2017.2648880
- Friston, K. J. (2009). Modalities, modes, and models in functional neuroimaging. *Science* 326 (5951), 399–403. doi:10.1126/science.1174521
- Jiang, Y., Deng, Z., Chung, F. L., Wang, G., Qian, P., Choi, K. S., et al. (2016). Recognition of epileptic EEG signals using a novel multiview TSK fuzzy system. *IEEE Trans. Fuzzy Syst.* 25 (1), 3–20. doi:10.1109/tfuzz.2016.2637405
- Jiang, Y., Zhang, Y., Lin, C., Wu, D., and Lin, C. T. (2020). EEG-based driver drowsiness estimation using an online multi-view and transfer TSK fuzzy system. *IEEE Trans. Intell. Transp. Syst.* 22 (3), 1752–1764. doi:10.1109/tits.2020.2973673
- Karikari, T. K., Benedet, A. L., Ashton, N. J., Lantero Rodriguez, J., Snellman, A., Suarez-Calvet, M., et al. (2021). Diagnostic performance and prediction of clinical progression of plasma phospho-tau181 in the Alzheimer's Disease Neuroimaging Initiative. *Mol. Psychiatry* 26 (2), 429–442. doi:10.1038/s41380-020-00923-z
- Klöppel, S., Abdulkadir, A., Jack, C. R., Jr, Koutsouleris, N., Mourão-Miranda, J., Vemuri, P., et al. (2012). Diagnostic neuroimaging across diseases. *Neuroimage* 61 (2), 457–463. doi:10.1016/j.neuroimage.2011.11.002
- Kohannim, O., Hua, X., Hibar, D. P., Lee, S., Chou, Y. Y., Toga, A. W., et al. (2010). Boosting power for clinical trials using classifiers based on multiple biomarkers. *Neurobiol. Aging* 31, 1429–1442. doi:10.1016/j.neurobiolaging.2010.04.022
- Li, Tianjie, and Wang, Yuanyuan (2012). Multiscaled combination of MR and SPECT images in neuroimaging: a simplex method based variable-weight fusion. *Comput. Methods Programs Biomed.* 105 (1), 31–39. doi:10.1016/j.cmpb.2010.07.012
- Liu, F., Zhou, L., Shen, C., and Yin, J. (2013). Multiple kernel learning in the primal for multimodal Alzheimer's disease classification. *IEEE J. Biomed. Health Inf.* 18 (3), 984–990. doi:10.1109/JBHI.2013.2285378
- Madusanka, N., Choi, H. K., So, J. H., and Choi, B. K. (2019). Alzheimer's Disease classification based on multi-feature fusion. *Curr. Med. Imaging Rev.* 15 (2), 161–169. doi:10.2174/1573405614666181012102626
- Rakotomamonjy, A., Bach, F., Canu, S., and Grandvalet, Y. (2008). SimpleMKL. *J. Mach. Learn. Res.* 9, 2491–2521.
- Shukla, P., Verma, A., Verma, S., and Kumar, M. (2020). Interpreting SVM for medical images using Quadtree. *Multimed. Tools Appl.* 79 (39), 29353–29373. doi:10.1007/s11042-020-09431-2
- Suk, H. I., Lee, S. W., and Shen, D. (2014). Hierarchical feature representation and multimodal fusion with deep learning for AD/MCI diagnosis. *NeuroImage* 101, 569–582. doi:10.1016/j.neuroimage.2014.06.077
- Wang, G., Deng, Z., and Choi, K. S. (2015). "Detection of epileptic seizures in EEG signals with rule-based interpretation by random forest approach," in International Conference on Intelligent Computing, Fuzhou, China, 20–23 Aug 2015 (Cham: Springer), 738–744.
- Wang, P., Qiu, C., Wang, J., Wang, Y., Tang, J., Huang, B., et al. (2021). Multimodal data fusion using non-sparse multi-kernel learning with regularized label softening. *IEEE J. Sel. Top. Appl. Earth Obs. Remote Sens.* 14, 6244–6252. doi:10.1109/jstars.2021.3087738

Acknowledgments

We thank the reviewers whose comments and suggestions helped improve this manuscript.

Conflict of interest

The authors declare that the research was conducted in the absence of any commercial or financial relationships that could be construed as a potential conflict of interest.

Publisher's note

All claims expressed in this article are solely those of the authors and do not necessarily represent those of their affiliated organizations, or those of the publisher, the editors, and the reviewers. Any product that may be evaluated in this article, or claim that may be made by its manufacturer, is not guaranteed or endorsed by the publisher.

Xia, K., Zhang, Y., Jiang, Y., Qian, P., Dong, J., Yin, H., et al. (2020). TSK fuzzy system for multi-view data discovery underlying label relaxation and cross-rule & cross-view sparsity regularizations. *IEEE Trans. Ind. Inf.* 17 (5), 3282–3291. doi:10.1109/tii.2020.3007174

Xiang, S., Nie, F., Meng, G., Pan, C., and Zhang, C. (2012). Discriminative least squares regression for multiclass classification and feature selection. *IEEE Trans. Neural Netw. Learn. Syst.* 23 (11), 1738–1754. doi:10.1109/TNNLS.2012.2212721

Zeng, N., Qiu, H., Wang, Z., Liu, W., Zhang, H., Li, Y., et al. (2018). A new switching-delayed-PSO-based optimized SVM algorithm for diagnosis of Alzheimer's disease. *Neurocomputing* 320, 195–202. doi:10.1016/j.neucom.2018.09.001

Zhang, D., Wang, Y., Zhou, L., Yuan, H., and Shen, D. (2011). Multimodal classification of Alzheimer's disease and mild cognitive impairment. *Neuroimage* 55 (3), 856–867. doi:10.1016/j.neuroimage.2011.01.008

Zhang, Y., Chung, F. L., and Wang, S. (2020). Clustering by transmission learning from data density to label manifold with statistical diffusion. *Knowledge-Based Syst.* 193, 105330. doi:10.1016/j.knosys.2019.105330

Zhang, Y., Ishibuchi, H., and Wang, S. (2017). Deep Takagi–Sugeno–Kang fuzzy classifier with shared linguistic fuzzy rules. *IEEE Trans. Fuzzy Syst.* 26 (3), 1535–1549. doi:10.1109/tfuzz.2017.2729507

Zhang, Y., Xia, K., Jiang, Y., Qian, P., Cai, W., Qiu, C., et al. (2022a). Multi-modality fusion & inductive knowledge transfer underlying non-sparse multi-kernel learning and distribution adaption. *IEEE/ACM Trans. Comput. Biol. Bioinform.*, 1. doi:10.1109/TCBB.2022.3142748

Zhang, Y., Lam, S., Yu, T., Teng, X., Zhang, J., Lee, F. K. H., et al. (2022b). Integration of an imbalance framework with novel high-generalizable classifiers for radiomics-based distant metastases prediction of advanced nasopharyngeal carcinoma. *Knowledge-Based Syst.* 235, 107649. doi:10.1016/j.knosys.2021.107649

Zhang, Y., Wang, S., Xia, K., Jiang, Y., and Qian, P. (2021). Orosomucoid-like protein 3, rhinovirus and asthma. *World J. Crit. Care Med.* 66, 170–182. doi:10.5492/wjccm.v10.i5.170



OPEN ACCESS

EDITED BY
Khairunnisa Hasikin,
University of Malaya, Malaysia

REVIEWED BY
Jun Dang,
Chinese Academy of Medical Sciences
and Peking Union Medical College,
China
Xiangkun Xu,
University of Texas Southwestern
Medical Center, United States
Qingyi Liu,
Shandong University of Science and
Technology, China

*CORRESPONDENCE
Hong Ge,
gehong666@126.com
Jing Cai,
jing.cai@polyu.edu.hk

SPECIALTY SECTION
This article was submitted to
Experimental Pharmacology and
Drug Discovery,
a section of the journal
Frontiers in Pharmacology

RECEIVED 17 June 2022
ACCEPTED 04 August 2022
PUBLISHED 19 September 2022

CITATION
Li B, Ren G, Guo W, Zhang J, Lam S-K,
Zheng X, Teng X, Wang Y, Yang Y, Dan Q,
Meng L, Ma Z, Cheng C, Tao H, Lei H,
Cai J and Ge H (2022), Function-Wise
Dual-Omics analysis for radiation
pneumonitis prediction in lung
cancer patients.
Front. Pharmacol. 13:971849.
doi: 10.3389/fphar.2022.971849

COPYRIGHT
© 2022 Li, Ren, Guo, Zhang, Lam,
Zheng, Teng, Wang, Yang, Dan, Meng,
Ma, Cheng, Tao, Lei, Cai and Ge. This is
an open-access article distributed
under the terms of the [Creative
Commons Attribution License \(CC BY\)](#).
The use, distribution or reproduction in
other forums is permitted, provided the
original author(s) and the copyright
owner(s) are credited and that the
original publication in this journal is
cited, in accordance with accepted
academic practice. No use, distribution
or reproduction is permitted which does
not comply with these terms.

Function-Wise Dual-Omics analysis for radiation pneumonitis prediction in lung cancer patients

Bing Li¹, Ge Ren², Wei Guo¹, Jiang Zhang², Sai-Kit Lam²,
Xiaoli Zheng¹, Xinzhi Teng², Yunhan Wang¹, Yang Yang¹,
Qinfu Dan¹, Lingguang Meng¹, Zongrui Ma², Chen Cheng¹,
Hongyan Tao¹, Hongchang Lei¹, Jing Cai^{2*} and Hong Ge^{1*}

¹Department of Radiation Oncology, The Affiliated Cancer Hospital of Zhengzhou University and Henan Cancer Hospital, Zhengzhou, China, ²Department of Health Technology and Informatics, The Hong Kong Polytechnic University, Hong Kong SAR, China

Purpose: This study investigates the impact of lung function on radiation pneumonitis prediction using a dual-omics analysis method.

Methods: We retrospectively collected data of 126 stage III lung cancer patients treated with chemo-radiotherapy using intensity-modulated radiotherapy, including pre-treatment planning CT images, radiotherapy dose distribution, and contours of organs and structures. Lung perfusion functional images were generated using a previously developed deep learning method. The whole lung (WL) volume was divided into function-wise lung (FWL) regions based on the lung perfusion functional images. A total of 5,474 radiomics features and 213 dose features (including dosiomics features and dose-volume histogram factors) were extracted from the FWL and WL regions, respectively. The radiomics features (R), dose features (D), and combined dual-omics features (RD) were used for the analysis in each lung region of WL and FWL, labeled as WL-R, WL-D, WL-RD, FWL-R, FWL-D, and FWL-RD. The feature selection was carried out using ANOVA, followed by a statistical F-test and Pearson correlation test. Thirty times train-test splits were used to evaluate the predictability of each group. The overall average area under the receiver operating characteristic curve (AUC), accuracy, precision, recall, and f1-score were calculated to assess the performance of each group.

Results: The FWL-RD achieved a significantly higher average AUC than the WL-RD group in the training (FWL-RD: 0.927 ± 0.031 , WL-RD: 0.849 ± 0.064) and testing cohorts (FWL-RD: 0.885 ± 0.028 , WL-RD: 0.762 ± 0.053 , $p < 0.001$). When using radiomics features only, the FWL-R group yielded a better classification result than the model trained with WL-R features in the training (FWL-R: 0.919 ± 0.036 , WL-R: 0.820 ± 0.052) and testing cohorts (FWL-R: 0.862 ± 0.028 , WL-R: 0.750 ± 0.057 , $p < 0.001$). The FWL-D group obtained an average AUC of 0.782 ± 0.032 , obtaining a better classification performance than the WL-D feature-based model of 0.740 ± 0.028 in the training cohort, while no significant difference was observed in the testing cohort (FWL-D: 0.725 ± 0.064 , WL-D: 0.710 ± 0.068 , $p = 0.54$).

Conclusion: The dual-omics features from different lung functional regions can improve the prediction of radiation pneumonitis for lung cancer patients under IMRT treatment. This function-wise dual-omics analysis method holds great promise to improve the prediction of radiation pneumonitis for lung cancer patients.

KEYWORDS

lung functional imaging, radiation pneumonitis, radiomics, dosiomics, radiotherapy

Introduction

Lung cancer is the leading cause of cancer-related death worldwide (Sung et al., 2021). Radiation therapy or radiotherapy (RT) is one of the golden-standard treatment techniques for patients with locally advanced non-small-cell lung cancer (NSCLC) (Kong et al., 2005; Chang et al., 2016). Study shows a higher radiation dose can achieve better tumor control and improve the treatment outcome (Kong et al., 2005). However, dose escalation of lung cancer is greatly limited by radiation-induced side effects, such as radiation pneumonitis (RP). RP may occur in up to 30% of lung RT patients and is lethal in 2% of them (Zhang et al., 2012; Kipritidis et al., 2015). Hence, predicting RP is highly desirable for better dose optimization and personalization to maximize the treatment outcome in lung cancer RT.

At present treatment planning of lung cancer RT, several dosimetric factors from the dose-volume histogram (DVH) were found to be associated with RP, such as V_5 , V_{20} , and D_{mean} (Baisden et al., 2007; Barriger et al., 2012; Bongers et al., 2013; Palma et al., 2013; Cai et al., 2014; Pinnix et al., 2015). These parameters are commonly used as dose constraints in clinical plan evaluation (Ganti et al., 2021). Meanwhile, several prevalent models using DVH parameters, such as normal tissue complication probability (NTCP), were proposed to predict high risk RP patients (Begosh-Mayne et al., 2020; Wang et al., 2020). However, DVH parameters can only distinguish statistical one-dimensional dose information rather than characterizing the dose distribution heterogeneity. With the aid of the radiomics definition (Lambin et al., 2017), dosiomics features were calculated based on the three-dimensional dose distribution to describe the dose spatial information (Liang et al., 2019). Several studies also have demonstrated significantly superior models with the dosiomics feature compared to the DVH-based model or the NTCP model for predicting RP (Liang et al., 2019; Palma et al., 2019; Adachi et al., 2021). Meanwhile, CT-based radiomics features describe the statistical information, shaped, and textual characteristics in a certain volume. The dual-omics combines the radiomics and dose features and is able to further improve the prediction for RP (Adachi et al., 2021; Jiang et al., 2021; Puttanawarut et al., 2022). However, those radiomics or dose features utilized in current studies were calculated from the whole lung region, rather than considering

the heterogeneity inside the lung, for example, the difference in high- and low- functional lung regions.

Lung function information has been proven to be associated with RP, which promises to improve the RP prediction accuracy (Bucknell et al., 2018; Lee et al., 2018; Weller et al., 2019; Bourbonne et al., 2020; O'Reilly et al., 2020). O'Reilly et al. demonstrated the RP prediction improvement using the DVH factor (V_{20}) from three high functional lung regions and compared these biomarkers to the entire lung region (O'Reilly et al., 2020). Lee et al. evaluated the correlation between several DVH factors (V_5 , V_{20} , and D_{mean}) between the high functional lung region and the whole lung region, showing the potential of stratifying patients for pneumonitis prediction (Lee et al., 2018). Owen et al. demonstrated that irradiating to low functional lung region may increase radiation toxicity (Owen et al., 2021). Several studies also showed the potential of using dosimetry parameters based on functional lung images in predicting RP (Wang et al., 2012; Farr et al., 2015; Kimura et al., 2015; Xiao et al., 2018; Owen et al., 2021). However, these studies only explored the association between the dose factors and the RP without investigating the correlation between anatomical CT images and the RP. Besides, most studies focused on the dose features in the high functional lung region rather than the low functional lung region.

In this study, we developed a function-wise lung (FWL) analysis approach by integrating radiomics and dose features from both whole lung (WL) and FWL (including separated high- and low- functional lung) to predict RP for NSCLC patients. The radiomics features, dose features, and combined dual-omics features of each group were utilized for analysis. The feature selection metrics are the ANOVA followed by the statistical F-test and the Pearson correlation test. Thirty times train-test splits were used to evaluate the predictability of each group. The overall average area under the receiver operating characteristic curve (AUC), accuracy, precision, recall, and f1-score were calculated to assess the performance of each group.

Materials and methods

Data characteristics

The inclusion criteria are as follows: 1) diagnosed as primary locally-advanced lung cancer (stages IIIA/IIIC (AJCC 8th)); 2)

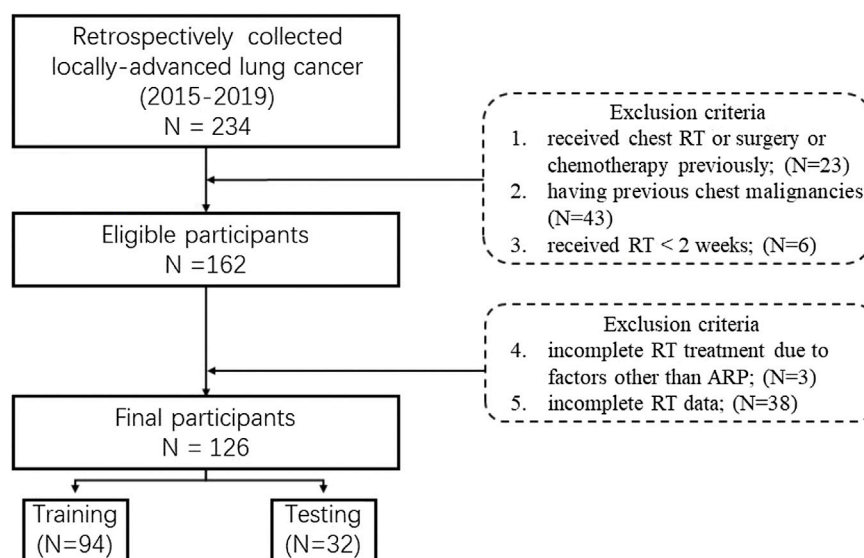


FIGURE 1
Flowchart of the inclusion and exclusion criteria.

having no distant metastasis; 3) treated with curative intensity-modulated radiotherapy (IMRT); 4) receiving contrast-enhanced CT for RT; 5) 18–70 years old. And the exclusion criteria are as follows: 1) received chest RT or surgery or chemotherapy previously; 2) having previous chest malignancies; 3) received RT < 2 weeks; 4) incomplete RT treatment due to factors other than acute RP; 5) incomplete RT data.

The study was approved by the Institutional Review Board of the Affiliated Cancer Hospital of Zhengzhou University. Initially, a total of 162 pathological confirmed NSCLC patients staging IIIA/IIIC between 2015 and 2019 were retrospectively collected from the hospital. Considering the excluded criteria (shown in below), 126 cases were final enrolled in the study (Figure 1). All patients were treated by the 6 MV IMRT with a 50–70 Gy total prescription dose and 1.8–2.2 Gy fractional dose for 5 days per week. The radiation pneumonitis (RP) case was consecutively followed up at least 6 months after the first radiotherapy, and then graded with the Common Terminology Criteria for Adverse Events (CTCAE) V4.0. by one qualified imaging physician based on the CT scans. In this study, RP patients with grading ≥ 2 are defined as severe RP events because of dose escalation consideration.

Image acquisition

Three types of image data were involved in this study, including planning CT images, three-dimension dose distribution images, and organs-at-risk (OAR) structures. All planning CT images were acquired from a 16-slice Brilliance Big

Bore CT (Philips Medical System, Cleveland, OH, U.S.). The scanning parameters were as follows: scanning X-ray tube voltage = 120 kV, current = 321 mA, thickness = 3 mm, slice pixels = 512×512 and spacing = $1.152 \text{ mm} \times 1.152 \text{ mm}$. The scanning range was from the level of the cricoid cartilage to the lower border of the 12th thoracic vertebra covering the WL volume (Bradley et al., 2020). The 3D dose was calculated with a grid of 3 mm in the treatment planning system (TPS). The gross tumor volume was excluded from the lung volume with manually contouring by a qualified physician.

Function-wise lung region

In this study, the functional images were generated using a previously developed deep learning neural network, which can translate the pulmonary anatomy information into functional information (Ren et al., 2021a; Ren et al., 2021b). In general, a 3D attention residual neural network was utilized to extract high level features from CT images and synthesize the perfusion images. This model was trained with CT and single-photon emission computerized tomography (SPECT) perfusion images of lung disease patients. This model used a 3D encoding-decoding structure to capture the hierarchical texture features of the input CT images with two attention modules to help focus on the defect regions, which is able to achieve a medium-to-high approximation with the ground truth SPECT perfusion images.

After image synthesis, the functional image was normalized to the range of 0–1 by subtracting the minimum value and then

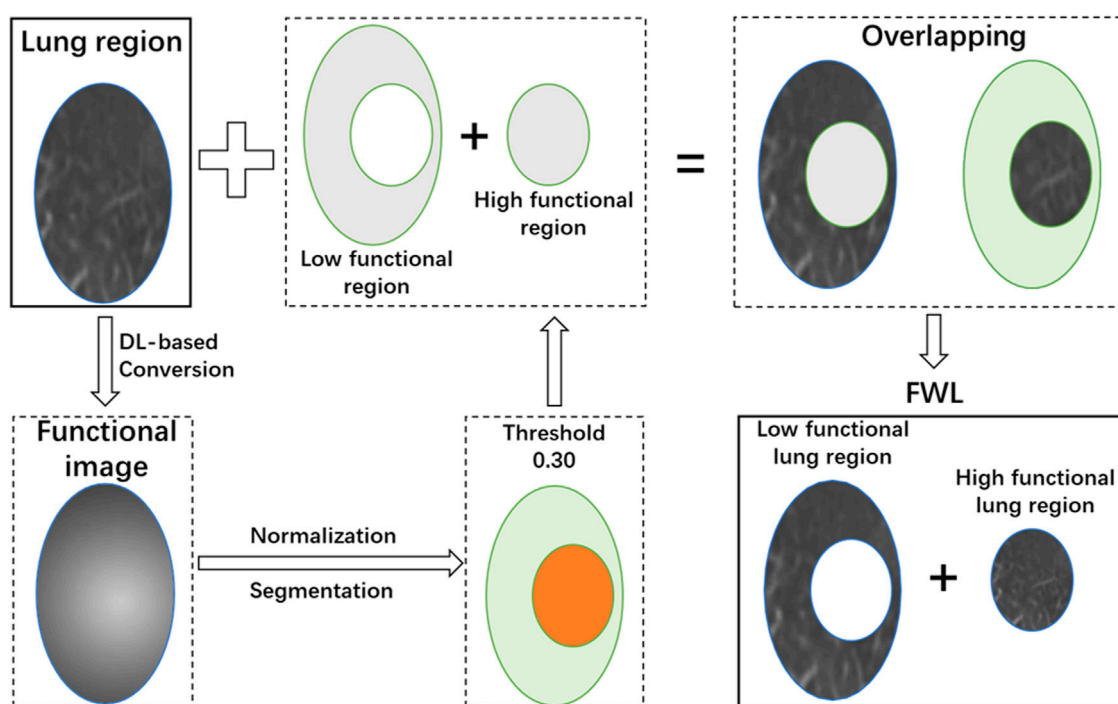


FIGURE 2
The scheme of the function-wise lung region generation.

divided by the maximum pixel value of function images. A threshold of 0.3 was used to divide the lung into high- and low- functional regions. Then the high- and low- functional lung regions were segmented on the CT image. This procedure is illustrated in Figure 2. After thresholding, the FWL was defined as the combination of the high- and low- functional lung regions. Besides, the WL region was also utilized as the basic comparison model.

Feature extraction

In the study, radiomics features (Lambin et al., 2017) and dose features of the previous regions were extracted from the CT images and 3D dose distribution.

For radiomics features, the first-order and high-order radiomics features were extracted based on the original image and 11 filter-based images. The details of these radiomics features were described in the study (Lam et al., 2021). The only difference was the settings of bin counts, in the range of [20, 50, 100, 150, 200] and a total of 5,474 radiomics features were extracted from a region of interest (ROI).

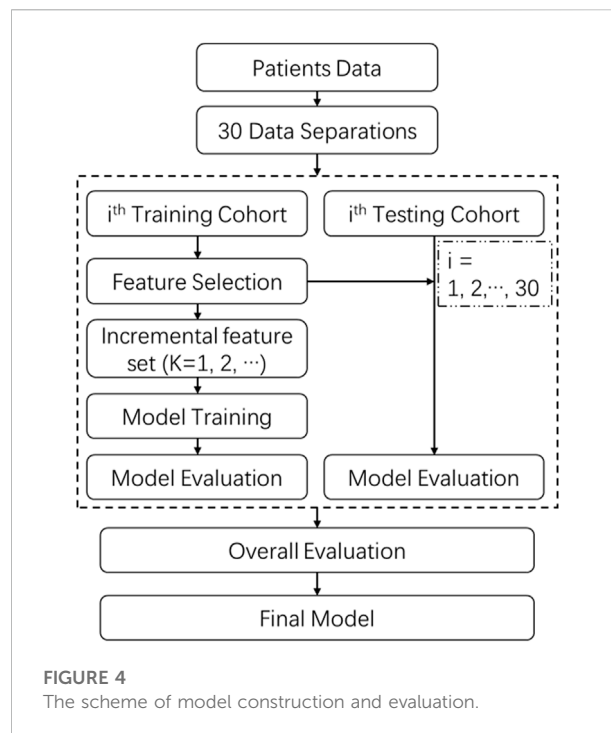
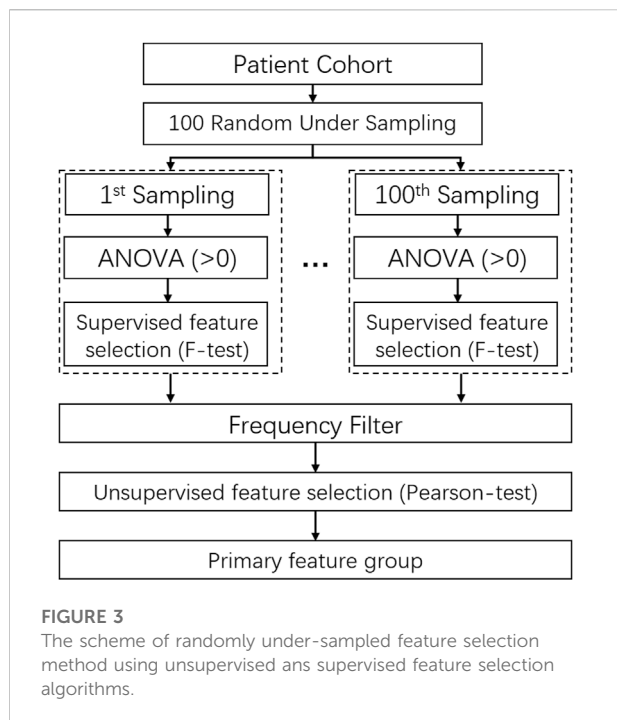
The dose features can be categorized into three types: 1) scale-invariant 3D dose statistical moments (Pham et al., 2011), 2) DVH parameters (Marks et al., 2010; Faught et al., 2017), and 3) dosiomics features (Liang et al., 2019). The scale-invariant 3D

dose statistical moments described the dose spatial distribution along three directions of anterior-posterior, medial-lateral, and craniocaudal (Pham et al., 2011). Except for the constant value of the order of [0, 0, 0], a total of 63 dose statistical moments were employed in the dose features. The DVH parameters consisted of Dx and Vx, where Dx is the dose larger than x% volume, and Vx is the volume larger than the x Gy or x% of the prescription dose. A total of 59 DVH parameters were included. The dosiomics features were radiomics features based on the image of 3D dose distribution. In the study, only the original image type was adopted in extracting dosiomics features. A number of 91 dosiomics features were extracted from the original 3D dose distribution in an ROI. Eventually, a total of 213 dose features were included.

In the study, two kinds of regions (WL and FWL) were used to extract features with a total of 5,687 features and 11,374 features, respectively.

Feature selection

The feature dimension reduction is a crucial step to avoid model overfitting or underfitting. A combination of the F-test and the Pearson correlation test was utilized for the feature selection on the scikit-learn package in Python (version 1.0.1) (Pedregosa et al., 2011; Buitinck et al., 2013). Besides, the randomly under-sampling method



was performed for comprehensively screening out the optimal feature group, which was described in the study (Yu et al., 2019; Lam et al., 2021).

The detail of feature selection is illustrated in Figure 3. 70% patients were randomly under-sampled from the whole patient cohorts by 100 times. At each sampling, all features with a variance of zero were filtered out to reduce the feature dimensions and the subsequent computational complexity. After that, the F-score of all features was calculated by combining the label data based on the F-test, and an F-score with a p -value smaller than 0.01 was marked as 1, otherwise as 0. Through 100 times sampling, a matrix with $100 \times N$ (N : feature quantity with variance > 0) was obtained. It is followed by the frequency filtering process to acquire more stable and robust features. Then, 10% of the quantity of all features or at least 40 features were reserved. Finally, the primary feature group was chosen by the Pearson correlation test with the threshold of coefficient of 0.5 as keeping the higher frequency one for two correlated features.

Model construction and evaluation

In the study, two single-omics models, radiomics model (R) and dosiomics model (D), and the combined model (RD) were developed for WL and FWL regions separately, producing six models in total, labeled as WL-R, WL-D, WL-RD, FWL-R, FWL-D, and FWL-RD.

The schematic diagram of the model development and evaluation is shown in Figure 4. All patient cohort was randomly

divided into training and testing cohorts with a ratio of 3:1 across a repeat stratified splitting process of 30 times with different randomization, which simulated various patients' data distributions to assess the model performance. At each split, training cohorts were sent to the procedure of feature selection, and the relevant primary feature group was obtained. Then, different feature combinations owning from one to all primary features were explored. The finally optimal feature group was determined by the maximum of the following overall average area under the receiver operating characteristic curve (ROC) curve (AUC) in the testing cohort. With the optimal feature combination, a classification regression algorithm of Ridge was utilized to develop a classification model using 10-fold cross-validation and hyper-parameters optimization search in the training cohort. The loss function for the Ridge classifier is $\min \|X_{\omega} - y\|_2^2 + \alpha \|\omega\|_2^2$, where α is complexity parameter with $\alpha > 0$. After that, the model performance in the training and testing cohorts was performed by using a series of evaluation metrics, including accuracy, precision, recall, F1-score, and AUC. The average and the standard deviation (STD) were calculated in the training and testing cohorts by considering all splitting. The final model was evaluated by using the optimal feature group.

Model comparison and statistic analysis

For each omics feature, the model performance using the corresponding omics features extracted from the function-

TABLE 1 Patients' characteristics.

Characteristics	Overall (126)
Gender	$p = 0.04$
Male (N/%)	109/86.5%
Female(N/%)	17/13.5%
Age, median (range)	61 (29 -- 82) ($p = 0.67$)
Pathology	$p = 0.46$
SCC (N/%)	79/62.7%
ADC (N/%)	42/33.3%
Others (N/%)	5/4.0%
RT Dose, median (range)	60 (50–70) Gy ($p = 0.94$)
Smoking	$p = 0.23$
Activity or former (N/%)	97/77.0%
Never (N/%)	29/23.0%
Overall Stage	$p = 0.30$
IIIA (N/%)	72/57.1%
IIIB (N/%)	37/29.4%
IIIC (N/%)	17/13.5%
Treatment method	$p = 0.97$
SCRT (N/%)	83/65.9%
CCRT (N/%)	42/33.3%
RT (N/%)	1/0.8%
RP (N/%)	64/50.8%

SCC, squamous carcinoma cancer; ADC, adenocarcinoma cancer; SCRT, sequence chemoradiotherapy; CCRT, concomitant chemoradiotherapy.

wise lung regions was compared against the WL region in the training and testing cohorts using the five evaluation metrics. For each involved lung region, the model using dual-omics features was compared against the single-omics features in both training and testing cohorts using five evaluation metrics. Besides, net clinical benefits for all models were investigated using decision curve analyses (DCA) (Vickers and Elkin, 2006; Vickers et al., 2019). The DCA is a method to evaluate the clinical valuation of models overcoming the limitations of both traditional statistical metrics, such as discrimination and calibration.

The two-sided paired student t -test was utilized to compare the above-mentioned models with a group of features. On the other hand, the two-sided paired student t -test was also performed for the continuous clinical characteristics, while the Chi-square test was applied for the categorical variables. A p -value smaller than 0.05 was considered statistically significant. Except for the previously mentioned five evaluation metrics, the 95% confidence interval (CI) by the Delong method with (DeLong et al., 1988) 2000 times for all metrics was provided to access the ability to discriminate between severe RP cases and non-RP cases. Statistical analysis was performed with Python 3.7 and Pingouin 0.5.0 (Vallat, 2018).

Results

Patients characteristics

A total of 126 NSCLC patients were retrospectively involved in the study. The main characteristics of the patients are listed in Table 1. As shown in the table, 50.8% of patients (64 cases) developed the radiation pneumonitis with a grade ≥ 2 . Except for the gender with a p -value of 0.04, the other clinical factors had no statistically significant difference between severe RP cases and non-RP cases.

Optimal feature group

The final optimal features for six sets of WL-R, WL-D, WL-RD, FWL-R, FWL-D, and FWL-RD were listed in Supplementary Table S1. The model performance with different feature numbers was plotted in Supplementary Figure S1. A total of 39, 24, and 34 features were kept in the final optimal feature groups for FWL-R, FWL-D, and FWL-RD, respectively. The FWL-RD features consisted of 6 dosiomics and 28 radiomics features. For the region of WL, a total of 31, 4, and 29 features were utilized in the final optimal feature group for the R, D, and RD sets, respectively. The RD features consist of 6 dosiomics and 23 radiomics features. The feature number in the model of WL-R set was 35 with the maximum testing AUC. However, only 31 features were utilized in the final optimal feature group.

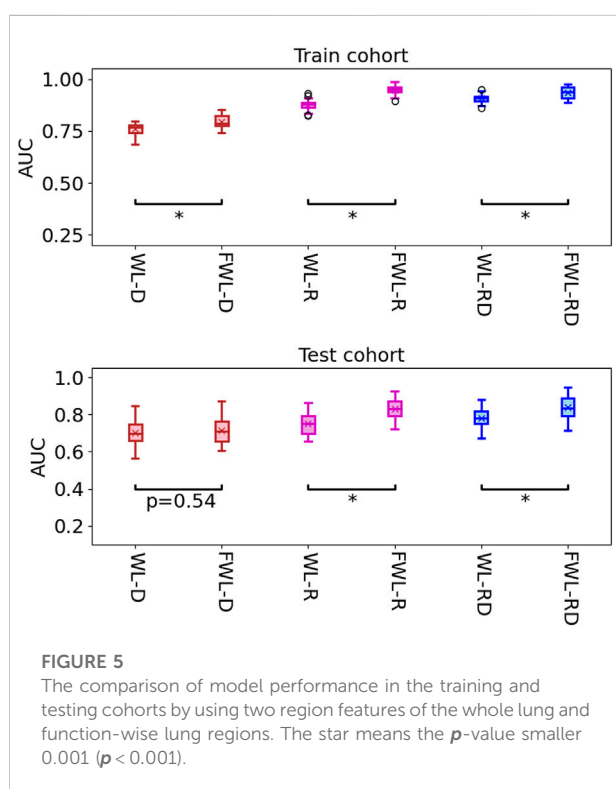
Model performance

Table 2 shows the average model performance for six feature sets of WL-D, WL-R, WL-RD, FWL-D, FWL-R, and FWL-RD in training and testing cohorts. Figure 5 shows model performance comparison between the WL and FWL models using each feature modality by considering 30 times data separations. For using dual-omics, the model using FWL-RD achieved significantly higher performance than the model using WL-RD in both training and testing cohorts, with an average AUC \pm STD and 95% confidence interval of 0.927 ± 0.031 [0.917, 0.939]/ 0.849 ± 0.064 [0.823, 0.869] and 0.885 ± 0.028 [0.874, 0.893]/ 0.762 ± 0.053 [0.743, 0.781] ($p < 0.001$), respectively. For using radiomics, the model using FWL-R feature yielded a better classification result than the model using WL-R features both in the training and testing cohorts with AUC \pm STD [95% CI] of 0.919 ± 0.036 [0.907, 0.933]/ 0.820 ± 0.052 [0.802, 0.838] and 0.862 ± 0.028 [0.851, 0.871]/ 0.750 ± 0.057 [0.730, 0.771] ($p < 0.001$), respectively. The FWL-D feature-based model performance with AUC \pm STD [95% CI] of 0.782 ± 0.032 [0.771, 0.794] obtained a better classification performance than the WL-D feature-based model with AUC \pm STD [95% CI] of 0.740 ± 0.028 [0.729, 0.750],

TABLE 2 The average model performance in the training and testing cohorts using six feature sets of WL-D, WL-R, WL-RD, FWL-D, FWL-R, FWL-RD. The dark red color represents higher values.

	Cohorts	WL-D	WL-R	WL-RD	FWL-D	FWL-R	FWL-RD
AUC	Train	0.761	0.877	0.908	0.796	0.949	0.936
	Test	0.704	0.751	0.781	0.715	0.829	0.840
ACC	Train	0.690	0.785	0.811	0.727	0.876	0.877
	Test	0.640	0.665	0.677	0.664	0.747	0.764
Pre	Train	0.685	0.770	0.829	0.701	0.882	0.924
	Test	0.630	0.642	0.662	0.638	0.739	0.799
Re	Train	0.589	0.749	0.742	0.696	0.844	0.794
	Test	0.536	0.603	0.602	0.639	0.683	0.665
F1	Train	0.631	0.757	0.778	0.696	0.860	0.852
	Test	0.570	0.611	0.624	0.629	0.705	0.716

AUC, area under the receiver operator characteristic curve; ACC, accuracy; Pre, Precision; Re, Recall; F1, F1-score.



however there were no significant difference in the testing cohorts with AUC \pm STD [95% CI] of 0.725 ± 0.064 [0.703, 0.746] against to 0.710 ± 0.068 [0.686, 0.734] ($p = 0.37$).

The decision curve analysis for all models is shown in Figure 6. The models using the FWL region's feature performed a better clinical value than the models using WL region's feature for both single and dual-omics. And, the model using FWL-RD achieved the highest overall net benefit across the majority of the range of reasonable threshold probabilities in

both training and testing cohorts compared with the other feature group. ROC in the training and testing cohorts for all six models and their comparison in each feature modality and lung region were shown in Supplementary Figures S2, S3. For the best model with FWL-RD feature set, the weights of each final optimal features are displayed in Supplementary Table S3.

Discussion

In the study, we proposed an FWL sub-region generation method to benefit the prediction of acute radiation pneumonitis using pre-treatment imaging data. The predictability of each single omics and dual-omics (radiomics, dosiomics, and their combination) from the FWL were investigated and compared with the features from the WL region. As shown in Table 2 and Figure 6, the evaluation metrics and the decision curve analysis revealed that the FWL subregion generation method presented a significant prediction improvement in terms of radiomics and dual-omics features than using the WL region ($p < 0.001$), but not for dosiomics features.

For the models using FWL feature sets, the prediction accuracy has significant improvement as compared with the models using WL feature sets. This may suggest the features from both high and low functional lung regions have better prognostic power than the WL region. In FWL-R, FWL-D, and FWL-RD final features sets, there are 16, 7, and 15 features from the high functional regions, while they are 23, 2, and 19 for low functional regions. It should be noted that the high FWL dosiomics features played a more critical role in the FWL-D signatures. Several studies have showed the same conclusion for predicting RP when using the dose features from the high functional region (Yorke et al., 2002; Hunt et al., 2006; Wang et al., 2012; Hoover et al., 2014; Faught et al., 2017; Bucknell et al., 2018; Lee et al., 2018; O'Reilly et al., 2020). The low functional

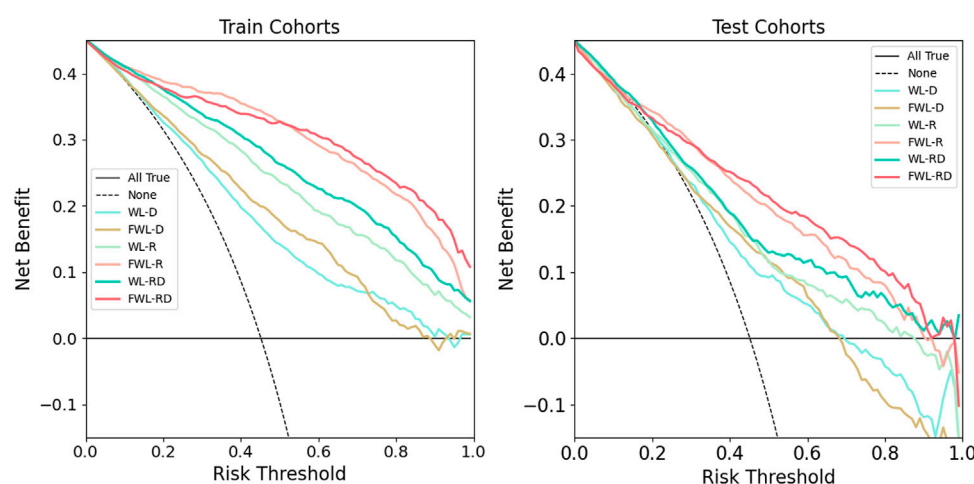


FIGURE 6

The comparison of clinical application values using decision curve analysis. The left and right plots showed the results of training and testing cohorts, respectively. The solid cyan line, solid brown line, solid light green line, solid pink line, solid green line, and solid red line represent the results of WL-D, FWL-D, WL-R, FWL-R, WL-RD, FWL-RD sets, respectively. The horizontal solid black line denotes that all patients didn't suffer from RP. On the contrary, the dashed black line represents a condition that all patients occurred RP.

lung radiomics occupied a slightly more quantity than high FWL regions. The lower FWL's radiomics signatures further lead to the more low FWL's dual-omics signatures. It may imply that the heterogeneity of lung tissue, characterized by radiomics feature, presented both in high and low functional regions. The improvement for FWL-R to WL-R and FWL-RD to WL-RD may come from the smaller volume of region (high or low functional regions) than the WL region can benefit from extracting and distinguishing more heterogeneous radiomics features. Palm *et al.* (Palma *et al.*, 2019) also found that the lower right lung has a significant correlation with radiation pneumonitis. In general, the lower functional region covers part of the lower right lung region. This may be one reason for the improvement by integrating the features from the low functional lung region.

For the FWL-RD signatures, except for one radiomics feature, the other radiomics signatures come from filtered CT images. The other radiomics signatures of FWL-RD are high-order features to describe gray level textural information of the lung region. For dosiomics signatures of FWL-RD, most of the signatures come from high-order features describing the dose distribution in the lung region or subregion. The selected final features are dominated by high-order omics features, which are also similar to previous studies (Hirose *et al.*, 2020; Bourbonne *et al.*, 2021; Jiang *et al.*, 2021; Puttanawarut *et al.*, 2022). None of DVH parameters (such as V_5 , V_{20} , D_{mean}) were included in our data study, which is inconsistent with the previous studies (Palma *et al.*, 2013; Glick *et al.*, 2018; Onishi *et al.*, 2018).

In our dataset, the threshold of 0.3 only was adopted in dividing the lung into high and low functional lung regions.

Previous studies report that the threshold can be different, ranging from 20% to the value of the maximum functional lung image pixel (Seppenwoolde *et al.*, 2000; Kawakami *et al.*, 2007; Lavrenkov *et al.*, 2007; Ohno *et al.*, 2011; Ding *et al.*, 2018). Following their method, we have investigated the model performance using three omics features from the FWL regions using a list threshold from 0.2 to 0.8 with a step of 0.1, as shown in Supplementary Figure S4. Besides, we statistically analyzed the difference for the testing AUC between the threshold of 0.3 and the others by using the *t*-test, as shown in Supplementary Table S4. As shown in the figure and table, except for dosiomics, the threshold of 0.3 achieved a statistical higher classification result in testing cohorts for the majority of feature groups of radiomics and dual-omics (except for the threshold of 0.2, 0.6 and 0.8 in RD feature groups with $p = 0.107$, 0.054 and $p = 0.343$ respectively), which is consistent with a previous study (Seppenwoolde *et al.*, 2000). Based on the previous observations, we determine the threshold of 0.3 as an optimal threshold by considering three kinds of features. For dosiomics, the threshold of 0.2 obtained a maximum AUC value, which agreed with the study (Ding *et al.*, 2018). In addition, an optimal threshold only using the high functional lung region's omics features was also assessed with the threshold list, as shown in Supplementary Figure S5. And the corresponding statistical analysis was shown in Supplementary Table S5. However, non-significant improvement ($p > 0.05$) was observed by comparing the high-functional lung regions to the whole lung region.

The current study still faces several limitations. First, the functional lung images generated by DL model may have uncertainties. Even though the DL-based approach can make

the image acquisition convenient and less costly for patients, the uncertainty caused by the DL model can cause a discrepancy in high and low functional lung regions. This variance may finally affect the correlation relation between some omics features and the RP, thus changing final signature features. This proposed FWL approach should be verified using the real perfusion lung image. Second, all involved patients were treated by the IMRT technique. The other radiotherapy, such as volumetric modulated arc therapy and proton radiotherapy, should be investigated for our proposed FWL region method to further explore its feasibility and capability. Third, the unbalanced between the small sample cohort and a large number of features can induce overfitting both in training and testing cohorts (Hawkins, 2004). To minimize this effect, we adopted randomly under-sampling method in the feature selection to enhance the stability of final feature signatures. However, a large prospective cohort should be carried out to access the validation of our proposed FWL method. Finally, the reproducibility and stability of omics features were not validated against disturbance. Some studies have demonstrated that the reproducibility and stability of features can be affected by the dose calculation grid size and algorithm (Placidi et al., 2020), CT image acquisition, ROI segmentation (Zwanenburg et al., 2019), and time or volume change in 4D-CT (Larue et al., 2017; Lafata et al., 2018), etc. Therefore, it is important to validate the feature robustness before clinical application.

Conclusion

In the study, we proposed an FWL approach to deeply explore the heterogeneous lung tissue and omics features and evaluated the approach in improvement of the prediction of the RP for lung cancer IMRT patients. The dual-omics features from different functional regions can improve the prediction of radiation pneumonitis for lung cancer patients under IMRT treatment. This function-wise dual-omics analysis method holds great promise to improve the prediction of radiation pneumonitis for lung cancer patients.

Data availability statement

The datasets generated for this study are available on request to the corresponding author.

Ethics statement

The studies involving human participants were reviewed and approved by the Institutional Review Board of the Affiliated Cancer Hospital of Zhengzhou University. Written informed

consent for participation was not required for this study in accordance with the national legislation and the institutional requirements.

Author contributions

BL and GR contributed to the study for data analyzing and writing. HG and JC designed and organized the study. WG, CC, YW and, YY collected the image data. XZ, QD, and LM collected clinical data. JZ, XT, and ZM contributed to the study for model construction and evaluation. S-KL, HT, and HL reviewed and edited the manuscript. All authors contributed to the article and approved the submitted version.

Funding

This research was partly supported by the Provincial and Ministry Co-constructed Project of Henan Province Medical Science and Technology Research (SBGJ202103038 and SBGJ202102056), Henan Province Key R&D and Promotion Project (Science and Technology Research) (222102310015), research grants of General Research Fund (GRF 15103520), the Research Grants Council, and Health and Medical Research Fund (HMRF 07183266), the Food and Health Bureau, the Government of the Hong Kong Special Administrative Region.

Conflict of Interest

The authors declare that the research was conducted in the absence of any commercial or financial relationships that could be construed as a potential conflict of interest.

Publisher's note

All claims expressed in this article are solely those of the authors and do not necessarily represent those of their affiliated organizations, or those of the publisher, the editors and the reviewers. Any product that may be evaluated in this article, or claim that may be made by its manufacturer, is not guaranteed or endorsed by the publisher.

Supplementary material

The Supplementary Material for this article can be found online at: <https://www.frontiersin.org/articles/10.3389/fphar.2022.971849/full#supplementary-material>

References

- Adachi, T., Nakamura, M., Shintani, T., Mitsuyoshi, T., Kakino, R., Ogata, T., et al. (2021). Multi-institutional dose-segmented dosimetric analysis for predicting radiation pneumonitis after lung stereotactic body radiation therapy. *Med. Phys.* 48, 1781–1791. doi:10.1002/mp.14769
- Baisden, J. M., Romney, D. A., Reish, A. G., Cai, J., Sheng, K., Jones, D. R., et al. (2007). Dose as a function of lung volume and planned treatment volume in helical tomotherapy intensity-modulated radiation therapy-based stereotactic body radiation therapy for small lung tumors. *Int. J. Radiat. Oncol. Biol. Phys.* 68, 1229–1237. doi:10.1016/j.ijrobp.2007.03.024
- Barriger, R. B., Forquer, J. A., Brabham, J. G., Andolino, D. L., Shapiro, R. H., Henderson, M. A., et al. (2012). A dose-volume analysis of radiation pneumonitis in non-small cell lung cancer patients treated with stereotactic body radiation therapy. *Int. J. Radiat. Oncology*Biophysics* 82, 457–462. doi:10.1016/j.ijrobp.2010.08.056
- Begosh-Mayne, D., Kumar, S. S., Toffel, S., Okunieff, P., and O'Dell, W. (2020). The dose-response characteristics of four NTCP models: Using a novel CT-based radiomics method to quantify radiation-induced lung density changes. *Sci. Rep.* 10, 1–9. doi:10.1038/s41598-020-67499-0
- Bongers, E. M., Botticella, A., Palma, D. A., Haasbeek, C. J. A., Warner, A., Verbakel, W. F. A. R., et al. (2013). Predictive parameters of symptomatic radiation pneumonitis following stereotactic or hypofractionated radiotherapy delivered using volumetric modulated arcs. *Radiotherapy Oncol.* 109, 95–99. doi:10.1016/j.radonc.2013.10.011
- Bourbonne, V., Da-Ano, R., Jaouen, V., Lucia, F., Dissaux, G., Bert, J., et al. (2021). Radiomics analysis of 3D dose distributions to predict toxicity of radiotherapy for lung cancer. *Radiother. Oncol.* 155, 144–150. doi:10.1016/j.radonc.2020.10.040
- Bourbonne, V., Lucia, F., Dissaux, G., Bert, J., Visvikis, D., Pradier, O., et al. (2020). Pulmonary and esophageal toxicity in lung cancer treated by (Chemo)-radiotherapy: A radiomics-based prediction model. *Int. J. Radiat. Oncology*Biophysics* 108, S31. doi:10.1016/j.ijrobp.2020.07.2127
- Bradley, J. D., Hu, C., Komaki, R. R., Masters, G. A., Blumenschein, G. R., Schild, S. E., et al. (2020). Long-Term results of NRG oncology RTOG 0617: Standard-versus high-dose chemoradiotherapy with or without cetuximab for unresectable stage III non-small-cell lung cancer. *Jco* 38, 706–714. doi:10.1200/JCO.19.01162
- Bucknell, N. W., Hardcastle, N., Bressel, M., Hofman, M. S., Kron, T., Ball, D., et al. (2018). Functional lung imaging in radiation therapy for lung cancer: A systematic review and meta-analysis. *Radiother. Oncol.* 129, 196–208. doi:10.1016/j.radonc.2018.07.014
- Buitinck, L., Louppe, G., Blondel, M., Pedregosa, F., Mueller, A., Grisel, O., et al. (2013). API design for machine learning software: Experiences from the scikit-learn project, 1–15. arXiv.
- Cai, J., Malhotra, H. K., and Orton, C. G. (2014). A 3D-conformal technique is better than IMRT or VMAT for lung SBRT. *Med. Phys.* 41, 040601–040604. doi:10.1118/1.4856175
- Chang, C.-K., Lin, H.-W., Ip, W.-H., Prince, T. A., Kulkarni, S. R., Levitan, D., et al. (2016). Large super-fast rotator hunting using the intermediate palomar transient factory. *ApJS* 227, 20. doi:10.3847/0067-0049/227/2/20
- DeLong, E. R., DeLong, D. M., and Clarke-Pearson, D. L. (1988). Comparing the areas under two or more correlated receiver operating characteristic curves: A nonparametric approach. *Biometrics* 44, 837. doi:10.2307/2531595
- Ding, X., Man, X., Sun, M., Xing, J., Fan, T., Gao, M., et al. (2018). Which is the optimal threshold for defining functional lung in single-photon emission computed tomography lung perfusion imaging of lung cancer patients? *Nucl. Med. Commun.* 39, 103–109. doi:10.1097/MNM.0000000000000774
- Farr, K. P., Kallehauge, J. F., Møller, D. S., Khalil, A. A., Kramer, S., Bluhme, H., et al. (2015). Inclusion of functional information from perfusion SPECT improves predictive value of dose-volume parameters in lung toxicity outcome after radiotherapy for non-small cell lung cancer: A prospective study. *Radiotherapy Oncol.* 117, 9–16. doi:10.1016/j.radonc.2015.08.005
- Faught, A. M., Yamamoto, T., Castillo, R., Castillo, E., Zhang, J., Miften, M., et al. (2017). Evaluating which dose-function metrics are most critical for functional-guided radiation therapy. *Int. J. Radiat. Oncol. Biol. Phys.* 99, 202–209. doi:10.1016/j.ijrobp.2017.03.051
- Ganti, A. K. P., Loo, B. W., Bassetti, M., Blakely, C., Chiang, A., D'Amico, T. A., et al. (2021). Small cell lung cancer, version 2.2022, NCCN clinical practice guidelines in oncology. *JNCCN J. Natl. Compr. Cancer Netw.* 19, 1441–1464. doi:10.6004/JNCCN.2021.0058
- Glick, D., Lyen, S., Kandel, S., Shaper, S., Le, L., Lindsay, P., et al. (2018). Impact of pretreatment interstitial lung disease on radiation pneumonitis and survival in patients treated with lung stereotactic body radiation therapy (SBRT). *Clin. Lung Cancer* 19, e219–e226. doi:10.1016/j.clcc.2017.06.021
- Hawkins, D. M. (2004). The problem of overfitting. *J. Chem. Inf. Comput. Sci.* 44, 1–12. doi:10.1021/ci0342472
- Hirose, T., Arimura, H., Ninomiya, K., Yoshitake, T., Fukunaga, J., and Shioyama, Y. (2020). Radiomic prediction of radiation pneumonitis on pretreatment planning computed tomography images prior to lung cancer stereotactic body radiation therapy. *Sci. Rep.* 10, 1. doi:10.1038/s41598-020-77552-7
- Hoover, D. A., Reid, R. H., Wong, E., Stitt, L., Sabondjian, E., Rodrigues, G. B., et al. (2014). SPECT-based functional lung imaging for the prediction of radiation pneumonitis: A clinical and dosimetric correlation. *J. Med. Imaging Radiat. Oncol.* 58, 214–222. doi:10.1111/1754-9485.12145
- Hunt, M. A., Jackson, A., Narayana, A., and Lee, N. (2006). Geometric factors influencing dosimetric sparing of the parotid glands using IMRT. *Int. J. Radiat. Oncology*Biophysics* 66, 296–304. doi:10.1016/j.ijrobp.2006.05.028
- Jiang, W., Song, Y., Sun, Z., Qiu, J., and Shi, L. (2021). Dosimetric factors and radiomics features within different regions of interest in planning CT images for improving the prediction of radiation pneumonitis. *Int. J. Radiat. Oncol. Biol. Phys.* 110, 1161–1170. doi:10.1016/j.ijrobp.2021.01.049
- Kawakami, Y., Suga, K., Zaki, M., Iwanaga, H., Yamashita, T., Hayashi, N., et al. (2007). Semi-quantitation of pulmonary perfusion imaging correlates with the dosimetric parameters of radiation pneumonitis in radiation therapy planning for lung cancer. *Ann. Nucl. Med.* 21, 577–584. doi:10.1007/s12149-007-0071-6
- Kimura, T., Doi, Y., Nakashima, T., Imano, N., Kawabata, H., Nishibuchi, I., et al. (2015). Combined ventilation and perfusion imaging correlates with the dosimetric parameters of radiation pneumonitis in radiation therapy planning for lung cancer. *Int. J. Radiat. Oncol. Biol. Phys.* 93, 778–787. doi:10.1016/j.ijrobp.2015.08.024
- Kipritidis, J., Hofman, M. S., Siva, S., Callahan, J., Le Roux, P. Y., Woodruff, H. C., et al. (2015). Estimating lung ventilation directly from 4D CT Hounsfield unit values. *Med. Phys.* 43, 33–43. doi:10.1118/1.4937599
- Kong, F. M., Ten Haken, R. K., Schipper, M. J., Sullivan, M. A., Chen, M., Lopez, C., et al. (2005). High-dose radiation improved local tumor control and overall survival in patients with inoperable/unresectable non-small-cell lung cancer: Long-term results of a radiation dose escalation study. *Int. J. Radiat. Oncol. Biol. Phys.* 63, 324–333. doi:10.1016/j.ijrobp.2005.02.010
- Lafata, K., Cai, J., Wang, C., Hong, J., Kelsey, C. R., and Yin, F. F. (2018). Spatial-temporal variability of radiomic features and its effect on the classification of lung cancer histology. *Phys. Med. Biol.* 63, 225003. doi:10.1088/1361-6560/AAE56A
- Lam, S.-K., Zhang, Y.-P., Zhang, J., Li, B., Sun, J.-C., Liu, Y.-T. C., et al. (2021). Multi-organ omics-based prediction for adaptive radiation therapy eligibility in nasopharyngeal carcinoma patients undergoing concurrent chemoradiotherapy. *Front. Oncol.* 11, 5406. doi:10.3389/FONC.2021.792024
- Lambin, P., Leijenaar, R. T. H., Deist, T. M., Peerlings, J., de Jong, E. E. C., van Timmeren, J., et al. (2017). Radiomics: The bridge between digital imaging and personalized medicine. *Nat. Rev. Clin. Oncol.* 14, 749–762. doi:10.1038/nrclinonc.2017.141
- Larue, R. T. H. M., Van De Voorde, L., van Timmeren, J. E., Leijenaar, R. T. H., Berbee, M., Sosef, M. N., et al. (2017). 4DCT imaging to assess radiomics feature stability: An investigation for thoracic cancers. *Radiother. Oncol.* 125, 147–153. doi:10.1016/j.radonc.2017.07.023
- Lavrenkov, K., Christian, J. A., Partridge, M., Niotsikou, E., Cook, G., Parker, M., et al. (2007). A potential to reduce pulmonary toxicity: The use of perfusion SPECT with IMRT for functional lung avoidance in radiotherapy of non-small cell lung cancer. *Radiother. Oncol.* 83, 156–162. doi:10.1016/j.radonc.2007.04.005
- Lee, H. J., Zeng, J., Vesselle, H. J., Patel, S. A., Rengan, R., and Bowen, S. R. (2018). Correlation of functional lung heterogeneity and dosimetry to radiation pneumonitis using perfusion SPECT/CT and FDG PET/CT imaging. *Int. J. Radiat. Oncol. Biol. Phys.* 102, 1255–1264. doi:10.1016/j.ijrobp.2018.05.051
- Liang, B., Yan, H., Tian, Y., Chen, X., Yan, L., Zhang, T., et al. (2019). Dosimetrics: Extracting 3D spatial features from dose distribution to predict incidence of radiation pneumonitis. *Front. Oncol.* 9, 269. doi:10.3389/fonc.2019.00269
- Marks, L. B., Bentzen, S. M., Deasy, J. O., Kong, F. M., Bradley, J. D., Vogelius, I. S., et al. (2010). Radiation dose-volume effects in the lung. *Int. J. Radiat. Oncology*Biophysics* 76, S70–S76. doi:10.1016/j.ijrobp.2009.06.091
- Ohno, Y., Koyama, H., Nogami, M., Takenaka, D., Onishi, Y., Matsumoto, K., et al. (2011). State-of-the-art radiological techniques improve the assessment of postoperative lung function in patients with non-small cell lung cancer. *Eur. J. Radiology* 77, 97–104. doi:10.1016/j.ejrad.2009.07.024
- Onishi, H., Yamashita, H., Shioyama, Y., Matsumoto, Y., Takayama, K., Matsuo, Y., et al. (2018). Stereotactic body radiation therapy for patients with pulmonary interstitial change: High incidence of fatal radiation pneumonitis in a retrospective multi-institutional study. *Cancers* 10, 257. doi:10.3390/cancers10080257

- O'Reilly, S., Jain, V., Huang, Q., Cheng, C., Teo, B. K. K., Yin, L., et al. (2020). Dose to highly functional ventilation zones improves prediction of radiation pneumonitis for proton and photon lung cancer radiation therapy. *Int. J. Radiat. Oncology*Biophysics* 107, 79–87. doi:10.1016/j.ijrobp.2020.01.014
- Owen, D. R., Sun, Y., Boonstra, P. S., McFarlane, M., Viglianti, B. L., Balter, J. M., et al. (2021). Investigating the SPECT dose-function metrics associated with radiation-induced lung toxicity risk in patients with non-small cell lung cancer undergoing radiation therapy. *Adv. Radiat. Oncol.* 6, 100666. doi:10.1016/j.adro.2021.100666
- Palma, D. A., Senan, S., Tsujino, K., Barriger, R. B., Rengan, R., Moreno, M., et al. (2013). Predicting radiation pneumonitis after chemoradiation therapy for lung cancer: An international individual patient data meta-analysis. *Int. J. Radiat. Oncology*Biophysics* 85, 444–450. doi:10.1016/j.ijrobp.2012.04.043
- Palma, G., Monti, S., Xu, T., Scifoni, E., Yang, P., Hahn, S. M., et al. (2019). Spatial dose patterns associated with radiation pneumonitis in a randomized trial comparing intensity-modulated photon therapy with passive scattering proton therapy for locally advanced non-small cell lung cancer. *Int. J. Radiat. Oncology*Biophysics* 104, 1124–1132. doi:10.1016/j.ijrobp.2019.02.039
- Pedregosa, F., Varoquaux, G., Gramfort, A., Michel, V., Thirion, B., Grisel, O., et al. (2011). Scikit-learn: Machine learning in Python. *J. Mach. Learn. Res.* 12, 2825–2830.
- Pham, M. T., Woodford, O. J., Perbet, F., Maki, A., Stenger, B., and Cipolla, R. (2011). A new distance for scale-invariant 3D shape recognition and registration. *Proc. IEEE Int. Conf. Comput. Vis.* 2011, 145–152. doi:10.1109/ICCV.2011.6126236
- Pinnix, C. C., Smith, G. L., Milgrom, S., Osborne, E. M., Reddy, J. P., Akhtari, M., et al. (2015). Predictors of radiation pneumonitis in patients receiving intensity modulated radiation therapy for Hodgkin and non-hodgkin lymphoma. *Int. J. Radiat. Oncol. Biol. Phys.* 92, 175–182. doi:10.1016/j.ijrobp.2015.02.010
- Placidi, L., Lenkowicz, J., Cusumano, D., Boldrini, L., Dinapoli, N., and Valentini, V. (2020). Stability of dosimetric features extraction on grid resolution and algorithm for radiotherapy dose calculation. *Phys. Medica* 77, 30–35. doi:10.1016/j.ejmp.2020.07.022
- Puttanawarut, C., Sirirutbunkajorn, N., Tawong, N., Jiarpinitnun, C., Khachonkham, S., Pattaranutaporn, P., et al. (2022). Radiomic and dosimetric features for the prediction of radiation pneumonitis across esophageal cancer and lung cancer. *Front. Oncol.* 12, 1–9. doi:10.3389/fonc.2022.768152
- Ren, G., Lam, S. K., Zhang, J., Xiao, H., Cheung, A. L., Ho, W. Y., et al. (2021). Investigation of a novel deep learning-based computed tomography perfusion mapping framework for functional lung avoidance radiotherapy. *Front. Oncol.* 11, 1–12. doi:10.3389/fonc.2021.644703
- Ren, G., Zhang, J., Li, T., Xiao, H., Cheung, L. Y., Ho, W. Y., et al. (2021). Deep learning-based computed tomography perfusion mapping (DL-CTPM) for pulmonary CT-to-perfusion translation. *Int. J. Radiat. Oncol. Biol. Phys.* 110, 1508–1518. doi:10.1016/j.ijrobp.2021.02.032
- Seppenwoolde, Y., Muller, S. H., Theuvs, J. C. M., Baas, P., Belderbos, J. S. A., Boersma, L. J., et al. (2000). Radiation dose-effect relations and local recovery in perfusion for patients with non-small-cell lung cancer. *Int. J. Radiat. Oncol. Biol. Phys.* 47, 681–690. doi:10.1016/S0360-3016(00)00454-5
- Sung, H., Ferlay, J., Siegel, R. L., Laversanne, M., Soerjomataram, I., Jemal, A., et al. (2021). Global cancer statistics 2020: GLOBOCAN estimates of incidence and mortality worldwide for 36 cancers in 185 countries. *CA A Cancer J. Clin.* 71, 209–249. doi:10.3322/caac.21660
- Vallat, R. (2018). Pingouin: Statistics in Python. *Joss* 3, 1026. doi:10.21105/joss.01026
- Vickers, A. J., and Elkin, E. B. (2006). Decision curve analysis: A novel method for evaluating prediction models. *Med. Decis. Mak.* 26, 565–574. doi:10.1177/0272989X06295361
- Vickers, A. J., van Calster, B., and Steyerberg, E. W. (2019). A simple, step-by-step guide to interpreting decision curve analysis. *Diagn. Progn. Res.* 3, 1–8. doi:10.1186/s41512-019-0064-7
- Wang, D., Sun, J., Zhu, J., Li, X., Zhen, Y., and Sui, S. (2012). Functional dosimetric metrics for predicting radiation-induced lung injury in non-small cell lung cancer patients treated with chemoradiotherapy. *Radiat. Oncol.* 7, 1. doi:10.1186/1748-717X-7-69
- Wang, Z., Chen, M., Sun, J., Jiang, S., Wang, L., Wang, X., et al. (2020). Lyman-Kutcher-Burman normal tissue complication probability modeling for radiation-induced esophagitis in non-small cell lung cancer patients receiving proton radiotherapy. *Radiother. Oncol.* 146, 200–204. doi:10.1016/j.radonc.2020.03.003
- Weller, A., Dunlop, A., Oxer, A., Gunapala, R., Murray, I., Gray, M. J., et al. (2019). Spect perfusion imaging versus CT for predicting radiation injury to normal lung in lung cancer patients. *Br. J. Radiol.* 92, 20190184–20190189. doi:10.1259/bjr.20190184
- Xiao, L., Yang, G., Chen, J., Yang, Y., Meng, X., Wang, X., et al. (2018). Comparison of predictive powers of functional and anatomic dosimetric parameters for radiation-induced lung toxicity in locally advanced non-small cell lung cancer. *Radiother. Oncol.* 129, 242–248. doi:10.1016/j.radonc.2018.09.005
- Yorke, E. D., Jackson, A., Rosenzweig, K. E., Merrick, S. A., Gabrys, D., Venkatraman, E. S., et al. (2002). Dose-volume factors contributing to the incidence of radiation pneumonitis in non-small-cell lung cancer patients treated with three-dimensional conformal radiation therapy. *Int. J. Radiat. Oncol. Biol. Phys.* 54, 329–339. doi:10.1016/S0360-3016(02)02929-2
- Yu, T.-T., Lam, S.-K., Kar, F., Lee, -H., Au, K. H., Wai-Yi Yip, C., et al. (2019). Constructing novel prognostic biomarkers of advanced nasopharyngeal carcinoma from multiparametric MRI radiomics using ensemble-model based iterative feature selection. arXiv.
- Zhang, X. J., Sun, J. G., Sun, J., Ming, H., Wang, X. X., Wu, L., et al. (2012). Prediction of radiation pneumonitis in lung cancer patients: A systematic review. *J. Cancer Res. Clin. Oncol.* 138, 2103–2116. doi:10.1007/S00432-012-1284-1
- Zwanenburg, A., Leger, S., Agolli, L., Pilz, K., Troost, E. G. C., Richter, C., et al. (2019). Assessing robustness of radiomic features by image perturbation. *Sci. Rep.* 9, 614. doi:10.1038/s41598-018-36938-4

Advantages of publishing in Frontiers



OPEN ACCESS

Articles are free to read
for greatest visibility
and readership



FAST PUBLICATION

Around 90 days
from submission
to decision



HIGH QUALITY PEER-REVIEW

Rigorous, collaborative,
and constructive
peer-review



TRANSPARENT PEER-REVIEW

Editors and reviewers
acknowledged by name
on published articles

Frontiers

Avenue du Tribunal-Fédéral 34
1005 Lausanne | Switzerland

Visit us: www.frontiersin.org

Contact us: frontiersin.org/about/contact



REPRODUCIBILITY OF RESEARCH

Support open data
and methods to enhance
research reproducibility



DIGITAL PUBLISHING

Articles designed
for optimal readership
across devices



FOLLOW US

@frontiersin



IMPACT METRICS

Advanced article metrics
track visibility across
digital media



EXTENSIVE PROMOTION

Marketing
and promotion
of impactful research



LOOP RESEARCH NETWORK

Our network
increases your
article's readership